

# Disordered Spin Systems: Ground States and Ordering Kinetics

A thesis submitted for the degree of  
*Doctor of Philosophy*

Manoj Kumar



School of Physical Sciences  
Jawaharlal Nehru University  
New Delhi - 110067, India

July 2017

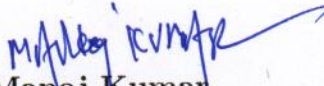
*To my family*

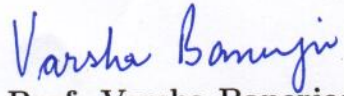
## Declaration

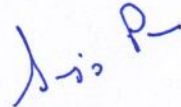
---


I hereby declare that the work reported in this thesis is entirely original and has been carried out by me under the joint supervision of Prof. Sanjay Puri at the School of Physical Sciences, Jawaharlal Nehru University, New Delhi, and Prof. Varsha Banerjee at the Department of Physics, Indian Institute of Technology Delhi, New Delhi. I further declare that it has not formed the basis for the award of any degree, diploma, associateship or similar title of any university or institution.

July 2017

  
Manoj Kumar

  
Prof. Varsha Banerjee  
Thesis Co-supervisor  
Department of Physics  
Indian Institute of Technology Delhi  
New Delhi - 110016.

  
Prof. Sanjay Puri  
Thesis Supervisor  
School of Physical Sciences  
Jawaharlal Nehru University  
New Delhi - 110067.

  
Prof. Riddhi Shah  
Dean  
School of Physical Sciences  
Jawaharlal Nehru University  
New Delhi - 110067.

# Acknowledgements

---

First and foremost, I express my deep and sincere gratitude to my supervisors, Prof. Sanjay Puri and Prof. Varsha Banerjee. Without their supervision, this work had never been possible. I am grateful to them for their continuous support, encouragement, and motivation in this long journey. It has been a great learning experience to work with them. I am very thankful to Prof. Sanjay Puri for introducing me to stimulating areas of statistical physics and providing me an opportunity to work in this field. During these years he has not only supervised but also has been a great teacher for me. My sincere thank to Prof. Varsha Banerjee for her inspiring guidance, constant support, and help.

I would like to acknowledge my collaborators, Dr. Federico Corberi (Physics Department, University of Salerno, Italy), Dr. Martin Weigel (Applied Mathematics Research Centre, Coventry University, England) and Dr. Raja Paul (Indian Association of Cultivation of Science, Kolkata, India) and others. I am very thankful, especially to Dr. Martin Weigel for hosting all my three visits to the Coventry University, UK, under IRSEP (International Research Staff Exchange Programme) through DIONICOS project. These were really beneficial visits and a great learning experience for me. I am also thankful to Dr. Federico Corberi for his valuable suggestions and guidance. I also thank Ravinder Kumar (Coventry University, England; and Leipzig University, Germany) and Swarnajit Chatterjee (IACS, Kolkata). I am honored to have worked with all my collaborators.

I would like to extend my gratitude towards all my teachers of SPS who taught me, especially Late Prof. Deepak Kumar, Prof. Akhilesh Pandey, Prof. Subir Sarkar, Prof. Shankar Prasad Das, Dr. Tanuja Mohanty, Prof. Subhasis Ghosh, Prof. Debashis Ghoshal. I greatly acknowledge Late Prof. Deepak Kumar for his wonderful lectures on Many Body Theory during my Pre-PhD.

I am grateful to CSIR, INDIA for providing the financial support during my MTech and PhD. I also thank all office staff members of SPS and JNU administration. I highly acknowledge for all facility provided by JNU, particularly the computational cluster, library, hostel, etc.

---

The group members of the statistical physics lab at SPS, have contributed immensely to my personal as well as my professional matters. I enjoyed the cooperative behavior of the group which immensely helped me to learn many new things. Thanks to Raishma, Prabhat, Awadhesh, Gaurav, Awaneesh, Avanish, Nisha, Shankar, Arindam. I thank all of them for contributing their best. I also thank to all my friends at IIT Delhi: Arun, Manish, Rupesh, Konark who have been very supporting during all these years. I am very thankful to Arun for having many fruitful discussions during all my PhD years. I also had enjoyed fruitful and valuable discussions with Prabhat, Awadhesh, Awaneesh, Avanish. Further, I warmly thank Arun, Gaurav, Prabhat and Avanish for reading and suggesting corrections in my thesis chapters. I had many wonderful memories and good times with all these friends.

I would also like to acknowledge the company of some senior friends of SPS: Ashwani, Ravi, Priya, Amrita, Gyaneshwar, Santosh, Vishwa Pal, Satyendra, Arun, Ambuj. Many Thanks to Ashwani and Ravi for helping during an initial stages of my PhD and later on valuable discussions from time to time. I also thank my classmates: Nidhi, Jyotsana, Varsha, Anshu, Premlata; and other friends of SPS: Jyoti, Him Shweta, Jyoti, Jogesh, Kamalesh and Bhagwana. Special thanks to Nidhi for having a great friendship. I had enjoyed a lot in the company of all my colleagues and friends.

I am very fortunate to have a very supporting family. My parents have always been a great source of strength and inspired me to work hard. I also appreciate the kindness, affection, and support from my sisters Lalita, Savita, brother-in-law Aman. I also thank for help and support from my wife Meenu in the final stages of PhD. Thanks to all my family and relatives.

JNU Campus has been an excellent place for me during my stay. I enjoyed a lot my PhD Life at JNU.

## List of Publications

---

1. Gaurav P. Shrivastav, **Manoj Kumar**, Varsha Banerjee and Sanjay Puri, *Ground-state morphologies in the random-field Ising model: Scaling properties and non-Porod behavior*, [Physical Review E \*\*90\*\*, 032140, 2014.](#)
2. **Manoj Kumar**, Varsha Banerjee and Sanjay Puri, *Random field Ising model with conserved kinetics: Super-universality violation, logarithmic growth law and the generalized Tomita sum rule*, [Europhysics Letters \*\*117\*\*, 10012, 2017.](#)
3. Federico Corberi, **Manoj Kumar**, Sanjay Puri and Eugenio Lippiello, *Equilibrium structure and off-equilibrium kinetics of a magnet with tunable frustration*, [Physical Review E \*\*95\*\*, 062136, 2017.](#)
4. **Manoj Kumar**, Varsha Banerjee and Sanjay Puri, *Random field Ising model in a uniform magnetic field: Ground states, pinned clusters and scaling laws*, Manuscript submitted to Physical Review E.
5. Arunkumar Bupathy, **Manoj Kumar**, Varsha Banerjee and Sanjay Puri, *Random field Ising models: Fractal interfaces and their implications*, Proceedings of CCP2016, Journal of Physics: Conference Series (2016).
6. **Manoj Kumar**, Ravinder Kumar, Martin Weigel, Varsha Banerjee and Sanjay Puri, *Study of approximate ground states in the  $q$ -state random-field Potts model*, Manuscript under preparation.
7. **Manoj Kumar**, Swarnajit Chatterjee, Raja Paul and Sanjay Puri, *Ordering kinetics in the random-bond XY model*, Manuscript under preparation.

## List of abbreviations

---

AFM	Antiferromagnetic
CF	Correlation function
COP	Conserved order parameter
DAFs	Dilute antiferromagnets
FM	Ferromagnetic
FSS	Finite size scaling
GC	Graph cut
GS	Ground state
IM	Ising model
LRO	Long range order
MC	Monte Carlo
MF	Mean field
NCOP	Non-conserved order parameter
NN	Nearest-neighbor
PM	Paramagnetic
PT	Parallel tempering
RB	Random bond
RBIM	Random bond Ising model
RBXYM	Random bond $XY$ model
RF	Random field
RFIM	Random field Ising model
RFPM	Random field Potts model
SF	Structure factor
SU	Superuniversality

# Contents

<b>Contents</b>	<b>vii</b>
<b>1 Introduction to Disordered Spin Systems</b>	<b>1</b>
1.1 Introduction . . . . .	1
1.2 Disordered Spin Models . . . . .	3
1.2.1 Random Field Ising Model . . . . .	3
1.2.2 Random Field Potts Model . . . . .	4
1.2.3 Random Bond Ising Model . . . . .	5
1.2.4 Random Bond $XY$ Model . . . . .	6
1.3 The Monte Carlo Method . . . . .	6
1.4 The Ground State Problem . . . . .	9
1.4.1 The Graph Cut Method . . . . .	9
1.5 Numerical Tools for Studying the Morphologies . . . . .	14
1.5.1 The Correlation Function and Structure Factor . . . . .	15
1.5.2 Characterization of Morphologies . . . . .	16
1.6 Phase Ordering Kinetics . . . . .	18
1.6.1 Domain Growth Laws in Pure Systems . . . . .	18
1.6.2 Domain Growth Laws in Disordered Systems . . . . .	20
1.7 Overview of the Thesis . . . . .	22
1.7.1 Overview of Part <b>I</b> . . . . .	23
1.7.2 Overview of Part <b>II</b> . . . . .	24
<b>References</b>	<b>26</b>



<b>I</b>	<b>Ground States in Disordered Spin Systems</b>	<b>29</b>
<b>2</b>	<b>Ground State Morphologies in the Random Field Ising Model</b>	<b>30</b>
2.1	Introduction . . . . .	30
2.2	The Ground State Method . . . . .	33
2.3	Detailed Numerical Results . . . . .	34
2.3.1	Ground States of the $d = 2$ RFIM . . . . .	34
2.3.2	Ground States of the $d = 3$ RFIM . . . . .	38
2.4	Experimental Evidence of Non-Porod Behavior . . . . .	43
2.5	Summary and Discussion . . . . .	44
	<b>References</b>	<b>47</b>
<b>3</b>	<b>Random Field Ising Model in a Uniform Magnetic Field</b>	<b>50</b>
3.1	Introduction . . . . .	50
3.2	The Model . . . . .	51
3.3	Detailed Numerical Results . . . . .	52
3.3.1	Ground State Morphologies . . . . .	52
3.3.2	Magnetization Curves . . . . .	53
3.3.3	Statistical Properties of Pinned Clusters . . . . .	56
3.4	Experimental Verification of non-Porod Results . . . . .	62
3.5	Summary and Discussion . . . . .	63
	<b>Appendix A Glossary of Variables, Scaling Functions, and the Critical Exponents</b>	<b>65</b>
	<b>References</b>	<b>67</b>
<b>4</b>	<b>Approximate Ground States in the Random Field Potts Model</b>	<b>69</b>
4.1	Introduction . . . . .	69
4.2	The Model and Methodology . . . . .	71
4.2.1	Parallel Tempering Method . . . . .	72
4.3	Numerical Results . . . . .	74
4.3.1	Approximate Ground States from the GC Method . . . . .	76
4.3.2	Comparisons with the PT Method . . . . .	79

4.3.3	Performance and Efficiency of the GC Method . . . . .	81
4.4	Critical Behavior in the $q = 3$ RFPM . . . . .	83
4.4.1	Binder Cumulant . . . . .	84
4.4.2	Specific Heat . . . . .	85
4.4.3	Magnetization or the Order Parameter . . . . .	89
4.5	Summary and Discussion . . . . .	91
<b>References</b>		<b>93</b>
 <b>II Ordering Kinetics in Disordered Spin Systems</b>		 <b>96</b>
 <b>5 Domain Growth in Random Field Ising Model with Conserved Kinetics</b>		 <b>97</b>
5.1	Introduction . . . . .	97
5.2	Simulation Details . . . . .	100
5.3	Numerical Results . . . . .	102
5.3.1	Domain Growth Morphologies . . . . .	102
5.3.2	Superuniversality Violation . . . . .	104
5.3.3	Domain Growth Law . . . . .	105
5.3.4	Interfacial Properties of the Domain Morphologies . . . . .	110
5.3.5	Generalized Tomita Sum Rule . . . . .	111
5.4	Summary and Conclusion . . . . .	113
<b>References</b>		<b>115</b>
 <b>6 Equilibrium Structure and Off-equilibrium Kinetics in a Tunable Frustrated Magnet</b>		 <b>118</b>
6.1	Introduction . . . . .	118
6.2	The Model . . . . .	121
6.2.1	The Geometry of the Bond Network . . . . .	121
6.3	The Structure of the Equilibrium States . . . . .	123
6.3.1	Ground States . . . . .	124
6.3.1.1	Ferromagnetic phase ( $0 \leq a < a_f$ ) . . . . .	125
6.3.1.2	Paramagnetic phase ( $a_f \leq a \leq a_a$ ) . . . . .	126

6.3.1.3	Defective antiferromagnet ( $a_a \leq a \leq 1$ ) . . . . .	128
6.3.2	Equilibrium States at a Finite Temperature . . . . .	129
6.4	Off-equilibrium Study of Growth Kinetics . . . . .	130
6.4.1	Simulation Details . . . . .	130
6.4.2	Numerical Results . . . . .	132
6.4.2.1	Ferromagnetic region $0 \leq a \leq a_f$ . . . . .	135
6.4.2.2	Paramagnetic region $a_f < a < a_a$ . . . . .	139
6.4.2.3	Antiferromagnetic region $a \geq a_a$ . . . . .	141
6.5	Summary and Conclusion . . . . .	142
 <b>Appendix B Suppression of Ferromagnetic Order for <math>a \gtrsim a_f</math></b>		<b>144</b>
 <b>Appendix C Suppression of Antiferromagnetic Order for <math>a \lesssim a_a</math></b>		<b>146</b>
 <b>References</b>		<b>148</b>
 <b>7 Ordering Kinetics in the Random Bond XY Model</b>		<b>151</b>
7.1	Introduction . . . . .	151
7.2	Modeling and Simulation Details . . . . .	154
7.2.1	Simulation Details for the Study of Critical Temperature .	154
7.2.2	Simulation Details for Study of Ordering Kinetics . . . . .	156
7.2.3	Growth Law for Pure XY Model . . . . .	157
7.3	Numerical Results . . . . .	159
7.3.1	Numerical Results for $d = 2$ RBXYM . . . . .	159
7.3.1.1	Estimation of transition temperatures . . . . .	159
7.3.1.2	Ordering kinetics . . . . .	159
7.3.2	Numerical Results for $d = 3$ RBXYM . . . . .	165
7.3.2.1	Estimation of transition temperatures . . . . .	166
7.3.2.2	Ordering kinetics . . . . .	166
7.4	Summary and Discussion . . . . .	170
 <b>References</b>		<b>172</b>

# Chapter 1

## Introduction to Disordered Spin Systems

### 1.1 Introduction

Spin systems with quenched disorder have been widely studied in condensed matter physics. Although these systems are ubiquitous, the complex nature of the spin-spin interactions creates difficulties in studying them analytically and computationally. In general, the disorders are of two types—*annealed* and *quenched*. A system is said to have quenched disorder if the random impurities are frozen and are not allowed to move. In the case of annealed disorder, the random impurities move and evolve with time. Indeed, the systems with quenched disorder are harder to analyze as compared to the annealed disorder and quite popular in statistical physics. An issue of interest for these systems is the nature of their thermodynamic *ground state* (GS) [1]. It contains important information about the critical behavior and *equilibrium* properties such as low temperature susceptibility, specific heat, etc. However, finding the GS in the disordered spin systems is not a trivial problem.

The quenched disorder introduces deep valleys in the free-energy landscape yielding a complicated scenario. The system can get stuck in a deep valley, i.e., opt for a local minimum which can be arbitrarily far from the global minimum, and may not reflect any of its GS properties. Standard numerical techniques such

as *Monte Carlo* (MC) with Metropolis algorithm [2], or simulated annealing [3], are often used to minimize the energy and access the GS, starting from an arbitrary initial condition. However, these techniques have several drawbacks such as lack of self-averaging, diverging computation times, and trapping in metastable states. Therefore, we still lack a complete understanding of the GS of disordered spin systems and many issues related to the *equilibrium* or the critical behavior of these systems remain unanswered.

Another fascinating class of problems in these systems is *phase-ordering dynamics*, which is the *nonequilibrium* evolution dynamics of a system when it is rendered thermodynamically unstable by a sudden change of external parameters such as, temperature  $T$ , pressure  $P$ , etc. The system will then grow as a function of time until it reaches the equilibrium or gets stuck into a metastable state. The dynamics of this non-equilibrium evolution of the system is described as *domain growth* or *coarsening* or *phase ordering dynamics* or *ordering kinetics*. The problem of the kinetics of phase transitions has been a subject of intense research interests in statistical physics during last two decades. This thesis focuses on the both, equilibrium as well as non-equilibrium aspects of the disordered spin systems. In equilibrium, we study the GS problem using *graph cut* (GC) method. In non-equilibrium, we study the ordering kinetics in these disordered system using MC techniques.

This chapter provides an overview and the organization of the thesis. Section 1.2 discusses the various types of disordered spin models which have been studied in this thesis. Sections 1.3 and 1.4 are devoted to the details of numerical techniques used to study these systems, namely, the MC method and the GC method. Section 1.5 describes the various numerical tools. Section 1.6 provides a detailed discussion of ordering kinetics in disordered models. Finally, in section 1.7, there is an overview of the thesis.

## 1.2 Disordered Spin Models

The typical Hamiltonian of a disordered spin system consists of two terms: spin-spin interaction term and a local field term [1, 4, 5], i.e.,

$$\mathcal{H} = - \sum_{\langle ij \rangle} J_{ij} s_i s_j - \sum_i h_i s_i. \quad (1.1)$$

Here,  $\langle ij \rangle$  denotes the *nearest-neighbor* (NN) sites  $i$  and  $j$ , and  $s_i$  is the spin variable at site  $i$ , which takes a value  $+1$  or  $-1$ . The parameter  $J_{ij}$  is the strength of exchange interaction between the NN pairs of spins  $s_i$  and  $s_j$ .  $\{h_i\}$  are the quenched random field variables extracted from a certain probability distribution, e.g., Gaussian, bimodal, etc. For *ferromagnetic* (FM) systems,  $\{J_{ij}\} \geq 0$  while for *antiferromagnetic* (AFM) systems,  $\{J_{ij}\} < 0$ . On the other hand, in *frustrated* systems,  $\{J_{ij}\}$  takes both, positive as well as negative values.

These models are broadly classified into two categories: *random field* (RF) models and *random bond* (RB) models. For RF models,  $\{J_{ij}\} = J$  and  $\{h_i\}$  are random. For RB models,  $\{J_{ij}\}$  are random and  $h_i = \text{constant}$ . In the RF category, we study the *random field Ising model* (RFIM) and *random field Potts model* (RFPM), and in the RB category, we study the *random bond Ising model* (RBIM) and *random-bond XY model* (RBXYM).

### 1.2.1 Random Field Ising Model

In the RFIM, all spins interact with the equal amount of strength, i.e.,  $\{J_{ij}\} \equiv J > 0$  and the disorder is introduced via random values of  $\{h_i\}$ . Therefore, with reference to Eq. (1.1), the Hamiltonian reads

$$\mathcal{H} = -J \sum_{\langle ij \rangle} s_i s_j - \sum_i h_i s_i, \quad s_i = \pm 1. \quad (1.2)$$

Usually, the quenched RF variables  $\{h_i\}$  are drawn from a Gaussian distribution

$$P(h_i) = \frac{1}{\sqrt{2\pi\Delta^2}} e^{-h_i^2/(2\Delta^2)}, \quad (1.3)$$

---

## 1.2. Disordered Spin Models

where  $\Delta$  is the standard deviation, which is a measure of the disorder strength. Other common choices of the distribution of random-fields are the uniform and bimodal:

$$P_u(h_i) = \begin{cases} [\sqrt{12}\Delta]^{-1}, & |h_i| \leq \sqrt{3}\Delta, \\ 0, & |h_i| > \sqrt{3}\Delta, \end{cases} \quad (1.4)$$

$$P_b(h_i) = \frac{1}{2} [\delta(h_i - \Delta) + \delta(h_i + \Delta)]. \quad (1.5)$$

All three distributions Gaussian, uniform and bimodal have zero mean and variance  $\Delta^2$ .

The interaction term energetically prefers to have a parallel alignment of spins, but the disorder tends to align the spins towards their local field  $h_i$ . The competition between these two terms yield the complex energy landscape and therefore, finding the GS is an optimization problem. In the zero-temperature GS study of the RFIM, the continuous type of the distribution, e.g., Gaussian and uniform, give rise to the non-degenerate ground states whereas the discrete distribution (e.g., bimodal) produces the degenerate ground states [6].

### 1.2.2 Random Field Potts Model

The RFPM is a natural generalization of RFIM for  $q$  possible states of spins [7, 8] and is defined by the Hamiltonian [9]

$$\mathcal{H} = -J \sum_{\langle ij \rangle} \delta_{s_i, s_j} - \sum_i \sum_{\alpha=0}^{q-1} h_i^\alpha \delta_{s_i, \alpha}, \quad s_i \in \{0, 1, \dots, q-1\}. \quad (1.6)$$

Here,  $\delta_{x,y}$  is the Kronecker delta function, and  $q$  is the total number of labels or the Potts state. Therefore, each spin  $s_i$  can take any value from the set  $\{0, 1, \dots, q-1\}$ .  $\{h_i^\alpha\}$  are the quenched RF variables at site  $i$  acting on the state  $\alpha$ , which can be drawn from the distributions as described above.

### 1.2.3 Random Bond Ising Model

Setting  $\{h_i\} = 0$  in Eq. (1.1), the Hamiltonian for the RBIM can be written as

$$\mathcal{H} = - \sum_{\langle ij \rangle} J_{ij} s_i s_j, \quad s_i = \pm 1. \quad (1.7)$$

The quenched RB variables  $\{J_{ij}\}$  are often drawn from the uniform distribution [10]:

$$P_u(J_{ij}) = \begin{cases} \epsilon^{-1}, & (1 - \epsilon/2) \leq J_{ij} \leq (1 + \epsilon/2), \\ 0, & \text{otherwise.} \end{cases} \quad (1.8)$$

Another distribution that is commonly used is the bimodal distribution [11, 12]:

$$P_b(J_{ij}) = a [\delta(J_{ij} - (J_0 - \epsilon))] + (1 - a) [\delta(J_{ij} - (J_0 + \epsilon))], \quad (1.9)$$

where  $\epsilon$ ,  $a$ , and  $J_0$  are the non-negative parameters.  $a$  is a disorder parameter.

A system with all  $J_{ij} > 0$  is called a *random magnet* [10] and a combination of both positive as well as negative values of  $J_{ij}$  is called a *frustrated magnet* [12]. In a random magnet, one usually considers a uniform distribution where  $\epsilon$  gives the amount of disorder. While the bimodal distribution in Eq. (1.9) is more general and several useful models can be realized depending on the various possibilities in  $\epsilon$  and  $J_0$  as follows.

- (i)  $\epsilon = 0$  corresponds to the pure Ising model (IM) ( $\{J_{ij}\} = J_0$ ).
- (ii)  $\epsilon < J_0$  corresponds to an FM *asymmetric random-bond Ising model* (AR-BIM) ( $\{J_{ij}\} > 0$ ).
- (iii)  $\epsilon = J_0$  corresponds to a bond-diluted case of IM in which  $J_{ij} = 0$  with probability  $a$ , i.e., a fraction  $a$  of total bonds are removed. In other words,  $a$  is a dilution parameter.
- (iv)  $\epsilon > J_0$  corresponds to a frustrated case. However, the frustration is weak because positive bonds are stronger than the negative ones, i.e.,  $(J_0 + \epsilon) > |J_0 - \epsilon|$ .



- (v)  $J_0 = 0$  represents the Ising spin-glass system [13–15], where  $J_{ij}$  takes the values  $-\epsilon$  with probability  $a$  or  $+\epsilon$  with the probability  $1 - a$ . In Edwards-Anderson (EA) spin-glass model [15],  $a = 0.5$ , i.e.,  $\{J_{ij}\}$  takes  $\pm\epsilon$  with equal probability. However, a more common choice of  $\{J_{ij}\}$  is from the Gaussian distribution of zero mean and variance  $\epsilon^2$ . Therefore, in this case,  $\epsilon$  is a disorder parameter.

#### 1.2.4 Random Bond XY Model

In the XY model, spins are the two-component ( $n = 2$ ) vector quantities, which are restricted to move in an  $xy$  plane. Considering the vectors are of unit magnitude, each spin  $\mathbf{S}_i = (\cos \theta_i, \sin \theta_i)$  is characterized by an angle  $\theta_i$ . Therefore, the Hamiltonian that describes the RBXYM [16, 17] is

$$\begin{aligned} \mathcal{H} &= - \sum_{\langle ij \rangle} J_{ij} \mathbf{S}_i \cdot \mathbf{S}_j, \quad |\mathbf{S}_i| = 1, \\ &= - \sum_{\langle ij \rangle} J_{ij} \cos(\theta_i - \theta_j), \end{aligned} \tag{1.10}$$

where  $\theta_i$  lies in the interval  $(-\pi, \pi)$  or  $(0, 2\pi)$ . The RB variables  $\{J_{ij}\}$  are uniformly distributed in the interval  $[1 - \epsilon/2, 1 + \epsilon/2]$ , according to the distribution in Eq. (1.8).

As stated earlier, the important features of these disordered models are in the underlying low-temperature phase. Therefore, to minimize the energy Hamiltonian and to equilibrate these systems at low- $T$  are the interesting issues. There are two important numerical techniques, the MC and the GC methods, which are used to deal such issues in these systems.

## 1.3 The Monte Carlo Method

MC methods are the standard sampling techniques used in statistical physics. The general approach of a MC method is to thermally equilibrate a system, which is placed in contact with a heat bath at temperature  $T$ . The system reaches

### 1.3. The Monte Carlo Method

---

the thermal equilibrium via taking different possible spin configurations  $\{s_i\}$  in the phase space [18, 19]. Once the system is equilibrated, the thermodynamic observables can be easily determined.

Let  $P(\{s_i\}, t)$  be the probability that the system has a spin configuration  $\{s_i\}$  at a given time  $t$ . If the underlying stochastic process of evolution is assumed to be a Markov chain of states, i.e., a system in a given state at time  $t + \Delta t$  depends only on the previous state at time  $t$ . Then, in a small interval of time  $\Delta t$ , the system makes a transition to  $\{s'_i\}$  from  $\{s_i\}$  via a suitable transition probability  $W(\{s_i\} \rightarrow \{s'_i\})$  such that in the limit of  $t \rightarrow \infty$ , the probability distribution of these states generated by this Markov process approaches the equilibrium maxwell-Boltzmann distribution, i.e.,

$$P_{\text{eq}}(\{s_i\}) = \frac{\exp(-\beta\mathcal{H}(\{s_i\}))}{Z}. \quad (1.11)$$

Here,  $\beta = 1/k_B T$  and  $Z$  is the partition-function defined as

$$Z = \sum_{\{s_i\}} \exp(-\beta\mathcal{H}(\{s_i\})). \quad (1.12)$$

Now, we can write down the following master equation for the rate of change of  $P(\{s_i\}, t)$  [20]:

$$\frac{dP(\{s_i\}, t)}{dt} = \sum_{\{s'_i\} \neq \{s_i\}} \left[ -W(\{s_i\} \rightarrow \{s'_i\})P(\{s_i\}, t) + W(\{s'_i\} \rightarrow \{s_i\})P(\{s'_i\}, t) \right]. \quad (1.13)$$

The first term on the right-hand-side denotes the loss of probability  $P(\{s_i\}, t)$  of  $\{s_i\}$  in making a transition to  $\{s'_i\}$  at time  $t + \Delta t$  and second term denotes the probability gain of  $\{s_i\}$  from  $\{s'_i\}$  at  $t - \Delta t$ . Notice that the negative sign in first term is due to probability loss of  $P(\{s_i\}, t)$ .

At thermal equilibrium, the system will reach a steady state, and therefore  $dP(\{s_i\}, t)/dt = 0$ . This gives

$$\sum_{\{s'_i\} \neq \{s_i\}} \left[ W(\{s_i\} \rightarrow \{s'_i\})P_{\text{eq}}(\{s_i\}) - W(\{s'_i\} \rightarrow \{s_i\})P_{\text{eq}}(\{s'_i\}) \right] = 0. \quad (1.14)$$

### 1.3. The Monte Carlo Method

---

The general form of  $W$ , which gives  $P_{\text{eq}}$  as  $t \rightarrow \infty$ , is very difficult to obtain from Eq. (1.14). However, a particular solution can be quickly identified as

$$W(\{s_i\} \rightarrow \{s'_i\})P_{\text{eq}}(\{s_i\}) - W(\{s'_i\} \rightarrow \{s_i\})P_{\text{eq}}(\{s'_i\}) = 0. \quad (1.15)$$

Eq. (1.15) is known as the *detailed balance condition*. Thus, the detailed balanced condition is a sufficient—but not necessary—condition to ensure equilibration. Using  $P_{\text{eq}}$  from Eq. (1.11), Eq. (1.15) takes a simpler form

$$\frac{W(\{s_i\} \rightarrow \{s'_i\})}{W(\{s'_i\} \rightarrow \{s_i\})} = \exp(-\beta\Delta E). \quad (1.16)$$

Here,  $\Delta E = \mathcal{H}(\{s'_i\}) - \mathcal{H}(\{s_i\})$  is the change in energy due to the transition  $\{s_i\} \rightarrow \{s'_i\}$ . The transition probability  $W$  is chosen such that it satisfies the condition of detailed balance (Eq. (1.16)).

There are two frequent choices of  $W$  [18, 21]:

$$\begin{aligned} W &= \frac{1}{2} \left[ 1 - \tanh\left(\frac{\beta\Delta E}{2}\right) \right] \\ &= \frac{1}{1 + \exp(\beta\Delta E)}, \end{aligned} \quad (1.17)$$

and

$$W = \begin{cases} e^{-\beta\Delta E}, & \text{if } \Delta E > 0, \\ 1, & \text{otherwise.} \end{cases} \quad (1.18)$$

It is easy to check that both Eqs. (1.17) and (1.18) satisfy the detailed balance condition (Eq. (1.16)). Eq. (1.17) corresponds to the *Glauber* rate of transition and Eq. (1.18) to the *Metropolis* rate of transition. In Metropolis algorithm, as the acceptance probability is 1 for  $\Delta E \leq 0$ , therefore, it is more efficient and has become a popular choice in the MC studies of various statistical models [19].

## 1.4 The Ground State Problem

At  $T = 0$ , the system relaxes into the GS, which is a state with the lowest possible energy  $\mathcal{H}\{s_i\}$ . Though, MC techniques are useful to minimize the energy Hamiltonian, at  $T = 0$ , they have several limitations, e.g., violation of self-averaging, trapping in a metastable state because of lack of thermal fluctuations by which the system can overcome the energy barriers. Therefore, the system will never reach its GS.

Further, the numerical studies of such spin systems must restrict themselves to finite-size systems to model an infinite-size system. Therefore, it is computationally very demanding to simulate large system sizes. For larger system sizes, one obtains better agreement with the behavior of the actual physical system. However, MC methods place severe restrictions on the maximum system sizes because of *non-polynomial* (NP) divergence of computation time with the system size ( $\sim \exp(L^\varphi)$ ).

Therefore, with limited computational resources, there is a need for fast and efficient optimization algorithms to deal such systems. Particularly fruitful are the application of the GC methods. The GC methods have traditionally been used in computer science to obtain optimal solutions to the hard combinatorial problems [22, 23]. These methods have the advantage of being much faster than the standard algorithms. As a result, very large system sizes are accessible in dimensions  $d = 2$  and  $d = 3$ . Let us now discuss the approach of a GC method, which has many potential applications for energy minimization in complex spin systems.

### 1.4.1 The Graph Cut Method

The GC method can be applied to the standard energy function (e.g., a Hamiltonian), which is typically of the form:

$$E(S) = \sum_{\{ij\} \in \mathcal{N}} V_{ij}(s_i, s_j) + \sum_{i \in \mathcal{S}} D_i(s_i), \quad (1.19)$$

## 1.4. The Ground State Problem

---

where  $\mathcal{S}$  is the set of sites and  $\mathcal{N}$  is the set of all interacting pairs of sites. Consider  $\mathcal{L}$  is a set of labels. Each site  $i \in \mathcal{S}$  is assigned a label  $s_i \in \mathcal{L}$ , and related to the neighboring site  $j \in \mathcal{N}_i$  in the well-defined neighborhood system  $\mathcal{N} = \{\mathcal{N}_i \mid \forall i \in \mathcal{S}\}$ , where  $\mathcal{N}_i$  is the set of sites neighboring  $i$ . Typically,  $\mathcal{N}$  consists of neighboring sites but it can be arbitrary.  $D_i$  is an arbitrary function which measures the cost (or penalty) of assigning the label  $s_i$  to the site  $i$ ; and  $V_{ij}(s_i, s_j)$  measures the cost of assigning labels  $s_i$  and  $s_j$  to neighboring sites  $i$  and  $j$ . A system comprising  $N$  sites is then defined by a configuration  $S = (s_1, s_2, \dots, s_N)$  in the configuration space of size  $|\mathcal{L}|^N$ , where  $|\mathcal{L}|$  denotes the total number of elements of  $\mathcal{L}$ . Our goal is to find an optimal labeling  $S^*$  that minimizes the energy function  $E$ .

The starting point in a GC method is to construct a specialized graph for the energy function  $E$  such that the minimum cut on the graph yields the minimization of the energy (either globally or locally). A graph  $\mathcal{G}$  is an ordered pair of disjoint sets  $(\mathcal{V}, \mathcal{E})$  such that  $\mathcal{V}$  is the set of vertices and  $\mathcal{E}$  is the set of edges. An edge  $ij$  joining vertices  $i$  and  $j$  is assigned a weight  $V_{i,j}$ . Then, a cut  $C$  is a partition of the vertices  $\mathcal{V}$  into two disjoint sets  $\mathcal{R}$  and  $\mathcal{Q}$ . Any edge  $ij \in \mathcal{E}$  with  $i \in \mathcal{R}$  and  $j \in \mathcal{Q}$  (or vice-versa) is said to be crossing the cut and is a cut edge. The cost (or size) of the cut is defined to be the sum of the weights of the cut edges, and the minimum cut is the cut that has the smallest cost. To find the cut with the smallest cost is called the *min-cut problem*.

A natural question to ask is the following. What class of energy functions are graph-representable such that they can be efficiently minimized by computing the minimum cut on the graph? In the case of binary labels, viz.,  $\mathcal{L} \in \{0, 1\}$  (e.g., RFIM), the energy function  $E$  is graph-representable if and only if each term  $V_{ij}$  satisfies the regularity condition [23]

$$V_{ij}(0, 0) + V_{ij}(1, 1) \leq V_{ij}(1, 0) + V_{ij}(0, 1). \quad (1.20)$$

Functions which satisfy the above condition are called *regular* functions. Regularity is the necessary and sufficient condition for graph-representability. Additionally, if  $E$  is quadratic in Eq. (1.19), a global minimum is guaranteed in *polynomial* (P) time.

### *Exact ground states for random field Ising model*

The spin-variables ( $s_i = \pm 1$ ) of the RFIM Hamiltonian in Eq. (1.2) can be transformed into occupation-number variables ( $n_i = 0, 1$ ) through the transformation  $n_i = (1 + s_i)/2$ . Then, neglecting constant terms, one has

$$\mathcal{H}(\{n_i\}) = -4J \sum_{\langle ij \rangle} n_i n_j - 2 \sum_i (h_i - q'J) n_i, \quad n_i = 0, 1. \quad (1.21)$$

Here,  $q'$  denotes the number of NNs of a lattice site. It is straightforward to check that the interaction term of Eq. (1.21) satisfies the regularity condition [Eq. (1.20)]. Thus, the energy function of the RFIM (Eq. (1.21)) is graph-representable and can be minimized using a GC method to yield the exact GS. This computation is done via graph cuts on the specialized graph representing the energy function  $\mathcal{H}(\{n_i\})$ . Each iteration of the GC method finds an optimal subset of nodes with a fixed label  $n_i$  ( $= 0$  or  $1$ ) that gives the largest decrease in energy. The algorithm repeatedly cycles through the labels  $n_i$  until the global minimum is reached.

The literature on combinatorial optimization provides several GC algorithms with different polynomial (P) complexity times, e.g., Ford-Fulkerson (FF) method of augmenting paths [24], the Goldberg-Tarjan (GT) push-relabel method [25], and the more recent Boykov-Kolmogorov (BK) method [26], etc. A benchmarking of these algorithms on a number of typical graphs has revealed that the BK method is faster than any other. While the runtime to search the global minima in FF and GT algorithms has  $O(N^3)$  dependence on the system size  $N$ , the BK method has  $O(N)$  [26]. In our study, we use the BK implementation of the GC method. The details of the BK method and the pseudo-code are provided in Secs. 3.1 and 3.2 of Ref. [26]. The source code of its implementation and usage instructions are openly available online [27].

### *Approximate ground states for random field Potts model*

For the systems having binary labels (e.g., RFIM), the GC method yields the exact GS in P time. However, for the systems having more than two labels (e.g., RFPM), minimizing energy function as in Eq. (1.6) is a NP hard prob-

lem [28]. Therefore, an efficient method for the exact GS is extremely unlikely to exist. Boykov, Veksler and Zabih (BVZ) [22] developed two efficient energy minimization algorithms in GC techniques, namely,  $\alpha$ -*expansion* and  $\alpha$ - $\beta$ -*swap*, which allow arbitrary label sets  $\mathcal{L} = (\alpha, \beta, \dots, \gamma)$ , arbitrary data terms  $D_i$  and a very wide class of pair-wise interactions  $V$ . These algorithms are for multi-dimensional energy functions and allow simultaneous relabeling of large number of spins. They obtained approximate solutions in energy minimization of the NP-hard problem with guaranteed optimality bounds.

Both of these algorithms make use of graph cuts iteratively in energy minimization. The basic structure of both these algorithms is described as follows (see Ref. [22]):

### Expansion Algorithm

1. Start with an arbitrary labeling  $S$
2. Set success = 0
3. For each label  $\alpha \in \mathcal{L}$ 
  - (a) Find  $\hat{S} = \arg \min E(S')$  among  $S'$  within one  $\alpha$ -expansion of  $S$
  - (b) If  $E(\hat{S}) < E(S)$ , set  $S = S'$  and success = 1
4. If success = 1 goto step 2
5. Return  $S$

### Swap Algorithm

1. Start with an arbitrary labeling  $S$
2. Set success = 0
3. For each pair of labels  $\{\alpha, \beta\} \subset \mathcal{L}$ 
  - (a) Find  $\hat{S} = \arg \min E(S')$  among  $S'$  within one  $\alpha$ - $\beta$  swap of  $S$
  - (b) If  $E(\hat{S}) < E(S)$ , set  $S = S'$  and success = 1
4. If success = 1 goto step 2

### 5. Return $S$

A single execution of step 3 is an *iteration* and an execution of steps 2-4 is one *cycle*. In each cycle, the expansion algorithm performs an iteration for every label  $\alpha \in \mathcal{L}$ , while the swap algorithm performs for every pair of labels  $\{\alpha, \beta\} \in \mathcal{L}$ . Both algorithms are guaranteed to find the local minima in a finite number of cycles. These algorithms are so efficient that they terminate in a few cycles and most of the spins in configurational space are sampled in a first cycle. However, the expansion algorithm converges faster as compared to the swap algorithm. A cycle in the expansion algorithm takes  $|\mathcal{L}|$  iterations, while a cycle in the swap algorithm takes  $|\mathcal{L}|^2$  iterations. Further, the expansion algorithm finds the local minimum within a known factor of the global minimum whereas the swap algorithm does not have any guaranteed optimality properties, but it handles the more general energy functions. Ref. [22] provides the details of the graph cuts of both algorithms.

In our study of the RFPM, we have used the graph cuts of  $\alpha$ -expansion algorithm. In an expansion move, the  $\alpha$ -expansion algorithm cycles for each  $\alpha \in \mathcal{L}$  in some order (fixed or random) and assign a set of spins  $s_i$ 's to a new value  $s'_i = \alpha$  if the energy is lowered, i.e.,

$$s'_i = \begin{cases} \alpha & \text{if } E(\{s'_i\}) < E(\{s_i\}), \\ s_i, & \text{otherwise.} \end{cases} \quad (1.22)$$

The algorithm then repeatedly iterates until no further improvement can be made. It is called expansion as the set of spins which are flipped to  $\alpha$  has increased in moving from  $\{s_i\}$  to  $\{s'_i\}$ . The key step in the algorithm is to use graph cuts to compute efficiently an expansion move.

Boykov et al. (BVZ) [22] have shown the optimality properties of the expansion algorithm that the algorithm produces a solution within a known factor of the global solution. They prove that if  $S^*$  is the global minimum of any energy function  $E(S)$  for an arbitrary set of labels and given the expansion moves  $\hat{S}$  is a local minimum, then  $E(\hat{S}) \leq 2cE(S^*)$ , where

$$c = \frac{\max_{s_i \neq s_j \in \mathcal{L}} V(s_i, s_j)}{\min_{s_i \neq s_j \in \mathcal{L}} V(s_i, s_j)}. \quad (1.23)$$



## 1.5. Numerical Tools for Studying the Morphologies

---

BVZ described a special case of multilabel energy function of the form of Potts model, for which they prove that the minimizing the energy function is NP-hard. The energy function which they consider is

$$E(\{s_i\}) = \sum_{\{i,j\} \in \mathcal{N}} u_{\{i,j\}} \cdot T(s_i \neq s_j) + \sum_{i \in \mathcal{S}} D_i(s_i), \quad (1.24)$$

where  $V_{ij} \equiv u_{\{i,j\}} \cdot T(s_i \neq s_j)$  is the Potts interaction penalty which is *metric* on the space of labels  $\mathcal{L}$ .  $u_{\{i,j\}}$  represents a penalty of assigning different weight to the neighboring sites  $i$  and  $j$ .  $T(\cdot) = 1$  if its argument is true, and otherwise 0. In this case  $c = 1$ , so the expansion move allows us to get the local minimum within a factor of two of the global minimum.

BVZ [22] presented the experimental results for the effectiveness of these algorithms in a variety of computer vision problems such as image restoration with multiple labels, stereo, segmentation, and motion. These problems are solved by computing a minimum cost multiway cut on a graph. On comparing the real data with the known ground truth, they obtained 98% accuracy. Therefore, these algorithms are proved to be a powerful tool in solving many computer vision problems.

## 1.5 Numerical Tools for Studying the Morphologies

Consider the RFIM at  $T = 0$ , which has the Hamiltonian in Eq. (1.2). For large enough disorder  $\Delta$ , the GS of the system is a *paramagnetic* (PM) state, in which spins are aligned with their local fields. As  $\Delta$  is reduced, the system develops an FM order, in which all spins energetically prefer to align parallel to each other. The onset of this FM order involves the formation of domains (or blobs) which are rich in either up or down spins. The domains are separated by an interface and characterized by a length scale, i.e., the *correlation length*  $\xi(\Delta)$ . The effect of quenched disorder is in pinning and roughening of interfaces. As a result, these interfaces become fractal in nature.

There are many relevant questions about the domain structure and the inter-

## 1.5. Numerical Tools for Studying the Morphologies

---

face texture. For instance, what are the appropriate length scales to investigate the domains structure and fractal properties of interfaces?; How different are these properties at different length scales? For morphologies having rough or fractal interfaces, what are the roughness exponents and the fractal dimension? and how the exponents are affected by the disorder? The most useful quantities to answer these questions, and for quantifying the domain structure are the *correlation function* (CF) and the *structure factor* (SF).

### 1.5.1 The Correlation Function and Structure Factor

The CF [29] is defined as

$$C(\mathbf{r}, \Delta) = \langle s_i s_j \rangle - \langle s_i \rangle \langle s_j \rangle, \quad (1.25)$$

where  $\mathbf{r} \equiv \mathbf{r}_j - \mathbf{r}_i$ , and the angular brackets denote an ensemble averaging. In another representation,

$$C(\mathbf{r}, \Delta) = \frac{1}{N} \sum_{\mathbf{r}'} [\langle s_{\mathbf{r}'} s_{\mathbf{r}'+\mathbf{r}} \rangle - \langle s_{\mathbf{r}'} \rangle \langle s_{\mathbf{r}'+\mathbf{r}} \rangle]. \quad (1.26)$$

For determining scattering properties, interfaces separating domains are probed in the small-angle scattering experiments using X-rays, neutron, light, etc. These scattering experiments measure the SF, which is the Fourier transform of the CF,

$$S(\mathbf{k}, \Delta) = \int d\mathbf{r} e^{-i\mathbf{k}\cdot\mathbf{r}} C(\mathbf{r}, \Delta), \quad (1.27)$$

where  $\mathbf{k}$  is the wave vector of the scattered beam. In the isotropic case,  $C(\mathbf{r}, \Delta)$  and  $S(\mathbf{k}, \Delta)$  are spherically averaged to make them directionally independent [30]. Then, the CF and the SF depend on their vector magnitudes  $r = |\mathbf{r}|$  and  $k = |\mathbf{k}|$ , respectively.

If the system is characterized by a single length scale, the morphology of the domains does not change with  $\Delta$ , apart from a scale factor. In this case, the CF exhibits a scaling property [29, 31]:

$$C(\mathbf{r}, \Delta) \equiv g \left( \frac{r}{\xi(\Delta)} \right). \quad (1.28)$$

## 1.5. Numerical Tools for Studying the Morphologies

---

Using Eq. (1.27), the corresponding scaling form for the SF is

$$S(\mathbf{k}, \Delta) = \xi^d f(k\xi), \quad (1.29)$$

where  $d$  is the dimension of the system.  $f$  and  $g$  are the scaling functions, which are related as

$$f(p) = \int d\mathbf{x} e^{-i\mathbf{p}\cdot\mathbf{x}} g(x). \quad (1.30)$$

These functions characterize the morphology of the domains and interfaces. In experiments or simulations related to the formation of domains, the main interest is in determining the functional forms of  $g(x)$  and  $f(p)$ . The characteristic length scale  $\xi(\Delta)$  is defined as the distance over which the CF decays to (say) half of its maximum value. We study the scaling behavior of the domain structure and characterize the scattering or interfacial properties resulting due to scattering from rough interfaces of domains.

### 1.5.2 Characterization of Morphologies

Consider a typical domain structure of size  $\xi$  with an interface width  $w$  on an underlying lattice with spacing  $a$  as shown in Fig 1.1. The microscopic length scale  $a$  could be the diameter of the spherical particles which aggregate to yield domains, e.g., diffusion limited aggregation (DLA) clusters, colloidal aggregates, etc., or the underlying lattice spacing when domains consist of point particles (e.g., Ising models).

At short distances ( $r \ll \xi$ ), the correlation function is well approximated as [32–34]

$$1 - C(r, \Delta) \equiv \tilde{C}(r, \Delta) \simeq A(r/\xi)^\zeta + B(r/\xi) + \dots, \quad a \ll r \ll \xi, \quad (1.31)$$

where  $A$  and  $B$  are constants. The first term conveys information about the interfacial structure, which can be probed by length scales  $a \ll r \ll w$ . In this regime,  $C(r)$  exhibits a *cusp singularity* characterized by the roughness exponent  $\zeta$  ( $\zeta < 1$ ), and is a consequence of rough fractal interfaces. They are generally described as self-affine fractals with a dimension  $d_f = d - \zeta$ . The linear term in

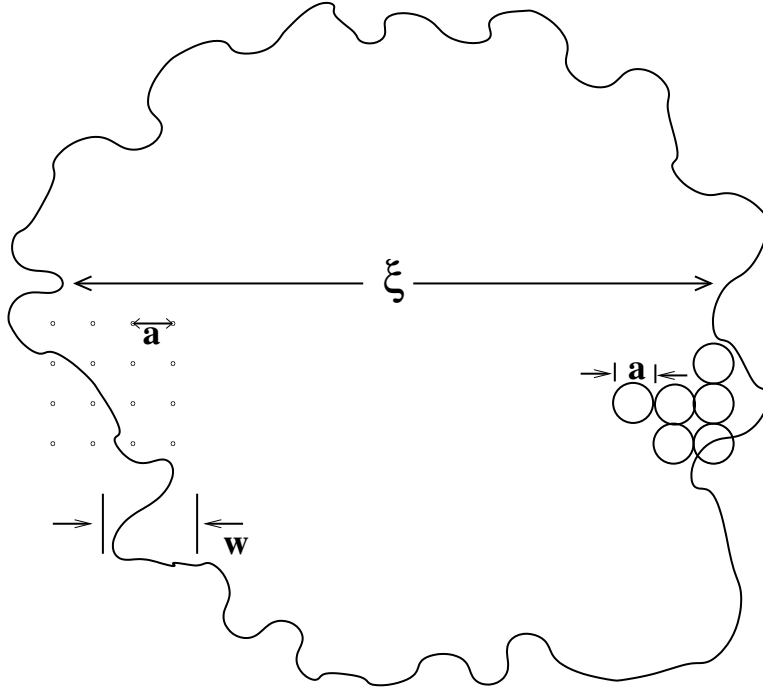


Figure 1.1: Schematic of a domain of size  $\xi$ , with an interface of width  $w$ . The microscopic lattice spacing is  $a$ . The domain can also result from the aggregation of spherical particles of diameter  $a$ .

Eq. (1.31) corresponds to smooth interfaces, probed at length scales  $w \ll r \ll \xi$ . It is characteristic of scattering arising from smooth interfaces in inhomogeneous systems, meaning that the domain has no internal structure. This is referred to as the *Porod law*, which was first discussed in the context of scattering from porous rocks [35, 36]. The crossover between the cusp singularity regime and the Porod regime can be identified as  $r_c \simeq \xi(A/B)^{1/(1-\zeta)}$ .

The short-distance cusp singularity in  $C(r, \Delta)$  has important implications for the structure factor  $S(k, \Delta)$ , which decays with an asymptotic power-law form [37, 38]:

$$S(k, \Delta) \sim \tilde{A}(\xi k)^{-(d+\zeta)} + \tilde{B}(\xi k)^{-(d+1)}. \quad (1.32)$$

The dominant large- $k$  behavior in Eq. (1.32) is the cusp regime with  $S(k) \sim (\xi k)^{-(d+\zeta)}$ . At intermediate values of  $k$ , there is a Porod regime characterized by  $S(k) \sim (\xi k)^{-(d+1)}$ . The crossover from a Porod regime to an asymptotic cusp

regime is an indication of a fractal architecture in the domains or interfaces. In the Porod-regime, the  $C(r)$  and  $S(k)$  shows power-law decay with an integer exponent while in the cusp-regime, the  $C(r)$  and  $S(k)$  shows power-law decay with a non-integer exponent. The GS morphologies in RFIM shows a crossover to this non-Porod behavior [33, 34]. We study the RFIM system with and without an external field  $h$  to obtain this non-integer roughness exponent  $\zeta$ .

## 1.6 Phase Ordering Kinetics

To study ordering kinetics, we rapidly quench the system from an arbitrary random initial state mimicking the high-temperature phase to a low temperature  $T < T_c$  (where  $T_c$  is the critical temperature). The system becomes thermodynamically unstable and evolves toward its new equilibrium state. We study the nonequilibrium evolution via the MC method. The system coarsens via the formation and growth of domains. These domains have a typical size  $L(t)$ , which grow as a function of time  $t$  in the unit of *Monte-Carlo steps* (MCS). One MCS corresponds to the sweeping over whole system size.

The most commonly used quantity to study the dynamics of phase-ordering is the correlation function  $C(r, t)$  and the corresponding Fourier transform  $S(k, t)$  as defined in the previous section. If the typical structure of domains does not change with time  $t$ , apart from a scale factor  $L$  that depends on  $t$ , then the growth process is isotropic and characterized by a single length-scale  $L(t)$ , and the correlation function exhibits the dynamical scaling:  $C(r, t) \equiv g(r/L)$ . The corresponding structure factor has the dynamical scaling:  $S(k, t) = L^d f(kL)$ , where  $f$  and  $g$  are the scaling function related by the Eq. (1.30). A natural question is to ask how  $L(t)$  depends on  $t$ ? The behavior of  $L(t)$  vs.  $t$  is defined as *domain growth law* or *domain growth problem*.

### 1.6.1 Domain Growth Laws in Pure Systems

For pure (without disorder) and isotropic system, we have a very good understanding of domain growth problem. The growth law shows a power law behavior  $L(t) \sim t^{1/z}$  [31, 39], where the exponent  $z$  is temperature independent and varies

among different dynamical universality classes determined by the nature of dynamics, e.g., in the presence of conservation laws governing the order parameter evolution, the presence of hydrodynamics velocity-fields, etc. For the case of evolution with *non-conserved order parameter* (NCOP),  $z = 2$ , and for the case of evolution with *conserved order parameter* (COP),  $z = 3$ . In the presence of hydrodynamic field effects, e.g., in phase separation of a fluid, the growth is faster than  $t^{1/3}$  and the exponent  $z$  shows the crossover from  $3 \rightarrow 1 \rightarrow 3/2$  [40–42]. Let us understand the physical arguments for the domain growth law in the systems with the case of NCOP and COP.

### ***Non-conserved order parameter***

Ordering in a ferromagnet into up and down domains is an example of a system with NCOP. The appropriate order parameter, in this case, is the *spontaneous magnetization*. The growth is driven by the reduction in the curvature of interfaces, and thus, the rate of domain growth ( $dL/dt$ ) is proportional to the local curvature of interfaces, which scales as  $1/L$ . Therefore,  $dL/dt \sim 1/L$ , which yields the growth-law  $L(t) \sim t^{1/2}$ . This is referred to as *Lifshitz-Allen-Cahn* (LAC) growth-law. In this case of NCOP, the appropriate kinetics of domain growth in the MC evolution of spin systems is the *spin-flip kinetics*.

### ***Conserved order parameter***

Phase separation in a binary (AB) mixture into A- and B-rich domains is an example of a system with COP. In this case, the composition or the concentration of each species in the mixture remain fixed, and the appropriate order parameter is the local density difference of the two species in the mixture. The growth is driven by the diffusion. Huse [43] demonstrate that the typical value of the chemical potential on the surface of a domain is  $\mu \sim 1/L$ , which means the concentration gradient  $|\vec{\nabla}\mu| \sim 1/L^2$ . Then, the diffusion current,  $J \propto |\vec{\nabla}\mu|$ , which leads to the growth of domains, scales as  $1/L^2$ . Therefore, the rate of domain growth  $dL/dt \sim 1/L^2$ , which yields the growth law  $L(t) \sim t^{1/3}$ . This is referred to as *Lifshitz-Slyozov* (LS) growth-law [44]. In this case of COP, the appropriate kinetics of domain growth in the MC evolution of spin systems is

the *spin-exchange kinetics*, which preserves the overall magnetization during the evolution.

### 1.6.2 Domain Growth Laws in Disordered Systems

When a system is characterized by the disorder (or defects, impurities, etc.), our understanding of domain growth problem is much poorer. The disorder has a strong effect on the scaling functions and in slowing down of domain growth.

A general framework for understanding of domain growth law has been proposed by Lai, Mazenko, and Valls (LMV) [45]. The growth process involves the motion of interfaces or domain walls. In disordered systems, this motion is impeded by the presence of free-energy barriers. LMV classified the systems on the basis of free-energy barriers required to coarsen a domain of typical size  $L$ . In their scheme, domain size  $L(t)$  grows as

$$\frac{dL}{dt} = \frac{a(L, T)}{L}, \quad (1.33)$$

where  $a(L, T)$  is the diffusion constant that depends on domain size  $L$  and temperature  $T$ . Eq. (1.33) is for the non-conserved case of curvature-driven growth process. For the conserved case of diffusion-driven growth process, we have (from Huse equation [43])

$$\frac{dL}{dt} = \frac{a(L, T)}{L^2}. \quad (1.34)$$

In LMV classification scheme, four different classes of the systems have been identified depending on the behavior of  $a(L, T)$ . These are described as follow:

#### ***Class 1 systems***

Class 1 systems belongs to pure systems for which  $a(L, T) = a_0$ . Then, for the non-conserved case, Eq. (1.33) gives the LAC growth law,  $L(t) \sim t^{1/2}$ ; and for the conserved case, Eq. (1.34) yields the LS growth law,  $L(t) \sim t^{1/3}$ . Pure FM Ising model [31] is an example of this class.

***Class 2 systems***

Class 2 consists of systems whose energy barriers are independent of  $L$  but have a single barrier height  $E_B$ , i.e.,

$$a(L, T) = a_0 \exp(-E_B/T). \quad (1.35)$$

As a result, the growth is still power-law, but with a temperature dependent prefactor, i.e.,

$$L(t) = D(T)t^{1/z}, \quad (1.36)$$

where

$$D(T) \sim a_0 \exp[-E_B/(zT)], \quad (1.37)$$

with  $z = 2$  and  $3$  for the non-conserved and conserved cases, respectively. Typical example of this class is the  $d = 1$  random magnet [46].

***Class 3 systems***

Class 3 refers to the case in which the barrier heights grow linearly with  $L$ , i.e.,  $E_B(L) \sim E_0 L$ , where  $E_0$  is the energy barrier per unit length. Using  $E_B(L)$  in Eq. (1.35) and integrating Eq. (1.33) and Eq. (1.34), yields the power-law growth in a short-time

$$L(t) \simeq (za_0 t)^{1/z}, \quad (1.38)$$

which crosses over to a logarithmic growth:

$$L(t) \simeq \frac{T}{E_0} \ln\left(\frac{t}{t_0}\right). \quad (1.39)$$

Here,  $t_0(T) \sim a_0^{-1}(T/E_0)^z$  and  $z = 2, 3$  corresponding to the non-conserved and conserved case of growth, respectively.

***Class 4 systems***

In Class 4, the energy barrier scales as  $E_B(L) \sim E_0 L^\varphi$  with  $\varphi \neq 1$  (as  $\varphi = 1$  belongs to class 3). Again, from Eqs. (1.33), (1.34), and (1.35), one obtains the



asymptotic logarithmic growth-law:

$$L(t) \simeq \left[ \frac{T}{E_0} \ln \left( \frac{t}{t_0} \right) \right]^{1/\varphi}, \quad (1.40)$$

where

$$t_0(T) = \frac{1}{a_0 \varphi} \left( \frac{T}{E_0} \right)^{z/\varphi}. \quad (1.41)$$

A complete functional form of the cross-over behavior can be expressed as

$$L(t) \simeq L_0(T) h \left( \frac{t}{t_0} \right), \quad (1.42)$$

with

$$L_0(T) = \left( \frac{T}{E_0} \right)^{1/\varphi}, \quad (1.43)$$

and

$$h(x) = \begin{cases} \left( \frac{z}{\varphi} x \right)^{1/z}, & x \ll 1, \\ (\ln x)^{1/\varphi}, & x \gg 1. \end{cases} \quad (1.44)$$

Typical examples of Class 3 and Class 4 are the systems with quenched disorder in the Hamiltonian, e.g., RFIM, RBIM. Eq. (1.40) states that the typical time to cross the free-energy barriers scales as the exponential of barrier height, i.e.,  $t \sim t_0 \exp(E_B/T)$ . Thus, to access the logarithmic regime of domain growth in these disordered systems, a huge numerical effort is required. Therefore, domain growth problem in such systems—particularly in higher dimensions  $d = 2, 3$ —is still controversial and we do not have a complete understanding.

In the thesis, we provide a large scale numerical study of these disordered systems, which enables us to understand domain growth problem in the asymptotic large-time regime without having a finite-size effect.

## 1.7 Overview of the Thesis

This thesis comprises two parts. In part [I](#), we present the ground states study of disordered spin systems using the GC method. In part [II](#), we study ordering

kinetics in disordered spin systems using the MC method.

### 1.7.1 Overview of Part I

In this part of the thesis, we undertake the GS study in the RFIM and the RFPM. With GC method, we obtain exact GS in the RFIM and an approximate GS in the RFPM. This study is described in the following chapters.

In Chapter 2, we study the GS morphologies of the RFIM in  $d = 2, 3$  using the computationally efficient GC method. We analyze the morphologies by computing the CF and the SF. Using these quantities, we characterize the non-Porod behavior in the RFIM and evaluate the characteristic properties, e.g., domain sizes, scaling functions, roughness exponents, fractal dimensions, etc.

In Chapter 3, we study the RFIM in an external magnetic field  $h$  for three different disorder types: Gaussian, uniform, and bimodal. In the external field  $h$ , the GS morphologies contain clusters of spins, which are distributed in the form of power-law. We consider the pinning effect due to the local field  $h_i$  and study the GS morphologies via pinned cluster distribution, spin-spin correlation functions, and structure factors. We obtain the corresponding scaling function for pinned clusters distributions, correlation functions, structure factors, and find that the scaling function is universal for all disorder types and independent of  $h$ .

In Chapter 4, we study the  $q$ -state RFPM for the approximate GS. The GS problem for the RFIM is polynomial, and can be solved using some of the well-known algorithms for maximum flow, but the analogue random-field Potts model corresponds to a multi-terminal flow problem that is known to be NP-hard. Hence, an efficient algorithm which gives the exact GS is extremely unlikely to exist. Still, it is possible to use GC methods to solve approximately the corresponding GS problem in the RFPM in the polynomial time. We show that this works relatively well. We compare results produced by this heuristic algorithm to energy minima found by an appropriately tuned parallel tempering method that is configured to find ground states for the considered system sizes with high probability. The method based on graph cuts finds the same states in a fraction of the time. The new method is used for a first exploratory study of the RFPM in  $d = 2, 3$ . We use the GC method to study the critical behavior in the  $q = 3$

RFPM and obtain the relevant critical exponent.

### 1.7.2 Overview of Part II

In this part of the thesis, we present a comprehensive MC study of phase ordering kinetics in the conserved case of the RFIM (C-RFIM), frustrated case of the RBIM, i.e., frustrated magnet, and the random-bond  $XY$  model (RBXYM). These studies have been described in the following chapters.

In Chapter 5, we study phase ordering dynamics in the RFIM with conserved order parameter (C-RFIM) in  $d = 2, 3$ . We perform an extensive MC simulations which enable us to reach into the asymptotic regime of domain growth. The evolving morphologies  $\{s_i\}(t)$  are analyzed using CF and SF. From this study, Our observations are:

- (a) For a fixed disorder value ( $\Delta$ ), the CF exhibits dynamical scaling, and by varying  $\Delta$ , the scaling function gets modified. Thus, super-universality (SU) is violated and the scaling function is not robust with respect to  $\Delta$ .
- (b) At early times, the domains follow algebraic growth with a disorder-dependent exponent ( $L(t, \Delta) \sim t^{1/\bar{z}(\Delta)}$ ). At late times, there is a cross-over to logarithmic growth:  $L(t, \Delta) \sim (\ln t)^{1/\varphi}$ , where  $\varphi$  is a disorder-independent exponent.
- (c) The small- $r$  behavior of the CF exhibits a cusp singularity and the corresponding SF shows the non-Porod behavior.

In Chapter 6, we study the frustrated magnet in  $d = 2$  where frustration can be tuned by varying the fraction  $a$  of AFM coupling constants  $J_{ij}$ . At low temperatures, the model exhibits a phase with FM order for sufficiently small values of  $a$ ,  $a < a_f$ . In an intermediate range,  $a_f < a < a_a$ , the system is paramagnetic, with spin glass order expected right at zero temperature. For even larger values,  $a > a_a$ , an AFM phase exists. After a deep quench from high temperatures, slow evolution is observed for any value of  $a$ . We show that different amounts of frustration, tuned by  $a$ , affect the dynamical properties in a highly non trivial way. In particular, the kinetics is logarithmically slow in phases with FM or AFM order, whereas evolution is faster, i.e., algebraic, when spin glass order is prevailing. We provide the interpretation in terms of the different nature

of the system in a phase space.

In Chapter 7, we study the RBXYM with the non-conserved kinetics in  $d = 2, 3$ . In  $d = 2$ , we observe a power-law growth with a disorder-dependent exponent on the time-scale of our simulation. In  $d = 3$ , we find that the growth is slower than the power-law at late-times, but our data is inadequate to understand the asymptotic growth law in the time-scale of our simulation. Therefore, our simulations do not access the asymptotic regime of logarithmic growth known to exist for disordered Ising models.

# References

- [1] T. Nattermann, in *Spin Glasses and Random Fields*, edited by A.P. Young (World Scientific, Singapore, 1998).
- [2] N. Metropolis, A. W. Rosenbluth, M. N. Rosenbluth, A.H. Teller and E. Teller, *J. Chem. Phys* **21**, 1087 (1953).
- [3] S. Kirkpatrick, C. D. Gelatt Jr., and M. P. Vecchi, *Science* **220**, 671 (1983); S. Kirkpatrick, *J. Stat. Phys.* **34**, 975 (1984).
- [4] S.-k. Ma, *Modern Theory of Critical Phenomena* (Benjamin, Reading, 1976).
- [5] *Phase Transitions and Critical Phenomena* , edited by C. Domb and M. S. Green, Vol. 1 (Academic Press, London, 1972).
- [6] S. Bastea and P. M. Duxbury, *Phys. Rev. E* **58**, 4261 (1998).
- [7] F. Y. Wu, *Rev. Mod. Phys.* **54**, 235 (1982).
- [8] R. B. Potts, *Proc. Camb. Phil Soc.* **48**, 106 (1952).
- [9] D. Blankschtein, Y. Shapir, and A. Aharony, *Phys. Rev. B* **29**, 1263 (1984).
- [10] R. Paul, S. Puri, and H. Rieger, *Europhys. Lett.* **68**, 881 (2004); *Phys Rev. E* **71**, 061109 (2005).
- [11] F. Corberi, M. Zannetti, E. Lippiello, R. Burioni, and A. Vezzani, *Phys. Rev. E* **91**, 062122 (2015).
- [12] F. Corberi, M. Kumar, S. Puri, and E. Lippiello, *Phys. Rev. E* **95**, 062136 (2017).

- 
- [13] E. Marinari, G. Parisi, and J. J. Ruiz-Lorenzo, in *Spin Glasses and Random Fields*, edited by A.P. Young (World Scientific, Singapore, 1998).
- [14] K. Binder and A. P. Young, *Rev. Mod. Phys.* **58**, 801 (1986).
- [15] S. F. Edwards and P. W. Anderson, *J. Phys. F: Metal Phys.* **5**, 965 (1975).
- [16] D. Yi-Bo and G. Qiang, *Chin. Phys. Lett.* **31**, 020504 (2014).
- [17] P. Ray and M. A. Mouri, *Phys. Rev. B* **45**, 5361 (1992).
- [18] K. Binder and D. W. Heerman, *Monte Carlo Simulation in Statistical Physics: An Introduction*, fourth ed. (Springer-Verlag, Berlin, 2002).
- [19] M. E. J. Newman and G. T. Barkema, *Monte Carlo Methods in Statistical Physics* (Oxford University Press, Oxford, 1999).
- [20] N. G. Van Kampen, *Stochastic Processes in Physics and Chemistry*, North-Holland, Amsterdam (1981).
- [21] M. Suzuki and R. Kubo, *J. Phys. Soc. Jpn.* **24**, 51 (1968).
- [22] Y. Boykov, O. Veksler, and R. Zabih, *IEEE Trans. PAMI* **23**, 1222 (2001).
- [23] V. Kolmogorov and R. Zabih, *IEEE Trans. PAMI* **26**, 147 (2004).
- [24] L. Ford and D. Fulkerson, *Flows in Networks* (Princeton University Press, Princeton, 1962).
- [25] A.V. Goldberg and R.E. Tarjan, *J. ACM* **32**, 921 (1988).
- [26] Y. Boykov and V. Kolmogorov, *IEEE Transactions on PAMI* **26**, 1124 (2004).
- [27] see “maxflow-v3.04.src.zip” at <http://pub.ist.ac.at/~vnk/software.html>.
- [28] J. C. Angles d’Auriac, M. Preissmann and R. Rammal, *J. Physique Lett.* **46**, L-173 (1985).
- [29] S. Puri, in *Kinetics of Phase Transitions*, edited by S. Puri and V.K. Wadhawan (Taylor and Francis, Boca Raton, 2009).

- 
- [30] A. Chakrabarti, R. Toral, and J.D. Gunton, Phys. Rev. B **39**, 4386 (1989);  
J.D. Gunton, R. Toral and A. Chakrabarti, Physica Scripta **T33**, 12 (1990).
- [31] A. J. Bray, Adv. Phys. **43**, 357 (1994).
- [32] G. P. Shrivastav, S. Krishnamoorthy, V. Banerjee, and S. Puri, Europhys. Lett. **96**, 36003 (2011).
- [33] G. P. Shrivastav, M. Kumar, V. Banerjee, and S. Puri, Phys. Rev. E **90**, 032140 (2014).
- [34] G. P. Shrivastav, V. Banerjee, and S. Puri, Eur. Phys. J. E **37**, 98 (2014).
- [35] G. Porod, in *Small-Angle X-ray Scattering*, edited by O. Glatter and O. Kratky (Academic Press, New York, 1982).
- [36] Y. Oono and S. Puri, Mod. Phys. Lett. B **2**, 861 (1988).
- [37] H. D. Bale and P. W. Schmidt, Phys. Rev. Lett. **53**, 596 (1984).
- [38] P.-Z. Wong, Phys. Rev. B **32**, 7417 (1985); P.-Z. Wong and A. J. Bray, Phys. Rev. B **37**, 7751 (1988); Phys. Rev. Lett. **60**, 1344 (1988).
- [39] A. Onuki, *Phase Transition Dynamics* (Cambridge University Press, Cambridge, 2002).
- [40] E.D. Siggia, Phys. Rev. A **20**, 595 (1979).
- [41] H. Furukawa, Phys. Rev. A **31**, 1103 (1985).
- [42] S. Ahmad, S. K. Das, S. Puri, Phys. Rev. E **82**, 040107 (2010); Phys. Rev. E **85**, 031140 (2012).
- [43] D. A. Huse, Phys. Rev. B **34**, 7845 (1986).
- [44] I. M. Lifshitz and V. V. Slyozov, J. Phys. Chem. Solids **19**, 35 (1961).
- [45] Z. Lai, G. F. Mazenko, and O. T. Valls, Phys. Rev. B **37**, 9481 (1988).
- [46] E. Lippiello, A. Mukherjee, S. Puri and M. Zannetti, Europhys. Lett. **90**, 46006 (2010).

# Part I

## Ground States in Disordered Spin Systems



# Chapter 2

## Ground State Morphologies in the Random Field Ising Model

### 2.1 Introduction

The random-field Ising model (RFIM) is the simplest example of a system with quenched disorder [1, 2]. In spite of its simplicity, diverse systems have been studied using the RFIM. Some examples are *diluted anti-ferromagnets* (DAFs) in a uniform magnetic field [3, 4] (e.g.,  $\text{FeF}_2$ ,  $\text{CoF}_2$ , and  $\text{MnF}_2$  diluted with non-magnetic compounds such as  $\text{ZnF}_2$  [5–7]), colloid-polymer mixtures [8], relaxor ferroelectrics [9], Barkhausen noise in magnetic hysteresis [10], etc. Recently, switchable magnetic domains and diluted dipolar magnets such as  $\text{LiHo}_x\text{Y}_{1-x}\text{F}_4$  have also been modeled by the RFIM [11]. It is described by the Hamiltonian in Eq. (1.2), in which  $\Delta$  gives the amount of disorder.

The quenched disorder play an important role in the behavior of phases and phase transitions in the RFIM system. Due to which, there have been very much discussion, which remain controversial. An early controversy was regarding the lower critical dimension  $d_l$ , below which the system has no *long-range order* (LRO) or a FM order. The domain-wall stability arguments of Imry and Ma [12] predicted  $d_l = 2$ , whereas perturbative field-theoretic calculations by Young [13] predicted  $d_l = 3$ . However, rigorous proofs by Imbrie [14], Bricmont and Kupiainen [15], and later by Aizenmann and Wehr [16] ruled out LRO in the  $d = 2$

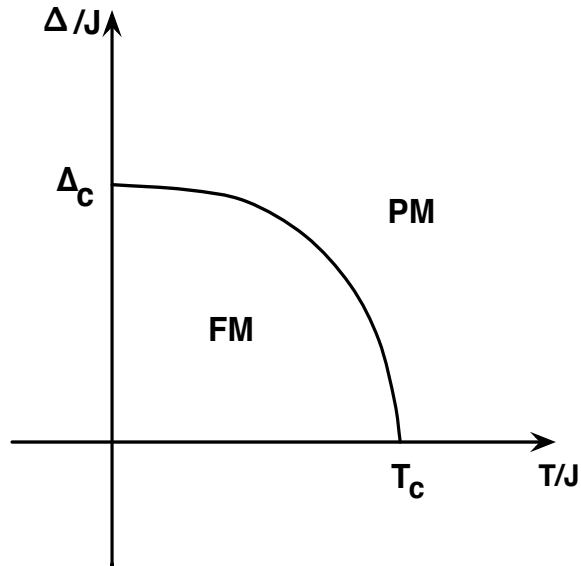


Figure 2.1: A schematic of phase diagram of  $d = 3$  RFIM. Labels PM and FM refer to the paramagnetic phase and the ferromagnetic phase, respectively.

RFIM for any non-zero value of disorder  $\Delta$ , however small. These authors also showed that, in the  $d = 3$  RFIM, there exist a small region of  $(T, \Delta)$  values where the equilibrium state has an FM order. Because of no LRO in the  $d = 2$  RFIM,  $\Delta_c = 0$  and thus  $d_l = 2$ .

Then, there have been questions and debates about nature of phase transitions in the RFIM. The earliest MC study by Young and Nauenberg [17] reported a first-order transition. While later studies involving GS calculations reported a second-order transition [18–20]. Further, using the replica symmetry breaking technique, Mezard et al. [21] predicted an intermediate glassy phase separating the FM and PM phases. However, a detailed numerical study of Middleton and Fisher [22] showed that the transition between FM and PM phase of the RFIM is continuous and there is no intermediate glassy phase.

A schematic of a phase diagram of the  $d = 3$  RFIM is shown in Fig. 2.1. The FM phase consist of the macroscopic domains of up (+1) spins with the impurities of down (-1) spins or vice-versa. With increasing disorder  $\Delta$ , the impurity regions grow, finally yielding the PM phase in which up and down spins

are in the random fashion. At  $\Delta = 0$ , the RFIM becomes pure IM, which in  $d = 3$  has a second-order phase transition from FM to PM phase at a critical temperature  $T_c \simeq 4.515$  [23]. As we introduce disorder  $\Delta$ ,  $T_c$  decreases. With increasing  $\Delta$ , there is decrease in  $T_c$ , and at a critical disorder  $\Delta_c$ ,  $T_c$  becomes 0. At  $T = 0$ , the RFIM shows a phase transition from FM to PM with a critical point at  $\Delta_c$ . According to the zero-temperature fixed point hypothesis, transitions which take place at  $T = 0$  and  $T \neq 0$  falls in the same universality class [24, 25]. Thus, the low-temperature phase of the RFIM is controlled by the  $T = 0$  fixed point. It is therefore of great interest to obtain  $T = 0$  ground states of the RFIM.

Let us review the earlier works on the  $T = 0$  ground states of the RFIM. An early significant work is due to Fytas and Martin-Mayor [26], who perform a high-statistics simulation of the zero-temperature RFIM in  $d = 3$  for different types of RF distributions, viz., Gaussian, double Gaussian, and Poissonian distributions. They showed that the RFIM is ruled by a single universality class. They also compute the relevant critical exponents with high numerical accuracy including the scaling corrections. Another interesting recent work is due to Picco and Sourlas [27]. These authors also undertook a comprehensive simulation of the  $d = 3$  RFIM at  $T = 0$  and obtained precise estimates of the critical exponents. Another important study of the  $d = 3$  RFIM at  $T = 0$  is due to Middleton and Fisher [22]. They studied a wide range of physical properties and obtained the critical exponents. There have been many other significant contributions on the scaling theory of  $T = 0$  phase transition in the RFIM [24, 28, 29].

In this Chapter, we study the GS morphologies of the  $d = 2$  and  $d = 3$  RFIM as a function of  $\Delta$  and compare our result with experimental scattering data. We analyze these morphologies using correlation function  $C(r, \Delta)$  and structure factor  $S(k, \Delta)$  and characterize the interfacial properties such as fractal dimension and non-Porod behavior. The tools for characterization of morphologies via the correlation functions and the structure factors are described in the Sec. 1.5.2. The results that we obtain are as follows.

- (a) In the  $d = 2$  RFIM,  $C(r, \Delta)$  exhibits universal scaling with respect to different disorder amplitudes. At short distances, it shows a cusp singularity as a consequence of rough, fractal interfaces. We obtain a precise estimate of the fractal dimension.

- (b) Interfaces in the PM phase are always fractal, but in the  $d = 3$  RFIM, interfaces in the FM phase are also fractal with a fractal dimension different from that in the PM phase.
- (c) The correlation length  $\xi(\Delta)$  diverges as  $\Delta \rightarrow \Delta_c$ . We obtain a precise functional forms for the divergence of the  $\xi(\Delta)$  in both, the  $d = 2$  and  $d = 3$  RFIM.
- (d) Then, we explain the non-Porod behavior of the SF obtained in small-angle neutron-scattering experiments on DAFs.

This chapter is organized as follows. In Sec. 2.2, we discuss the ground state method. Then, we present the detailed numerical results in Sec. 2.3. The ground states of the  $d = 2$  RFIM and their properties are discussed in Sec. 2.3.1. A corresponding study of the  $d = 3$  RFIM is presented in Sec. 2.3.2. In Sec. 2.4, we present experimental evidence of the crossover from the Porod regime to the cusp or non-Porod regime. Finally, we conclude this chapter with a summary and discussion in Sec. 2.5.

## 2.2 The Ground State Method

In Sec. 1.4.1, we discussed that the Hamiltonian of the RFIM belongs to the class of energy function which are quadratic and satisfy a regularity condition, and we are assured of getting the *exact* GS in the energy minimization of the RFIM using GC methods (See section 1.4.1 for the details of the GC method). Typically, the search time in these methods for a global minimum or a “good quality” local minimum has a polynomial (P) dependence on the system size. There are several algorithms in GC techniques, which have different P complexity time.

In this Chapter, we use the BK implementation of “max-flow–min-cut” algorithm [30], which has a linear dependence on the system size  $O(N)$  in searching the global minima. The  $O(N)$  complexity allows us to simulate systems of large sizes. We have numerically confirmed this  $O(N)$  complexity for  $d = 2, 3$ , and will present these results in Chapter 4 in the context of ground state study of the Random-field Potts model. For the RFIM, typically the BK-GC method finds

the exact GS in its first iteration itself. Therefore, with the use of BK algorithm [30] of the GC method, we obtain the exact GS and study the GS morphologies in the RFIM.

## 2.3 Detailed Numerical Results

In this section, we present the numerical results for the ground state properties in the  $d = 2, 3$  RFIM. The initial configuration of the system is chosen to be a random mixture of  $s_i = \pm 1$ , corresponding to the paramagnetic state at  $\Delta = \infty$ . The simulations were performed on regular lattices,  $L^2$  in  $d = 2$  and  $L^3$  in  $d = 3$ , with periodic boundary conditions applied in all directions. We present each numerical result averaged over 100 configurations of  $\{h_i\}$ . In our results, the error bars are not shown if these are smaller than the symbol sizes.

### 2.3.1 Ground States of the $d = 2$ RFIM

The  $d = 2$  RFIM offers the simplest paradigm to study the effects of quenched disorder. Although there is no ferromagnetic LRO, the GS (at  $T = 0$ ) is nontrivial due to the competition between FM strength of interaction  $J$  and the disorder  $\Delta$  (in units of  $J$ ). In the limit of weak disorder ( $\Delta < 1$ ), the exchange coupling between the spins dominates and the GS comprises large domains of up spins (or down spins) which percolate through the system. For strong disorder ( $\Delta > 1$ ), the spins point along their local random-fields. A study of the GS morphology is important to understand the effect of disorder on the geometrical correlations and phase transitions in the  $d = 2$  RFIM [31–35].

All the statistical data presented here, unless otherwise specified, is for a square lattice with  $L = 4096$ . We choose  $\Delta$  values which are not very close to  $\Delta_c$  as we are primarily interested in the rough interfaces which form deep inside a particular phase. In the  $d = 2$  RFIM, as  $\Delta_c = 0$ , the minimum value of disorder we consider is  $\Delta_{\min} = 0.8$ . As we see later, the typical size of domain is  $O(100)$  lattice spacings at  $\Delta_{\min}$ , which is much less than the system size  $L = 4096$ . Therefore, we do not expect *scaling corrections* to play a significant role, and the system sizes and averaging used are adequate for our purposes. The same is true

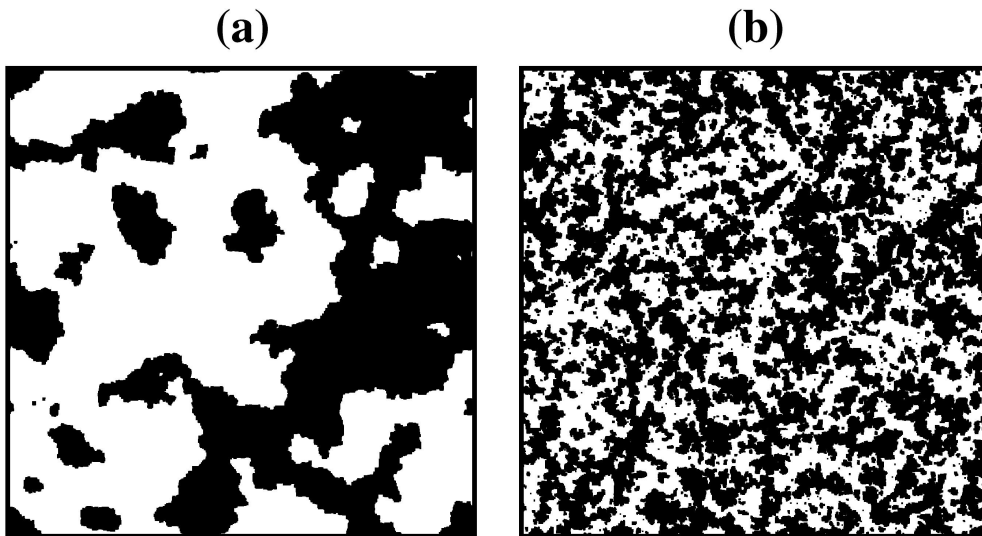


Figure 2.2: GS morphologies of the RFIM in  $d = 2$  obtained from the GC method for (a)  $\Delta = 0.8$  and (b)  $\Delta = 1.2$ . These morphologies correspond to a  $1024^2$  lattice. Regions with up and down spins are marked black and white, respectively.

for the  $d = 3$  RFIM, which is discussed in Sec. 2.3.2.

The ground-state morphology in the paramagnetic state ( $\Delta = \infty$ ) has the following features. The spins are uncorrelated and typically the correlation length  $\xi \rightarrow 0$ . As the disorder strength  $\Delta$  is reduced, the GS consists of correlated regions or domains of size  $\xi$ , enriched in either up or down spins. These regions grow in size with  $\xi \rightarrow \infty$  as  $\Delta \rightarrow 0$ . These features are captured in Fig. 2.2, where we show snapshots of ground-state morphologies for  $\Delta = 0.8$  and  $\Delta = 1.2$ .

After obtaining the GS morphologies, we compute the CF  $C(r, \Delta)$  and define the correlation length as the distance over which the CF decays to 0.2 of its maximum value. In Fig. 2.3(a), we plot the correlation length  $\xi(\Delta)$  vs  $1/\Delta$  on a semilog scale. The correlation length diverges with an essential singularity as  $\Delta \rightarrow 0$ :

$$\xi(\Delta) \sim e^{a/\Delta}, \quad (2.1)$$

where  $a$  is a constant. However in earlier works [31–35], the  $\xi$  diverges as exponential of  $1/\Delta^2$  instead of  $1/\Delta$ . But, our data do not follow this stretched-exponential divergence  $\xi(\Delta) \sim e^{a/\Delta^2}$ . To demonstrate this, we plot  $\xi(\Delta)$  vs  $1/\Delta^2$  on a semilog

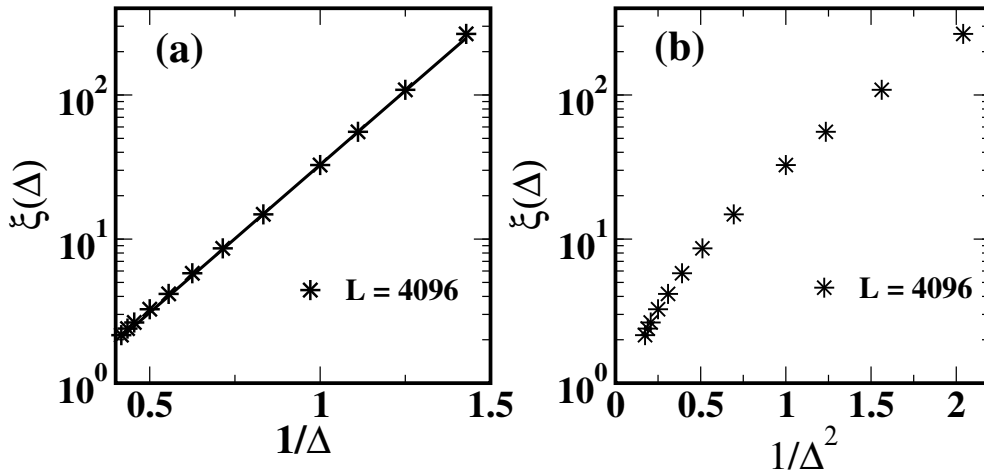


Figure 2.3: (a) Plot of correlation length  $\xi(\Delta)$  vs  $1/\Delta$  for a  $4096^2$  system on a semilog scale. The correlation length is defined as the distance over which the CF falls to  $0.2 \times$  maximum value. The straight line shows the exponential-fit of  $\xi$  with  $1/\Delta$ . (b)  $\xi(\Delta)$  vs  $1/\Delta^2$ .

scale in Fig. 2.3(b). Clearly, this plot does not show a linear regime. (Of course, it is possible that a linear regime may appear even closer to the critical point.)

Now, we expect the divergent correlation length to be saturated by the finite size ( $L$ ) of the system. To investigate finite-size effects, in Fig. 2.4(a) we plot  $\xi(\Delta)$  vs  $1/\Delta$  for system sizes  $L$  ranging from 256 to 4096. The correlation length diverges as  $\xi(\Delta) \sim e^{a/\Delta}$  when  $\Delta \rightarrow 0$ , but this is limited by the lattice linear size  $L$ . The *finite-size scaling* (FSS) ansatz,

$$\xi(\Delta) \sim e^{a/\Delta} \mathcal{R}(Le^{-a/\Delta}), \quad (2.2)$$

results in the data collapse shown in Fig. 2.4(b), yielding  $a \simeq 4.798 \pm 0.003$ .

### *Characterization of morphologies*

Next, we focus on the characterization of the domain morphologies for fractal dimension and non-Porod behavior. As mentioned in Sec. 1.5.1, if the system is characterized by a unique length scale, then the CF and SF exhibit the scaling property:  $C(r, \Delta) \equiv g(r/\xi)$ ,  $S(k, \Delta) = \xi^d f(k\xi)$ . In Fig. 2.5, we show the scaling

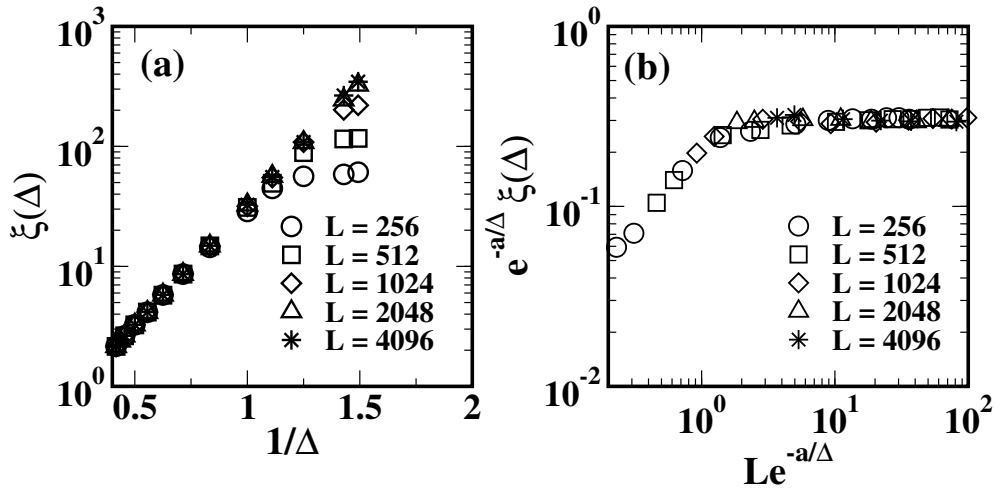


Figure 2.4: (a) Plot of  $\xi(\Delta)$  vs  $1/\Delta$  for different system sizes on a semilog scale. We present data for square lattices of size  $L = 256, 512, 1024, 2048, 4096$ , denoted by the specified symbols. (b) Data collapse resulting from the finite-size scaling ansatz  $\xi(\Delta) \sim e^{a/\Delta} \mathcal{R}(Le^{-a/\Delta})$ , yielding  $a \simeq 4.8$ .

of  $C(r, \Delta)$  vs  $r/\xi$  for different disorder amplitudes  $\Delta$ , which confirm that the domain morphologies are scale invariant for these values of  $\Delta$ . (Note that the domain structure breaks up for  $\Delta \gg 1$ , and the characteristic domain size becomes  $\xi \sim 1$  lattice spacing. In that case, the CF decays to 0 almost immediately.)

Based on the discussion in Sec. 1.5.2, we expect the CF to have two regimes:

$$\begin{aligned} 1 - C(r, \Delta) \equiv \tilde{C}(r, \Delta) &\simeq B(r/\xi), & w \ll r \ll \xi, \\ &\simeq A(r/\xi)^\zeta & r \ll w. \end{aligned} \quad (2.3)$$

The first regime corresponds to Porod scattering off smooth domains [36, 37] on length scales  $\gg w$ , where  $w$  is the interface width. The second regime (for  $r \ll w$ ) corresponds to scattering off rough fractal interfaces with cusp exponent  $\zeta = d - d_f$ .

In Fig. 2.6(a), we plot  $\tilde{C}(r, \Delta) = 1 - C(r, \Delta)$  vs  $r/\xi$  for  $\Delta = 0.8, 0.9, 1.0, 1.2$  on a log-log scale. We obtain the cusp exponent  $\zeta \simeq 0.88$ , yielding  $d_f \simeq 1.12$ . In Fig. 2.6(b), we present a scaling plot of the structure-factor data, i.e.,  $\xi^{-2} S(k, \Delta)$  vs  $\xi k$ , for  $\Delta = 0.8, 0.9, 1.0, 1.2$ . Again, the collapse of different data sets onto



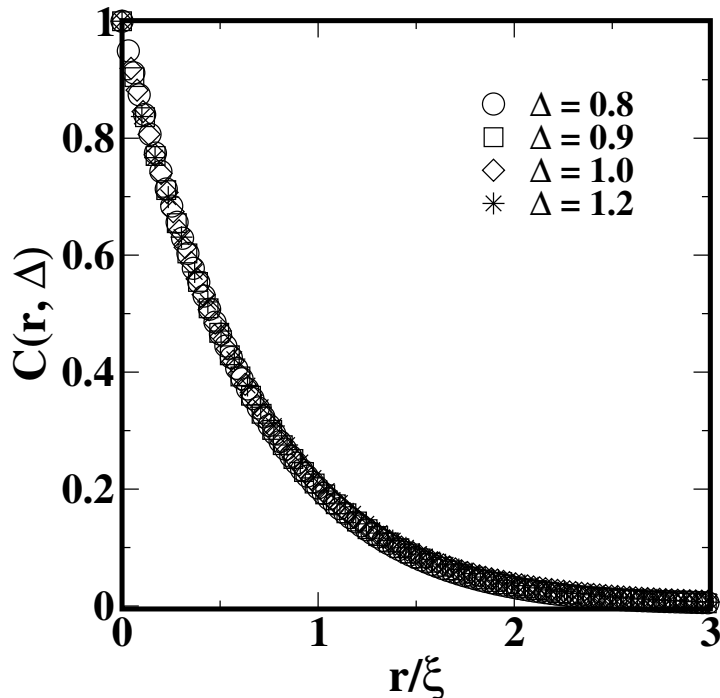


Figure 2.5: Scaled correlation functions,  $C(r, \Delta)$  vs  $r/\xi$ , for specified disorder strengths  $\Delta$ .

a single master curve confirms that the morphologies are scale invariant. Further, the scaling function exhibits an asymptotic cusp or non-Porod regime:  $S(k, \Delta) \simeq \tilde{A}k^{-2.88}$ , which is consistent with the small- $r$  behavior of the CF. As mentioned earlier, this non-Porod behavior is characteristic of scattering from fractal interfaces.

### 2.3.2 Ground States of the $d = 3$ RFIM

We next focus on the ground states of the  $d = 3$  RFIM. The GC simulations were performed on  $d = 3$  lattices of size  $L^3$  with  $L \leq 256$ . All the statistical data presented here, unless otherwise specified, are for a cubic system with  $L = 256$ .

A major distinction between the  $d = 2$  and  $d = 3$  RFIM is that the later exhibits a phase transition from a FM phase to the PM phase at non-zero value of  $\Delta$ . At  $T = 0$ , the phase transition occur at critical disorder  $\Delta_c$ . An important study of the  $d = 3$  RFIM at  $T = 0$  is due to Middleton and Fisher [22]. They

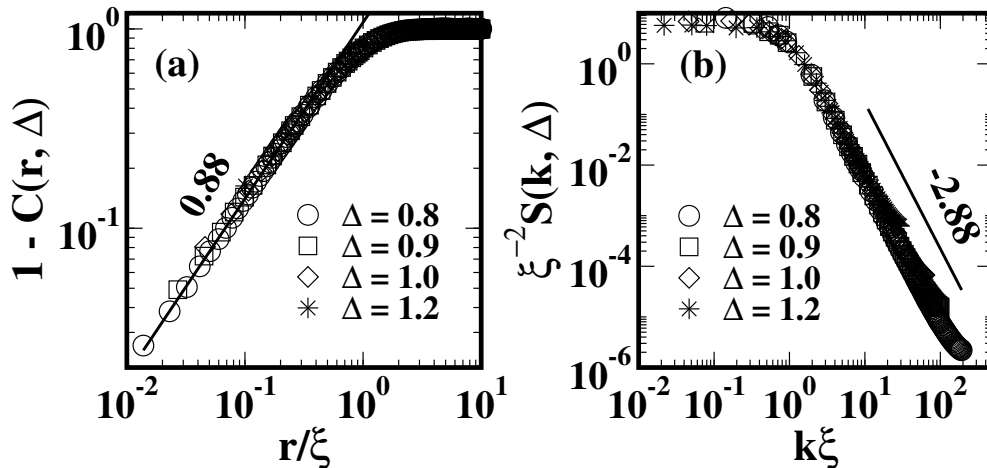


Figure 2.6: (a) Log-log plot of  $1 - C(r, \Delta)$  vs  $r/\xi$  for the data sets in Fig. 2.5. The solid line denotes the power-law fit  $1 - C(r, \Delta) \sim (r/\xi)^\zeta$ , with the cusp exponent is estimated as  $\zeta \simeq 0.88$ . (b) Log-log plot of  $\xi^{-2} S(k, \Delta)$  vs  $k\xi$ . The line of slope  $-2.88$  denotes the non-Porod behavior corresponding to the cusp singularity in the CF.

studied a wide range of physical properties and convincingly demonstrated that there is a second-order phase transition at  $\Delta_c \simeq 2.270$ .

One of the most efficient procedures to determine the critical disorder is the fourth-order Binder cumulant [31, 38, 39], defined as

$$U_4(\Delta, L) = 1 - \frac{\langle m^4 \rangle}{3\langle m^2 \rangle^2}, \quad (2.4)$$

where  $m$  is the magnetization of the system and  $\langle \dots \rangle$  denotes average over many RF configurations  $\{h_i\}$ . The FSS ansatz for Binder-cumulant,

$$U_4(\Delta, L) = \mathcal{U} [L^{1/\nu}(\Delta - \Delta_c)], \quad (2.5)$$

has no explicit  $L$  dependence. Thus, this cumulant, when plotted against disorder  $\Delta$  for different lattice sizes, intersects at a critical point. In Figure 2.7, we show the plot of  $U_4$  vs  $\Delta$  for different values of  $L$ . The data has been averaged over many disorder realizations ( $\{h_i\}$ ); typically  $10^5, 5 \times 10^4, 4 \times 10^4, 3 \times 10^4, 2 \times 10^4, 10^4$ , for  $L = 16, 24, 32, 48, 64$ , respectively. First, we vary  $\Delta$  in steps of 0.02 and find

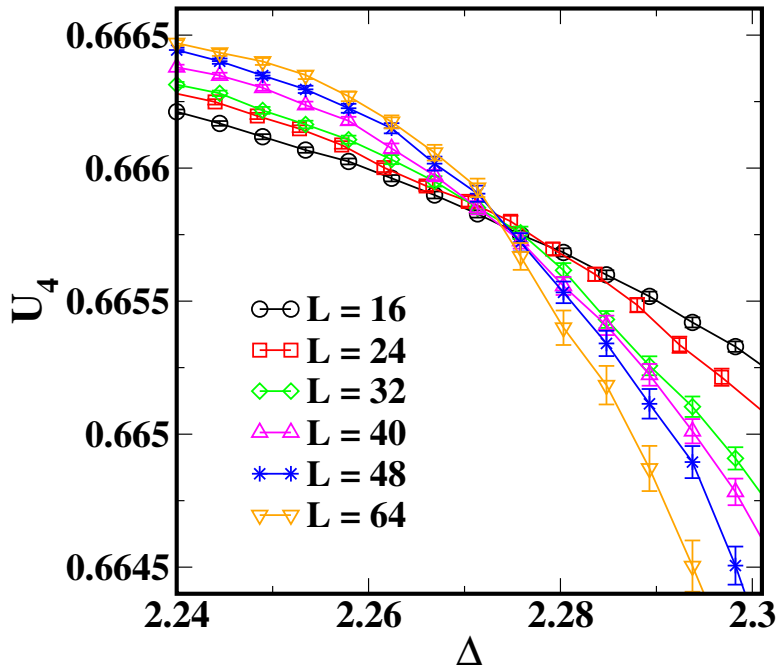


Figure 2.7: The Binder cumulant  $U_4$  vs.  $\Delta$  for cubic lattices of size  $L = 16, 24, 32, 40, 48, 64$ . The appropriate error bars are shown. Upon zooming the critical region, the intersection point of the data sets yields  $\Delta_c \simeq 2.278 \pm 0.002$ .

that the crossing occurs between  $\Delta = 2.26$  and  $\Delta = 2.28$ . We then zoom into the region from  $\Delta = 2.26$  to  $\Delta = 2.28$  by changing the step size from 0.02 to 0.002. This shows that the crossing occurs between  $\Delta = 2.278$  and  $\Delta = 2.28$ . We can further zoom into the region between  $\Delta = 2.278$  and  $\Delta = 2.28$  by reducing the step size again, but we restrict our analysis to the disorder step size 0.002. This choice of step size sets an error bar of  $\pm 0.002$  on  $\Delta_c$ . Hence, the estimated value of  $\Delta_c$  is  $2.278 \pm 0.002$ . This compares well with the most accurate estimate of  $\Delta_c$  for the  $d = 3$  RFIM to date, which is  $\Delta_c \simeq 2.2727$  (Fytas and Martin-Mayor [26]).

We define the correlation length  $\xi(\Delta)$  as the distance over which the CF decays to 0.2 of its maximum value. In Fig 2.8(a), we plot  $\xi(\Delta, L)$  vs  $\Delta$  for lattice size  $L$  ranging from 16 to 256. For large  $\Delta \gg \Delta_c$ , typically  $\Delta \simeq 4$ , the system is in highly paramagnetic state and there is essentially no domain structure, and thus the correlation length  $\xi \simeq 1$ . As we reduce  $\Delta$ , the correlation length grows and

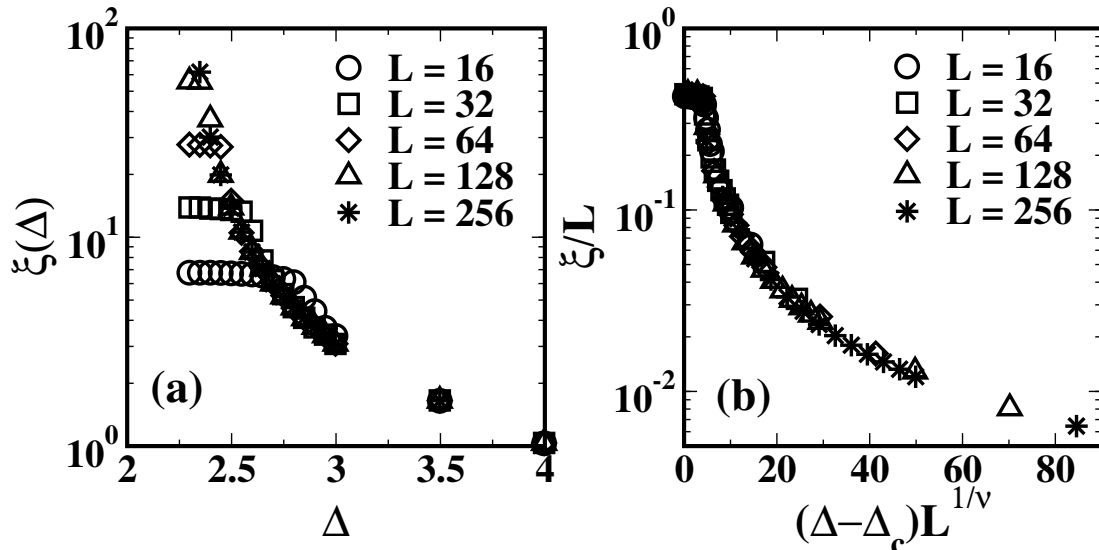


Figure 2.8: (a) Plot of correlation length  $\xi(\Delta, L)$  vs  $\Delta$  for  $L = 16, 32, 64, 128, 256$ , denoted by the specified symbols. (b) The data collapse resulting from the FSS ansatz  $\xi/L = \mathcal{R}[L^{1/\nu}(\Delta - \Delta_c)]$ , yielding  $\nu \simeq 1.308$ .

diverges as  $\xi \sim (\Delta - \Delta_c)^{-\nu}$  in the limit  $\Delta \rightarrow \Delta_c^+$ . As usual, the divergence is limited by the finite lattice size  $L$  as shown in Fig. 2.8(a). The presence of finite-size effects can be used to estimate the critical exponent  $\nu$ . The FSS ansatz,

$$\xi(\Delta, L) = L \mathcal{R}[L^{1/\nu}(\Delta - \Delta_c)], \quad (2.6)$$

results in the data collapse seen in Fig. 2.8(b), yielding  $\nu \simeq 1.308 \pm 0.005$ . This is consistent with earlier estimates of  $\nu = 1.37 \pm 0.09$  (Middleton and Fisher [23]),  $\nu = 1.32 \pm 0.07$  (Hartmann and Young [40]), and  $\nu = 1.38 \pm 0.02$  (Fytas et al. [41]).

### *Characterization of morphologies*

We now analyze the domain morphologies in the FM as well as PM phases, using  $C(r, \Delta)$  and  $S(k, \Delta)$ . In both phases,  $C(r, \Delta)$  is characterized by a universal scaling function for different disorder amplitudes. To understand the interfacial properties characterized by the small- $r$  behavior, we plot  $\tilde{C}(r, \Delta) = 1 - C(r, \Delta)$

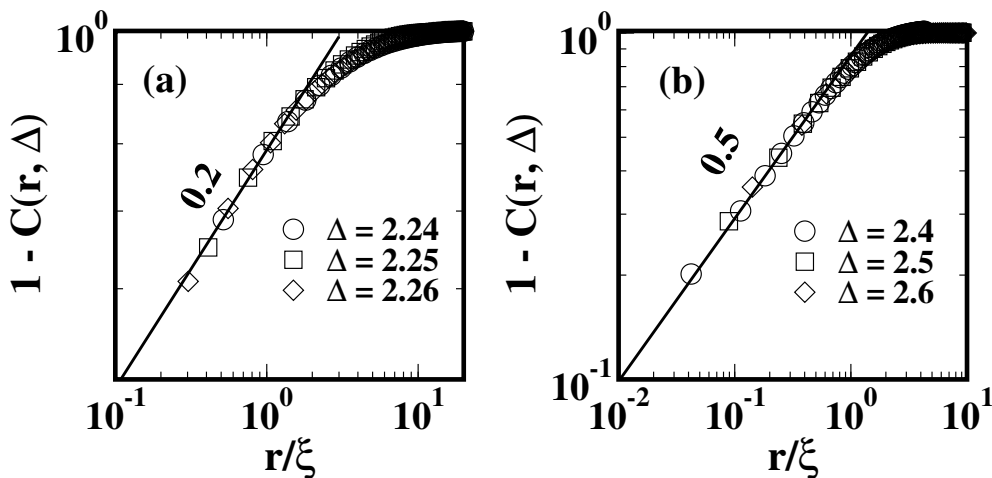


Figure 2.9: Log-log plot of  $1 - C(r, \Delta)$  vs  $r/\xi$  for the  $d = 3$  RFIM for the specified values of  $\Delta$ . The solid lines shows the power-law fit,  $1 - C(r, \Delta) \sim (r/\xi)^\zeta$ , with the cusp exponent estimated as (a)  $\zeta \simeq 0.2$  in the FM phase, and (b)  $\zeta \simeq 0.5$  in the PM phase.

vs  $r/\xi$  on a log-log scale in Fig. 2.9. We see that both phases exhibit a cusp singularity. In the FM phase [Fig. 2.9(a)], the cusp exponent is  $\zeta \simeq 0.2$ , yielding a fractal dimension  $d_f \simeq 2.8$  for the interfaces. It should be kept in mind that the FM morphology consists of a macroscopic up (or down) phase with impurity islands of down (or up) spins. In the PM phase [Fig. 2.9(b)],  $\zeta \simeq 0.5$ , yielding a fractal dimension  $d_f \simeq 2.5$ . We point out that the percolation cluster in the  $d = 3$  RFIM also has the same fractal dimension [42].

In Fig. 2.10, we present a scaling plot of the structure-factor data. We plot  $\xi^{-3}S(k, \Delta)$  vs  $\xi k$  for  $\Delta = 2.24, 2.25, 2.26$  [FM phase  $\Delta < \Delta_c$ , Fig. 2.10(a)] and  $\Delta = 2.4, 2.5, 2.6$  [PM phase  $\Delta > \Delta_c$ , Fig. 2.10(b)]. The different data sets collapse onto universal scaling functions for  $\Delta < \Delta_c$  and  $\Delta > \Delta_c$ , demonstrating that the morphologies are scale invariant. For  $\Delta < \Delta_c$ , the scaling function shows a non-Porod tail,  $S(k, \Delta) \sim k^{-3.2}$ , which is consistent with the cusp singularity in Fig. 2.9(a). For  $\Delta > \Delta_c$ , the corresponding non-Porod tail is  $S(k, \Delta) \sim k^{-3.5}$ , also consistent with Fig. 2.9(b).

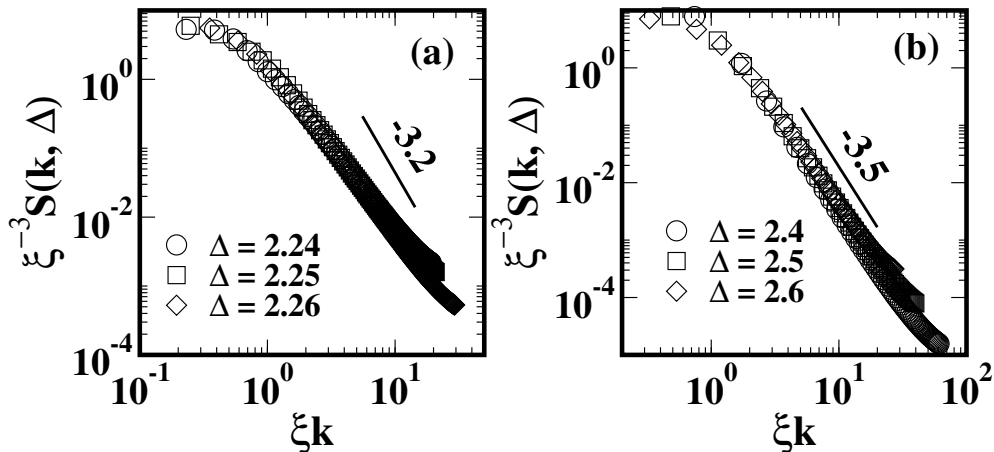


Figure 2.10: (a) Log-log plot of scaled SF:  $\xi^{-3}S(k, \Delta)$  vs  $\xi k$ , corresponding to the correlation functions in Fig. 2.9. The solid lines denote a non-Porod regime [ $S(k, \Delta) \sim k^{-(d+\zeta)}$ ] with (a) slope  $\simeq -3.2$  in the FM phase; (b) slope  $\simeq -3.5$  in the PM phase.

## 2.4 Experimental Evidence of Non-Porod Behavior

A surge of experimental and theoretical activity was initiated by Fishman and Aharony [3], who showed that effective random fields can be generated in dilute antiferromagnets (DAFs) upon application of a uniform field. Since then, scattering data from DAFs have been frequently used to support theories of phase transitions, critical exponents, and scaling laws in the RFIM [43]. In this section, we reinterpret some experimental data to verify our numerical results on scattering properties of ground-state morphologies in the RFIM. We will provide the two common examples of DAFs, realized by the RFIM.

The most commonly studied realization of the  $d = 2$  RFIM is the dilute antiferromagnet  $\text{Rb}_2\text{Co}_x\text{Mg}_{1-x}\text{F}_4$  [44]. This is a layered compound and the dominant magnetic interaction between the  $\text{Co}^{2+}$  ions is short-ranged. The two-dimensional character of spin ordering is the result of a large intraplanar exchange interaction relative to the interaction between the planes. In Fig. 2.11, we replot neutron-scattering data obtained by Birgeneau et al. [6] for  $\text{Rb}_2\text{Co}_{0.7}\text{Mg}_{0.3}\text{F}_4$ . We choose data recorded for (a)  $T = 5$  K, (b)  $T = 45$  K, and (c)  $T = 60$  K. All data sets

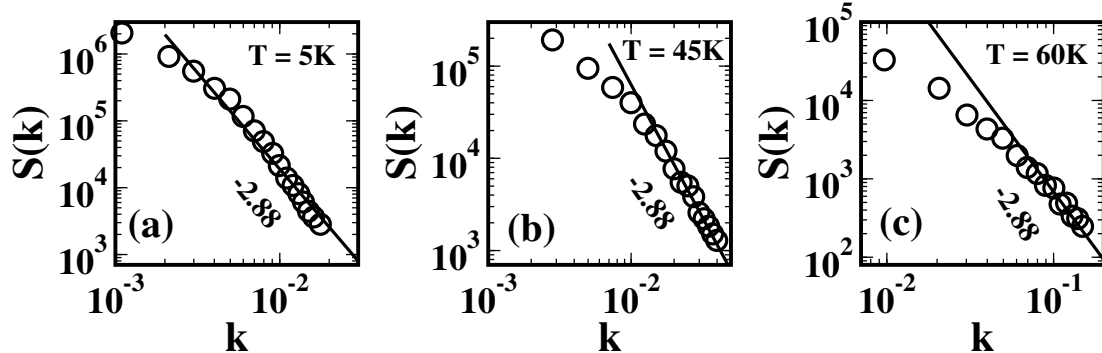


Figure 2.11: Scattering data obtained for a  $\text{Rb}_2\text{Co}_{0.7}\text{Mg}_{0.3}\text{F}_4$  sample [6] at (a)  $T = 5$  K, (b)  $T = 45$  K, and (c)  $T = 60$  K. The solid line with slope  $-2.88$  denotes the asymptotic non-Porod regime.

are consistent with a non-Porod regime of  $S(k, \Delta) \sim k^{-2.88}$  shown by solid lines, signifying the presence of fractal interfaces as seen in our simulations of Sec. 2.3.1.

Antiferromagnets which mimic the  $d = 3$  RFIM rather well are  $\text{Co}_x\text{Zn}_{1-x}\text{F}_2$  and  $\text{Fe}_x\text{Zn}_{1-x}\text{F}_2$  [45]. These are also layered compounds, but the interplanar coupling is comparable in strength to the intraplanar coupling. In Fig. 2.12, we plot the neutron-scattering data obtained by Hagen et al. [7] for  $\text{Co}_{0.35}\text{Zn}_{0.65}\text{F}_2$  on a log-log scale. The parameter values are (a)  $H = 3.5$  T,  $T = 7$  K, and (b)  $H = 5.0$  T,  $T = 2$  K. In both data sets, the structure-factor tail shows an asymptotic non-Porod regime  $S(k, \Delta) \sim k^{-3.5}$ , indicated by the solid line. The cusp exponent is consistent with that reported in Sec. 2.3.2 for the PM phase of the  $d = 3$  RFIM.

Therefore, the large- $k$  behavior of the experimental SF exhibits a distinct non-Porod regime signifying fractal interfaces, and the corresponding cusp exponents agree with our theoretical predictions.

## 2.5 Summary and Discussion

Let us conclude this chapter with a summary and discussion of our results. We have used a computationally efficient BK algorithm of GC method to obtain exact ground states of the RFIM in  $d = 2, 3$ . The usage of the BK-GC method [30] allowed us to access the ground-state morphologies of large system sizes. We

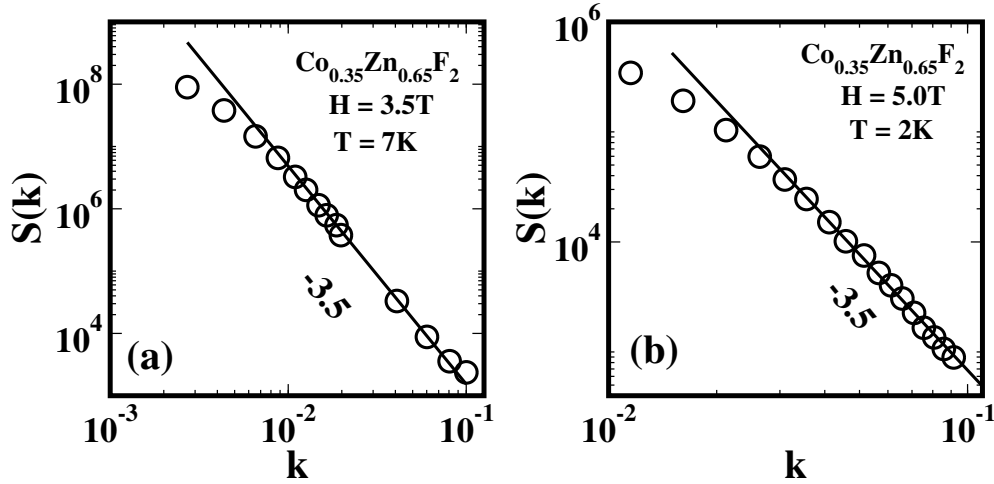


Figure 2.12: Scattering data obtained for a  $\text{Co}_{0.35}\text{Zn}_{0.65}\text{F}_2$  sample [7] at (a)  $H = 3.5\text{ T}$ ,  $T = 7\text{ K}$ ; and (b)  $H = 5\text{ T}$ ,  $T = 2\text{ K}$ . The solid line with slope  $-3.5$  denotes the asymptotic non-Porod regime.

characterize these morphologies using correlation functions  $C(r, \Delta)$  and structure factors  $S(k, \Delta)$ , which contain information averaged over all domains and interfaces. Therefore, our numerical results have a high degree of precision.

The main results of this chapter are as follows.

- (a) For the  $d = 2$  RFIM with  $\Delta_c = 0$ , the correlation length  $\xi(\Delta)$  diverges as  $e^{a/\Delta}$  for  $\Delta \rightarrow 0$ .
- (b) For the  $d = 2$  RFIM with  $\Delta_c = 0$ ,  $C(r, \Delta)$  is characterized by a universal scaling function for different disorder amplitudes up to  $\Delta \simeq 1$ . For higher values of  $\Delta$ , there is essentially no domain structure and the correlation length is  $O(1)$  lattice spacing.
- (c) For the  $d = 2$  RFIM, the small- $r$  behavior of  $C(r, \Delta)$  and the large- $k$  behavior of  $S(k, \Delta)$  show a non-Porod behavior:  $1 - C(r, \Delta) \sim r^{0.88}$  and  $S(k, \Delta) \sim k^{-2.88}$ . This corresponds to scattering off fractal interfaces with  $d_f \simeq 1.12$ .
- (d) For the  $d = 3$  RFIM, using the fourth-order Binder-cumulant, we obtain  $\Delta_c = 2.278 \pm 0.002$ , consistent with the earlier predictions. The correlation



## 2.5. Summary and Discussion

---

length  $\xi(\Delta) \sim (\Delta - \Delta_c)^{-\nu}$  as  $\Delta \rightarrow \Delta_c^+$  with  $\nu \simeq 1.308$ .

- (e) For the  $d = 3$  RFIM,  $C(r, \Delta)$  is characterized by distinct scaling functions for  $\Delta > \Delta_c$  (PM phase) and  $\Delta < \Delta_c$  (FM phase). The cusp exponent is  $\zeta \simeq 0.5$  with  $d_f \simeq 2.5$  for  $\Delta > \Delta_c$ ; and  $\zeta \simeq 0.2$  with  $d_f \simeq 2.8$  for  $\Delta < \Delta_c$ . These results are consistent with both analytical predictions and experiments.
- (f) The non-Porod behavior of the SF in small angle neutron-scattering experiments on DAFs is due to fractal interfaces.

Fractal morphologies arise in many physical systems, ranging from thin films to colloidal aggregates to cometary dust. The techniques discussed in this chapter are convenient to probe textures and organizational properties of domains and interfaces. For example, similar non-Porod or cusp behavior has been reported recently in the context of *fluctuation-dominated phase separation* [46, 47]. The CF and the SF contain information averaged over all domains and interfaces. Therefore, quantities such as the roughness exponent, fractal dimension, domain size, interface width, etc., can be obtained with great precision. We hope that it will stimulate further experimental and theoretical studies of systems with fractal interfaces.

# References

- [1] T. Nattermann and J. Villain, *Phase Transitions* **11**, 5 (1988).
- [2] T. Nattermann, in *Spin Glasses and Random Fields*, edited by A.P. Young (World Scientific, Singapore, 1998).
- [3] S. Fishman and A. Aharony, *J. Phys. C.* **12**, L-729 (1979).
- [4] D.P. Belanger, A.R. King, and V. Jaccarino, *Phys. Rev. Lett.* **48**, 1050 (1982).
- [5] J. P. Hill, Q. Feng, R. J. Birgeneau, and T. R. Thurston, *Z. Phys. B* **92**, 285 (1993).
- [6] R. J. Birgeneau, H. Yoshizawa, R. A. Cowley, G. Shirane, and H. Ikeda, *Phys. Rev. B* **28**, 1438 (1983).
- [7] M. Hagen, R. A. Cowley, S. K. Satija, H. Yoshizawa, G. Shirane, R. J. Birgeneau, and H. J. Guggenheim, *Phys. Rev. B* **28**, 2602 (1983).
- [8] R.L.C. Vink, K. Binder, and H. Löwen, *Phys. Rev. Lett.* **97**, 230603 (2006).
- [9] B. Tadic, *Eur. Phys. J. B* **28**, 81 (2002).
- [10] J.P. Sethna, K.A. Dahmen, and C.R. Myers, *Nature* **410**, 242 (2001).
- [11] Y.G. Pollack and M. Schechter, *Phys. Rev. B* **89**, 064414 (2014).
- [12] Y. Imry and S. K. Ma, *Phys. Rev. Lett.* **35**, 1399 (1975).
- [13] A. P. Young, *J. Phys. C: Solid State Phys.* **10**, L-257 (1977).

- 
- [14] J. Z. Imbrie, Phys. Rev. Lett. **53**, 1747 (1984); Commun. Math. Phys. **98**, 145 (1985).
- [15] J. Bricmont and A. Kupiainen, Phys. Rev. Lett. **59**, 1829 (1987).
- [16] M. Aizenman and J. Wehr, Phys. Rev. Lett. **62**, 2503 (1989).
- [17] A. P. Young and M. Nauenberg, Phys. Rev. Lett. **54**, 2429 (1985).
- [18] A. T. Ogielski, Phys. Rev. Lett. **57**, 1251 (1986); A. T. Ogielski and D. A. Huse, Phys. Rev. Lett. **56**, 1298 (1986).
- [19] H. Rieger and A. P. Young, J. Phys. A **26**, 5279 (1993); H. Rieger, Phys. Rev. B **52**, 6659 (1995).
- [20] M. E. J. Newman and G. T. Barkema, Phys. Rev. E **53**, 393 (1996).
- [21] M. Mézard and A. P. Young, Europhys. Lett. **18**, 653 (1992); M. Mézard and R. Monasson, Phys. Rev. B **50**, 7199 (1994).
- [22] A. A. Middleton and D. S. Fisher, Phys. Rev. B **65**, 134411 (2002).
- [23] M. E. Fisher, Rep. Prog. Phys. **30**, 615 (1967).
- [24] D. S. Fisher, Phys. Rev. Lett. **56**, 416 (1986).
- [25] Y. Wu and J. Machta, Phys. Rev. Lett. **95**, 137208 (2005).
- [26] N. G. Fytas and V. Martin-Mayor, Phys. Rev. Lett. **110**, 227201 (2013).
- [27] M. Picco and N. Sourlas, J. Stat. Mech., P03019 (2014).
- [28] J. Villain, Phys. Rev. Lett. **52**, 1543 (1984).
- [29] A. J. Bray and M. A. Moore, J. Phys. C **18**, L927 (1985).
- [30] Y. Boykov and V. Kolmogorov, IEEE Trans. PAMI **26**, 1124 (2004).
- [31] K. Binder, Z. Phys. B **50**, 343 (1983).
- [32] E. T. Seppala, V. Petaja, and M. J. Alava, Phys. Rev. E **58**, R5217 (1998); E. T. Seppala and M. J. Alava, Phys. Rev. E **63**, 066109 (2001).

- 
- [33] C. Fontera and E. Vives, *Comput. Phys. Commun.* **121**, 188 (1999).
- [34] L. Kornyei and F. Igloi, *Phys. Rev. E* **75**, 011131 (2007).
- [35] J. D. Stevenson and M. Weigel, *Europhys. Lett.* **95**, 40001 (2011).
- [36] G. Porod, in *Small-Angle X-ray Scattering*, edited by O. Glatter and O. Kratky (Academic Press, New York, 1982).
- [37] Y. Oono and S. Puri, *Mod. Phys. Lett. B* **2**, 861 (1988).
- [38] K. Binder and D. W. Heerman, *Monte Carlo Simulation in Statistical Physics: An Introduction*, fourth ed. (Springer-Verlag, Berlin, 2002).
- [39] M. E. J. Newman and G. T. Barkema, *Monte Carlo Methods in Statistical Physics* (Oxford University Press, Oxford, 1999).
- [40] A.K. Hartmann, A.P. Young, *Phys. Rev. B* **64**, 214419 (2001).
- [41] N. G. Fytas, P. E. Theodorakis, I. Georgiou, and I. Lelidis, *Eur. Phys. J. B* **86**, 268 (2013).
- [42] E. T. Seppala, A. M. Pulkkinen, and M. J. Alava, *Phys. Rev. B* **66**, 144403 (2002).
- [43] D. P. Belanger, in *Spin Glasses and Random Fields*, edited by A.P. Young (World Scientific, Singapore, 1998).
- [44] H. Yoshizawa, R. A. Cowley, G. Shirane, R. J. Birgeneau, H. J. Guggenheim, and H. Ikeda, *Phys. Rev. Lett.* **48**, 438 (1982).
- [45] D. P. Belanger and A. P. Young, *J. Magn. Mater.* **100**, 272 (1991).
- [46] D. Das and M. Barma, *Phys. Rev. Lett.* **85**, 1602 (2000); M. Barma, *Euro Phys. J. B* **64**, 387 (2008).
- [47] S. Mishra and S. Ramaswamy, *Phys. Rev. Lett.* **97**, 090602 (2006).

# Chapter 3

## Random Field Ising Model in a Uniform Magnetic Field

### 3.1 Introduction

As introduced before, the RFIM is one of the simplest examples of a system with quenched disorder. An important feature of the RFIM is the possibility of finding exact ground states at  $T = 0$  by using fast GC methods. A closely related topic of current interest is to study the GS morphologies, motion of domains and interfaces of the RFIM on the application of an external driving field.

In chapter 2, we studied the GS morphologies in the  $d = 2, 3$  RFIM without any external field using a computationally efficient GC method [1]. In this chapter, we extend this work in the presence of an external field  $h$  for the  $d = 3$  RFIM. We consider three different types of distributions of the random field: Gaussian (G), uniform (U) and bimodal (B). The external field  $h$  is augmented from  $-h_0$  to  $h_0$ . For each value of  $h$ , we determine the GS using the BK-GC method [1]. We define *pinned-sites* as those which point against the direction of  $h$ , and *pinned-clusters* as those which nucleate from the pinned sites when the field is incremented. We study the growth, morphologies and interfacial properties of these *pinned-clusters* in the paramagnetic phase ( $\Delta > \Delta_c$ ).

Our main results in this chapter are as follows:

- (a) We obtain universal scaling forms and critical exponents for magnetization

$m$  vs.  $h$  curves and pinned-cluster distributions.

- (b) We obtain pinning-field distributions, which exhibit sharp discontinuities. These yield estimates of energy barriers to be overcome for interfacial motion.
- (c) The CF  $C(r, \Delta, h)$  for the pinned clusters has a universal scaling form for all values of  $\Delta > \Delta_c$  and  $h$ . It is also independent of the disorder type. Further, at short distances,  $C(r, \Delta, h)$  exhibits a cusp singularity.
- (d) The corresponding SF  $S(k, \Delta, h)$  exhibits a cross-over from a Porod to a non-Porod regime signifying compact pinned-clusters with fractal interfaces. The fractal dimension does not depend on the disorder type.
- (e) We analyze experimental cluster morphologies created by polarization switching in  $(\text{PZT})_{0.95}(\text{BFO})_{0.05}$ , a typical relaxor ferroelectric well-represented by the RFIM. These exhibit fractal interfaces consistent with our numerical studies.

This chapter is organized as follows. In Sec. 3.2, we introduce the model in an external field. Our detailed numerical results are presented in Sec. 3.3. In Sec. 3.4, we present the experimental realization of pinned cluster morphologies in RFIM and analyze the non-Porod behavior in these morphologies. Section 3.5 contains a summary and discussion of our results. Finally, the Appendix A provides a glossary of the variables used in the course of this study; a table of scaling forms of relevant quantities; and a table of critical parameters and exponents.

## 3.2 The Model

In presence of an external field  $h$ , the Hamiltonian of the RFIM in Eq. 1.2 can be expressed as

$$\mathcal{H}(\{s_i\}) = -J \sum_{\langle ij \rangle} s_i s_j - \sum_{i=1}^N (h_i + h) s_i. \quad (3.1)$$

### 3.3. Detailed Numerical Results

---

We study this model for three different types of the RF distributions:

$$\text{Gaussian: } P_g(h_i) = \frac{1}{\sqrt{2\pi\Delta^2}} e^{-h_i^2/(2\Delta^2)}, \quad (3.2)$$

$$\text{Uniform: } P_u(h_i) = \begin{cases} [\sqrt{12}\Delta]^{-1}, & |h_i| \leq \sqrt{3}\Delta, \\ 0, & |h_i| > \sqrt{3}\Delta, \end{cases} \quad (3.3)$$

$$\text{Bimodal: } P_b(h_i) = \frac{1}{2} [\delta(h_i - \Delta) + \delta(h_i + \Delta)]. \quad (3.4)$$

The parameter  $\Delta$  is a measure of the disorder strength. All three distributions have zero mean and variance  $\Delta^2$ .

## 3.3 Detailed Numerical Results

Without loss of generality, we set  $J = 1$  in Eq. (3.1). The GC simulations were performed on a cubic lattice ( $L^3$ ) with linear size  $L = 128$ . The initial state is taken as  $s_i = -1 \forall i$ . The external field  $h$  is incremented from  $-1$  to  $1$  ( $-h_0 \rightarrow h_0$ ) in steps of  $\Delta h = 0.001$ . At each step, the corresponding GS is obtained using the BK-GC method. The statistical results presented here were averaged over 100 configurations of  $\{h_i\}$  for each value of  $\Delta$ . In all our plots, the error bars in the data are less than the symbol size. As mentioned earlier, we consider three disorder types: Gaussian, uniform and bimodal.

### 3.3.1 Ground State Morphologies

In Fig. 3.1, we show typical GS morphologies of the Gaussian RFIM for a fixed realization of the random fields  $\{h_i\}$  with  $\Delta = 2.5 > \Delta_c \simeq 2.278$  [2], i.e., in the paramagnetic phase. Fig. 3.1(a) shows the variation of the magnetization per spin  $m$  with  $h$ . The  $h$ -values corresponding to the GS snapshots in Figs. 3.1(b)-(f) are marked in Fig. 3.1(a). In Fig. 3.1(b), all sites with  $s_i = +1$ , pointing opposite to the external field  $h = -1$ , are designated as pinned-sites and are marked black. For these sites, the effective local field

$$h_i^{\text{eff}} = J \sum_{L_i} s_{L_i} + h_i + h > 0, \quad (3.5)$$

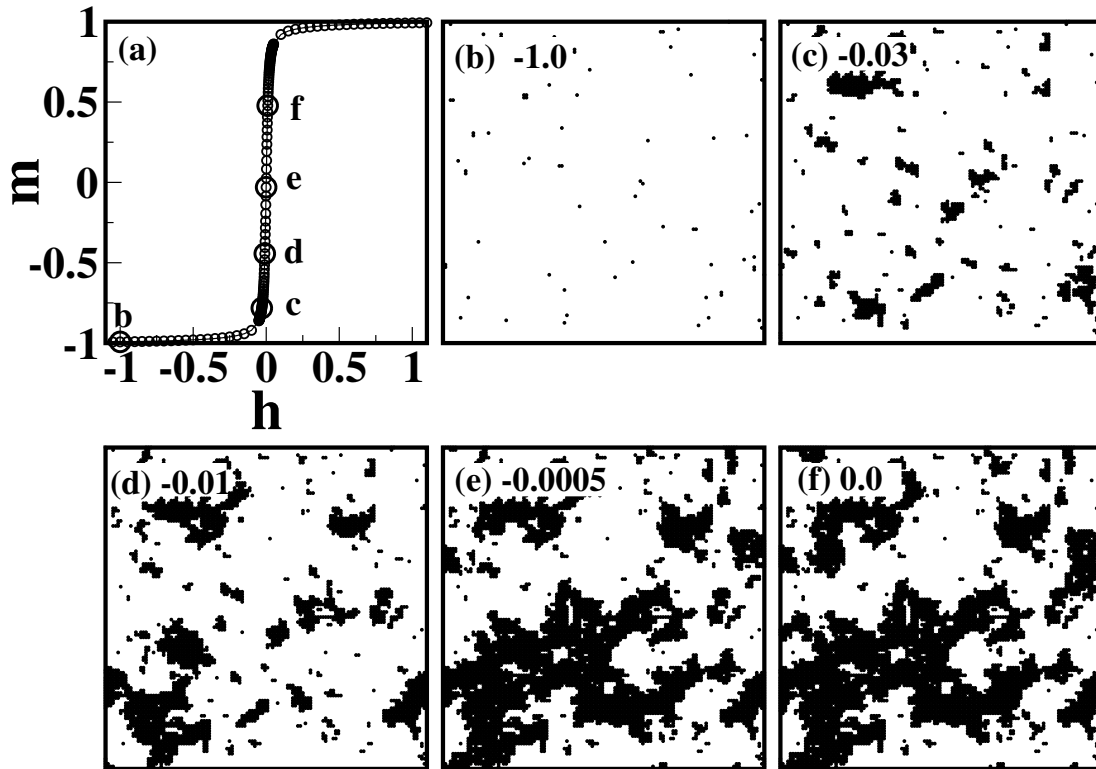


Figure 3.1: (a) Magnetization curve ( $m$  vs.  $h$ ) for Gaussian disorder with  $\Delta = 2.5$ . The panels (b)-(f) are snapshots of GS configurations in a  $(xy)$ -plane. These snapshots are taken at  $z = 64$  of  $128^3$  lattice at  $h = -1.0, -0.03, -0.01, -0.0005, 0.0$  for a fixed realization of the random fields  $\{h_i\}$ . Black regions denote up spins, and white regions denote down spins.

where  $L_i$  denotes the NN of site  $i$ . As  $h$  is increased, more spins flip to  $s_i = +1$ . The spin-up clusters or pinned clusters are marked black in Figs. 3.1(c)-(f). We focus on the statistical properties of these pinned clusters.

### 3.3.2 Magnetization Curves

The most commonly measured quantity is the magnetization  $m(h)$ , shown in Fig. 3.1(a) for  $\Delta = 2.5$ . If  $N(= L^3)$  is the total number of spins, the value of magnetization per spin is

$$m = \frac{1}{N} \sum_i^N s_i. \quad (3.6)$$



### 3.3. Detailed Numerical Results

Fig. 3.2(a) shows the GS magnetization for Gaussian disorder as  $h$  is increased from  $-1$  to  $1$  for several values of the disorder  $\Delta > \Delta_c$ . As the disorder decreases, there is a critical disorder value  $\Delta_c$  at which a discontinuous jump in the magnetization occurs at  $h_c = 0$ , typically when the number of spins pointing either up or down are of  $O(N)$ .

In a series of important papers, Sethna et al. [3–5] have studied hysteresis behavior across this first-order transition in the  $T = 0$  RFIM. They have also studied the critical behavior in the vicinity of  $(\Delta_c, h_c)$  via both mean-field theory and numerical simulations. In the study of Sethna et al., the RFIM transits between a sequence of metastable states as  $h$  is incremented. In our present study, the GC method finds the exact GS for an  $\{h_i\}$ -configuration at each value of  $h$ . Thus, there is no hysteresis in the  $m - h$  loops between the “forward” cycle ( $-h_0 \rightarrow h_0$ ) and the “backward” cycle ( $h_0 \rightarrow -h_0$ ). We are interested in the critical behavior reflected in these exact GS at different  $h$ -values.

First, let us consider the magnetization  $m(\Delta, h)$ , with the expected critical behavior:

$$m(\Delta, h) \sim |u|^\beta \mathcal{M}_\pm(h/|u|^{\beta\delta}). \quad (3.7)$$

Here,  $u = (\Delta - \Delta_c)/\Delta_c$  denotes the reduced disorder. Notice that the *critical magnetization*  $m_c = 0$  as we are studying exact GS. Further,  $\mathcal{M}_\pm$  is a universal scaling function in which  $\pm$  refers to the sign of  $u$ . The critical exponents  $\beta$  and  $\delta$  respectively give the power law singularities for  $m(\Delta, h)$  at  $h = 0$ :

$$\begin{aligned} m(\Delta, h = 0) &\sim |u|^\beta, & \Delta < \Delta_c, \\ &= 0, & \Delta > \Delta_c; \end{aligned} \quad (3.8)$$

and  $\Delta = \Delta_c$ :

$$m(\Delta_c, h) \sim h^{1/\delta} \quad \text{for } h \rightarrow 0^\pm. \quad (3.9)$$

For ease of reference, the scaling behaviors of the magnetization and other physical quantities used in this chapter are summarized in Table A.1. In Fig. 3.2(b), we collapse the  $m$  vs.  $h$  data from Fig. 3.2(a) using the scaling form in Eq. (3.7). The data collapse is excellent and enables us to determine  $\beta$  and  $\delta$ . The uniform and bimodal RFIMs also show excellent scaling with appropriate values of  $\beta, \delta$

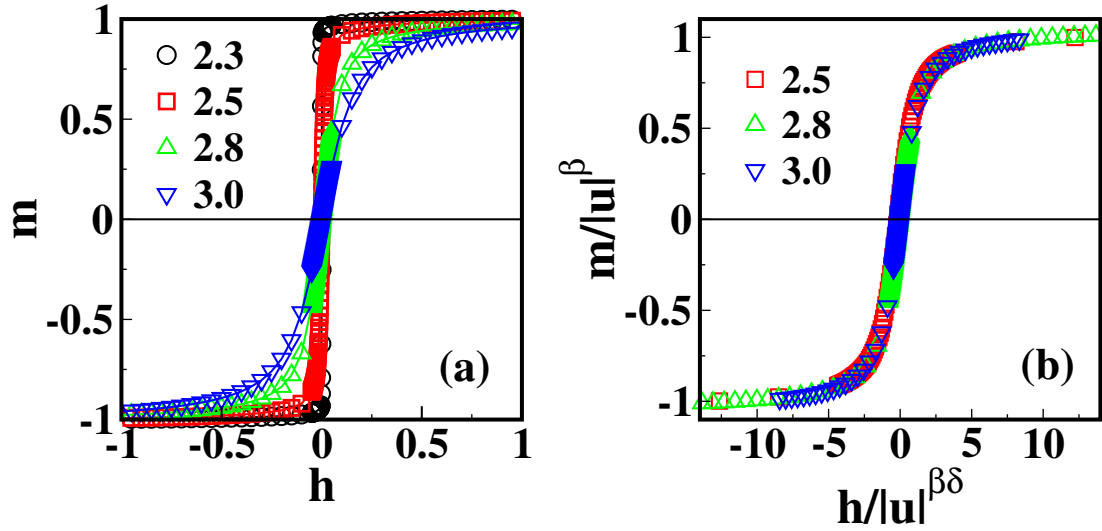


Figure 3.2: (a) Magnetization curves ( $m$  vs.  $h$ ) for Gaussian disorder with  $\Delta = 2.3, 2.5, 2.8, 3.0$ . These are obtained by averaging over 100  $\{h_i\}$  configurations. (b) Scaling of  $m$  vs  $h$  data in (a) using Eq. (3.7).

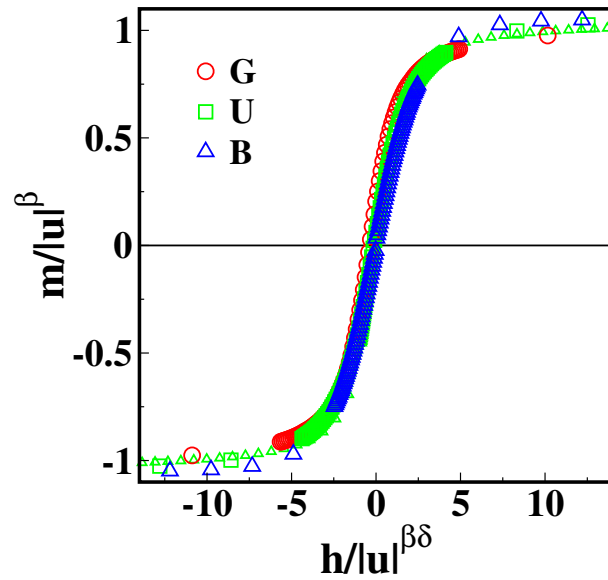


Figure 3.3: Scaling functions at  $\Delta = 2.5$  for the three disorder types: Gaussian (G), uniform (U), and bimodal (B). The critical exponents obtained from scaling collapse are provided in Table A.2.

### 3.3. Detailed Numerical Results

---

provided in Table A.2. The critical exponents  $\beta, \delta$  are independent of the disorder type. Further, the scaling functions are reasonably independent of the disorder type, as seen in Fig. 3.3, though the collapse is not perfect. This is consistent with the recent results of Fytas and Martín-Mayor [8], who argued that critical scaling behavior is independent of the disorder type for the RFIM.

For Gaussian disorder, we have determined the critical value of disorder ( $\Delta_c$ ) from Binder cumulant [6, 7] in Sec. 2.3.2. Also for other cases of disorder, we have verified the  $\Delta_c$  by evaluation of the Binder cumulants. The critical parameters and exponents for the three disorder types are summarized in Table A.2. It is interesting to note that the sequence of GS obtained as  $h$  is incremented from  $-h_0$  to  $h_0$  are linked, yielding scaling laws analogous to those obtained from the non-equilibrium evolution in the models of Sethna et al. [3–5]. In our study,  $h_c = 0$  for all the three distributions as the GC method yields exact GS, so our studies do not exhibit hysteresis. Our study is comparable to that of Sethna et al. in the adiabatic regime when the field is ramped infinitely slowly.

#### 3.3.3 Statistical Properties of Pinned Clusters

Next, we move on to study the statistical properties of pinned clusters, which are the primary focus of this study. Their typical evolution as a function of  $h$  was shown in Fig. 3.1 for Gaussian disorder with  $\Delta = 2.5$ . Recall that the pinning sites are those with  $s_i = +1$  when  $h < 0$ . As  $h$  is increased, these pinning sites forms connected regions or pinned clusters, shown in black. New sites with  $s_i = +1$  can also nucleate. The sequence of frames in Fig. 3.1 shows that pinned clusters grow rapidly, merge and eventually span the entire system. We are interested in the statistics of these clusters. We denote the number of spins in a cluster as  $q$ , and the corresponding distribution as  $D(q)$ .

In Fig. 3.4(a), we show the distributions  $D(q)$  vs.  $q$  for Gaussian disorder with  $\Delta = 2.3, 2.5$  at  $h = -0.5, -0.1$ . We compare these with  $D(q)$  vs.  $q$  at the critical point ( $\Delta_c \simeq 2.278, h_c = 0$ ), which obeys the power law  $D(q) \sim q^{-\tau}$  with  $\tau = 2.01 \pm 0.03$ , indicating that the clusters are scale-free at criticality. For other parameter values,  $D(q)$  shows power-law behavior over a limited  $q$ -window, and then crosses over to a more rapid decay—the crossover point depends

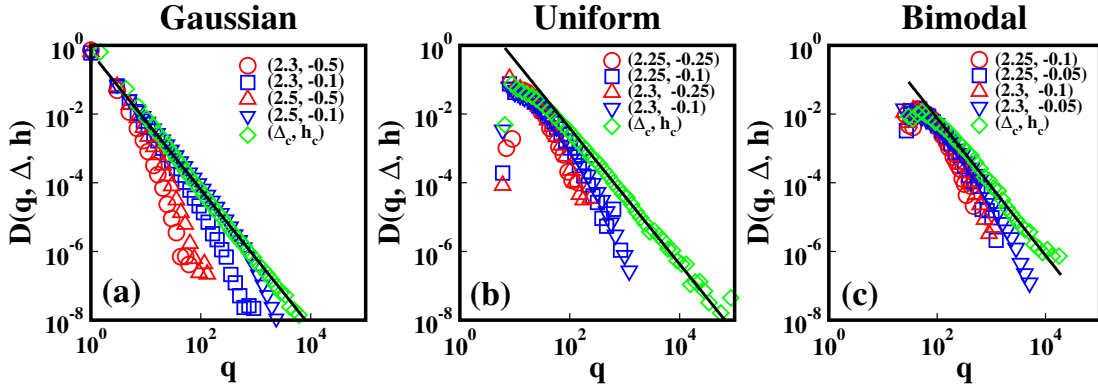


Figure 3.4: Pinned cluster distributions  $[D(q, \Delta, h) \text{ vs. } q]$  for the three disorder types: (a) Gaussian, (b) Uniform, (c) Bimodal. The values of  $(\Delta, h)$  are marked on the relevant frames. The solid lines denote the power-law fit to the distribution at the critical point  $(\Delta_c, h_c)$ . The slopes are (a)  $\tau \simeq 2.01 \pm 0.03$ , (b)  $\tau \simeq 1.98 \pm 0.05$ , (c)  $\tau \simeq 1.97 \pm 0.04$ .

on the proximity to the critical point and diverges as  $(\Delta, h) \rightarrow (\Delta_c, h_c)$ . A similar behavior is seen for uniform disorder [Fig. 3.4(b)] and bimodal disorder [Fig. 3.4(c)]. Following Sethna et al. [3–5], we propose the following scaling function for  $D(q)$  close to criticality:

$$D(q, \Delta, h) \sim q^{-\tau} \mathcal{D}_{\pm} \left( \frac{q}{|u|^{-1/\sigma}}, \frac{h}{|u|^{\beta\delta}} \right), \quad (3.10)$$

where  $\mathcal{D}_{\pm}$  denotes the two branches for  $u > 0$  and  $u < 0$ , respectively.

We can also study the integrated (over  $h \in [-\infty, 0]$ ) distribution of pinned clusters. From Eq. (3.10), the scaling function for this quantity is

$$\begin{aligned} D_{\text{int}}(q, \Delta) &= \int_{-\infty}^0 dh D(q, \Delta, h) \\ &\sim q^{-(\tau+\sigma\beta\delta)} \mathcal{D}_{\pm}^{\text{int}}(q|u|^{1/\sigma}). \end{aligned} \quad (3.11)$$

In Eq. (3.11), we have

$$\mathcal{D}_{\pm}^{\text{int}}(x) = x^{\beta\delta\sigma} \int_{-\infty}^0 dz \mathcal{D}_{\pm}(x, z). \quad (3.12)$$

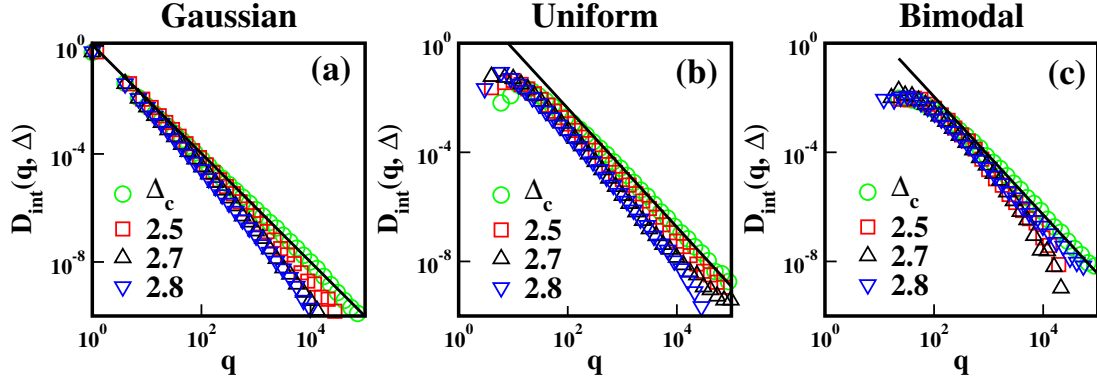


Figure 3.5: Integrated (over  $h$ ) pinned-cluster distributions for the three disorder types: (a) Gaussian, (b) Uniform, (c) Bimodal. The relevant values of  $\Delta$  are marked on the relevant frames. The solid lines denote the power-law fits to the distributions at  $\Delta_c$ :  $D_{\text{int}}(q) \sim q^{-(\tau+\sigma\beta\delta)}$ .

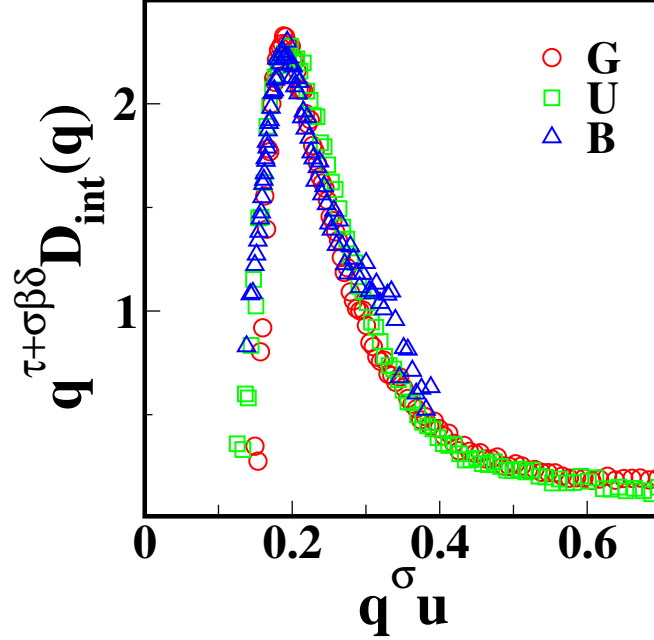


Figure 3.6: Scaling plot of integrated distributions from Fig. 3.5. We plot  $q^{(\tau+\sigma\beta\delta)} D_{\text{int}}(q)$  vs.  $q^\sigma |u|$  for all three disorder types with  $\Delta = 2.5$ . The exponents which yield the data collapse are provided in Table A.2.

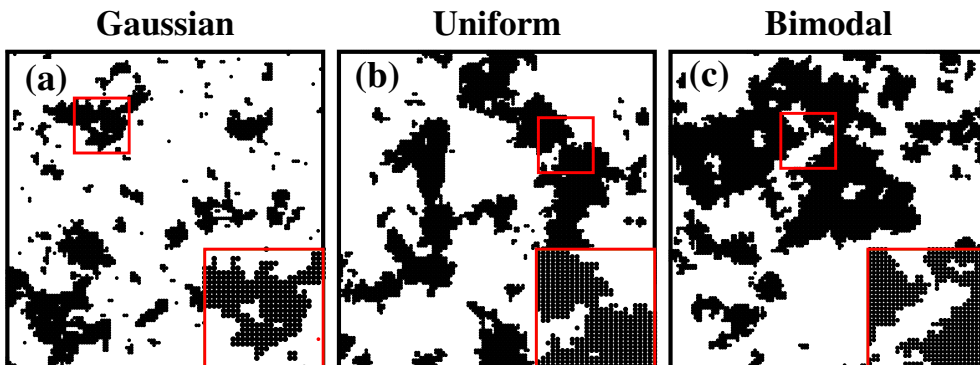


Figure 3.7: Ground-state snapshots obtained using BK-GC method for (a) Gaussian, (b) Uniform, and (c) Bimodal disorder. Each frame is a cross-section in the  $(xy)$ -plane taken at  $z = 64$  of a  $128^3$  lattice. These correspond to  $u = 0.1$  and  $h = -0.01$ . Pinned clusters are marked in black and down spins are shown in white. The bottom right corner in each frame shows an enlarged view of the region enclosed in the red square.

For  $u = 0$ ,  $D_{\text{int}}(q, \Delta)$  is scale-free with power-law exponent  $\tau + \sigma\beta\delta$ , as seen in Fig. 3.5(a) for Gaussian disorder. Notice that the power-law behavior is seen over more than 4 decades of  $q$ -values. The distributions for other values of  $u$  also show power-law behavior up to a cut-off value  $q_c \sim |u|^{-1/\sigma} \rightarrow \infty$  as  $u \rightarrow 0$ . Figs. 3.5(b) and 3.5(c) show the corresponding plots for the uniform and bimodal distributions, respectively. In Fig. 3.6, we plot  $q^{\tau+\sigma\beta\delta} D_{\text{int}}(q, \Delta)$  vs.  $q^\sigma u$  for all three disorder types with  $\Delta = 2.5$ . There is a reasonable collapse of the data sets, demonstrating that the scaling functions  $\mathcal{D}_{\pm}^{\text{int}}(x)$  are also independent of the disorder type. This is a stronger statement than the universality of critical exponents we have demonstrated earlier.

Next, we examine the characteristic textures of the clusters and interfaces. In Fig. 3.7, we show typical GS morphologies at  $u = 0.1$  for the three disorder types. The external field is  $h = -0.01$ . As before, the pinned clusters comprising of up spins are marked black. An enlarged view of the morphologies is provided in the bottom right corner of each figure. The following qualitative features are noteworthy: (a) For all three disorder types, the pinned clusters are compact with no internal structure. (b) For the same values of  $h$  and  $u$ , pinned clusters are smallest for Gaussian disorder and largest for bimodal disorder. (c) The interfaces of pinned clusters are rough in all three cases, and the morphologies

### 3.3. Detailed Numerical Results

are comparable.

As discussed in Sec. 1.5, a useful tool to quantify the textures of domains and interfaces is the spin-spin CF  $C(\mathbf{r})$ . As the system is isotropic, we spherically average  $C(\mathbf{r})$  to obtain the scalar function  $C(r)$ . The characteristic length scale  $\xi(\Delta, h)$  is defined as the distance over which  $C(r, \Delta, h)$  decays to  $0.2 \times$  maximum value. We follow the discussion in Secs. 1.5.1 and 1.5.2 that if the system is characterized by a single length scale, the morphology of the domains does not change with  $h$  and  $\Delta$ , apart from a scale factor. In that case, the CF exhibits scaling:  $C(r, \Delta, h) = g(r/\xi)$  and corresponding SF exhibits  $S(k, \Delta, h) = \xi^d f(k\xi)$ . Further, the small  $r/\xi$ -behavior of  $C(r, \Delta, h)$  exhibits a cusp singularity characterized by the roughness exponent  $\zeta$ , i.e.,  $1 - C(r, \Delta, h) \sim (r/\xi)^\zeta$ . The roughness or the cusp exponent  $\zeta$  is a consequence of rough interfaces separating domains, which are generally described as self-affine surface fractals with a dimension  $d_f = d - \zeta$ .

In Fig. 3.8(a), we plot  $C(r, \Delta, h)$  vs.  $r/\xi$  for different values of  $h$  for Gaussian disorder with  $\Delta = 2.3$ . The data collapse confirms that morphologies are scale-invariant for different  $h$ -values. In the inset of Fig. 3.8(a), we plot  $\tilde{C}(r, \Delta, h) = 1 - C(r, \Delta, h)$  vs.  $r/\xi$  on a log-log scale. The solid line in the inset denotes the best linear fit to the log-log data, corresponding to the power-law exponent  $\zeta = 0.5 \pm 0.01$ . This shows that the interfaces are fractal with  $d_f = 2.5$  for all values of  $h$ , consistent with our earlier results for the  $h = 0$  case (see Sec. 2.3.2). In Fig. 3.8(b), we plot the scaled structure factors,  $\xi^{-d} S(k, \Delta, h)$  vs.  $k\xi$ , corresponding to Fig. 3.8(a). In Fig. 3.9(a), we plot  $C(r, \Delta, h)$  vs.  $r/\xi$  for the three disorder types at  $h = -0.01$  and  $u = 0.1$ . The scaling functions are in good agreement with each other. Thus, the fractal interfaces in the RFIM are universal for different disorder types as well as the external fields. In Fig. 3.9(b), we plot the scaled structure factors corresponding to Fig. 3.8(b), i.e., for different disorder types. These plots are characterized by a non-Porod decay with a non-integer exponent  $\zeta \simeq 0.5$ .

An identical analysis was performed in the ferromagnetic phase ( $\Delta < \Delta_c$ ) and we did not observe a change in the corresponding roughness exponent ( $\zeta \simeq 0.66$  [9]) with disorder type or  $h$ -values. We emphasize that the calculation of the CF contains information averaged over all domains and interfaces. The estimates of the roughness exponent (and the fractal dimension) are therefore very accurate.

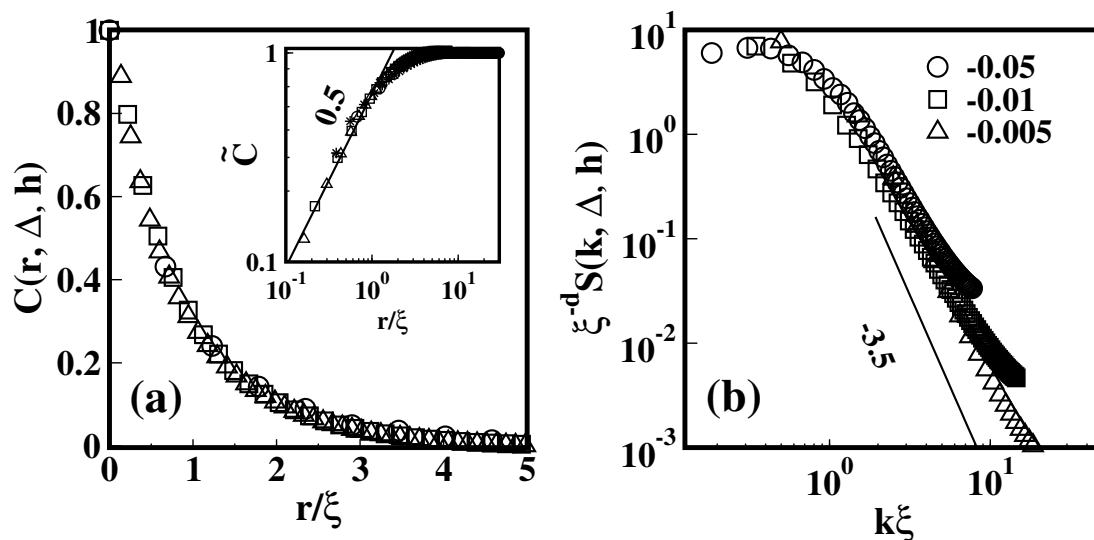


Figure 3.8: (a) Scaled correlation functions [ $C(r, \Delta, h)$  vs.  $r/\xi$ ] for Gaussian disorder with  $\Delta = 2.3$  and  $h = -0.05, -0.01, -0.005$ . The inset shows  $\tilde{C}(r, \Delta, h) = 1 - C(r, \Delta, h)$  vs.  $r/\xi$  on a log-log scale. The slope of the line in the inset gives the roughness exponent  $\zeta = 0.5 \pm 0.01$ . (b) Scaled structure factors,  $\xi^{-d} S(k, \Delta, h)$  vs.  $k\xi$ , for the data sets in (a). The solid line of slope  $-(d + \zeta)$  denotes a non-Porod regime, corresponding to the cusp in the CF.

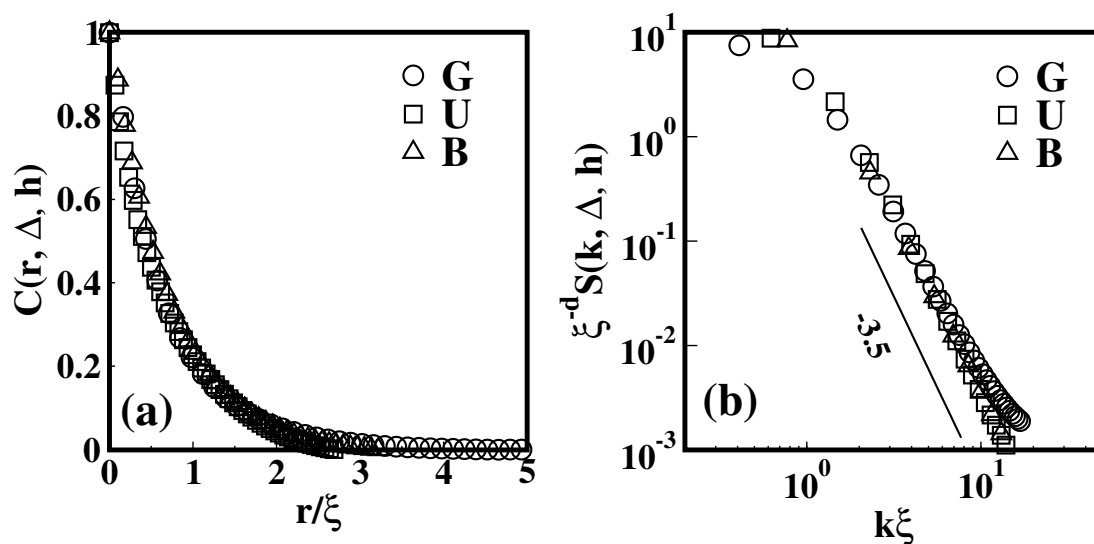


Figure 3.9: (a) Scaled CF for all three types of disorder with  $u = 0.1$  and  $h = -0.01$ . (b) Corresponding scaled SF for the data sets in (a).



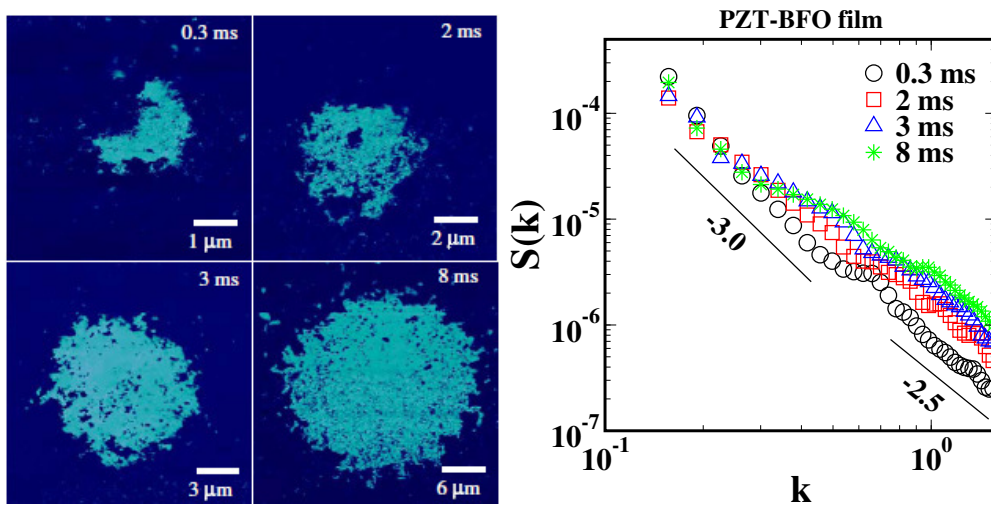


Figure 3.10: Left frame shows the evolution of the switched domain in a PZT-BFO film taken from Ref. [11]. The right frame show the corresponding scattering data,  $S(k)$  vs.  $k$ . The solid line of slope  $-3$  denotes the Porod regime in  $d = 2$ , which crosses over to a non-Porod regime of slope  $-2.5$  at large  $k$ .

### 3.4 Experimental Verification of non-Porod Results

Before ending this chapter, it is relevant to examine experimental realizations of the RFIM for validation of our numerical results. In this context, we study pinned cluster morphologies observed in  $(\text{PZT})_{1-x}(\text{BFO})_x$ , a prototypical relaxor ferroelectric. It is now well-established that these materials are modeled by the RFIM [10], with the random fields generated due to charge disorder arising from doping with BFO. Rodriguez et al. [11] used *piezo-response force microscopy* (PFM) to study the evolution of domains in  $(\text{PZT})_{0.95}(\text{BFO})_{0.05}$  due to polarization switching resulting from the application of voltage pulses of one sec duration. Fig. 3.10(a) reproduces the domain evolution observed by Rodriguez et al. at  $t = 0.3$  ms, 2 ms, 3 ms and 8 ms duration of the voltage pulse.

We digitized these images and evaluated the SF  $S(k)$  using the fast Fourier transform in Matlab. The adjoining Fig. 3.10(b) shows  $S(k)$  vs.  $k$  on a log-log scale. The solid lines with specified slopes are fits to different  $k$ -windows. There is a crossover from a Porod regime [with  $S(k) \sim k^{-(d+1)}$ ] at intermediate values

of  $k$  to an asymptotic cusp regime [with  $S(k) \sim k^{-(d+\zeta)}$ ,  $\zeta \simeq 0.5$ ]. Notice that  $d = 2$  in the present case as the sample has a thin-film geometry.

The fractal dimension of the interfaces from the  $S(k)$  vs.  $k$  plot is  $d_f = d - \zeta \simeq 1.5$ , in agreement with the value reported by Rodriguez et al. As seen in our numerical studies, the value of  $d_f$  is independent of the field. Further, the experimental  $d_f$ -value is consistent with our  $d_f$ -value reported here, if one accounts for the fact that our numerical studies are performed in  $d = 3$ , whereas the experiment is done in  $d = 2$ .

## 3.5 Summary and Discussion

The *random-field Ising model* (RFIM) is an archetypal example of a system with quenched disorder. As the latter is inherent in experimental systems, understanding of many phenomena in magnetism, superconductivity, porous flows, relaxor ferroelectrics, martensitic phase transitions, etc., has been possible from studies of the RFIM. In this chapter, we have analyzed the influence of an external field on properties of pinned domains and interfaces in the RFIM with (i) Gaussian (G), (ii) uniform (U), and (iii) bimodal (B) distributions of the random field. Such model studies are useful in the context of ferroelectric switches, for instance, having applications in sensors, actuators, random access memory, etc. [11]. Our results may be summarized as follows:

- (a) We have obtained detailed results regarding the critical behavior of the RFIM and the corresponding exponents. As expected, the critical properties are robust across different disorder types, in agreement with the recent studies of Fytas and Martin-Mayor [8].
- (b) We have characterized the pinned-cluster morphologies via their size distributions, which become scale-free at criticality. Another useful method of quantifying the pinned-cluster morphologies is via the CF  $C(r)$  and the SF  $S(k)$ . These quantities are independent of the disorder type, as well as the strength of the applied field. The CF shows a short-distance cusp singularity, and the SF exhibits a non-Porod tail at large wave-vectors. This

### 3.5. Summary and Discussion

---

feature results from scattering off fractal interfaces and provides an accurate estimate of the fractal dimension ( $d_f \simeq 2.5$  in all cases) of the interfaces.

- (c) The expected scaling forms (and associated exponents) of various physical quantities in (a) and (b) are summarized in Table A.1. The numerical values of various critical parameters and exponents are summarized in Table A.2.
- (d) We have analyzed domain morphologies from experiments on relaxor ferroelectrics, which are usually modeled by the RFIM. The corresponding  $S(k)$  vs.  $k$  curves also show a non-Porod tail with a universal fractal exponent independent of external field:  $d_f \simeq 1.5$  (in  $d = 2$ ). This is consistent with our numerical results on the RFIM.

In many physics problems and technological applications, it is crucial to understand the motion of interfaces under an external field. Interfaces in disordered systems become trapped by energy barriers which depend on disorder amplitude and the domain size  $\xi$ . Typically, there is a power-law dependence on  $\xi$  with an exponent which depends on the interfacial fractal dimension [12–14]. Our results in this chapter conclusively show that interfaces in the RFIM are robust to variations in the disorder type as well as the field strength. This demonstrates a broad universality in different physical scenarios. We hope that our theoretical results will motivate further experimental work on these important problems.

# Appendix A

## Glossary of Variables, Scaling Functions, and the Critical Exponents

$h$	Applied external field.
$h_c$	Critical field.
$\Delta$	Strength of disorder.
$\Delta_c$	Critical disorder strength.
$u$	Reduced disorder $(\Delta - \Delta_c)/\Delta_c$ .
$m(\Delta, h)$	Magnetization per spin at $(\Delta, h)$ .
$D(q, \Delta, h)$	Pinned-cluster size distribution at $(\Delta, h)$ .
$D_{\text{int}}(q, \Delta)$	Pinned-cluster size distribution integrated over $h$ at $\Delta$ .
$\xi(\Delta, h)$	Characteristic length scale at $(\Delta, h)$ .
$C(r, \Delta, h)$	Spin-spin CF at $(\Delta, h)$ .
$S(k, \Delta, h)$	Structure factor, the Fourier transform of $C(r, \Delta, h)$ .

---

Quantities	Scaling form	Exponents
$m(\Delta, h)$	$\sim  u ^\beta \mathcal{M}_\pm(h/ u ^{\beta\delta})$	$\beta, \delta$
$D(q, \Delta, h)$	$\sim q^{-\tau} \mathcal{D}_\pm(q u ^{1/\sigma}, h/ u ^{\beta\delta})$	$\tau, \sigma$
$D_{\text{int}}(q, \Delta)$	$\sim q^{-(\tau+\sigma\beta\delta)} \mathcal{D}_\pm^{\text{int}}(q u ^{1/\sigma})$	
$C(r, \Delta, h)$	$\simeq 1 - A(r/\xi)^\zeta$ at small $r/\xi$	$\zeta$
$S(k, \Delta, h)$	$\sim (\xi k)^{-(d+\zeta)}$ at large $k$	

Table A.1: Scaling forms of physical quantities and related exponents.

Disorder	$\Delta_c$	$h_c$	$\beta$	$\delta$	$\tau$	$\sigma$
Gaussian	2.278(2)	$0 \pm 0.004$	0.025(1)	$70 \pm 4$	$2.01 \pm 0.03$	$0.20 \pm 0.05$
Uniform	2.234(2)	$0 \pm 0.002$	0.020(5)	$72 \pm 2$	$1.98 \pm 0.05$	$0.20 \pm 0.02$
Bimodal	2.201(2)	$0 \pm 0.001$	0.025(5)	$74 \pm 1$	$1.97 \pm 0.04$	$0.17 \pm 0.01$

Table A.2: Values of critical parameters and exponents. Refs. [15, 16] provide values of  $\Delta_c$  for bimodal disorder.

# References

- [1] Y. Boykov and V. Kolmogorov, IEEE Trans. PAMI **26**, 1124 (2004).
- [2] G. P. Shrivastav, M. Kumar, V. Banerjee, and S. Puri, Phys. Rev. E **90**, 032140 (2014).
- [3] J.P. Sethna, K. Dahmen, S. Kartha, J.A. Krumhansl, B.W. Roberts, and D. Shore, Phys. Rev. Lett. **70**, 3347 (1993).
- [4] O. Perković, K.A. Dahmen, and J.P. Sethna, Phys. Rev. B **59**, 6106 (1999).
- [5] O. Perković, K.A. Dahmen, and J.P. Sethna, arXiv preprint cond-mat/0406320.
- [6] K. Binder and D.W. Heermann, *Monte Carlo Simulation in Statistical Physics: An Introduction*, 4th ed. (Springer-Verlag, Berlin, 2002).
- [7] M.E.J. Newman and G.T. Barkema, *Monte Carlo Methods in Statistical Physics*, (Oxford University Press, Oxford, 1999).
- [8] N.G. Fytas and V. Martín-Mayor, Phys. Rev. Lett. **110**, 227201 (2013).
- [9] A. Bupathy, V. Banerjee, and S. Puri, Phys. Rev. E **93**, 012104 (2016).
- [10] W. Kleemann, J. Dec, P. Lehnen, R. Blinc, B. Zalar and R. Pankrath, Europhys. Lett. **57**, 14 (2002).
- [11] B.J. Rodriguez, S. Jesse, A.P. Baddorf, S.-H. Kim, and S.V. Kalinin, Phys. Rev. Lett. **98**, 247603 (2007).
- [12] D. Huse and C.L. Henley, Phys. Rev. Lett. **54**, 2708 (1985).

- [13] T. Nattermann and I. Vilfan, *Phys. Rev. Lett.* **61**, 223 (1988).
- [14] S. Puri, *Phase Transitions* **77**, 469 (2004).
- [15] A.K. Hartmann and U. Nowak, *Eur. Phys. J. B* **7**, 105 (1999).
- [16] M.R. Swift, A.J. Bray, A. Maritan, M. Cieplak, and J.R. Banavar, *Europhys. Lett.* **38**, 273 (1997).

# Chapter 4

## Approximate Ground States in the Random Field Potts Model

### 4.1 Introduction

The Potts model is one of the popular spin model that finds many applications in statistical physics, e.g., in the study of normal grain-growth, nucleation, static and dynamic recrystallization, etc. The  $q$ -state Potts model is a generalization of Ising model for  $q$  possible states of spins [1, 2]. Naturally, the RFIM is a  $q = 2$  case of the  $q$ -state random-field Potts model (RFPM). There are physical and experimental realizations of the RFPM, e.g., orientational glass behavior and ordering in randomly diluted molecular crystals [3, 4], structural transition from a cubic or trigonal phase into the tetragonal phase in SrTiO<sub>3</sub> crystal [5], and phase transition in type I antiferromagnet (such as Ndsb, NdAs, CeAs) in a uniform field [6], etc.

As discussed earlier, one of the major interest in disordered systems is to find their ground states. It yields the important information about the equilibrium properties and the critical behavior of the system. While the RFIM is the simplest disordered system for which the GS problem has been exactly solved in polynomial (P) time using several graph cut (GC) techniques of maximum flow, the GS problem in RFPM is a multi-terminal flow problem that is known to be NP-hard. Hence an efficient exact algorithm is extremely unlikely to exist. However, it is



possible to use GC techniques to solve the corresponding ground-state problem approximately in P time. In this chapter, we show that this works very well. Before, we discuss our study, let us first review the earlier works on RFPM.

Previously, the RFPM has been studied analytically using the mean-field (MF) approximation [7, 8] and numerically by MC techniques [9–11]. These studies are for the phase diagram in a  $q$ - $d$  plane. The pure Potts model in  $d = 2$  has a second-order phase transition for  $q \leq 4$  and a first-order transition for  $q > 4$  [12]. On the other hand, in  $d = 3$ , there is a first-order transition for  $q \geq 3$ . With the disorder, Eichhorn and Binder (EB) [9, 10] studied the order of transition in  $q = 3$  and  $d = 3$  RFPM via MC approach. They found that the disorder turns the first order transition of the pure Potts model to the second order. But, this change of transition depends on the strength of disorder. For a weak enough disorder, the order of transition does not change. They proposed that the random fields strength shifts the tricritical curve  $q_c(d)$  to a higher value, consistent with the prediction of Blankschtein et al. [7] on the basis of MF theory. All values of  $q < q_c(d)$  show a second-order transition and  $q > q_c(d)$  show a first-order transition. In their phase diagram,  $q = 3$  and probably  $q = 4$  show the second-order transition. However, this disagrees with the result of Goldschmidt and Xu (GX) [13] who perform  $1/q$  expansions for  $q$ -state RFPM in  $d = 3$  and found that for  $q \geq 3$ , there is a first-order transition irrespective of the disorder strength.

In this chapter, we investigate the GS of the RFPM using the GC method. We compare the results of the energy minima produced by this heuristic algorithm to those found by an appropriately tuned *parallel tempering* (PT) method that is configured to find ground states for the considered system sizes with high probability. We observed that in most of the cases, the GC method finds the same states in a fraction of the time. In some cases, the PT method finds better estimate of the energy minima as compared to the GC, but in an exponential running time and also for restricted system sizes. On the other hand, the GC method efficiently computes good quality local energy minimum, close to the exact GS. The run-time typically scales linearly with the system size, which, therefore, allows to simulate large systems. Therefore, the GC method is used for a first exploratory study of the RFPM in  $d = 2, 3$ .

This chapter is organized as follows. In Sec. 4.2, we describe the model and

our methodology for studying the GS problem. Particularly, we describe the *parallel tempering* (PT) method. In Sec. 4.3, we present the detailed numerical results for the GS study of RFPM using GC method and compare the GS results of the GC method to the corresponding results from the PT method. Sec. 4.4 is devoted to the study of critical behavior in  $q = 3$  RFPM using GC method and to determine the critical exponents. Finally, in Sec. 4.5, we conclude this chapter with a summary of our results.

## 4.2 The Model and Methodology

Let us recall the Hamiltonian for the RFPM [7] as defined in Eq. (1.6) (considering  $h_i^\alpha \equiv \Delta \epsilon_i^\alpha$ )

$$\mathcal{H} = -J \sum_{\langle ij \rangle} \delta_{s_i, s_j} - \Delta \sum_i \sum_{\alpha=0}^{q-1} \epsilon_i^\alpha \delta_{s_i, \alpha}, \quad (4.1)$$

where each spin  $s_i$  can take any value from the set  $s_i = \{0, 1, \dots, q-1\}$ . The total number of spin-states  $q$  are also designated as the Potts states.  $\{\epsilon_i^\alpha\}$  are the quenched random-field (RF) variables, drawn from a Gaussian distribution of 0 mean and standard deviation 1. Notice that the RF variables are of  $q$  component. The parameter  $\Delta$  (in unit of  $J$ ) is a measure of disorder strength.

The other simpler form of Hamiltonian for RFPM, defined in Refs. [9, 13], is

$$\mathcal{H} = -J \sum_{\langle ij \rangle} \delta_{s_i, s_j} - \Delta \sum_i \delta_{s_i, h_i}. \quad (4.2)$$

Here, instead, the quenched random variables  $\{h_i\}$  are the random spin-states, chosen uniformly from the set  $s_i = \{0, 1, \dots, q-1\}$ . Thus, the distribution of random fields are discrete, which act with equal probability to any one of the  $q$  spin states, i.e.,

$$p(h_i) = \frac{1}{q} \sum_{\alpha=0}^{q-1} \delta(h_i - \alpha), \quad (4.3)$$

whereas in the previous Hamiltonian [Eq. (4.1)], the random fields are coupled to all  $q$  spin-states. Therefore, the Hamiltonian in Eq. (4.1) is more general and we use this Hamiltonian in our study of RFPM.

We have described the GC method in Sec. 1.4.1. Let us now discuss the PT method.

### 4.2.1 Parallel Tempering Method

PT or the replica exchange method is an efficient MC technique which allows for simultaneously studying a system at a set of many different temperatures, and at the same time overcomes the difficulties encountered in sampling the phase space of a disordered system. The general idea of the PT method is to simulate several replicas of the system at different temperatures and then exchanging the configurations at adjacent temperatures [14–19]. In this way, the system lowers its energy by overcoming the free energy barriers to reach into the GS. In the literature, many disordered systems have been studied for the ground states using the PT method [20–25].

Let  $N_T$  be the number of non-interacting independent replicas of the system that are simulated simultaneously at different temperatures. In each independent system, we perform single spin flip Metropolis move over the whole lattice. Once all the replicas are simulated, the configurations at adjacent temperatures are exchanged with the probability:

$$P_{\text{ex}} = \min [1, e^{-(\beta_{m+1}-\beta_m)(E_m-E_{m+1})}] , \quad (4.4)$$

where  $\beta_m$  and  $E_m$  are the inverse temperature and the energy of the  $m_{\text{th}}$  replica, respectively. The crucial, but non-trivial part of the algorithm is that how one chooses the temperatures of replicas in the PT simulation.

#### *Choosing optimal set of the temperatures*

There have been many studies [26–34], which proposed different ideas of finding the optimal choices of temperatures. Katzgaber *et.al.* [26] proposed that the optimal choice of temperatures corresponds to a maximum rate of round trips between the lowest and highest temperature. Their scheme uses an adaptive feedback-optimized algorithm with a recursive readjustment of temperatures to minimize the round trip times (or tunneling times). This feedback-optimized

## 4.2. The Model and Methodology

---

update scheme is a sophisticated and appealing method, but because of its complexity, other simpler methods have been more often implemented in comparative studies of PT.

A simpler method based on the acceptance rates was analyzed by Bittner *et.al.* [27]. In their method, adjacent temperatures are determined from an exchange acceptance rate given by

$$R(m \rightarrow m + 1) = \sum_{E_m, E_{m+1}} P_{T_m}(E_m) P_{T_{m+1}}(E_{m+1}) P_{ex}. \quad (4.5)$$

Here,  $P_{T_m}(E_m)$  is the probability for replica  $m$  at temperature  $T_m$  to have the energy  $E_m$ . It is obvious that the acceptance rate and tunneling time—average time taken by a replica to go from the lowest to the highest temperature—play the most important role to get an optimized set of temperatures.

In our work, we use a greedy optimization method to choose optimal temperatures. The temperature  $T_m$  of the  $m_{\text{th}}$  replica is chosen as

$$T_m = m^\eta T_{\text{norm}} + T_{\text{min}}, \quad (4.6)$$

where

$$T_{\text{norm}} = \frac{T_{\text{max}} - T_{\text{min}}}{(N_T - 1)^\eta}, \quad (4.7)$$

with maximum temperature  $T_{\text{max}} = 1.5$  and minimum temperature  $T_{\text{min}} = 0.2$ . This is chosen so as to avoid metastability and not to have large number of replicas.  $\eta$  is a parameter which we determine as follows: (a) choose a set of temperatures for some initial value of  $\eta$  and run simulations, (b) measure the acceptance rates and the tunneling time, and repeat the simulations with some modified value of  $\eta$ , (c) select that value of  $\eta$ , which maximizes the acceptance rate and minimize the tunneling time. The value of  $\eta$  and the number of replicas  $N_T$  for different lattices  $L$ , which we use in our simulation, are listed in a Table 4.1.

Though, the PT method has been used as an optimization technique for finding the global minima of disordered systems, it is not guaranteed that the lowest energy state found is a GS. But, for the smaller system sizes, the PT method should be able to find the ground states. Therefore, our aim is to generate the

### 4.3. Numerical Results

---

$L$	8	12	16	20	24	32	48
$N_T$	16	16	16	16	16	32	32
$\eta$	1.3	1.3	1.3	1.3	1.3	1.14	1.14

Table 4.1: The values of  $\eta$  and the number of temperatures  $N_T$  for different lattice sizes  $L$ .

exact ground states for typically smaller system sizes using PT and use them as a reference to compare the corresponding minimum energy states from the GC method.

In order to generate the typical ground states from PT, we measure the time  $t_0$  (in the units of Monte Carlo time steps) for the first occurrence of the lowest energy state during the simulation. The time  $t_0$  is measured for several disorder realizations. Out of the distribution of  $t_0$ 's for different disorder realization, we select the largest value and re-run our simulations ten times longer than this time. This process is repeated until the lowest energy found does not change for all simulations for different disorder realizations. We refer this lowest energy state as the GS in our work. Fig. 4.1 shows a schematic representation of time  $t_0$  and the GS energy  $E_0$ .

Fig. 4.2 is a plot for mean and median of  $t_0$  as a function of Potts states  $q$  and system size  $L$ . The shaded area shows the region of the data fluctuations. These plots are shown on a log-linear scale. In Fig. 4.2a, we observe that  $t_0$  increases non-exponentially with the number of Potts-states  $q$ , while in Fig. 4.2b, we observe an exponential increase of  $t_0$  for system sizes  $L \geq 16$ . From the plot, as mean values are smaller than the medians, it shows an asymmetrical and tail heavy distribution of  $t_0$ . The distribution is positively skewed and one is interested in higher moments.

## 4.3 Numerical Results

We present the detailed numerical results for the GS problem in RFPM in the following order. (i) Verify the GC method for the approximate ground states. (ii) Compare the GS results of GC method to the exact results from the PT method.

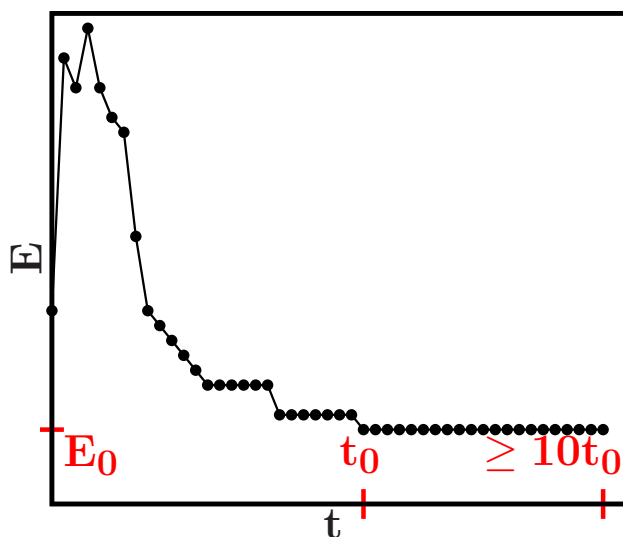
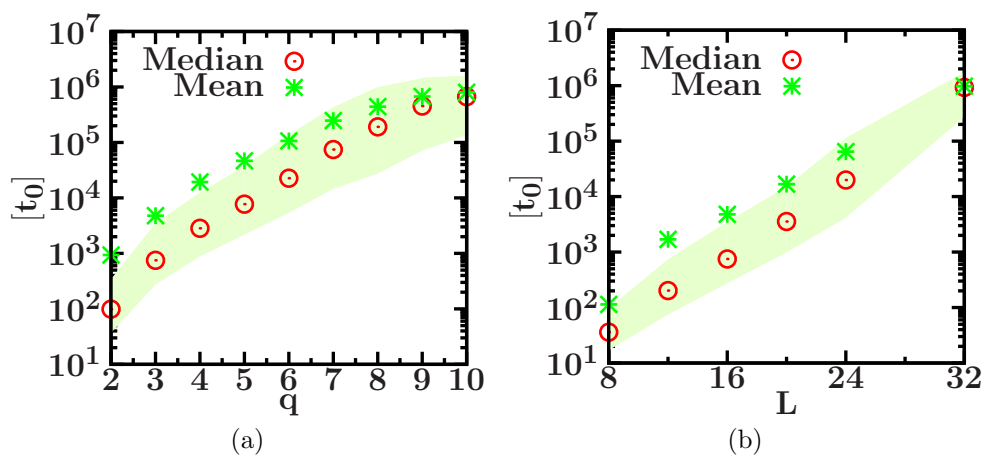
Figure 4.1: Schematic diagram showing  $t_0$  and  $E_0$ 

Figure 4.2: Plots of  $t_0$ , the time of first appearance of the GS obtained from a very long simulation as a function of (a) number of Potts states  $q$  and (b) system size  $L$ . The data is shown on a log-linear scale. The shaded area shows the fluctuations of the data. The number of disorder realizations are 1500.

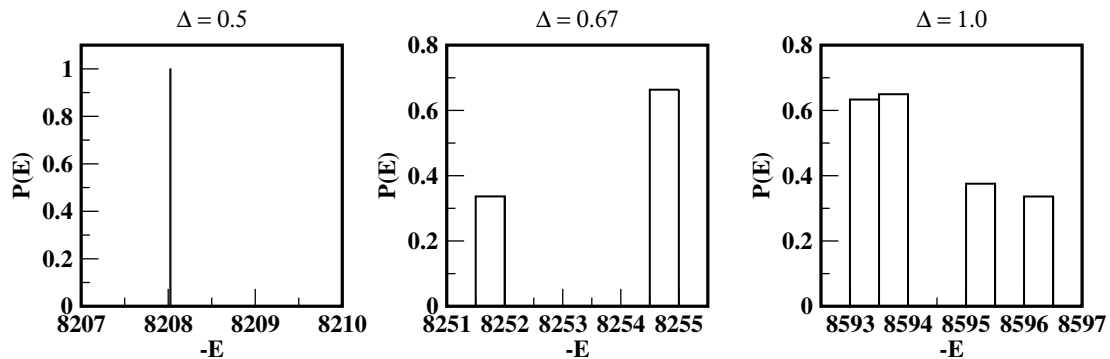


Figure 4.3: Energy histograms of metastable states for the  $q = 3$  RFPM on a  $64^2$  lattice. These histograms are for a fixed disorder configuration  $\{\epsilon_i^\alpha\}$  and 10000 independent runs of GC for different initial configurations  $\{s_i\}$ .

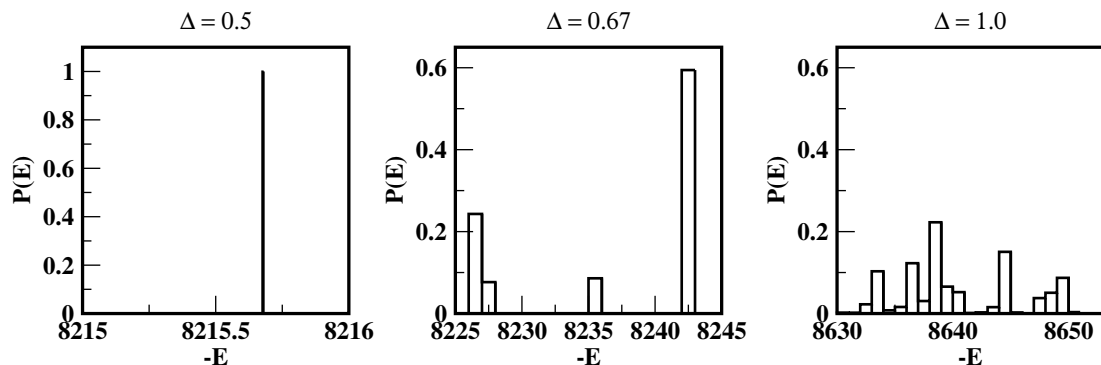


Figure 4.4: Analogous to Fig. 4.3 but for the  $q = 4$  RFPM.

(iii) Discuss the performance and efficiency of the GC method.

### 4.3.1 Approximate Ground States from the GC Method

Let us begin by testing the GC for the approximate ground states in RFPM. In order to do this, we fix the disorder configuration  $\{\epsilon_i^\alpha\}$  and obtain the minimum energy states from several runs of the GC for different initial labeling  $\{s_i\}$ . Fig. 4.3 shows the histograms of energies of such metastable states for the  $q = 3$  RFPM. The simulations are performed on a  $64^2$  lattice for 10000 runs of different initial conditions.  $E = \mathcal{H}(\{s_i\})$  is the total energy of the RFPM from the Hamiltonian in Eq. (4.1) (Note that  $E$  is negative and we have plotted  $-E$ ). For  $\Delta = 0.5$ , we always have a same energy state for several runs of different initial conditions and

therefore, the histogram shows a sharp peak corresponding to that energy state. As we increase the disorder strength  $\Delta$ , the histogram shows the distribution over multiple energy states. The GC method therefore does not produce the exact ground states of the RFPM. Fig. 4.4 shows similar histograms for the  $q = 4$  RFPM. It can be clearly seen that the histograms are wider as compared to  $q = 3$ .

To quantify the energy spread in the histogram, we determine the standard deviation in energy,  $\sigma_E = \sqrt{\langle (E - \langle E \rangle)^2 \rangle}$ .  $\langle E \rangle$  is the mean of energies obtained for different runs of GC for a fixed disorder realization; and for any quantity,  $[\dots]$  denotes the average over different disorder realizations. In Fig. 4.5, we show the energy spread plot with disorder  $\Delta$  for  $q = 3$  and  $q = 4$  RFPM on a square lattice ( $L^2$ ) of linear size  $L = 32, 62, 128$ . The energy spread is determined from 1000 independent runs for a fixed disorder realization and then averaged over 100 disorder realizations. The figure shows that the energy spread grows with increase in  $L$ . In order to check the  $L$ -dependence of  $[\sigma_E]$ , we plot  $\sigma_E/\sqrt{N}$  in inset of Fig. 4.5, which shows a nice data collapse. Therefore,  $\sigma_E \sim \sqrt{N}$ , as  $\langle E \rangle \propto N$ , it yields a well-known relation:

$$\left[ \frac{\sigma_E}{\langle E \rangle} \right] \sim \frac{1}{\sqrt{N}}, \quad (4.8)$$

which means that the energy fluctuations about the mean energy will vanish in the thermodynamic limit,  $N \rightarrow \infty$ .

In another plot in Fig. 4.6, we show an explicit  $q$ -dependence of the energy spread at a fixed  $\Delta$  and varying the  $q$ . Here, we can say that with increasing  $q$ , the number of metastable states increase and the GC method is getting worse in terms of the good quality energy minima. The inset of this figure again confirms  $\sigma_E \sim \sqrt{N}$ . We also perform a similar analysis of energy spread in the  $d = 3$  RFPM as shown in Fig. 4.7. Also, in this plot, the energy spread  $[\sigma_E]$  grows with lattice size  $L$  as well as total number of labels  $q$ . Near the critical region, the energy spread curves show a peak, meaning that the energy fluctuations become more pronounced as the critical region is approached.



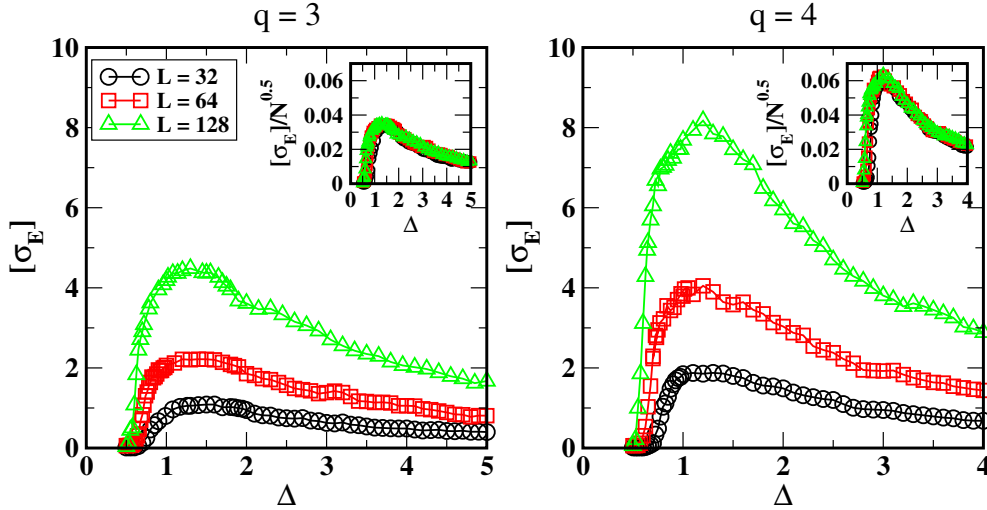


Figure 4.5: Disorder averaged standard deviation of energies denoted as  $[\sigma_E]$  for the  $q = 3$  (left) and  $q = 4$  (right) RFPM. For a fixed  $\{\epsilon_i^\alpha\}$ ,  $\sigma_E = \sqrt{(E - \langle E \rangle)^2}$  is calculated for a 1000 different initial  $\{s_i\}$  and then averaged over 100 disorder samples. It clearly shows that the energy spread  $[\sigma_E]$  grows with lattice size,  $L$ , and also with number of labels  $q$ . The inset shows the scaling of energy spread  $\sigma_E$ . The data collapse shows that  $\sigma_E \sim \sqrt{N}$ .

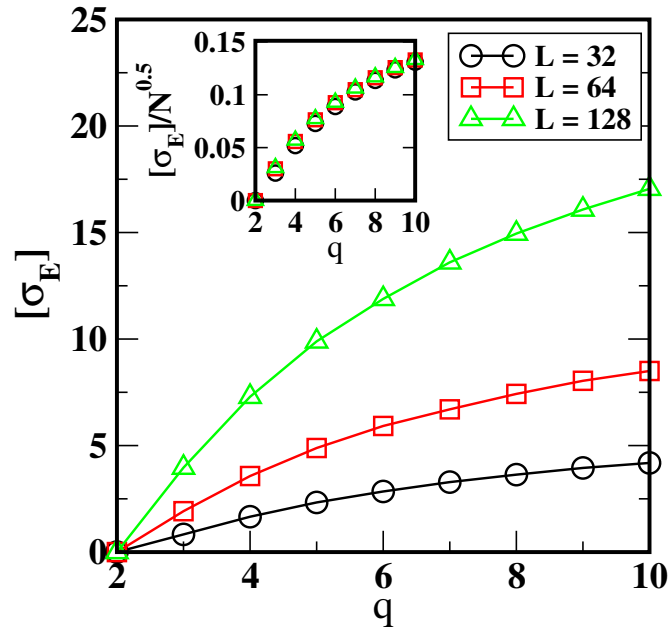


Figure 4.6:  $\sigma_E$  for fix  $\Delta = 1.0$  and varying  $q$ . This plot shows that the spread in metastable energy states increase with  $q$ . Again, the inset shows  $\sigma_E \sim \sqrt{N}$ .

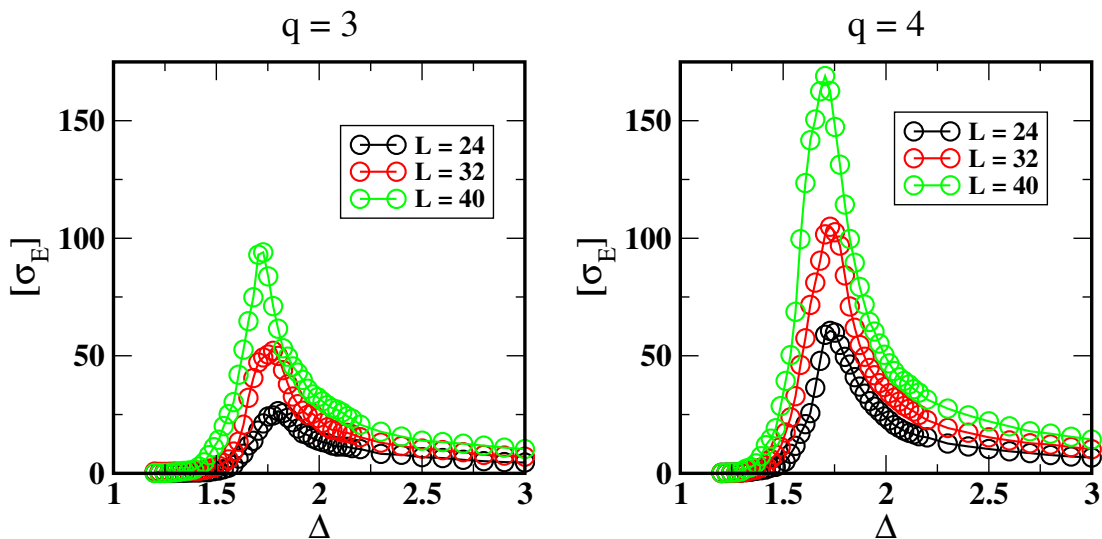


Figure 4.7:  $[\sigma_E]$  as a function of disorder strength  $\Delta$  for  $q = 3$  (left) and  $q = 4$  (right) RFPM in  $d = 3$ . For a fix  $\{\epsilon_i^\alpha\}$ ,  $\sigma_E = \sqrt{(E - \langle E \rangle)^2}$  is calculated for a 100 different initial  $\{s_i\}$  and then averaged over 100 disorder samples.

### 4.3.2 Comparisons with the PT Method

Now, intuitively, one can ask how reliable are the ground states from the GC method and how far are these from the exact ground states? In order to benchmark this, we compare the ground states from the GC method to the exact ground states from the PT method for small system sizes. The system sizes we choose are the square lattices of size  $L = 8, 16, 24, 32, 48$ . We study for  $q = 2, 3, 4, 5, 6, 7, 8, 9, 10$  RFPM. For each of these system sizes and  $q$ -values, the ground states are determined from the PT for 1500 disorder realizations. For the same sets of disorder realizations, the lowest energy states are determined from a single run (one initial condition) of GC.

We define a parameter  $\varepsilon$  which quantifies how far a minimum energy state of GC from its exact ground state is, i.e.,

$$\varepsilon = \frac{E_0 - E_{\min}}{E_0}. \quad (4.9)$$

Here,  $E_{\min}$  is the energy of the lowest state from GC. In the best possible situation when a minimum energy state is the actual GS,  $\varepsilon = 0$ . Fig. 4.8 shows a plot of

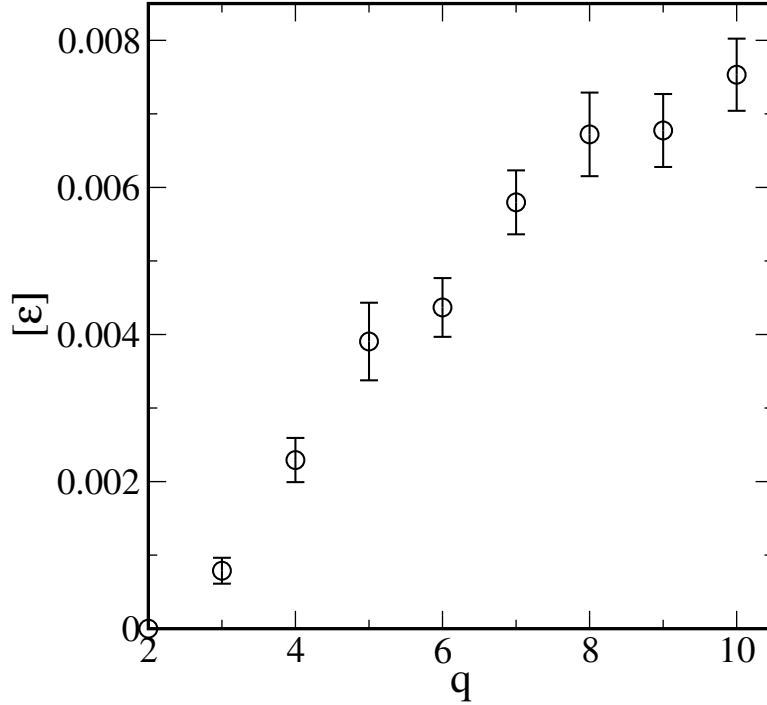


Figure 4.8: Plot of  $\varepsilon$  defined from Eq. (4.9) against the number of labels  $q$  for fixed  $L = 24$  and is averaged over 1500 disorder realizations.

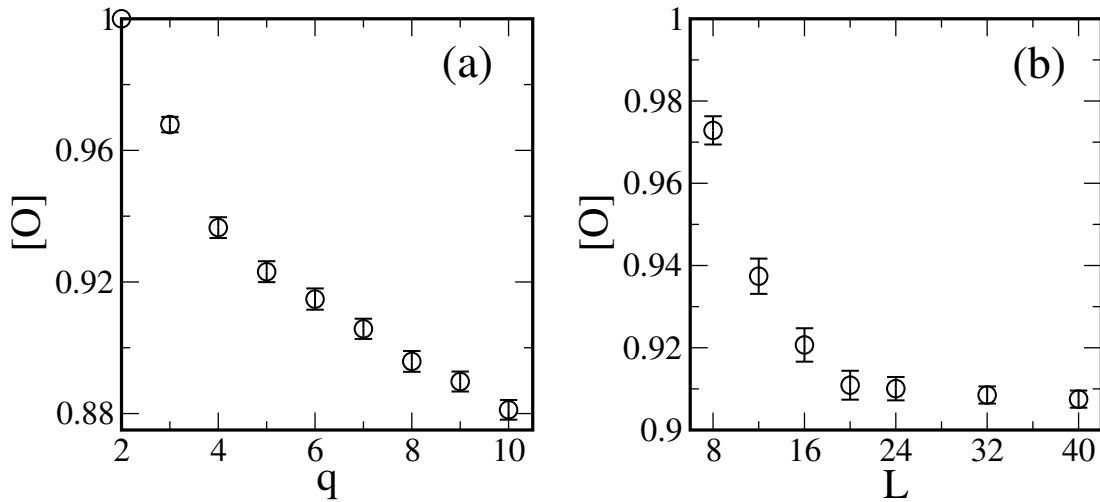


Figure 4.9: Plot of overlap  $[O]$  defined from Eq. (4.10) against (a) the number of labels  $q$  for fixed  $L = 24$  (b) the lattice size  $L$  for fixed  $q = 3$ . The quantity is averaged over 1500 disorder realizations.

$\varepsilon$  vs. the total number of spin states  $q$ . For  $q = 2$ , clearly,  $\varepsilon = 0$  as the method produces the exact ground states. With increasing  $q$ ,  $\varepsilon$  increases, meaning that the deviation from the exact ground states increases. Now, to check the reliability of the ground states, we define an overlap parameter:

$$O = \frac{1}{N} \sum_i \delta_{s_i, s_i^{GS}}. \quad (4.10)$$

Here,  $\{s_i^{GS}\}$  is the exact GS configuration from the PT and  $\{s_i\}$  is the lowest energy-state configuration from the GC.

Fig. 4.9 shows the plots of overlap  $O$  vs the total number of spin states  $q$  and lattice size  $L$ . Figure (a) shows that the overlap between the minimum energy states and the exact ground states decreases with  $q$  while from (b), one can notice that the overlap decreases and then saturates after  $L \geq 24$ . This states that with increase in  $L$ , the GC method is reliable for smaller  $q$  values.

#### 4.3.3 Performance and Efficiency of the GC Method

Let us now discuss the performance and the efficiency of the GC method in finding the minimum energy states of RFPM. We measure the CPU time  $r$  (in sec.) that the  $\alpha$ -expansion GC takes to find a minimum energy state. The simulations are performed for  $\Delta = 1.0$  and is averaged over 1000 disorder samples.

Fig. 4.10 is the plot of run-times  $r$  for  $q$ -state RFPM in  $d = 2$ . In Fig. 4.10(a), we plot  $r$  as a function of system size  $N$  for  $q = 10, 50, 100$ . The solid lines are the power-law fits with the exponents are specified in the figure, and a dashed line denotes a linear behavior of  $r$  against  $N$ . Clearly, the plot shows that the runtime is about linear in  $N$  and is independent of  $q$ . This shows the performance of GC method that the  $r \sim O(N)$ . Further, the runtime is of the order of few seconds which shows the efficiency of the GC. Fig. 4.10(b) is the run-time plot of varying the number of labels  $q$  and fixing  $N$ . In this plot, with increasing the system size, the runtime  $r$  grows faster in  $q$  and typically approaches the linear behavior.

We perform a similar analysis in  $d = 3$ . In this case also, approximately a linear behavior of run-time  $r$  is observed with the system size  $N$ . However,  $r$

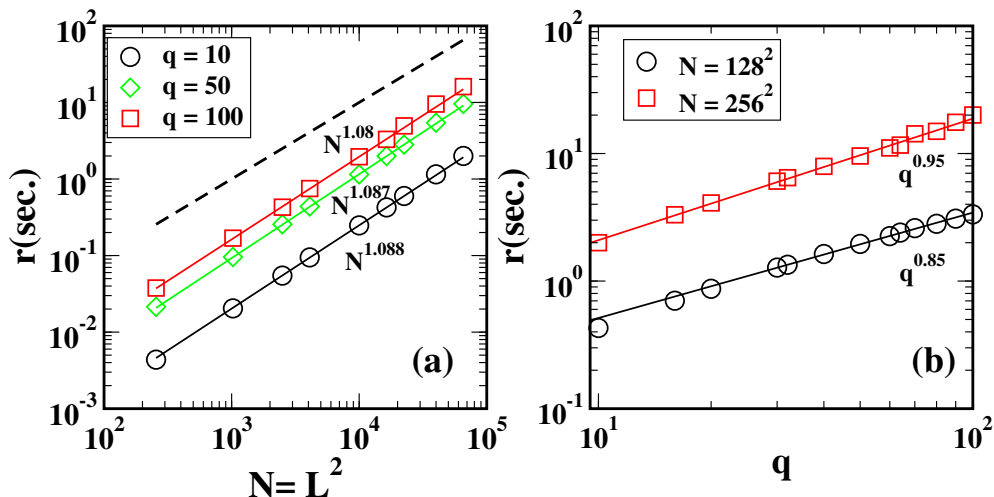


Figure 4.10: Running time  $r$  (in sec.) of  $\alpha$ -expansion GC in finding the lowest energy state in  $d = 2$  RFP. It is the CPU time that the GC takes to find a minimum energy state and averaged over 1000 disorder realizations. The left plot (a) shows the running time for different  $q = 10, 50, 100$  with varying the lattice size  $N$  and right plot (b) shows the runtime with varying  $q$  for fixed lattices  $N = 128^2$  and  $256^2$ . The solid lines are the power-law fits with the specified values of exponents and a dashed line is drawn as a reference for linear behavior of  $r \sim N$ . This plot clearly shows that the runtime is about linear in  $N$  and also, approximately linear in  $q$ .

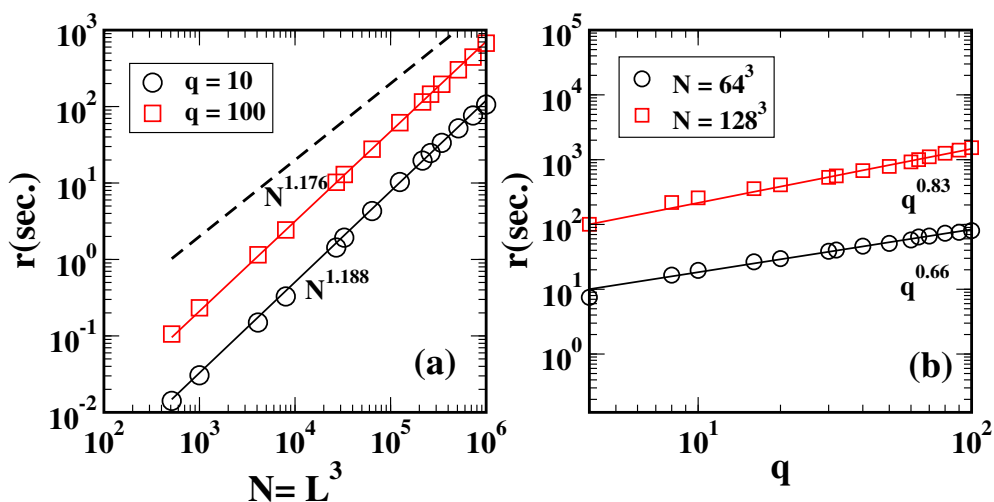


Figure 4.11: Analogous to Fig. 4.10 but for  $d = 3$  RFP. (a) Plot of  $r$  as a function of  $N$  for  $q = 10, 100$ . (b) Plot of  $r$  with varying  $q$  and keeping  $N$  fixed.

---

#### 4.4. Critical Behavior in the $q = 3$ RFPM

is slight faster in  $N$  as compared to  $d = 2$  (see Fig. 4.11). This confirms the  $O(N)$  polynomial complexity of the GC which makes it more suitable to study the disordered systems.

It is now clear that the GC is much efficient, but regarding the quality of approximate ground states, the method works very well for typically very small  $q$ . Considering the  $q = 3$  case of the RFPM, next we use the GC method to study the critical behavior.

## 4.4 Critical Behavior in the $q = 3$ RFPM

In this section, we study the critical behavior of the  $q = 3$  RFPM in  $d = 3$ . The simulations are performed on a  $128^3$  lattices. We determine the physical quantities such as Binder cumulant, magnetization and specific heat. We obtain the error bars in each quantity from the standard deviation of data for different disorder samples. These quantities predict the critical behavior of the system near the transition. Using finite-size scaling techniques, we obtain the critical exponents. The finite-size scaling is performed using a python program, namely, *autoscale.py* developed by O. Melchert [35]. This program uses the minimization procedure to optimize the scaling parameters via a downhill simplex algorithm [36].

We also determine the goodness-of-fit parameter  $Q$  which quantify the quality of fit. This is defined as the incomplete gamma function of *chi-square*  $\chi^2$  and the *degree of freedom*  $f$  [37]:

$$Q = \Gamma\left(\frac{\chi^2}{2}, \frac{f}{2}\right). \quad (4.11)$$

$Q$  determines the probability that the value of

$$\chi^2 = \sum_i^N \left(\frac{y_i - g(x_i)}{\sigma_i}\right)^2, \quad (4.12)$$

with  $N$  data points  $(x_i, y_i \pm \sigma_i)$  fitted to the function  $g$ , is worse than the current fit [37, 38]. If  $Q \gtrsim 0.1$ , then the goodness-of-fit is believable. If  $Q \gtrsim 0.001$ , then the fit may be acceptable if the errors are nonnormal or have been moderately underestimated. If  $Q < 0.001$ , then the fit is not acceptable (see, numerical

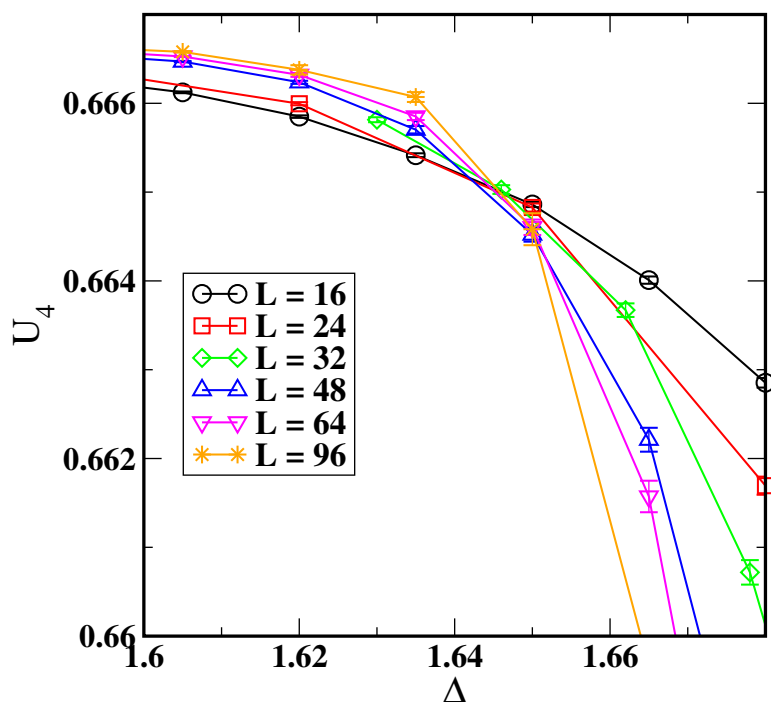


Figure 4.12: The Binder cumulant  $U_4$  vs.  $\Delta$  for square lattices of size  $L = 16, 24, 32, 48, 64, 96$ . The appropriate error bars are shown. The maximum intersection of these curves predict  $\Delta_c \simeq 1.64$ .

recipes in  $C$ , Ref. [37]).

#### 4.4.1 Binder Cumulant

To get a nature and location of transition point, a very first quantity to be determined is the Binder cumulant  $U_4(\Delta, L)$ , defined in Eq. (2.4). Here, the magnetization parameter is the order parameter  $\psi$  defined as [39, 40]

$$\psi = \frac{q\rho - 1}{q - 1}, \quad (4.13)$$

where

$$\rho = \frac{1}{N} \left( \sum_{\alpha} \delta_{s_i, \alpha} \right)_{\max_{\alpha}}. \quad (4.14)$$

In Fig 4.12, we plot Binder cumulant  $U_4(\Delta, L)$  against the disorder strength

---

#### 4.4. Critical Behavior in the $q = 3$ RFPM

$\Delta$ . The data has been averaged over many disorder realizations; typically  $10^5, 5 \times 10^4, 4 \times 10^4, 3 \times 10^4, 2 \times 10^4, 10^4$ , for  $L = 16, 24, 32, 48, 64$ , respectively. The error bars are shown which are quite small as the data has been averaged over large disorder samples. The maximum intersection of the Binder-cumulant curves occurs around 1.64, which predicts  $\Delta_c$ . Here, we stress that we do not obtain the exact GS with the GC method and near the critical region, there will be large fluctuations in approximate ground states as seen earlier from Fig. 4.7. This is also evident from the fact that the Binder-cumulant curves do not have a unique intersection. The Binder-cumulant plot helps us to get a rough estimate of  $\Delta_c \simeq 1.64$ . A more accurate value along with error bars is determined from a non-linear fit of pseudo-critical point  $\Delta^*(L)$  which we will see later.

#### 4.4.2 Specific Heat

Next we determine a specific-heat like quantity  $C(\Delta)$  at  $T = 0$ . At  $T = 0$ , the free energy and energy  $\mathcal{H}$  are identical. The bond energy per spin  $e_J$  plays a role of entropy. Therefore, the specific-heat is defined as a numerical derivative of the bond energy per spin (see Ref. [38] for details), i.e.,

$$C(\Delta) = \frac{\partial[e_J(\Delta)]}{\partial\Delta}, \quad (4.15)$$

where  $[\dots]$  denotes the average over disorder realizations and  $e_J(\Delta)$  is the bond energy per spin given by

$$e_J(\Delta) = -\frac{1}{N} \sum_{\langle ij \rangle} \delta_{s_i, s_j}. \quad (4.16)$$

Numerically, the derivative of  $e_J(\Delta)$  is determined using first-order finite difference in which the derivative is taken at the midpoint of the interval instead of either end points. With this approach, if  $\Delta_1$  and  $\Delta_2$  are the two nearby values of  $\Delta$ , then the specific-heat  $C(\Delta)$  is

$$C\left(\frac{\Delta_1 + \Delta_2}{2}\right) = \frac{[e_J(\Delta_2)] - [e_J(\Delta_1)]}{\Delta_2 - \Delta_1}. \quad (4.17)$$



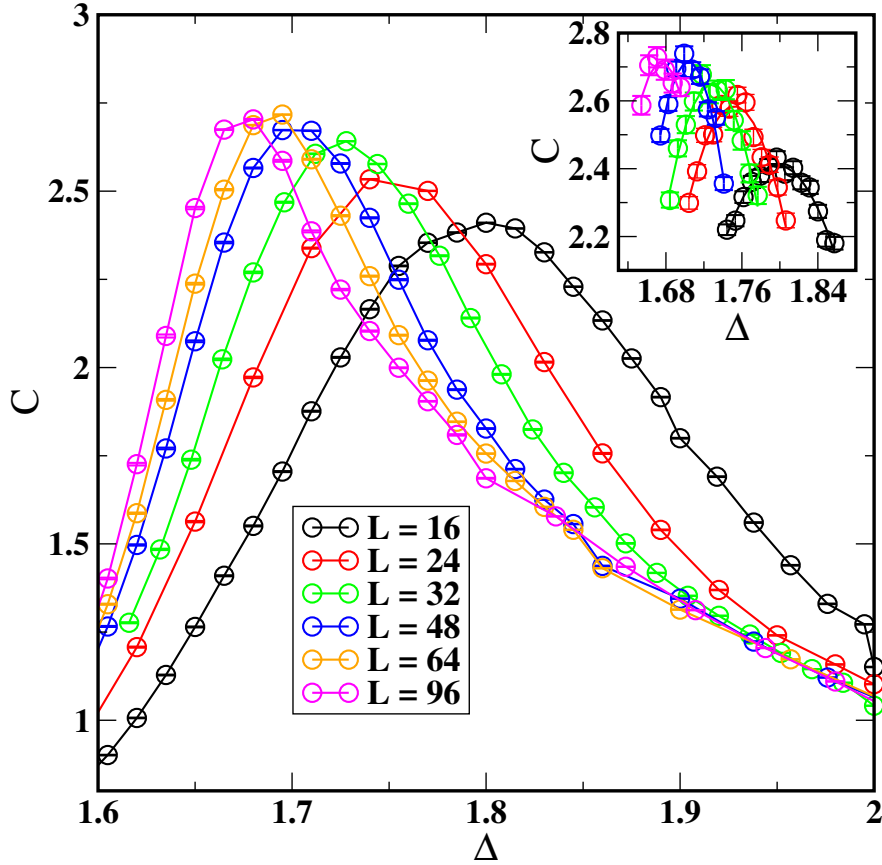


Figure 4.13: Specific-heat  $C(\Delta, L)$ , calculated from Eq. 4.17, as a function of disorder strength  $\Delta$  for different system sizes  $L = 16, 24, 32, 48, 64, 96$ . The inset is an enlargement of the peak region. The solid lines in the inset are the parabolic fits.

In Fig. 4.13, we plot  $C(\Delta)$  as a function of  $\Delta$ . One can see a clear peak in the specific heat, which moves towards lower  $\Delta$  with increasing system size and the height of the peak grows until it saturates. The error bars are shown which are much smaller than the symbol sizes. Near the peak, we perform simulations for more  $\Delta$ 's values, and the data has been averaged over more disorder realizations since the sample to sample fluctuations are large in this region. This is shown in the inset of Fig. 4.13. To get the locations of the peaks, the data for each  $L$  has been fitted to a parabola ( $y = a + bx + cx^2$ ). The solid lines in the inset are the parabolic fits. From these parabolic fits, one can obtain the height of the peaks  $C^{\max}(L)$  and the positions of the maxima  $\Delta^*(L)$ , which are the pseudo-critical

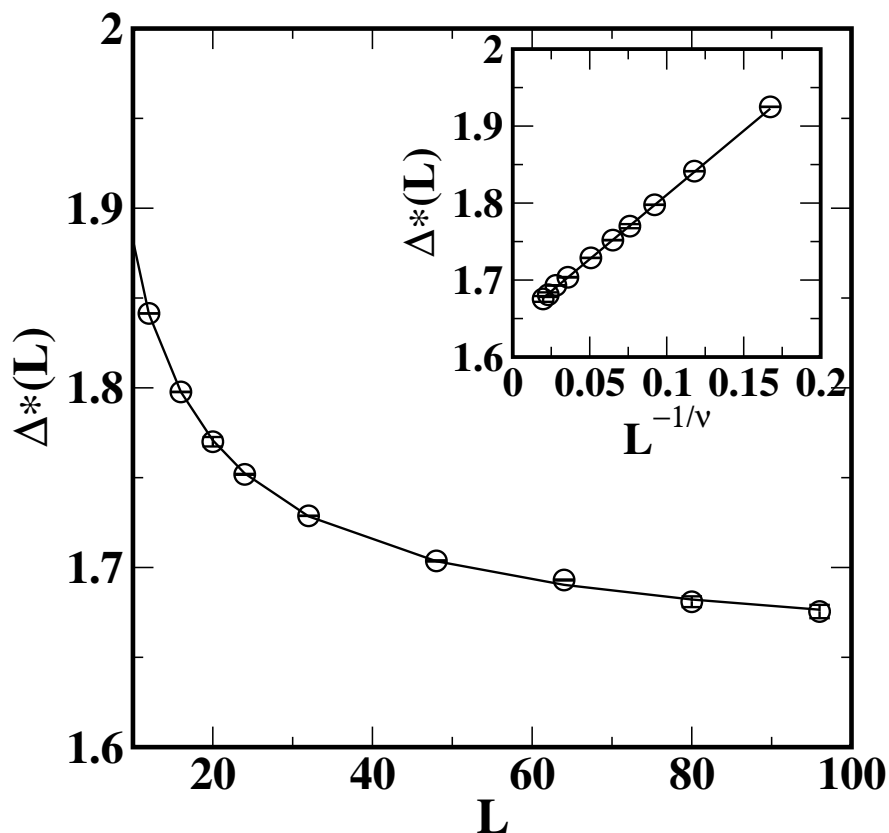


Figure 4.14: A plot of  $\Delta^*(L)$ , where the specific-heat attains its maximum, as a function of system size  $L$ . The solid line shows the best fit to the function  $\Delta^*(L) \approx \Delta_c + a_1 L^{-1/\nu}$  with  $\Delta_c = 1.688$ ,  $1/\nu = 0.862$ , and  $a_1 = 1.78$ . The inset shows the data as a function of  $L^{-1/\nu}$  and a solid line is the best-fitted straight line.

points.

In a finite-size system, the finite-size scaling of the *singular* part of the specific-heat predicts that

$$C_s \sim L^{\alpha/\nu} \tilde{C} [(\Delta - \Delta_c) L^{1/\nu}], \quad (4.18)$$

where  $\nu$  is the correlation-length exponent and  $\alpha$  is the specific-heat exponent. Now, at the peak, if the argument of the scaling function  $\tilde{C}$  takes some value, say  $b$ , then the peak position  $\Delta^*(L)$  varies as (see Ref. [38])

$$\Delta^*(L) \approx \Delta_c + a_1 L^{-1/\nu}, \quad (4.19)$$

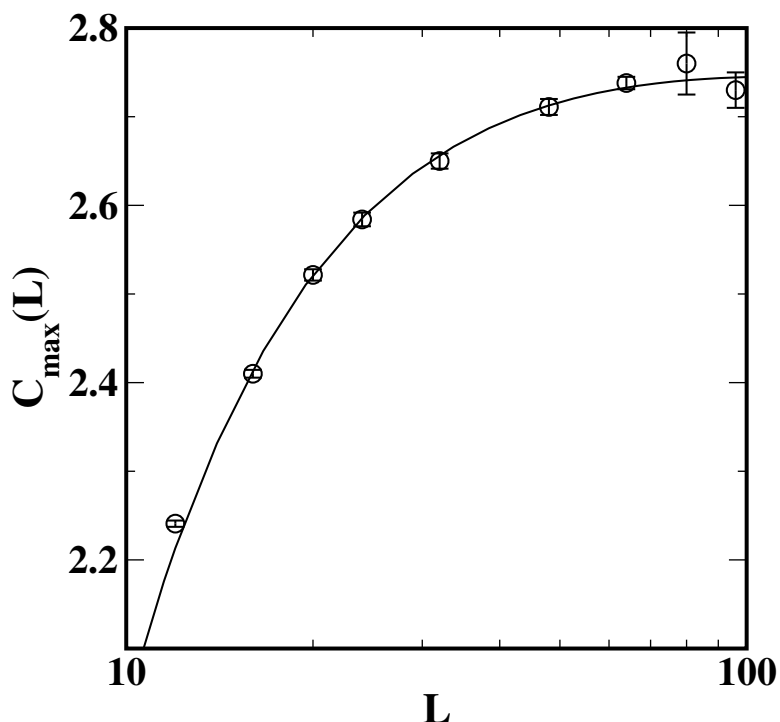


Figure 4.15: Plot of the maximum of the specific heat  $C^{\max}(L)$  as a function of system size  $L$ . The solid line is the fitting function of the form of Eq. (4.22) with  $C_0 = 2.975$ ,  $\alpha/\nu = -0.015$ ,  $b = -6.58$ , and  $\omega = -1.35$ .

and the maximum value of the singular part of the specific heat varies as

$$C_s^{\max}(L) \sim L^{\alpha/\nu}. \quad (4.20)$$

According to Eq. (4.19), the pseudo-critical points  $\Delta^*(L)$ , determined in Fig. 4.13, can be used to estimate the infinite-size critical disorder  $\Delta_c$  (see Fig. 4.14). In the main frame of Fig. 4.14, we show  $\Delta^*(L)$  as a function of  $L$ . The solid line denotes the power-law fit of the form of Eq. (4.19). The best fit gives

$$\Delta_c = 1.648 \pm 0.003 \quad \text{and} \quad 1/\nu = 0.862 \pm 0.001, \quad (4.21)$$

with the quality of fit  $Q = 0.2$ , which is fair. In the inset of Fig. 4.14, we plot  $\Delta^*(L)$  vs  $L^{-1/\nu}$ , using the value of  $\nu$  in Eq. (4.21). The solid line is the best linear fit.

---

#### 4.4. Critical Behavior in the $q = 3$ RFPM

We now turn to determine the specific-heat exponent  $\alpha$ . Fig. 4.15 shows the plot of the peak heights of the specific heat  $C^{\max}(L)$  as a function of  $L$ . Notice that the  $L$ -axis is plotted on a log scale. This plot clearly shows a curvature, suggesting that the specific heat converge to a finite value as  $L$  increase. When we try fitting this data to the form  $C_s^{\max}(L) = C_0 L^{\alpha/\nu}$ , it yields a strong negative value of  $\alpha$ , which seems unphysical. Further, the quality of the fit is bad. Then, we try a fit including the scaling corrections of the form

$$C^{\max}(L) = C_0 L^{\alpha/\nu} (1 + bL^{-\omega}), \quad (4.22)$$

where  $\omega$  is the leading correction to the scaling exponent and  $b$  is some constant. This fit yields

$$c_0 = 2.975 \pm 0.357, \quad \alpha/\nu = -0.015 \pm 0.024, \quad (4.23)$$

and  $\omega = -1.35 \pm 0.39$  with the quality of fit  $Q = 0.77$ , which is very good.

#### 4.4.3 Magnetization or the Order Parameter

Next, we focus on the critical behavior of the order-parameter  $\psi$ , which is defined in Eq. (4.13). Fig. 4.16 shows the plot of  $\psi$  as a function of disorder  $\Delta$  for various lattice sizes  $L = 16, 24, 32, 48, 64, 96$ . The error bars are extremely small ( $\sim O(10^{-5})$ ) as the data has been averaged over a large number of disorder realizations.

The finite-size scaling of order parameter predicts

$$\psi(\Delta, L) = L^{-\beta/\nu} \tilde{\mathcal{M}} [(\Delta - \Delta_c) L^{1/\nu}], \quad (4.24)$$

which means that if we plot  $\psi L^{\beta/\nu}$  against  $(\Delta - \Delta_c) L^{1/\nu}$  with the correct values of parameters  $\Delta_c$ ,  $\nu$  and  $\beta/\nu$ , then the data for different system sizes should collapse onto a single master curve near the critical region  $\Delta \approx \Delta_c$ . This is shown in Fig. 4.17. The finite-size scaling is performed using the python program `autoscale.py` [35] with the initial choices of parameters  $\Delta_c = 0.64$ ,  $1/\nu = 0.85$ ,  $\beta/\nu = 0.1$ . The best scaling is obtained with the following values of scaling

#### 4.4. Critical Behavior in the $q = 3$ RFPM

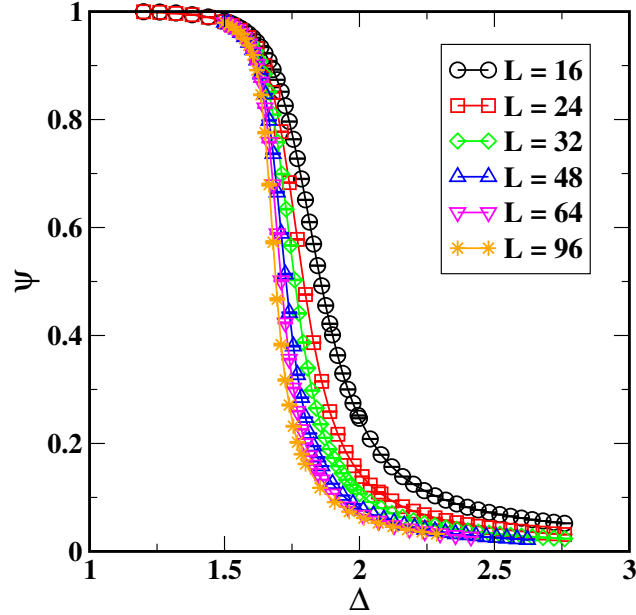


Figure 4.16: Plot of the order-parameter  $\psi$  as a function of  $\Delta$  for various system sizes  $L = 16, 24, 32, 48, 64, 96$ . Error bars are shown, which are much smaller than the symbol sizes.

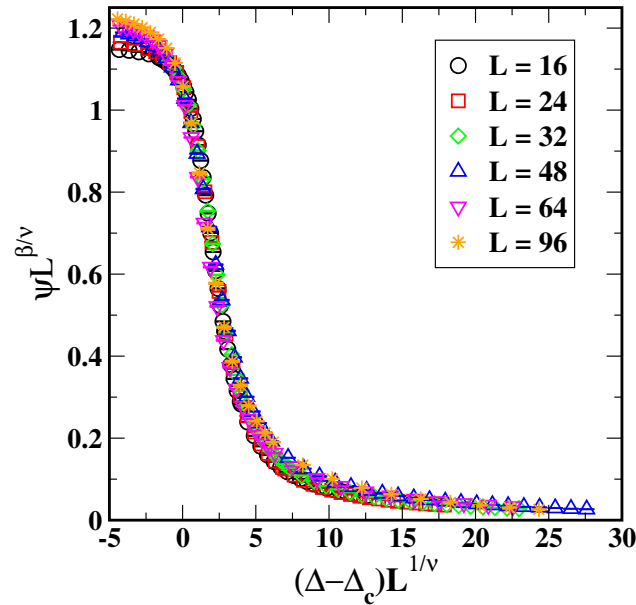


Figure 4.17: Scaling plot of  $\psi L^{\beta/\nu}$  as a function of  $(\Delta - \Delta_c)L^{1/\nu}$  with  $\Delta_c = 1.64532$ ,  $1/\nu = 0.87324$ ,  $\beta/\nu = 0.05036$  (see text).

## 4.5. Summary and Discussion

	References	$\nu$	$\alpha$	$\beta$
Previous studies for $d = 3$ RFIM at $T = 0$	Ref. [38]	$1.32 \pm 0.07$	$-0.63 \pm 0.07$	-
	Ref. [41]	$1.19 \pm 0.08$	-	$0.02 \pm 0.01$
	Ref. [42]	$1.37 \pm 0.09$	$-0.01 \pm 0.09$	$0.017 \pm 0.005$
	Ref. [43]	$1.25 \pm 0.02$	$-0.05 \pm 0.02$	-
	Ref. [44]	$1.1 \pm 0.1$	$0.1 \pm 0.1$	-
	Ref. [45]	$1.38 \pm 0.02$	$-0.09 \pm 0.05$	$0.018 \pm 0.002$
	Ref. [46]	$1.2 \pm 0.15$	-	$0.031 \pm 0.015$
$q = 3, d = 3$ RFPM at $T = 0$	This work	$1.145 \pm 0.001$	$-0.017 \pm 0.027$	$0.0577 \pm 0.0002$

Table 4.2: A summary of critical exponents of this study for  $q = 3, d = 3$  RFPM and previous studies for  $d = 3$  RFIM.

parameters.

$$\Delta_c = 1.64532 \pm 0.00002, \quad 1/\nu = 0.87324 \pm 0.00001, \quad \beta/\nu = 0.05036 \pm 0.00007. \quad (4.25)$$

The resulting plot for the best data collapse is shown in Fig. 4.17. In Table 4.2, we compare these determined exponents to the corresponding exponents of  $d = 3$  RFIM, obtained in the previous studies for zero-temperature ground states.

## 4.5 Summary and Discussion

We have undertaken a comprehensive numerical study of the  $q$ -state RFPM using the  $\alpha$ -expansion GC method and the PT method. Using GC method, we obtain approximate ground states. While the PT is asymptotically exact, the required run time increases exponentially with the system size. Therefore, using PT method, we obtained exact ground states for small system sizes and compared them to the corresponding lowest energy states from the GC method. We found that the GC method produces reliable ground states for typically small  $q$ . With increase in  $q$ , the quality of the ground states decreases. Then, we have confirmed a polynomial complexity of  $O(N)$  of the GC method in the both,  $d = 2$  and  $d = 3$ , that is, the run time is linear in the system size  $N$ .

Next, with the advantage of GC method for typically small  $q$ , we have studied

## 4.5. Summary and Discussion

---

the critical behavior in  $q = 3$  and  $d = 3$  RFPM. We have determined the physical quantities such as magnetization, Binder-cumulant, bond-energy, specific-heat. Using the finite-size scaling ansatz, we have obtained the critical exponents. The scaling has been performed using the python program, “autoscale.py”. Finally, we have summarize these exponents in the Table 4.2 and also provide the corresponding exponents for the  $d = 3$  RFIM, determined in the previous studies.

# References

- [1] F. Y. Wu, Rev. Mod. Phys. **54**, 235 (1982).
- [2] R. B. Potts, Proc. Camb. Phil Soc. **48**, 106 (1952).
- [3] K. Binder and J. D. Reeger, Adv. Phys. **42**, 547 (1992).
- [4] K. H. Michel, Phys. Rev. Lett. **57**, 2188 (1986); Phys. Rev. B **35**, 1414 (1987).
- [5] Amnon Aharony, K. A. Mller, and W. Berlinger, Phys. Rev. Lett. **38**, 33 (1977).
- [6] E Domany, Y Shnidman and D Mukamel, J. Phys. C: Solid State Phys. **15**, L495 (1982).
- [7] D. Blankschtein, Y. Shapir and A. Aharony, Phys. Rev. B **29**, 1263 (1984).
- [8] H. Nishimori, Phys. Rev. B **28**, 4011 (1983).
- [9] K. Eichhorn and K. Binder, J. Phys.: Condens. Matter **8**, 5209 (1996); Europhys. Lett. **30**, 331 (1995).
- [10] K. Eichhorn and K. Binder, Z. Phys. B **99**, 413 (1996).
- [11] P Reed, J. Phys. C: Solid State Phys. **18**, L615 (1985).
- [12] R. Baxter, J. Phys. C **6**, L445 (1973).
- [13] Y. Y. Goldschmidt and G. Xu, Phys. Rev. B **32** 1876 (1985); Nucl. Phys. B **265** 1 (1986).



- 
- [14] R. H. Swendsen and J. -S. Wang, Phys. Rev. Lett. **57**, 2607 (1986).
- [15] K. Hukushima and K. Nemoto, J. Phys. Soc. Jpn. **65**, 1604 (1996).
- [16] E. Marinari, G. Parisi, and J.J. Ruiz-Lorenzo, *in Spin Glasses and Random Fields, edited by A.P. Young* (World Scientific, Singapore,1998), p.59.
- [17] E. Marinari, arXiv: 9612010v1 (2008).
- [18] D. J. Earl and M. W. Deem, Phys. Chem. Chem. Phys., **7**, 3910 (2005).
- [19] H. G. Katzgraber, arXiv: 0905.1629v3 (2011).
- [20] M. Hasenbusch, A. Pelissetto, and E. Vicari, Phys. Rev. B **78**, 214205 (2008).
- [21] G. Ceccarelli, A. Pelissetto, and E. Vicari, Phys. Rev. B **84**, 134202 (2011).
- [22] A. Billoire, L.A. Fernandez, A. Maiorano, E. Marinari, V. Martín-Mayor and D. Yllanes, J. Stat. Mech. (2011) P10019.
- [23] K. Hukushima, H. Takayama, and H. Yoshiro, J. Phys. Soc. Jpn. **67**, 12 (1998).
- [24] H. G. Ballesteros, A. Cruz, L. A. Fernandez, V. Martin-Mayor, J. Pech, J.J. Ruiz-Lorenzo, A. Tarancon, P. Tellez, C . L. Ullod, and C. Ungil, Phys. Rev. B **62**, 14237 (2000).
- [25] H.G. Katzgraber, M. Palassini, and A. P. Young, Phys. Rev. B **63**, 184422 (2001); H.G. Katzgraber, M. Körner, and A.P. Young, Phys. Rev. B **73**, 224432 (2006).
- [26] H.G. Katzgraber, S. Trebst, D. A. Huse, and M. Troyer, J. Stat. Mech.: Theory Exp. P03018 (2006).
- [27] E. Bittner, Andreas Nußbaumer, and W. Janke, Phys. Rev. Lett. **101**, 130603 (2008).
- [28] D. A. Kofke, J. Chem. Phys. **117**, 6911 (2002); **120**, 10852 (2004).
- [29] A. Kone and D. A. Kofke, J. Chem. Phys. **122**, 206101 (2005).

- 
- [30] C. Predescu, M. Predescu, and C. V. Ciobanu, *J. Chem. Phys.* **120**, 4119 (2004).
- [31] D. Sabo, M. Meuwly, D. L. Freeman, and J. D. Doll, *J. Chem. Phys.* **128**, 174109 (2008).
- [32] J. P. Neirotti, F. Calvo, D. L. Freeman, and J. D. Doll, *J. Chem. Phys.* **112**, 10340 (2000).
- [33] F. Calvo, *J. Chem. Phys.* **123**, 124106 (2005).
- [34] P. Brenner, C. R. Sweet, D. VonHandorf, and J. A. Izaguirre, *J. Chem. Phys.* **126**, 074103 (2007).
- [35] O. Melchert, arXiv:0910.5403.
- [36] J. A. Nelder and R. Mead, *Computer J.* **7**, 308 (1965).
- [37] W. H. Press, S. A. Teukolsky, W. T. Vetterling, and B. P. Flannery, *Numerical Recipes in C*, 2nd ed. (Cambridge University Press, Cambridge, 1992).
- [38] A. K. Hartmann and A. P. Young, *Phys. Rev. B* **64**, 214419 (2001).
- [39] C. Chen, A. M. Ferrenberg, D. P. Landau, *Phys. rev. E* **52**, 1377 (1995).
- [40] W. Xiong and C. Xu, *Z. Guo*, *Phase Transitions* **87**, 193 (2014).
- [41] A.K. Hartmann and U. Nowak, *Eur. Phys. J. B* **7**, 105 (1999).
- [42] A. A. Middleton and D. S. Fisher, *Phys. Rev. B* **65**, 134411 (2002).
- [43] Y. Wu and J. Machta, *Phys. Rev. B* **74**, 064418 (2006).
- [44] I. Dukovski and J. Machta, *Phys. Rev. B* **67**, 014413 (2003).
- [45] N. G. Fytas and V. Martín-Mayor, *Phys. Rev. E* **93**, 063308 (2016); N. G. Fytas, P. E. Theodorakis, I. Georgiou, and I. Lelidis, *Eur. Phys. J. B* **86**, 268 (2013).
- [46] M. R. Swift, A. J. Bray, A. Maritan, M. Cieplak, and J. R. Banavar, *Europhys. Lett.* **38**, 273 (1997).

## Part II

# Ordering Kinetics in Disordered Spin Systems

# Chapter 5

## Domain Growth in Random Field Ising Model with Conserved Kinetics

### 5.1 Introduction

As we know, the RFIM is the simplest and most investigated system to study the effects of disorder and complexity. Quenched disorder is inherent in materials in the form of defects, impurities, and structural imperfections. The RFIM has provided a framework for understanding the properties of many such systems. Some prototypical examples are dilute anti-ferromagnets (DAFs) in a uniform field [1, 2]; insulating dipolar magnets  $\text{LiHo}_x\text{Y}_{1-x}\text{F}_4$  in a transverse field; colossal magnetoresistance oxides [3]; binary mixtures (AB) in a porous medium where A and B could be oil and water, colloids and polymers [4–6], random binary alloys [7], Immiscible fluids flowing through porous media [8, 9], etc.

As the Ising variables  $s_i$  in the RFIM do not have an intrinsic dynamics, they are placed in contact with a heat bath which generates stochastic spin-flips [10]. The resultant kinetic Ising model is the spin-flip or the Glauber model that describes non-conserved kinetics. The Glauber kinetics is appropriate for describing the dynamical properties of DAFs or  $\text{LiHo}_x\text{Y}_{1-x}\text{F}_4$ , for instance. On the other hand, the microscopic kinetics for a binary mixture involves  $A \leftrightarrow B$

interchanges, and the resultant model is the spin-exchange or the Kawasaki model with conserved kinetics. The conserved kinetics of Kawasaki spin-exchange is appropriate for describing, e.g., binary mixtures, binary alloys, Immiscible fluids, etc. With this kinetics, the composition of each species or component of a system remains preserved. It should be emphasized that the transition probabilities in both Glauber and Kawasaki models satisfy the detailed balance condition (Eq. (1.15)). Consequently, although the two models describe different time-dependent behavior, the equilibrium state is unique.

The problem of domain growth or phase ordering in the RFIM after a deep quench is a problem of long-standing interest for theorists, experimentalists and technologists [11–18]. More generally, the subject of domain growth in disordered systems has attracted much attention [11]. For studies on the random-bond Ising model (RBIM), see Puri et al. [19], Paul et al. [20, 21], Lippiello et al. [22, 23], Henkel and Pleimling [24, 25], Park and Pleimling [26]. For studies on the random-site or site diluted Ising model (DIM), see, for example, Corberi et al. [27], Park and Pleimling et al. [28], Paul et al. [29].

The quenched randomness causes pinning and roughening of interfaces, which are characterized by a fractal dimension. This pinning has deep implications for the ordering process due to the presence of a multitude of length scales, energy barriers and relaxation times [30]. The presence of energy barriers leads to the anomalous relaxation in these systems [31, 32]. Therefore, domain growth with disorder is complicated and not completely understood. Some questions of interest in this area are:

- (i) What is the growth law obeyed by the correlated regions or domains as they grow in size? Are there crossovers in the growth law with time?
- (ii) Do the correlation and response functions exhibit super-universality (SU), i.e., are the corresponding scaling functions independent of disorder?
- (iii) How do interfacial characteristics affect the evolution after a quench?

For the RFIM with non-conserved kinetics (NC-RFIM), some of these questions have satisfactory answers. Domain growth in the pure system ( $\Delta = 0$ ) obeys the well-known Lifshitz-Allen-Cahn (LAC) growth law,  $L(t) \sim t^{1/2}$  [10]. Early

studies by Oguz et al. [13] considered a continuum version of the  $d = 2$  RFIM with Langevin dynamics, i.e., the time-dependent Ginzburg-Landau (TDGL) equation. They predicted logarithmic growth at large times and a breakdown of SU. Puri-Parekh [33] and Rao-Chakrabarti [34] also had similar observations for the TDGL model in  $d = 2, 3$ . They reported an algebraic domain growth law  $L(t) \sim (\ln t)^{1/\varphi}$  with a disorder-dependent exponent  $\varphi$ . Recently, Corberi et al. [35] performed comprehensive MC simulations for the Glauber-RFIM in  $d = 2, 3$ . They demonstrated that there is a cross-over from a pre-asymptotic power law growth with a disorder-dependent exponent [ $L(t) \sim t^{1/z(\Delta)}$ ] to an asymptotic regime with logarithmic growth [ $L(t) \sim (\ln t)^{1/\varphi}$  with  $\varphi \simeq 1.5$ ]. Further, Corberi et al. also showed that the two-time autocorrelation function does not exhibit SU.

Let us next consider the conserved RFIM (C-RFIM or Kawasaki-RFIM). There are very few studies of this problem. Domain growth in the pure system exhibits the Lifshitz-Slyozov (LS) law,  $L(t) \sim t^{1/3}$  [36, 37]. Puri and Parekh studied the coarse-grained equivalent (i.e., the Cahn-Hilliard or CH equation) of the C-RFIM in  $d = 2$  [33]. They demonstrated that the scaled structure factor (SF) does not exhibit SU, and the growth law shows an asymptotic logarithmic behavior. A similar study has been done by Rao and Chakrabarti [38]. Their observations were consistent with those of Puri and Parekh [33].

In this chapter, we present the first lattice-model study of the  $d = 2, 3$  RFIM with conserved kinetics. We perform comprehensive MC simulations of ordering kinetics in C-RFIM in  $d = 2, 3$ . As mentioned in chapter 2 (Sec. 2.1), there is a fundamental difference between the RFIM in  $d = 2$  and  $d = 3$ . For  $d = 2$ , the RFIM does not show long-range order (LRO) for any non-zero  $\Delta$ . Therefore, the ordering kinetics can only proceed up to the equilibrium correlation length  $\xi(\Delta) \rightarrow \infty$  as  $\Delta \rightarrow 0^+$ . On the other hand, for the  $d = 3$  RFIM, there is a FM phase and therefore, it is possible to study domain growth up to infinite length scales.

The major observations from our MC study are as follows:

- (a) The correlation function  $C(r, t; \Delta)$  and its Fourier transform, the structure factor  $S(k, t; \Delta)$ , exhibit dynamical scaling. The growth process is isotropic and characterized by a unique length scale  $L(t, \Delta)$ .

- (b) SU is violated by  $C(r, t; \Delta)$ . The disorder  $\Delta$  modifies the scaling function. Therefore, the scaling function is not robust with respect to disorder.
- (c) At early times, the domains follow algebraic growth  $L(t, \Delta) \sim t^{1/\bar{z}}$  with a disorder-dependent exponent  $\bar{z}(\Delta)$ . At late times, there is a cross-over to logarithmic domain growth  $L(t, \Delta) \sim (\ln t)^{1/\varphi}$ , where  $\varphi$  is a disorder-independent exponent. We find that  $\varphi \simeq 3.3$  for  $d = 2$ , and  $\varphi \simeq 5.6$  for  $d = 3$ .
- (d) The small- $r$  behavior of  $C(r, \Delta)$  exhibits a *cusp singularity*:  $1 - C(r) \sim r^{\zeta(\Delta)}$ , where the disorder-dependent *cusp exponent*  $\zeta(\Delta)$  signifies rough interfaces with a fractal dimension  $d_f = d - \zeta$ .
- (e) Consequently, the SF exhibits *non-Porod decay*  $S(k, t; \Delta) \sim k^{-(d+\zeta)}$ , and obeys a *generalized Tomita sum rule* [10]:

$$\int_0^\infty dp p^{1-\zeta} [p^{d+\zeta} f(p) - \mathcal{C}] = 0, \quad (5.1)$$

where  $f(p)$  is the scaling function, and  $\mathcal{C}$  is a constant.

This chapter is organized as follows. In Sec. 5.2, we discuss the details of our numerical simulations. In Sec. 5.3, we present the detailed numerical results in  $d = 2, 3$  C-RFIM. Finally, in Sec. 5.4, we conclude this chapter with a summary of our main results.

## 5.2 Simulation Details

The Hamiltonian of the model is described in Eq. 1.2. We choose the Gaussian distribution of RF (Eq. 1.3, where  $\Delta$  is the amount of disorder). In  $d = 2$ , the model does not show LRO for any non-zero value of  $\Delta$ , i.e.,  $\Delta_c = 0$ . In  $d = 3$ , there is a small region of  $(T, \Delta)$ -values where the equilibrium phase is ferromagnetic A phase boundary separates the ferro-phase from the para-phase (see Sec. 2.1). This boundary intersects the  $T$ -axis ( $\Delta = 0$ ) at  $T_c \simeq 4.51$  [39] and the  $\Delta$ -axis ( $T = 0$ ) at  $\Delta_c \simeq 2.28$  (Sec. 2.3.2).

## 5.2. Simulation Details

The details of our numerical simulations are as follows. To study phase ordering kinetics, we rapidly quench the system at time  $t = 0$  from high-temperature [ $T > T_c(\Delta)$ ] to a lower temperature [ $T < T_c(\Delta)$  in  $d = 3$ ]. The high-temperature state is mimicked by a random initial configuration  $\{s_i = \pm 1\}$ . The system is then let to evolve via MC procedure of Metropolis algorithm. The Kawasaki spin-exchange kinetics [10] proceeds as follows. A randomly selected spin  $s_i$  is exchanged with a randomly chosen neighbor  $s_j$ . The exchange is accepted with the Metropolis transition probability [Eq. (1.18)]

$$W = \min[1, \exp(-\beta\Delta\mathcal{H})], \quad (5.2)$$

where  $\beta = (k_B T)^{-1}$  and  $\Delta\mathcal{H}$  is the change in energy resulting from the spin exchange  $s_i \leftrightarrow s_j$ , which depends only on the energy contribution arising from spins  $s_i$  and  $s_j$ . Thus, the initial and final value—upon spin-exchange  $s_i \leftrightarrow s_j$ —of energy in term of contributions due to spins  $s_i$  and  $s_j$  are

$$\mathcal{H}_{\text{initial}} = -Js_i \sum_{N_i \neq j} s_{N_i} - Js_j \sum_{N_j \neq i} s_{N_j} - Js_i s_j - h_i s_i - h_j s_j + \text{contribution due to other terms}, \quad (5.3)$$

and

$$\mathcal{H}_{\text{final}} = -Js_j \sum_{N_i \neq j} s_{N_i} - Js_i \sum_{N_j \neq i} s_{N_j} - Js_j s_i - h_i s_j - h_j s_i + \text{contribution due to other terms}. \quad (5.4)$$

Here,  $N_i$  refers to the nearest-neighbors of the lattice site  $i$ . Therefore, the change in energy

$$\begin{aligned} \Delta\mathcal{H} &= \mathcal{H}_{\text{final}} - \mathcal{H}_{\text{initial}} \\ &= (s_i - s_j) \left( J \sum_{N_i \neq j} s_{N_i} - J \sum_{N_j \neq i} s_{N_j} + h_i - h_j \right). \end{aligned} \quad (5.5)$$

A single Monte Carlo step (MCS) corresponds to attempted updates of  $N$  spins.



Then evolution time  $t$  is measured in the unit of MCS. The Kawasaki spin-exchange kinetics preserve the overall magnetization of the RFIM during the evolution process.

The evolution morphology at time  $t$  is characterized by the CF of the spin configuration  $\{s_i\}$  averaged over several independent runs. As we know that if the ordering system is isotropic and characterized by a single length scale  $L(t)$ , then the CF has a dynamical scaling form:  $C(\mathbf{r}, t; \Delta) = g(r/L)$ , where  $g(x)$  is a scaling function [10], and the corresponding dynamical-scaling form for SF is  $S(\mathbf{k}, t; \Delta) = L^d f(kL)$ , where  $f(p)$  is the Fourier transform of  $g(x)$  [10].

## 5.3 Numerical Results

We now present our numerical results on ordering morphologies after a deep temperature quench. In  $d = 2$ , all simulations are done for square lattices of size  $N = 512^2$  with periodic boundary conditions. The system is quenched from a disordered phase to  $T = 1$  (in units of  $J$ ) and allowed to evolve up to  $10^8$  MCS. In  $d = 3$ , all simulations are done for cubic lattices of size  $N = 128^3$ . The system was cooled from the disordered phase to  $T = 2 < T_c(\Delta)$ , and evolved up to  $10^7$  MC time steps. All data ( $d = 2, 3$ ) have been averaged over at least 10 (sometimes more) independent runs with distinct field configurations  $\{h_i\}$  and initial spin configurations  $\{s_i(0)\}$ .

### 5.3.1 Domain Growth Morphologies

In Fig. 5.1, we show the typical morphologies of the C-RFIM in  $d = 3$  for (a)  $\Delta = 1.0$ ,  $t = 10^5$  MCS; (b)  $\Delta = 1.0$ ,  $t = 10^7$  MCS; and (c)  $\Delta = 2.0$ ,  $t = 10^7$  MCS. The snapshots (a) and (b) in Fig. 5.1 correspond to same disorder and different time, which shows that the domains of up and down spins grow in size as time evolves. The snapshots (b) and (c) in Fig. 5.1 correspond to same time and different disorder, which reveal that (i) the correlated regions are smaller for larger  $\Delta$ , and (ii) the interfaces become rougher with increasing disorder. The effect of disorder can be seen clearly in Fig. 5.2 for  $d = 2$  C-RFIM, which shows the pinning and roughening of the interfaces with increasing  $\Delta$ .

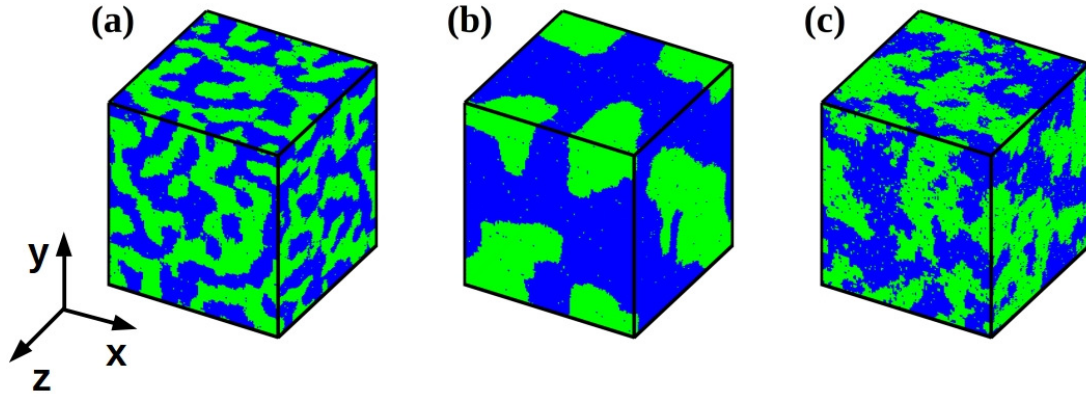


Figure 5.1: Domain growth in  $d = 3$  C-RFIM for (a)  $\Delta = 1.0$ ,  $t = 10^5$  MCS; (b)  $\Delta = 1.0$ ,  $t = 10^7$  MCS; and (c)  $\Delta = 2.0$ ,  $t = 10^7$  MCS. The lattice size is  $128^3$  and the temperature  $T = 2 < T_c(\Delta)$ . The green and blue regions correspond to  $s_i = 1$  and  $s_i = -1$ , respectively.

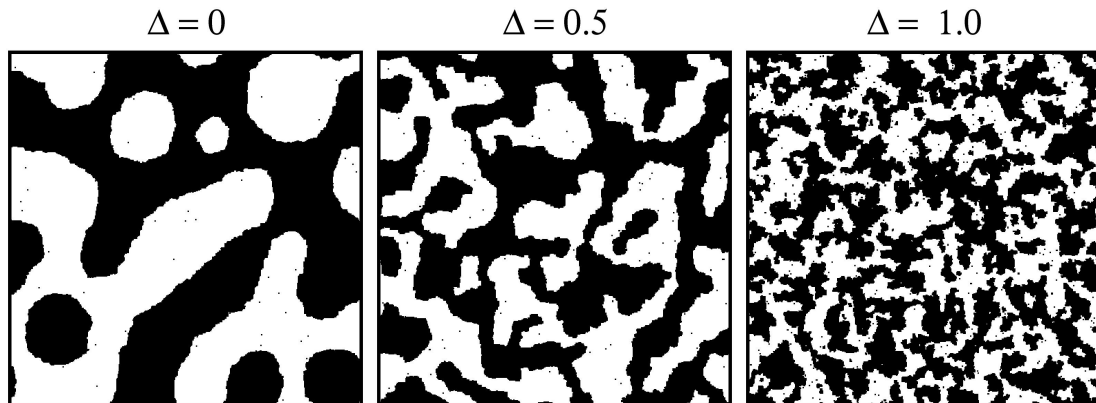


Figure 5.2: Typical morphologies in  $d = 2$  C-RFIM at  $t = 10^8$  MCS for  $\Delta = 0$ ,  $\Delta = 0.5$ , and  $\Delta = 1.0$ . The lattice size is  $512^2$  and the quench temperature is  $T = 1$ . The black and white regions correspond to  $s_i = 1$  and  $s_i = -1$ , respectively.

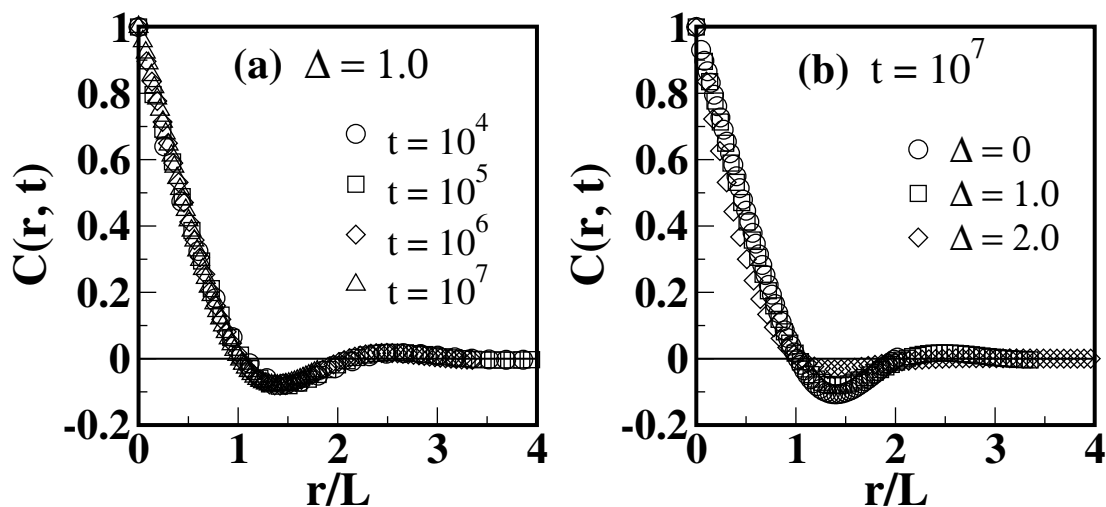


Figure 5.3: Scaled correlation functions,  $C(r, t)$  vs.  $r/L$ , for  $d = 3$  C-RFIM. The length scale  $L(t)$  is the first zero-crossing of  $C(r, t)$ . (a)  $C(r, t)$  vs.  $r/L$  for disorder  $\Delta = 1.0$  and time  $t = 10^4, 10^5, 10^6, 10^7$  MCS. The data collapse is a signature of dynamical scaling. (b)  $C(r, t)$  vs.  $r/L$  for  $t = 10^7$  MCS and  $\Delta = 0, 1.0, 2.0$ . The distinct scaling form of correlation functions for different  $\Delta$  shows the violation of SU.

$\Delta = 0$  corresponds to the pure Ising model.

### 5.3.2 Superuniversality Violation

In Fig. 5.3(a), we plot correlation functions  $C(r, t; \Delta)$  vs.  $r/L$  for  $\Delta = 1.0$  and four different times:  $t = 10^4, 10^5, 10^6$  and  $10^7$ . The data collapse for different times is excellent, confirming that  $C(r, t; \Delta)$  exhibits dynamical scaling and the morphologies are scale-invariant. In Fig. 5.3(b), we plot  $C(r, t; \Delta)$  vs.  $r/L$  at  $t = 10^7$  for three different values of disorder:  $\Delta = 0, 1.0$  and  $2.0$ . The scaling functions are seen to be distinct, clearly demonstrating the violation of SU in the C-RFIM [33, 38]. The disorder breaks up the bicontinuous morphology of the pure case, as seen from the snapshots in Fig. 5.1 and Fig. 5.2. This bicontinuous structure is responsible for the oscillations in the CF, seen clearly for  $\Delta = 0$  in Fig. 5.3(b). Fig. 5.3 corresponds to  $d = 3$ . An analogous picture for  $d = 2$  is shown in Fig. 5.4.

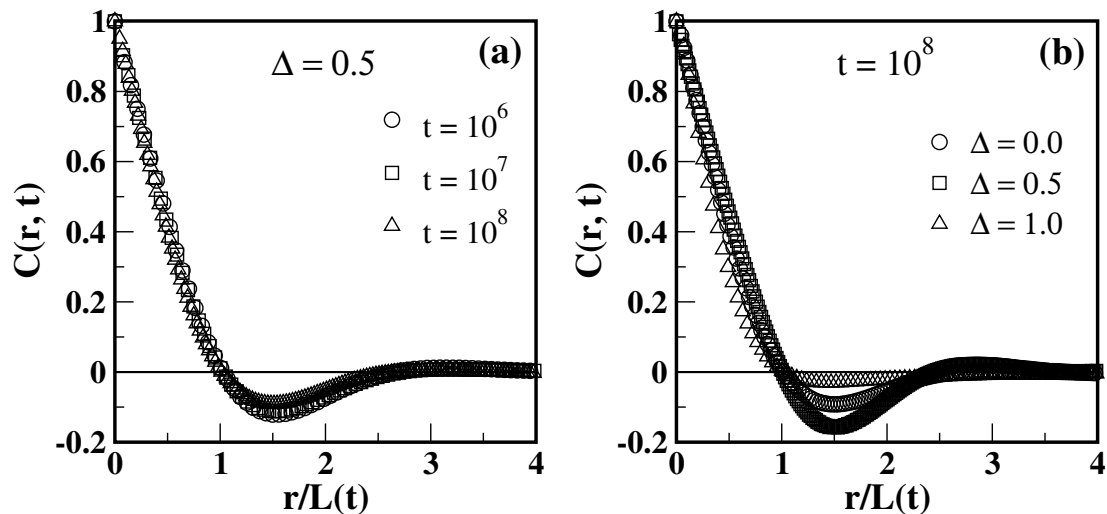


Figure 5.4: Scaled correlation functions,  $C(r, t)$  vs.  $r/L$ , for  $d = 2$  C-RFIM. (a)  $C(r, t)$  vs.  $r/L$  for  $\Delta = 0.5$  and time  $t = 10^6, 10^7, 10^8$  MCS. Again, the data collapse is a signature of dynamical scaling. (b)  $C(r, t)$  vs.  $r/L$  for  $t = 10^8$  MCS and  $\Delta = 0, 0.5, 1.0$ , which clearly shows a violation of SU.

### 5.3.3 Domain Growth Law

Next, we focus on the time-dependence of the typical domain size  $L(t)$ . We define it as the distance at which the CF decays to zero. Fig. 5.5 shows the plot of  $L(t)$  vs  $t$  on a log-log scale for  $\Delta = 0, 0.5, 1.0, 1.5, 2.0$ . Similarly, the Fig. 5.6 shows the plot of  $L(t)$  vs  $t$  for  $d = 2$  C-RFIM. In both the Figs. 5.5 and 5.6, a deviation from the power law for the pure case ( $L \sim t^{1/z}$  with  $z = 3$ ) is observed at large times in the presence of disorder. To analyze this cross-over, we use the framework introduced in Corberi et al. [35]. They propose the following scaling form for the growth law:

$$L(t, \Delta) \sim t^{1/z_{\text{eff}}} = t^{1/z} F(\Delta/t^\phi). \quad (5.6)$$

Here,  $z_{\text{eff}}$  is the *effective* growth exponent, and  $\phi$  is the crossover exponent. The scaling function behaves as ( $x = \Delta/t^\phi$ )

$$F(x) \sim \begin{cases} \text{const.}, & \text{for } x \rightarrow 0, \\ x^{1/\phi z} \ell(x^{-1/\phi}), & \text{for } x \rightarrow \infty. \end{cases} \quad (5.7)$$

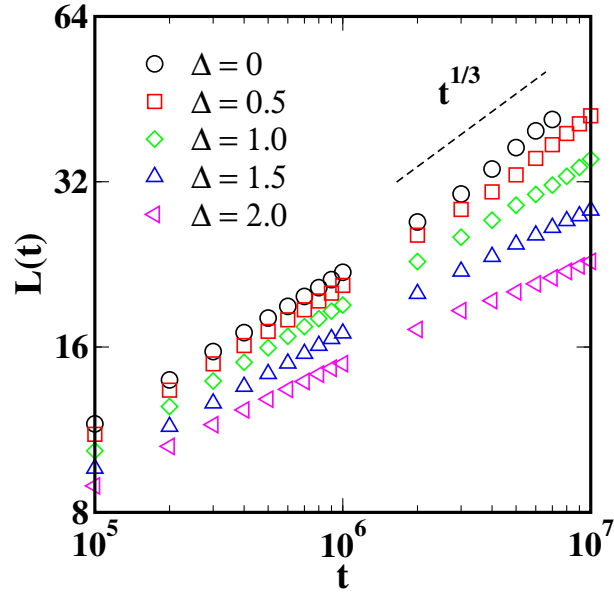


Figure 5.5: Plot of the characteristic length scale,  $L(t)$  vs.  $t$  on a log-log scale, for different values of  $\Delta$  in the  $d = 3$  C-RFIM. The dashed line indicates the Lifshitz-Slyozov (LS) law:  $L(t) \sim t^{1/3}$ , which applies for pure systems ( $\Delta = 0$ ). Notice the slowing down of domain growth at late times for higher disorder strengths.

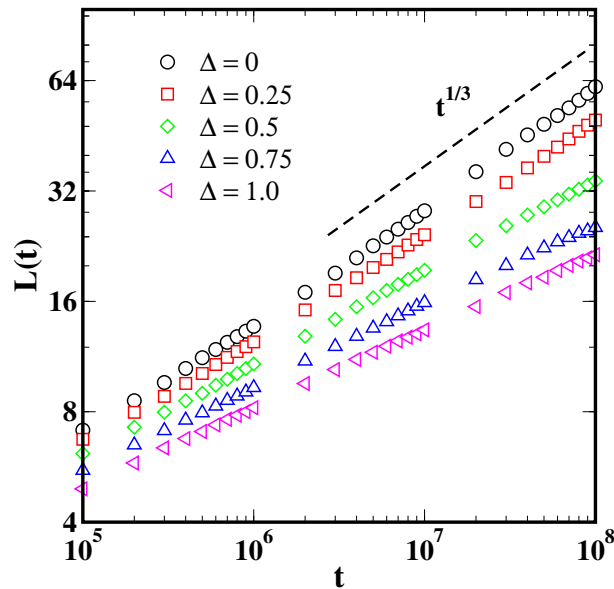


Figure 5.6: Analogous to Fig. 5.5 but for  $d = 2$  C-RFIM.

### 5.3. Numerical Results

For  $\phi < 0$ , Eq. (5.6) describes a crossover from the power-law form  $L \sim t^{1/z}$  to an asymptotic behavior  $L \sim \ell(t\Delta^{1/|\phi|})$ . The evaluation of the effective growth exponent  $z_{\text{eff}}$  is easier using the inverted form:

$$t = L^z G(L/\lambda). \quad (5.8)$$

Here, the crossover length scale  $\lambda = \Delta^{1/\phi z}$ , and  $G(y) = [F(x)]^{-z}$  with  $y = L/\lambda$ . The effective exponent as a function of  $y$  is then

$$z_{\text{eff}}(y) \equiv \frac{\partial \ln t}{\partial \ln L} = z + \frac{\partial \ln G(y)}{\partial \ln y}. \quad (5.9)$$

In Fig. 5.7(a), we show the time-dependence of  $z_{\text{eff}}(t, \Delta)$  for  $d = 3$ . For  $\Delta = 0$ , we expect  $z_{\text{eff}}$  to saturate to  $\bar{z} = 3$  at late times to yield the LS growth law. For non-zero  $\Delta$ , the plots show a power-law regime where  $z_{\text{eff}} \simeq \bar{z}$ , a disorder-dependent constant. This is followed by a late regime where  $z_{\text{eff}}$  is time-dependent, corresponding to logarithmic growth. This appears to be a universal scenario for domain growth in disordered systems, as stressed by Corberi et al. [35]. We generalize Eqs. (5.6)-(5.9) by replacing  $z \rightarrow \bar{z}$ .

Next, let us examine the variation of  $z_{\text{eff}}$  with  $L$ . From Eq. (5.9), we expect  $z_{\text{eff}} - \bar{z}$  to depend only on  $y = L/\lambda$ . In Fig. 5.7(b), we plot  $z_{\text{eff}} - \bar{z}$  vs.  $L/\lambda$  for different  $\Delta$ -values. The values of  $\lambda$  are chosen to ensure data collapse, which is seen to be good. The corresponding values of  $\lambda$  are provided in Table 5.1. The disorder-dependent values of  $\bar{z}$  [seen clearly for  $\Delta = 1.0, 1.5, 2.0$  in Fig. 5.7(a)] are also listed in Table 5.1. The solid curve in Fig. 5.7(b) is the best power-law fit of the form

$$z_{\text{eff}} - \bar{z} = by^\varphi, \quad (5.10)$$

with  $b \simeq 0.022$  and  $\varphi \simeq 5.6$ . The  $\Delta$ -dependence of  $\lambda$  is shown in Fig. 5.7(c) and is well-fitted by  $\lambda \sim \Delta^{-0.95}$ , suggesting  $\lambda \sim 1/\Delta$ . The negative exponent implies that disorder is indeed a relevant scaling field.

It is easy to confirm that Eq. (5.10) implies logarithmic domain growth. The

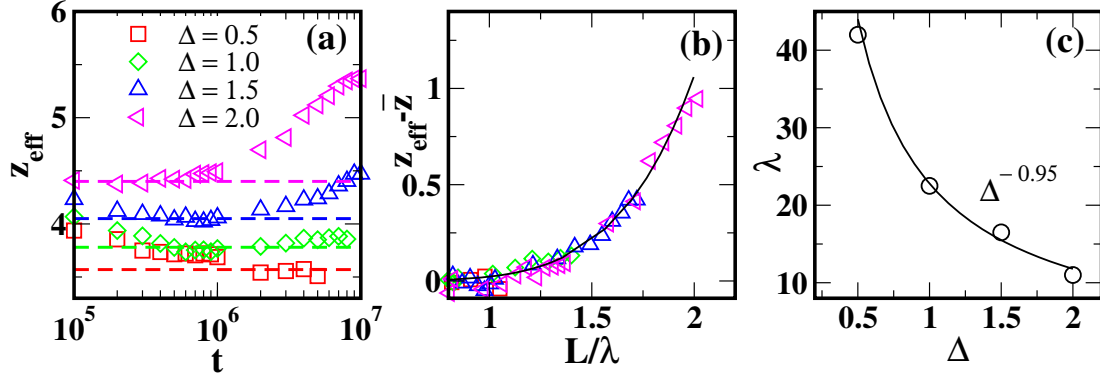


Figure 5.7: (a) Plot of effective exponent,  $z_{\text{eff}} = [d(\ln L)/d(\ln t)]^{-1}$  vs.  $t$  on a semi-log scale. The dashed lines indicate the disorder-dependent exponents  $\bar{z}(\Delta)$ . (b) Scaling collapse of  $z_{\text{eff}} - \bar{z}$  vs.  $L/\lambda$ . The solid line is the best power-law fit:  $z_{\text{eff}} - \bar{z} \simeq 0.022(L/\lambda)^{5.6}$ . (c) Plot of  $\Delta$ -dependence of  $\lambda$  ( $= \Delta^{1/\phi\bar{z}}$ ). The solid line is a power-law fit:  $\lambda \sim \Delta^{-0.95}$ .

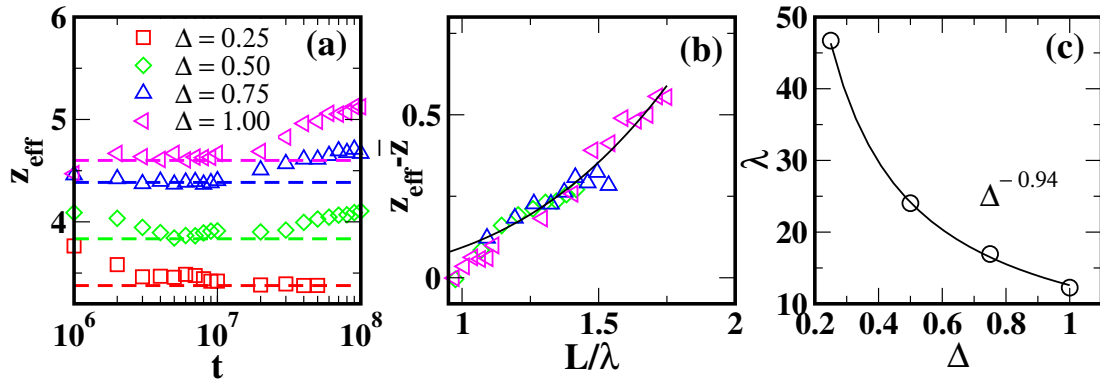


Figure 5.8: Analogous to Fig. 5.7 but for  $d = 2$  C-RFIM. (a) Plot of effective exponent  $z_{\text{eff}}$  vs.  $t$  on a semi-log scale. (b) Scaling collapse of  $z_{\text{eff}} - \bar{z}$  vs  $L/\lambda$ . The solid line is the best power-law fit:  $z_{\text{eff}} - \bar{z} \simeq 0.093(L/\lambda)^{3.3}$ . (c) Plot of  $\Delta$ -dependence of  $\lambda$ . The solid line is a power-law fit:  $\lambda \sim \Delta^{-0.94}$ .

### 5.3. Numerical Results

$d = 2$	$\Delta$	0	0.25	0.50	0.75	1.00
	$\bar{z}$	3.0	3.38	3.84	4.38	4.59
	$\lambda$	$\infty$	46.71	24.03	16.94	12.25
$d = 3$	$\Delta$	0	0.5	1.0	1.5	2.0
	$\bar{z}$	3.0	3.57	3.78	4.05	4.40
	$\lambda$	$\infty$	42.1	22.5	16.5	11.0

Table 5.1: Parameters  $\bar{z}$  and  $\lambda$  for the C-RFIM with different  $\Delta$ -values.

scaling function  $G(y)$  can be evaluated from Eq. (5.9) and Eq. (5.10), i.e.,

$$\frac{\partial \ln G(y)}{\partial \ln y} = by^\varphi,$$

$$\Rightarrow G(y) \sim \exp\left(\frac{b}{\varphi}y^\varphi\right). \quad (5.11)$$

Substituting for  $G(y)$  in Eq. (5.8) results in the asymptotic logarithmic growth form:

$$\frac{L}{\lambda} \simeq \left[\frac{\varphi}{b} \ln(t/\lambda^{\bar{z}})\right]^{1/\varphi}. \quad (5.12)$$

It is important to note that the exponent  $\varphi$  has great physical significance. According to the study of Huse and Henley (HH) [30] and Lai et al. (LMV) [40], domain growth in disordered systems of class 4 proceeds via activation over barriers of energy  $E_B \sim E_0 L^\varphi$  (see Sec. 1.6.2). Then, the asymptotic growth law is logarithmic:  $L(t) \sim (T/E_0)^{1/\varphi} (\ln t)^{1/\varphi}$ , as in Eq. (5.12).

We have also performed a similar analysis for the  $d = 2$  C-RFIM as shown in Fig 5.8. Recall that, there is no LRO in the system for  $T \neq 0$ , i.e., ordering kinetics is saturated by the correlation length. For  $T = 0$ , the thermal correlation length  $\xi$  diverges as  $\Delta \rightarrow 0$ :  $\xi(\Delta, T = 0) \sim \exp(a/\Delta)$  (see Sec. 2.3.1). We believe that  $L(t) \ll \xi(\Delta, T)$  in our simulations as we do not see any signs of saturation in the growth process. As discussed earlier, there have been preliminary studies [33, 38] of the coarse-grained version of this model. However, these were not sufficiently accurate to fix the value of the logarithmic exponent  $\varphi$ . The frames in Fig. 5.8 show (a) the effective exponent  $z_{\text{eff}}$  vs.  $t$ ; (b) the variation of  $z_{\text{eff}} - \bar{z}$  as a function of  $L/\lambda$  for different disorder values; and (c) the  $\Delta$ -dependence of



$\lambda$ . The corresponding values of  $\bar{z}$  and  $\lambda$  are provided in Table 5.1. The best-fit function,  $z_{\text{eff}} - \bar{z} = by^\varphi$ , in Fig. 5.8(b) yields  $b \simeq 0.093$  and  $\varphi \simeq 3.3$ . Thus, the logarithmic growth is faster for the  $d = 2$  C-RFIM than the  $d = 3$  C-RFIM.

### 5.3.4 Interfacial Properties of the Domain Morphologies

Finally, we analyze the properties of interfaces separating domains or correlated regions of up and down spins. These are known to be fractal in the ground state of the RFIM as shown in chapter 2 (Sec. 2.3).

Recall that an important signature of rough interfaces is the small- $r$  behavior of the CF, which exhibits a cusp singularity [41]:

$$C(r, t; \Delta) \equiv g(x) = 1 - Ax^\zeta + O(x^{2+\zeta}), \quad (5.13)$$

where,  $x = r/L$ ,  $A$  is a constant, and  $\zeta$  is the *cusp* exponent. For smooth interfaces,  $\zeta = 1$ . For fractal interfaces,  $0 < \zeta < 1$  and the fractal dimension  $d_f = d - \zeta$ .

The corresponding scaled SF  $f(p)$  [ $p = kL$ ] has an important implication:  $f(p) \sim p^{-(d+\zeta)}$  (Sec. 1.5.2). This can be obtained as

$$g(x) = \int \frac{d\mathbf{p}}{(2\pi)^d} e^{-i\mathbf{p}\cdot\mathbf{x}} f(p). \quad (5.14)$$

We use the following identity:

$$x^\theta = \int \frac{d\mathbf{p}}{(2\pi)^d} e^{-i\mathbf{p}\cdot\mathbf{x}} \frac{\mathcal{A}_d}{p^{d+\theta}}, \quad (5.15)$$

where  $\mathcal{A}_d$  is a  $d$ -dependent constant. From Eqs. (5.14) and (5.15), the cusp-like behavior in Eq. (5.13) yields a power-law decay:

$$f(p) \sim \frac{1}{p^{d+\zeta}}. \quad (5.16)$$

For sharp interfaces,  $\zeta = 1$  and we recover the well-known *Porod law*:  $f(p) \sim p^{-(d+1)}$  [42].

In Fig. 5.9(a), we plot  $1 - C(r, t)$  vs.  $r/L$  on a log-log scale for  $\Delta = 0, 1.0$  and

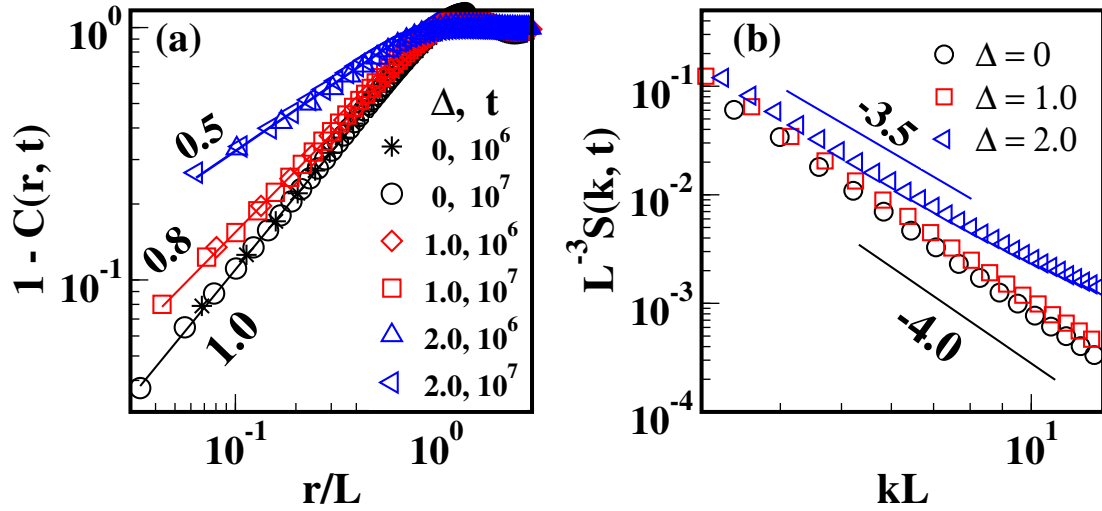


Figure 5.9: (a) Plot of  $1 - C(r, t)$  vs  $r/L$  on a log-log scale for C-RFIM in  $d = 3$  with  $\Delta = 0, 1.0, 2.0$  and  $t = 10^6, 10^7$  MCS. Notice that the data collapses for fixed  $\Delta$  and different values of  $t$ , but not for different values of  $\Delta$ , as the system exhibits dynamical scaling but not SU. The slope of the solid lines yields the disorder-dependent roughness exponent  $\zeta(\Delta) \simeq 1.0, 0.8, 0.5$  for  $\Delta = 0, 1.0, 2.0$ , respectively. (b) Plot of scaled SF,  $L^{-3}S(k, t)$  vs.  $kL(t)$ , for  $t = 10^7$  MCS and  $\Delta = 0, 1.0, 2.0$ . The solid lines denote relevant Porod and non-Porod tails.

2.0 at  $t = 10^6$  and  $10^7$ . The solid lines are the best linear fits in the small- $r/L$  regime with the indicated power-law exponents. The corresponding scaled SF,  $L^{-3}S(k, t)$  vs.  $kL$  at  $t = 10^7$  MCS, is shown alongside in Fig. 5.9(b). Notice that the cusp exponent  $\zeta$  is disorder-dependent and is unaffected by the coarsening process. This is consistent with our earlier observations that the scaling functions do not show SU for the C-RFIM.

### 5.3.5 Generalized Tomita Sum Rule

Let us consider  $\nabla^2 g$  in the limit  $x \rightarrow 0$ :

$$\begin{aligned} \lim_{x \rightarrow 0} \nabla^2 g(x) &= \lim_{x \rightarrow 0} \left( \frac{d^2 g}{dx^2} + \frac{d-1}{x} \frac{dg}{dx} \right) \\ &\simeq \lim_{x \rightarrow 0} -A\zeta(d + \zeta - 2)x^{\zeta-2}. \end{aligned} \quad (5.17)$$

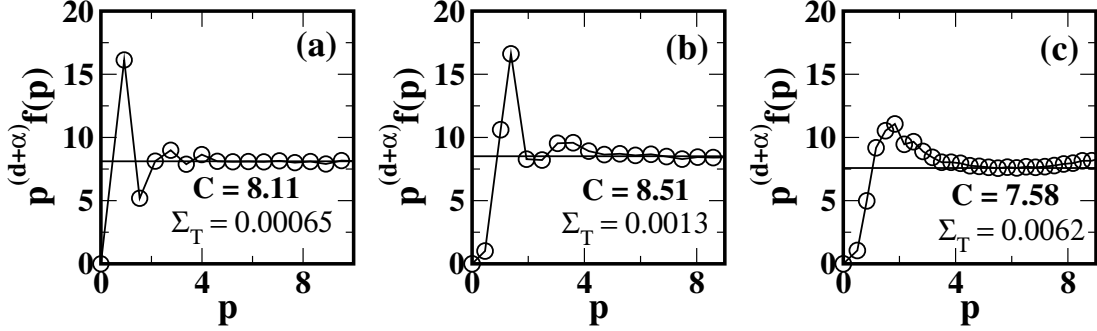


Figure 5.10: Plot of  $p^{(d+\zeta)}f(p)$  vs.  $p$  to demonstrate the *generalized Tomita sum rule* for (a)  $\Delta = 0$ , (b)  $\Delta = 1.0$ , and (c)  $\Delta = 2.0$ . The solid line in each plot indicates the value of the constant  $\mathcal{C}$  in Eq. (5.21). The values of  $\mathcal{C}$  and the Tomita sum  $\Sigma_T$ , obtained using numerical integration, are also specified in each frame.

From Eq. (5.14), we also have

$$\nabla^2 g(x) = - \int \frac{d\mathbf{p}}{(2\pi)^d} e^{-i\mathbf{p}\cdot\mathbf{x}} p^2 f(p). \quad (5.18)$$

We use Eq. (5.15) with  $\theta = \zeta - 2$  to obtain (when  $x \rightarrow 0$ )

$$\int \frac{d\mathbf{p}}{(2\pi)^d} p^2 f(p) = A\zeta(d + \zeta - 2) \int \frac{d\mathbf{p}}{(2\pi)^d} \frac{\mathcal{A}_d}{p^{d+\zeta-2}}, \quad (5.19)$$

or

$$\int \frac{d\mathbf{p}}{(2\pi)^d} \left[ p^2 f(p) - \frac{A\zeta(d + \zeta - 2)\mathcal{A}_d}{p^{d+\zeta-2}} \right] = 0. \quad (5.20)$$

This yields

$$\int_0^\infty dp p^{1-\zeta} [p^{d+\zeta} f(p) - \mathcal{C}] = 0, \quad (5.21)$$

where  $\mathcal{C}$  is a constant. The result in Eq. (5.21) with  $\zeta = 1$  (case with sharp interfaces) is referred to as *Tomita's sum rule* [10, 43]. Eq. (5.21) constitutes a generalization to the case with rough interfaces. To date, there is no theory available for the complete scaling function in the case with conserved kinetics [10]. The Tomita sum rule sets a useful constraint on reasonable functional forms for the CF or SF.

In Fig. 5.10, we demonstrate the generalized Tomita sum rule in Eq. (5.21) for the SF data in Fig. 5.9(b). We plot  $p^{(d+\zeta)}f(p)$  vs.  $p$  (where  $p = kL$ ) for (a)

$\Delta = 0$ , (b)  $\Delta = 1.0$ , and (c)  $\Delta = 2.0$ . The horizontal solid line corresponds to the value of the constant  $\mathcal{C}$ . The integral in Eq. (5.21) is denoted as  $\Sigma_T$ , and is specified in each frame. For all the three cases,  $\Sigma_T \simeq 0$ , verifying the *generalized Tomita sum rule* for *fractal* interfaces.

## 5.4 Summary and Conclusion

To summarize, we have undertaken a comprehensive MC study of domain growth in the RFIM with conserved dynamics (C-RFIM) in  $d = 2, 3$ . To the best of our knowledge, we present the first such study. There have been some earlier studies in  $d = 2$  of a coarse-grained counterpart of the C-RFIM. However, they did not yield conclusive answers regarding asymptotic growth laws. Our present work is an important step towards a complete understanding of domain growth laws.

The details of our study are as follows. After a deep temperature quench, the  $d = 2$  system was evolved up to  $t = 10^8$  MCS, and the  $d = 3$  system up to  $t = 10^7$  MCS. This significant computational effort enabled us to observe *clean* cross-overs from a disorder-dependent power-law growth to a disorder-independent logarithmic growth in  $d = 2, 3$ . A summary of our results is as follows:

- (a) For a fixed  $\Delta$ , there is dynamical scaling, signifying the presence of a unique length-scale. However, super-universality (SU) is violated in the  $d = 2, 3$  C-RFIM indicating that the systems are not robust to disorder.
- (b) At intermediate times, domain growth obeys a power law with disorder-dependent exponent:  $L(t) \sim t^{1/\bar{z}(\Delta)}$ . In the asymptotic regime, there is a cross-over to logarithmic growth with a disorder-independent exponent:  $L(t) \sim (\ln t)^{1/\varphi}$ . The logarithmic exponent  $\varphi \simeq 3.3$  in  $d = 2$ , and  $\varphi \simeq 5.6$  in  $d = 3$ .
- (c) The small- $r$  behavior of the CF exhibits a cusp singularity:  $1 - C(r) \simeq A(r/L)^{\zeta(\Delta)}$ , where  $\zeta$  is disorder-dependent cusp exponent. The cusp exponent  $\zeta$  yields the interfacial fractal dimension as  $d_f = d - \zeta$ . The corresponding SF exhibits a non-Porod decay:  $S(k, t, \Delta) \sim k^{-(d+\zeta)}$ , signifying scattering off fractal interfaces. Further, the scaling function for the SF obeys a *generalized Tomita sum rule*.

## 5.4. Summary and Conclusion

---

In conclusion, the C-RFIM is a generic model for a wide range of experimental systems. We hope that the novel results presented in this chapter will motivate further interest in this fascinating problem. We now have a reasonable understanding of nonconserved domain growth in disordered systems. This is an appropriate time to undertake an exhaustive study of the corresponding conserved models.

# References

- [1] S. Fishman and A. Aharony, J. Phys. C: Solid State Physics **12**, L729 (1979).
- [2] D. Belanger, A. King, and V. Jaccarino, J. App. Phys. **53**, 2702 (1982).
- [3] Y. G. Pollack and M. Schechter, Phys. Rev. B **89**, 064414 (2014).
- [4] F. Brochard and P.G. De Gennes, J. Phys. Lett. (Paris) **44**, 785 (1983).
- [5] P. G. De Gennes, J. Phys. Chem. Lett. **88**, 6469 (1984).
- [6] R.L.C. Vink, K. Binder, and H. Löwen, Phys. Rev. Lett. **97**, 230603 (2006).
- [7] J. D. Gunton, J. Stat. Phys. **34**, 1019 (1984).
- [8] M. A. Rubio, C. A. Edwards, A. Dougherty, and J. P. Gollub, Phys. Rev. Lett. **63**, 1685 (1989).
- [9] N. Martys, M. Cieplak, and M. O. Robbins, Phys. Rev. Lett. **66**, 1058 (1991).
- [10] S. Puri and V.K. Wadhawan (eds.), *Kinetics of Phase Transitions* (CRC Press, Boca Raton, 2009); S. Dattagupta and S. Puri, *Dissipative Phenomena in Condensed Matter: Some Applications* (Springer-Verlag, Heidelberg, 2004).
- [11] S. Puri, Phase Transitions, **77**, 407 (2004).
- [12] M. Grant and J. D. Gunton, Phys. Rev. B **29**, 1521 (1984).
- [13] E. Oguz, A. Chakrabarti, R. Toral, and J.D. Gunton, Phys. Rev. B **42**, 704 (1990).

- 
- [14] E. Gawlinski, K. Kaski, M. Grant, and J. Gunton, Phys. Rev. Lett. **53**, 2266 (1984).
- [15] S. R. Anderson, Phys. Rev. B **36**, 8435 (1987).
- [16] G. Grinstein and J. Fernandez, Phys. Rev. B **29**, 6389 (1984).
- [17] E. Gawlinski, S. Kumar, M. Grant, J. D. Gunton, and K. Kaski, Phys. Rev. B **32**, 1575 (1985).
- [18] E. Pytte and J. Fernandez, Phys. Rev. B **31**, 616 (1985).
- [19] S. Puri, D. Chowdhury and N. Parekh, J. Phys. A: Math. Gen. **24**, L1087 (1991); S. Puri and N. Parekh, J. Phys. A: Math. Gen. **25**, 4127 (1992).
- [20] R. Paul, S. Puri, and H. Rieger, Europhys. Lett. **68**, 881 (2004).
- [21] R. Paul, S. Puri, and H. Rieger, Phys. Rev. E **71**, 061109 (2005).
- [22] F. Corberi, E. Lippiello, A. Mukherjee, S. Puri, and M. Zannetti, J. Stat. Mech., P03016 (2011).
- [23] E. Lippiello, A. Mukherjee, S. Puri, and M. Zannetti, Europhys. Lett. **90**, 46006 (2010).
- [24] M. Henkel and M. Pleimling, Europhys. Lett. **76**, 561 (2006).
- [25] M. Henkel and M. Pleimling, Phys. Rev. B **78**, 224419 (2008).
- [26] H. Park and M. Pleimling, Eur. Phys. J. B **85**, 300 (2012).
- [27] F. Corberi, E. Lippiello, A. Mukherjee, S. Puri, and M. Zannetti, Phys. Rev. E **88**, 042129 (2013).
- [28] H. Park and M. Pleimling, Phys. Rev. B **82**, 144406 (2010).
- [29] R. Paul, G. Schehr, and H. Rieger, Phys. Rev. E **75**, 030104(R) (2007).
- [30] D. A. Huse and C. L. Henley, Phys. Rev. Lett. **54**, 2708 (1985).
- [31] T. Nattermann and I. Vilfan, Phys. Rev. Lett. **61**, 223 (1988).

- [32] F. Ye, M. Matsuda, S. Katano, H. Yoshizawa, D. P. Belanger, E. T. Seppala, J. A. Fernandez-Baca, and M. J. Alava, *J. Magn. Magn. Mater.* **272**, 1298 (2004).
- [33] S. Puri and N. Parekh, *J. Phys. A Math. Gen.* **26**, 2777 (1993).
- [34] M. Rao and A. Chakrabarti, *Phys. Rev. Lett.* **71**, 3501 (1993).
- [35] F. Corberi, E. Lippiello, A. Mukherjee, S. Puri, and M. Zannetti, *Phys. Rev. E* **85**, 021141 (2012).
- [36] J. G. Amar, F. E. Sullivan, and R.D. Mountain, *Phys. Rev. B* **37**, 196 (1988).
- [37] J. Marko and G. Barkema, *Phys. Rev. E* **52**, 2522 (1995).
- [38] M. Rao and A. Chakrabarti, *Phys. Rev. E* **48**, R25 (1993).
- [39] M. E. Fisher, *Rep. Prog. Phys.* **30**, 615 (1967).
- [40] Z. Lai, G. F. Mazenko, and O.T. Valls, *Phys. Rev. B* **37**, 9481 (1988).
- [41] P.-z. Wong, *Phys. Rev. B* **32**, 7417 (1985).
- [42] G. Porod, in *Small-Angle X-Ray Scattering*, O. Glatter and O. Kratky (eds.) (Academic Press, New York, 1982); Y. Oono and S. Puri, *Mod. Phys. Lett. B* **2**, 861 (1988).
- [43] H. Tomita, *Progr. Theor. Phys.* **72**, 656 (1984); *Progr. Theor. Phys.* **75**, 482 (1986).



# Chapter 6

## Equilibrium Structure and Off-equilibrium Kinetics in a Tunable Frustrated Magnet

### 6.1 Introduction

So far we have studied the disordered systems with random-field (RF) types of disorder, e.g., RFIM. In chapter 5, we have understood the phase-ordering in the conserved case of RFIM. Phase-ordering also occur in disordered systems with random-bond (RB) types of disorder, e.g., random coupling-constant, random dilution, or quenched vacancies [1, 2]. Concerning the domain growth law in these systems, either logarithmic [3–9] or temperature dependent power-laws [10–13] growth have been found. A number of experiments on these systems also report logarithmic [14, 15] or the power-law growth [16, 17]. Thus, there is yet no clear understanding of growth kinetics in these systems—e.g., on the basis of different dynamical universality classes or on the basis of some simple classification of different disordered magnetic models.

Further, as a rule of thumb that the more disorder in a system is responsible for more pinning, and due to which the simple fact that the slower the growth will be, has been recently found to be incorrect in quite a number of cases [6–8]. Considering, for instance, the Ising model with random dilution (namely a

fraction  $d$  of sites or bonds on the lattice are missing), it was shown that, although for sufficiently small values of  $d$ , the kinetics is slowed down upon increasing  $d$ , as naively expected, after a certain threshold, increasing  $d$  produces a faster growth. As it is explained in Refs. [6, 7], this happens because adding more disorder—in this case parametrized by  $d$ —not only introduces more pinning sources but, more importantly, the topological properties of the system are also changed. Indeed, when  $d$  gets close to the value  $d_c$ , where the set of non-diluted sites (or bonds) is at the percolation threshold, the fractal properties of the percolating network play an important role in speeding up the evolution because the pinning barriers are softened. This very effect, the nonmonotonous behavior of the growth with the amount of disorder is observed not only in diluted systems but also for Ising model with random *ferromagnetic* (FM) couplings [6].

All these systems—described insofar—are the disordered ferromagnetic, i.e., non-frustrated. The objective of this chapter is to generalize the nonmonotonous behavior of the growth in these systems with the addition of frustration. The frustration arises when it is impossible to simultaneously satisfy all the interactions between the microscopic constituents, e.g., an *antiferromagnetic* (AFM) Ising model on a triangular lattice. The slow evolution of disordered frustrated systems is by far a much more complicated problem. This is because even the basic structure of the low-temperature equilibrium states in finite-dimensional systems are still debated. The absence of a clear-cut indication on the static properties hinders the interpretation of what is dynamically observed [18].

Our aim is to study the kinetics of disordered systems with the gradual addition of frustration from the side of non-frustrated ones, where a better understanding has been to some extent achieved. In order to do that we consider an Ising model with a fraction  $a$  of negative coupling constants ( $J_{ij}$ ), and the remaining ones are positive. We study the model numerically in  $d = 2$  and vary the value of  $a$  in the interval  $[0, 1]$ . Clearly, by changing the parameter  $a$ , one can gradually tune the amount of frustration present in the system. Not enough, in order to avoid high frustration and to have a better understanding from a situation without frustration to one where it is relevant, we consider the case where the FM interactions (positive  $J_{ij}$ ) are much stronger than the AFM ones (negative  $J_{ij}$ ).

In the low-temperature equilibrium phase-diagram of the model, as  $a$  is progressively increased, one moves from a FM phase, where frustration plays a minor role, to a strongly frustrated *paramagnetic* (PM) phase which, right at  $T = 0$ , is expected to exhibit a spin-glass order [19, 20]. For even larger values of  $a$ , an AFM region is entered. Therefore, considering the evolution of the present model after a deep quench to a small finite temperature  $T_f > 0$ , we have the opportunity to study how different amounts of frustration—tuned by  $a$ —influence the off-equilibrium kinetics.

In doing that we observe a usual coarsening in the magnetic phases—either FM or AFM—which is characterized by a logarithmic growth, in agreement with previous studies on related Ising models with random bonds [3]. On increasing frustration via  $a$ , we find that the speed of phase-ordering changes in a non-monotonous way. This behavior is analogous to the one discussed above for non-frustrated systems and can be interpreted from similar arguments based on topology. Indeed, the geometry of the growing domains becomes fractal as  $a$  is increased and the transition to the PM region is approached, similar to what happens in the nonfrustrated diluted systems previously considered when the percolation threshold is approached. Also in this case, the fractal topology speeds up the evolution.

This shows that an off-equilibrium evolution getting faster and more efficient with the addition of the disorder is of a quite general nature, and occurs both in systems with and without frustration. At variance with the logarithmically slow evolution observed in the FM or AFM phases, a faster kinetics characterized by algebraic behaviors is found along the whole PM region, where frustration plays a prominent role. The faster evolution observed in this phase (as compared to the logarithmic one in the FM and AFM regions) can be perhaps because of the proximity to the spin-glass structure (at  $T = 0$ ), which has many quasi-isoenergetic levels that soften the energy barriers.

This chapter is organized as follows: In Sec. 6.2 we introduce the model and discuss the structure of the bond network in Sec. 6.2.1. Section 6.3 is devoted to the study of the low-temperature phase-diagram, where we present the equilibrium structure of the system in different phases. In Sec. 6.4, we study the off-equilibrium growth kinetics of the model after deep quenches to various final

temperatures and present the numerical results. Finally, in Sec. 6.5, we conclude and summarize our main results of this chapter.

## 6.2 The Model

Let us recall the Hamiltonian for the RBIM as defined in Eq. (1.7), i.e.,

$$\mathcal{H} = - \sum_{\langle ij \rangle} J_{ij} s_i s_j. \quad (6.1)$$

We consider the bimodal distribution of coupling-constants  $\{J_{ij}\}$  as given in Eq. (1.9):

$$P_b(J_{ij}) = a [\delta(J_{ij} - (J_0 - \epsilon))] + (1 - a) [\delta(J_{ij} - (J_0 + \epsilon))]. \quad (6.2)$$

$\epsilon \leq J_0$  corresponds to the non-frustrated case, which has been previously studied in Ref. [6]. Here, instead, we set

$$\epsilon > J_0, \quad (6.3)$$

meaning that the fraction  $a$  of bonds are AFM with  $J_{ij} < 0$  and the remaining ones are FM with  $J_{ij} > 0$ . We will also denote negative bonds with  $J_- = J_0 - \epsilon$  and positive ones with  $J_+ = J_0 + \epsilon$ .

### 6.2.1 The Geometry of the Bond Network

It is useful to discuss the geometrical properties of the network of bonds of the model, which is pictorially illustrated in the upper stripe of Fig. 6.1. With  $a = 0$  the system is a pure Ising ferromagnet, since all the coupling constants are the  $J_+$ . Moving to a finite value of  $a$  introduces the AFM bonds. If  $a$  is small, these will be separated apart by a typical distance

$$\lambda_a \sim a^{-1/d}, \quad (6.4)$$

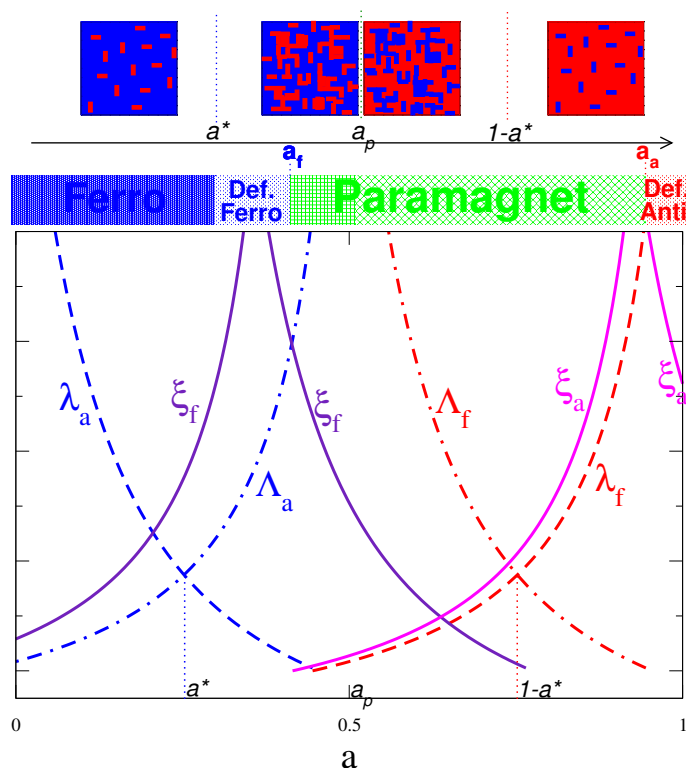


Figure 6.1: In the upper stripe, four typical bond configurations are pictorially shown, corresponding to  $0 < a < a^*$ ,  $a^* < a \lesssim a_p$ ,  $a_p \lesssim a < 1 - a^*$  and  $1 - a^* < a < 1$ , from left to right, respectively. FM bonds are drawn in blue, AFM ones in red. The bar below the configuration stripe describes the physical phases of the systems as  $a$  is varied, e.g., if FM, PM, etc. The graph in the lower part of the figure is a schematic representation of the behavior of the typical lengths characterizing the bond configuration and the physical properties (see text).

where  $d$  is the dimension of the system. This situation is schematically represented in the leftmost box on the upper stripe of the Fig. 6.1. Here the blue color corresponds to regions where the bonds are FM while AFM ones are drawn in red. The behavior of  $\lambda_a$  is shown by a dashed blue line in the lower graph of Fig. 6.1. It decreases as  $a$  increases, meaning that at some point it becomes of the order of the lattice spacing and then groups of AFM bonds start to coalesce.

Indeed, we know that at the bond percolation threshold  $a_p \equiv a = 1/2$ , such bonds form a percolating cluster. Due to this, right at  $a_p$  the size  $\Lambda_a$  of the regions of clustered AFM bonds is  $\Lambda_a = \infty$  and, for  $a$  smaller but not too far

### 6.3. The Structure of the Equilibrium States

---

from  $a = a_p$  one has the well-known percolative behavior,

$$\Lambda_a = (a_p - a)^{-\nu}, \quad (6.5)$$

with  $\nu = 4/3$ , which is shown by a dotted-dashed blue line in the lower part of Fig. 6.1. A pictorial representation of the bond configuration in the region  $a \lesssim a_p$  is shown in the second (from the left) box in the upper part of the figure. The transition between the region with isolated and clustered AFM bonds occur at a value  $a = a^*$ , which can be roughly identified as the point where  $\lambda_a \simeq \Lambda_a$ . The actual value of  $a^*$  is located [6] between  $a = 0.2$  and  $a = 0.3$ .

Clearly, as we move in the region  $a > a_p$  the situation mirrors that for  $a < a_p$  upon exchanging the roles of FM and AFM bonds and replacing  $a$  to  $1 - a$ , and substituting the lengths  $\lambda_a$  and  $\Lambda_a$  with the corresponding ones  $\lambda_f$  and  $\Lambda_f$ , respectively, then one has

$$\lambda_f = (1 - a)^{-1/d}, \quad (6.6)$$

and

$$\Lambda_f = (a - a_p)^{-\nu}. \quad (6.7)$$

## 6.3 The Structure of the Equilibrium States

As  $\epsilon > J_0$ , we consider the simple case with

$$J_0 < \epsilon < \frac{q}{q-2} J_0, \quad (6.8)$$

where  $q$  is the coordination number of the lattice. Eq. (6.8) corresponds to a *ferromagnetic-always-wins* condition as the FM strengths  $J_+$  is more stronger than the AFM ones  $J_-$ . When this condition holds, a spin to which at least a FM bond is attached will always lower its energy by pointing along the direction of the majority (if a majority exists) of spins to which it is connected by FM bonds. Notice also that the spin-glass systems do not obey Eq. (6.8) (since  $J_0 = 0$ ).

We choose  $\epsilon = 1.25J_0$  and  $J_0 = 1$ , which obviously satisfies Eq. (6.8). Then,  $J_+ = J_0 + \epsilon = 2.25$  and  $J_- = J_0 - \epsilon = -0.25$ , the FM bonds  $J_+$  are 9 times stronger than AFM ones, i.e.,  $J_+ = 9|J_-|$ . All the numerical data are presented

### 6.3. The Structure of the Equilibrium States

---

for square lattices of size  $512^2$  with periodic boundary conditions applied on both sides. Let us now discuss the structure of the low-temperature equilibrium states of the model as  $a$  is changed.

#### 6.3.1 Ground States

In the following, we will focus on the ground states, namely the equilibrium configurations at  $T = 0$ . The GS problem is based on the generalization of solving the graph-theoretic problem on planer graph [21] (without periodic boundary conditions) to the toroidal lattice (i.e., periodic boundary conditions). We found ground states using the minimum-weight-perfect-matching (MWPM) algorithm as introduced in [22, 23]. With this technique, the GS can be found in polynomial time.

To classify the ground states and the low-temperature equilibrium states of the model, it is useful to consider the two global order parameters, viz., the *spontaneous magnetization*  $m$  and the *staggered magnetization*  $M$ , defined as

$$m = \frac{1}{N} \sum_i s_i, \quad (6.9)$$

$$M = \frac{1}{N} \sum_i \sigma_i. \quad (6.10)$$

Here,  $\sigma_i$  is the staggered spin,

$$\sigma_i = (-1)^i s_i. \quad (6.11)$$

In Eq. (6.11), it is stipulated that the index  $i$  runs over the lattice sites in such a way that two nearest neighbors (NNs) always have an opposite value of  $(-1)^i$ .

The computed values of  $m$  and  $M$  in the ground states of the model for different values of  $a$ , are plotted in Fig. 6.2. We will classify the ground states according to  $m$  and  $M$  in the different regions of the parameter  $a$  in the following sections. This classification is reported in the upper bar of Fig. 6.1 and, similarly, in the lower bar of Fig. 6.2. Let us discuss the different magnetic phases of the model in this classification, viz., ferro-, defective ferro-, para-, and defective

### 6.3. The Structure of the Equilibrium States

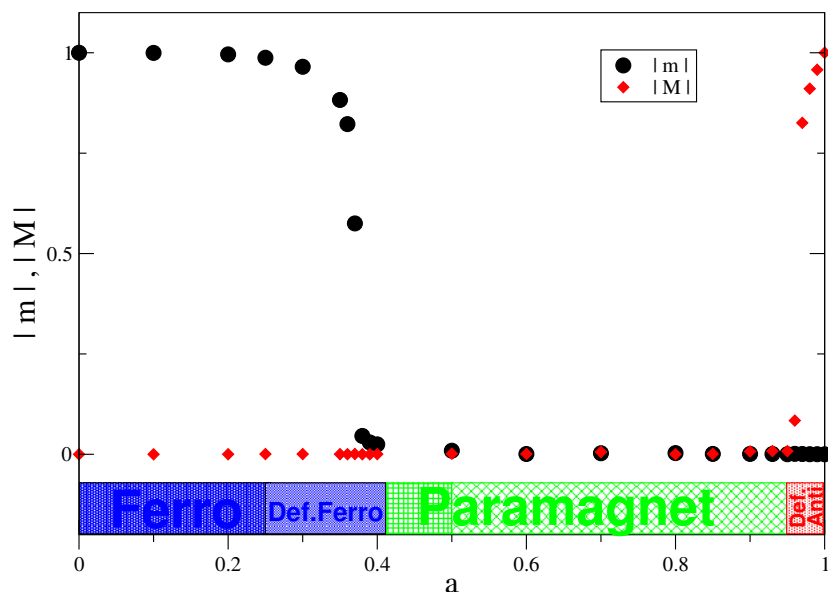


Figure 6.2:  $|m|$  and  $|M|$  in the ground states at  $T = 0$  for different values of  $a$ . The ground states are obtained on a  $512^2$  lattice with the periodic boundary condition.

antiferromagnetic.

#### 6.3.1.1 Ferromagnetic phase ( $0 \leq a < a_f$ )

The ferromagnetic phase can be split into the two sectors with  $0 \leq a < a^*$  and  $a^* \leq a < a_f$ , which will be considered separately below.

*Sector  $0 < a < a^*$*

As discussed above in Sec. 6.2.1, in this region, there are basically only isolated AFM links in a sea of FM ones. At  $T = 0$  spins in this sea necessarily align in a FM state. Eq. (6.8) implies that also the spins attached to the AFM bonds must be aligned with those in the sea. Hence, the GS is akin to a usual FM system. Of course, as  $a$  increases, there is a finite probability to find some AFM bonds nearby and this can cause some spin reversal with respect to a completely ordered configuration, but for  $a < a^*$  these are quite a few. Since the presence of AFM bonds is largely irrelevant in this parameter region, we expect  $|m| \simeq 1$  and  $M = 0$ . We can see in Fig. 6.2 that this is indeed the case.

A representation of a real GS for  $a = 0.2 < a^*$  (let us recall that  $a^*$  is expected



### 6.3. The Structure of the Equilibrium States

---

to be located between  $a = 0.2$  and  $a = 0.3$ ) is shown in the upper left panel of Fig. 6.3, which confirms the above description.

*Sector*  $a^* \leq a < a_f$

Fig. 6.2 shows that FM order extends up to a certain  $a = a_f$  (with  $a_f \gtrsim 0.4$ ), which is well beyond  $a^*$ . FM ordering occurring beyond  $a^*$  can be expected, as in the whole region  $a < a_p$  the number of FM bonds is larger than that of the AFM ones and also because of the ferromagnetic-always-wins condition in Eq. (6.8). Notice, however, this does not guarantee that the FM order is sustained up to  $a = a_p$  or beyond, for the reasons that will be explained in Sec. 6.3.1.2, but only up to a lower value  $a = a_f < a_p$ .

In the region  $a^* < a < a_f$ , there is still a prevalence of FM order, namely the fraction of up spins (say) prevails over the reversed ones, but since AFM bonds can coalesce, regions with down spins may be found locally, as it can be seen in Fig. 6.3 for  $a = 0.3$  and  $a = 0.4$  (upper central and right panel). This is why we call this situation *defective ferromagnet*. Clearly, the islands where spins are reversed increase upon raising  $a$ , as it can be checked in Fig. 6.3. Here one sees that the size  $\xi_f$  of these regions grows dramatically as  $a$  gets close to  $a_f$ , a fact that is pictorially sketched in Fig. 6.1. The presence of extended regions opposite to the dominant FM order depletes the magnetization of the system, so when  $a^* < a < a_f$  one has  $0 < |m| < 1$  (decreasing upon raising  $a$ ) and  $M = 0$ , as it can be observed in Fig. 6.2. The magnetization  $m$  vanishes at the transition point  $a = a_f$ .

#### 6.3.1.2 Paramagnetic phase ( $a_f \leq a \leq a_a$ )

Also in this phase, we consider separately the two subregions with  $a_f < a < a_p$  and  $a_p < a < a_a$ , as discussed below.

*Sector*  $a_f < a < a_p$

In this sector, the FM bonds still prevail and form a sea that spans the system. The difference with the FM region is that AFM bonds, besides being grouped together, can form sufficiently connected paths so as to destroy the FM state. This we will discuss in Appendix B.

### 6.3. The Structure of the Equilibrium States

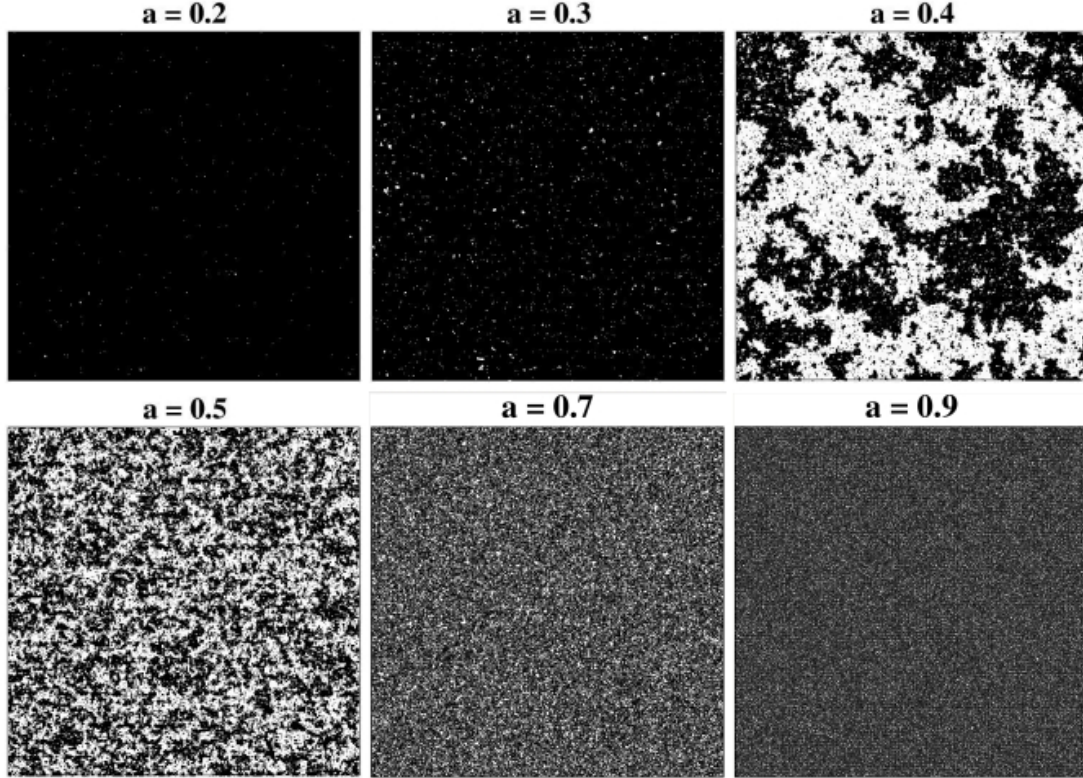


Figure 6.3: Configurations of the GS for a  $512^2$  lattice for different values of  $a$ . Spins up are marked in black and spins down are in white.

A real configuration of the system in this region looks like the one for  $a = 0.5$  in Fig. 6.3 (bottom row, left). By comparing this configuration with the one at  $a = 0.7$ , one can notice that the size  $\xi_f$  of the locally magnetized regions increases as  $a$  decreases toward  $a_f$ , suggesting that  $\xi_f$  diverges also on this side of  $a_f$ , as it is sketched in Fig. 6.1. Therefore, with the given structure of the GS as discussed above, one has  $m = 0$ . Clearly, it is also  $M = 0$ , since negative bonds are a minority because of which the AFM ordering cannot occur in this sector. This is confirmed in Fig. 6.2. Due to the fact that  $m = 0$  as well as  $M = 0$ , we generically call the region with  $a_f \leq a \leq a_a$  as *paramagnetic*. Let us anticipate, however, that right at  $T = 0$  some spin-glass order is expected, as we will further discuss in Sec. 6.4.2.2.

*Sector*  $a_p < a < a_a$

### 6.3. The Structure of the Equilibrium States

---

In this region, there is a sea of AFM bonds. If  $a$  is larger but sufficiently close to  $a_p$  there are also FM islands inside which spins are aligned. However, these islands are disconnected and hence they order incoherently. Therefore, we expect  $m = 0$  throughout the region  $a > a_p$ . This is observed in Fig. 6.2. Further, the presence of a spanning sea of AFM bonds is not sufficient to establish a global AFM order even when the  $a$  is so large that FM bonds are isolated, which happens for  $a > 1 - a^*$  (we recall that the  $a^*$  lies between 0.2 and 0.3). This is obviously due to the fact that AFM interactions are weak as compared to FM ones (due to the condition in Eq. (6.8)). Indeed, we see in Fig. 6.2 that the property  $M = 0$  extends up to  $a = a_a$ , where  $a_a$  is located around  $a \gtrsim 0.95$ . We will discuss it in Appendix C.

The development of AFM order cannot be easily observed by simply plotting the spins, as can be noticed in Fig. 6.3 that on a large scale one gets a uniform black plot. On the other hand, it can be clearly seen by plotting the staggered spin  $\sigma_i$  instead of  $s_i$ , as it is done in Fig. 6.4. In this figure, local AFM order results in black or white regions, and  $|M| > 0$  corresponds to a majority of one of the two colors. Beyond  $a_a$  the AFM order sets in. This region will be discussed as below.

#### 6.3.1.3 Defective antiferromagnet ( $a_a \leq a \leq 1$ )

In the region with  $a > a_a$ , there are very few and far apart FM bonds. As these bonds are more stronger than AFM ones, the pairs of spins attached to FM bonds will be aligned. This represents a defect in the otherwise perfectly ordered AFM state. Therefore, in this region, the system is an antiferromagnet with a fraction  $1 - a$  of isolated defects and that's why we name this region as *defective antiferromagnet*. Then, one has in this region, the  $m = 0$  and  $M \neq 0$ , as it can be seen in Fig. 6.2. We can see from Fig. 6.4 that the local AFM order parameter  $\sigma_i$  organizes in large regions as the critical point  $a_a$  is approached, similarly to what  $s_i$  does as in FM phase on reducing  $a$  below  $a_f$ . This suggests that the size  $\xi_a$  of such regions diverges at  $a = a_a$ , as it is sketched in Fig. 6.1.

### 6.3. The Structure of the Equilibrium States

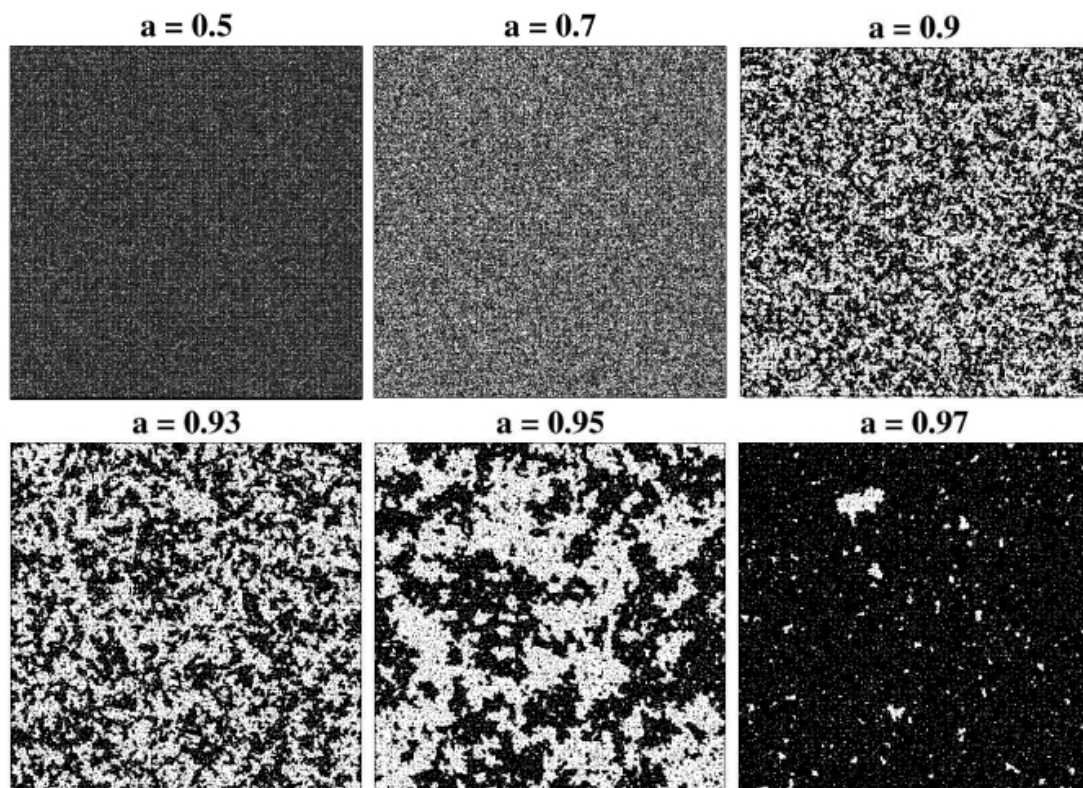


Figure 6.4: Configurations of the GS for a  $512^2$  lattice for different values of  $a$ . We plot the staggered spin  $\sigma_i$  defined in Eq. (6.11).  $\{\sigma_i\} = 1$  are marked in black and  $\{\sigma_i\} = -1$  are in white.

#### 6.3.2 Equilibrium States at a Finite Temperature

Since we will study the evolution of a system quenched to  $T_f > 0$ , it is worth to discuss briefly the modifications to the above equilibrium picture at  $T = 0$  introduced by a finite temperature. Let us recall that  $J_+ = 2.25$  and  $J_- = -0.25$ .

Consider the region with  $a < a_f$ , where FM order prevails. In this region the critical temperature  $T_c$  is expected to drop from the Ising value  $T_c(a = 0) \simeq 2.269J_+ \simeq 5.105$ , to  $T_c(a = a_f) = 0$  upon raising  $a$  (the temperature is in the units of  $J_0/k_B$ ,  $k_B$  is the Boltzmann constant). Similarly, on the AFM side,  $a > a_a$ , the corresponding  $T_c$  will drop from  $T_c(a = 1) \simeq 2.269|J_-| \simeq 0.567$  to  $T_c(a_a) = 0$  upon decreasing  $a$ .

In the PM region, the spin-glass phase is expected to be destroyed by thermal fluctuations, no matter how small. Hence,  $T_c = 0$  in this phase. However, as we

will discuss further below, the existence of spin-glass order at  $T = 0$  may strongly influence the dynamical properties at finite temperatures.

## 6.4 Off-equilibrium Study of Growth Kinetics

### 6.4.1 Simulation Details

To study the off-equilibrium growth kinetics, we prepare the system in a fully disordered initial state with uncorrelated spins pointing randomly up or down, corresponding to an equilibrium configuration at  $T = \infty$ , and then quench to a low temperature  $T_f$  at time  $t = 0$ . Let us say a few words on the role of the final temperature  $T_f$ . Here we are interested in a situation where  $T_f$  is very small. This is because usually the kinetics of magnetic systems is more easily interpreted in this limit, and also because low temperatures guarantees  $T_f < T_c(a)$  in a wider range of  $a$  [see previous discussion about  $T_c(a)$  in Sec. 6.3.2]. However, setting  $T_f$  to very small values has the undesirable consequence that the kinetics becomes so sluggish that no appreciable growth of  $L(t)$  can be detected in the range of simulated times.

In the following we will consider, out of many values  $T_f$  used in the simulations, the two choices  $T_f = 0.4$  and  $T_f = 0.75$ , which were found to represent a good compromise between the two contrasting issues discussed above. Notice that both these temperatures are much below the critical temperature  $T_c(a = 0) \simeq 5.105$  of the clean ferromagnet. On the other hand, while the former ( $T_f = 0.4$ ) is smaller than of the clean antiferromagnet  $T_c(a = 1) \simeq 0.567$ , the latter ( $T_f = 0.75$ ) is above. Let us stress that, in any case, since  $T_c(a_f \leq a \leq a_a) = 0$ , for some values of  $a$  the quench is necessarily made above the critical temperature. We will postpone the discussion on this matter in Sec. 6.4.2.2.

After quenching the system at time  $t = 0$  to a low final temperature  $T_f$ , we evolve the model using non-conserved dynamics [24, 25] of single spin flip via the Glauber transition rates [Eq. (1.17)]:

$$W(s_i \rightarrow -s_i) = \frac{1}{2} \left[ 1 - \tanh \left( \frac{\beta \Delta E}{2} \right) \right]. \quad (6.12)$$

## 6.4. Off-equilibrium Study of Growth Kinetics

---

Here,  $\Delta E$  is the change in energy resulting due to single spin-flip ( $s_i \rightarrow -s_i$ ). This can be obtained from the Hamiltonian in Eq. (6.1), i.e.,

$$\Delta E = 2s_i \sum_{j \in N_i} J_{ij} s_j, \quad (6.13)$$

$N_i$  refers to the set of NNs of site  $i$ . With this algorithm, we evolve the system as function of time upto  $10^7$  MCS and one MCS corresponds to attempted updates of  $N (= 512^2)$  spins in the lattice.

The main observable that we are interested is in the typical size of domains which grow as a function of time, i.e.,  $L(t)$ . We define it as the inverse of the excess energy

$$L(t) = N [\langle E(t) \rangle - E_\infty]^{-1}, \quad (6.14)$$

where  $\langle E(t) \rangle$  is the average value of energy as a function of time  $t$  and  $E_\infty$  is the average energy of the equilibrium state at  $T = T_f$ . The equilibrium state at  $T = T_f$  is obtained from the corresponding GS by evolving it at  $T = T_f$  until stationarity is achieved. For comparison, we have also found the equilibrium state directly by means of parallel tempering techniques. The values of  $E_\infty$  found with the two methods are consistent.

When the system has a simple FM or AFM order, as in pure or weakly disordered systems, the quantity in Eq. (6.14) can be straightforwardly identified with the size of the growing ordered regions or the domains. This is because in a coarsening process the interior of domains is in equilibrium and the excess energy is stored on the interface of domains, i.e., the *domain walls*, whose density scales as the inverse of typical domain size  $L(t)$  [24]. This can be derived from the simple arguments that the excess energy  $E(t) - E(\infty)$  is proportional to the total length of domains walls, which is given by the length of a single domain's boundary times the number of such domains. Now, the length of a single domain's boundary is  $\propto L(t)^{d-1}$  and the number of domains is  $\propto L^{-d}$ . This in turn yields that  $E(t) - E(\infty) \propto L(t)^{-1}$ , which therefore proves Eq. (6.14).

Of course, as we know that the most common method to measure the typical domain size is from the decay of the equal time real space spin-spin correlation function  $\langle s_i(t) s_{i+r}(t) \rangle$ , where  $i$  and  $i+r$  are two sites at distance  $r$ . However, this

## 6.4. Off-equilibrium Study of Growth Kinetics

---

definition can only be used in the FM phase. Analogously, in spin-glass phase, one might use the equal time overlap correlator  $\langle q_i(t)q_{i+r}(t) \rangle$ , where

$$q_i = s_i(t)s_i^{GS} \quad (6.15)$$

is the overlap with the GS ( $s_i^{GS}$  is the spin at site  $i$  in the GS). However, the result need not to be the same using different methods as explained below.

Consider a FM situation like the one of the GS at  $a = 0.4$  (upper right panel of Fig. 6.3) in which there are many islands with a finite extension. Then upon extracting a typical length from the correlation function at late times, one weights these many small islands, which at long times are already equilibrated (hence coarsening is interrupted in their interiors) together with a comparatively smaller number of large islands. The latter are the only non-equilibrated regions within which phase-ordering is still active. Instead, using Eq. (6.14) one only focuses on those parts of the system where coarsening is still active, since inside the small equilibrated islands  $E(t) \equiv E_\infty$  by definition. Hence, Eq. (6.14) is more suited to qualify how phase-ordering proceeds in the regions where it is still at work, while from the CF one obtains the average size of domains, irrespective of their state, weather in equilibrium or not. Since in this chapter we are more interested to address the dynamical mechanisms driving the kinetics, we focus on the definition in Eq. (6.14).

The difference between the value of  $L$  obtained from the definition of excess energy density in Eq. (6.14) or from the spin-spin CF can be appreciated by looking to the inset of the lower panel of Fig. 6.5. Here, for a quench to  $T_f = 0.75$ , the typical length-scale  $L(t)$  computed from Eq. (6.14) is plotted for several values of  $a$  in the main frame, while the one obtained from the spin-spin correlation is reported in the inset (only for values of  $a$  in the FM region). The latter determination grows much slowly than the former at  $a = 0.4$ , precisely because the ground states contains many small islands.

### 6.4.2 Numerical Results

We now present our numerical simulations on the growth kinetics for the temperature quench at  $T_f = 0.4$  and  $T_f = 0.75$ . The general behavior of  $L(t)$ , in

## 6.4. Off-equilibrium Study of Growth Kinetics

---

the whole range of values of  $a$ , is shown in Figs. 6.5(a) and (b), for  $T_f = 0.4$  and  $T_f = 0.75$ , respectively. Notice that we plot  $L(t)/L(t = 4)$  to better compare different  $L(t)$ -curves for different  $a$ .

As a general remark, we notice that at low temperature, such as for  $T_f = 0.4$  in Fig 6.5(a),  $L(t)$  exhibit an oscillating behavior on top of the *neat* growth (namely the kind of growth that one would have if such oscillations were smoothed out in some way). This is quite commonly observed in disordered or inhomogeneous systems at low  $T_f$  [6, 8, 26] and is usually interpreted as due to the stop and go mechanism due to the pinning of interfaces. As the final temperature of quench is raised, the stop and go mechanism, although still present, is less coherent, and the oscillations are smeared out. This can be observed in Fig 6.5(b) at  $T_f = 0.75$ . Moreover, the speed of ordering increases upon raising  $T_f$ , as it is expected in the presence of activated dynamics.

Let us check a rough estimate of the time taken by the system to escape from these pinning state of interfaces. Consider, e.g., the smallest energetic barrier  $E_B$  encountered by a piece of interface when it crosses from a single AFM bond to FM ones. This situation is likely to be observed when there are few AFM bonds around, namely for small  $a$ . In this case,  $E_B = J_+ - J_- = 2\epsilon$ . The associated Arrhenius time to escape the pinned state is  $\tau \simeq \exp(E_B/k_B T)$ . With the value  $\epsilon = 1.25$  in our simulations, one has  $\tau \simeq 518$  for  $T_f = 0.4$  and  $\tau \simeq 28$  for  $T_f = 0.75$ . One can see in Fig. 6.5 that, for  $T_f = 0.4$ , this value is very well compatible with the time where  $L(t)$ , after becoming very slow, starts growing faster again (a rough agreement is found also for  $T_f = 0.75$ , although in this case the oscillatory phenomenon is only hinted).

We now discuss separately the growth mechanism for quenches in the FM, PM, and AFM region, in sections 6.4.2.1, 6.4.2.2, and 6.4.2.3, respectively. Before discussing these, it is useful to define the effective growth exponent  $z_{\text{eff}}$ , used to interpret the behavior of growth, i.e.,

$$\frac{1}{z_{\text{eff}}(t)} = \frac{d[\ln L(t)]}{d[\ln t]}. \quad (6.16)$$



## 6.4. Off-equilibrium Study of Growth Kinetics

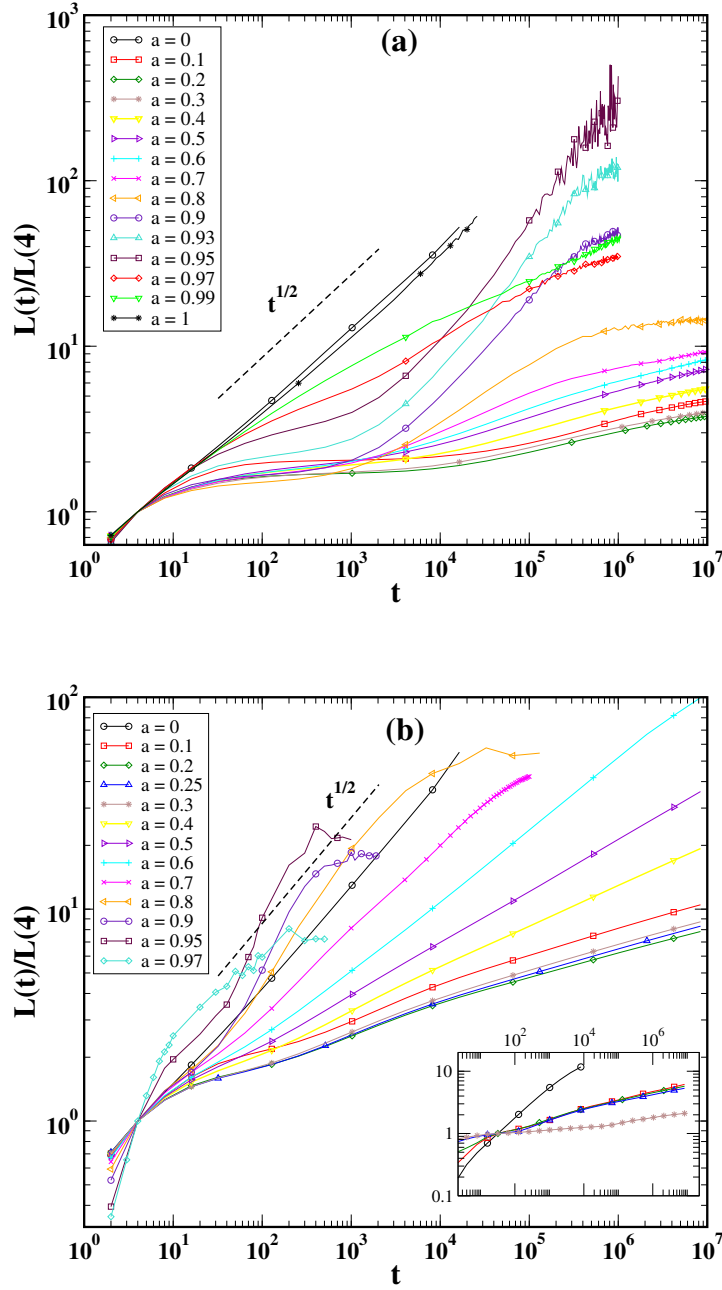


Figure 6.5: Log-log plot of  $L(t)$  vs  $t$  for the specified values of  $a$  for the temperature quench at (a)  $T_f = 0.4$  (upper panel) and (b)  $T = 0.75$  (lower panel). The dashed line denote the  $t^{1/2}$  power-law, which correspond to pure ferro- or antiferromagnets. The inset of the lower panel shows the behavior of the characteristic length extracted from the spin correlation function for the values of  $a$  restricted in the FM region (see text).

## 6.4. Off-equilibrium Study of Growth Kinetics

---

### 6.4.2.1 Ferromagnetic region $0 \leq a \leq a_f$

Fig. 6.6 shows the snapshots of the system's evolving morphologies at different times and for three different choices of  $a$  after a temperature quench to  $T_f = 0.4$ . For any value of  $a$ , one clearly observes a coarsening phenomenon with domains of the two phases growing in a self-similar way in time. Upon increasing  $a$ , domains look more jagged and indented, presumably due to the nearing of the critical point at  $a = a_f$  where a fractal structure is expected to appear.

Fig. 6.5 shows the general behavior of the growth mechanism. For  $a = 0$  (pure case), the growth is consistent with the expected behavior  $L(t) \propto t^{1/2}$ . As we introduce  $a$ , it slows down, but with increasing  $a$ , this occurs only up to a certain value, which we interpret as  $a = a^*$  and is located around  $a = 0.2$ . Upon increasing  $a$  beyond  $a^*$ , the phase-ordering process speeds up again, up to  $a_f$ . This is very well observed both for  $T_f = 0.4$  and  $T_f = 0.75$ . The value of  $a^*$ , at these two temperatures, is comparable, as it is expected since this quantity was previously defined in a purely geometrical way on the basis of bond-networks of the model.

This non-monotonous behavior of growth is consistent with the previous studies for the non-frustrated case [6–8], as we mentioned in the introduction. Specifically, these studies are for random-diluted models where  $d$  is the amount of disorder, meaning that a fraction  $d$  of lattice sites or bonds are randomly removed. It has been shown in these studies that as  $d$  increases from the pure case ( $d = 0$ ), the growth slows down logarithmically till a moderate value  $d^*$ . Then increasing  $d$  above  $d^*$ , the growth starts increasing again up to the largest possible value of  $d$ , namely the percolation threshold at  $d = d_c$ . For  $d > d_c$ , the fractal structure of the network becomes disconnected and the magnetic properties are lost, and hence, there will be no phase-ordering.

The interpretation of this non-monotonic behavior, given in Refs. [6–8], is the following: besides the pure case, where the speed of growth is at its maximum, the other network where  $L(t)$  grows relatively fast typically in an algebraic manner (but slower than in the pure case) is the percolation fractal at  $d = d_c$ . This is argued to be due to the critical properties of such network, which in turn are responsible for the fact that, right at  $d = d_c$ , the transition temperature of the

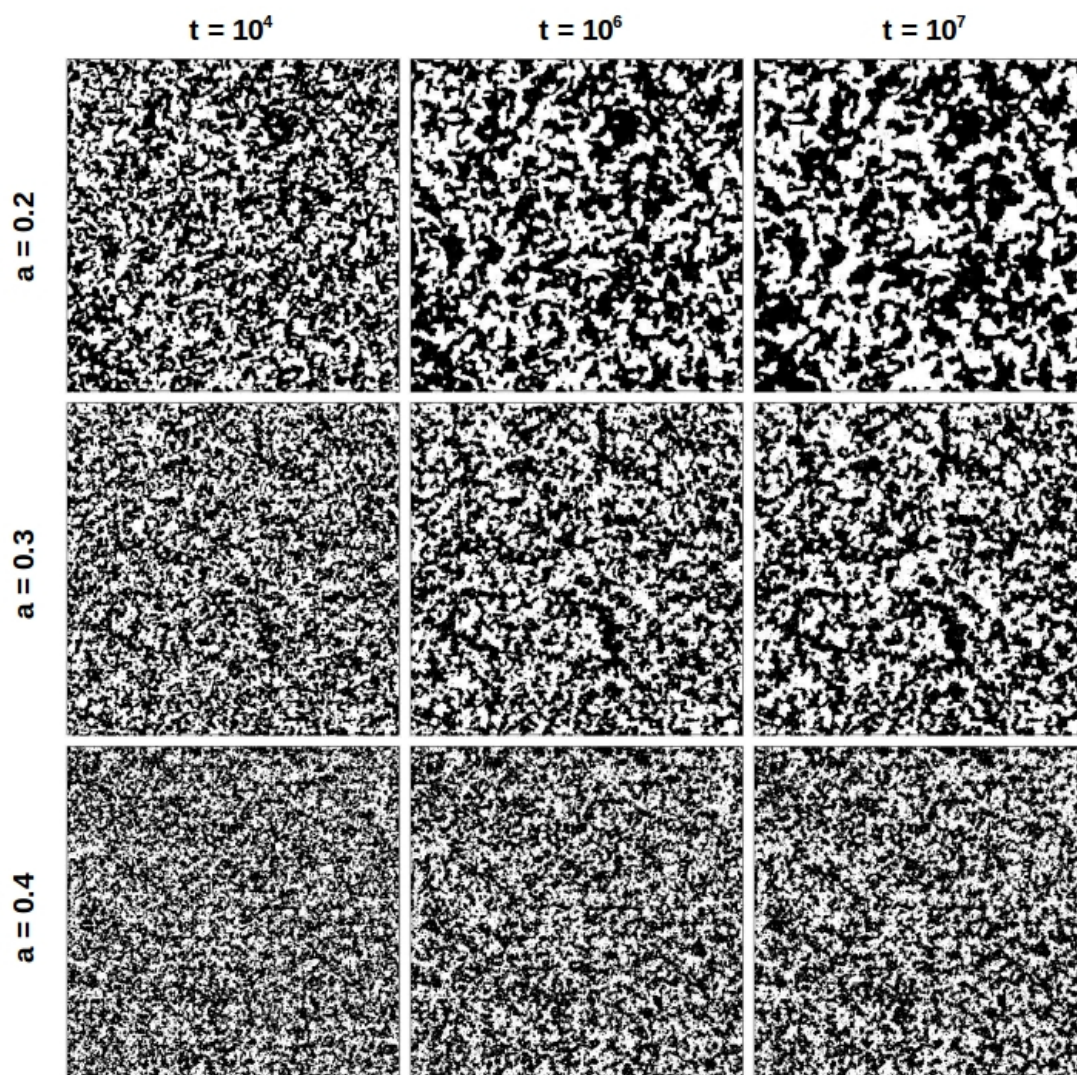


Figure 6.6: Evolution in the FM region for a quench to  $T_f = 0.4$ . These are  $\{s_i\}$ -configurations on a  $512^2$  lattice and shown for  $a = 0.2$  (upper row),  $a = 0.3$  (central row), and  $a = 0.4$  (lower row) at time  $t = 10^4$  (left column),  $t = 10^6$  (central column), and  $t = 10^7$  (right column).  $\{s_i\} = 1$  (up-spins) are marked in black and  $\{s_i\} = -1$  (down-spins) are marked in white.

## 6.4. Off-equilibrium Study of Growth Kinetics

---

model  $T_c(d = d_c)$  vanishes. Then, indeed, the fractal properties of the structure at  $d = d_c$  soften the energetic barriers, making in this way the evolution faster. Since the growth is globally and relatively maximum at  $d = 0$  and  $d = d_c$ , respectively, there must be a minimum somewhere in between. This value is  $d^*$  which is reported roughly in the middle of  $d = 0$  and  $d = d_c$ . This explains the non-monotonic behavior of growth.

Also in the present model the geometric properties of the system are such that there is a point, namely  $a = a_f$ , where  $T_c(a = a_f)$  vanishes<sup>1</sup>. Therefore, upon repeating the argument above (with the obvious replacements  $d \rightarrow a$  and  $d_c \rightarrow a_f$ ), one could expect the growth to be at its global maximum at  $a = 0$ , to decrease as  $a$  increases up to a value  $a^*$  located in between  $a = 0$  and  $a = a_f$ , and then to rise again up to  $a = a_f$ . This is precisely what we see in Fig. 6.5. The non-monotonic dependence of the speed of growth on the disorder, therefore, qualifies as a rather general property of ferromagnetic systems, and a common interpretation for different models can be provided.

Let us also mention a quantitative conjecture that Refs. [6–8] put forth: the asymptotic growth law is of the logarithmic type in the whole disordered region  $0 < d < d_c$ , while it ought to be algebraic  $L(t) \propto t^{1/z}$  both in the clean case  $d = 0$  (with  $z = 2$ ) and at  $d = d_c$  (with  $z > 2$  and  $T_f$ -dependent). As our present model also shows the non-monotonous behavior, one would expect an asymptotic logarithmic behavior (after a—possibly slow—crossover) in the range  $0 < a < a_f$ , and a power-law behavior of  $L(t)$  right at  $a = a_f$ . To test this conjecture, we compute the effective exponent  $z_{\text{eff}}$  as defined in Eq. (6.16). At  $T_f = 0.4$ , the oscillating nature of the curves shadow the genuine growth law, and it is therefore almost impossible to come up with any quantitative statement about the neat growth, e.g., if it consistent with a power-law or a logarithm or else. We check this conjecture for  $T_f = 0.75$ .

Fig. 6.7 shows the plot of  $z_{\text{eff}}$  for  $T_f = 0.75$ . For  $a = 0$ , it approaches the expected asymptotic value  $1/z_{\text{eff}} = 1/2$  starting from relatively early times  $t \simeq 10^3$ . Focus the  $z_{\text{eff}}$  at late time, as  $a$  is progressively increased from  $a = 0$  to  $a = 0.4 \simeq a_f$ , the effective exponent becomes initially smaller (in the range  $0 \leq a \leq a^* \simeq 0.2$ ) and then rises again (moving  $a$  in the range  $a^* \leq a \leq a_f$ ).

---

<sup>1</sup>Analogously the same occurs on AFM side at  $a = a_a$  which will be discussed later.

## 6.4. Off-equilibrium Study of Growth Kinetics

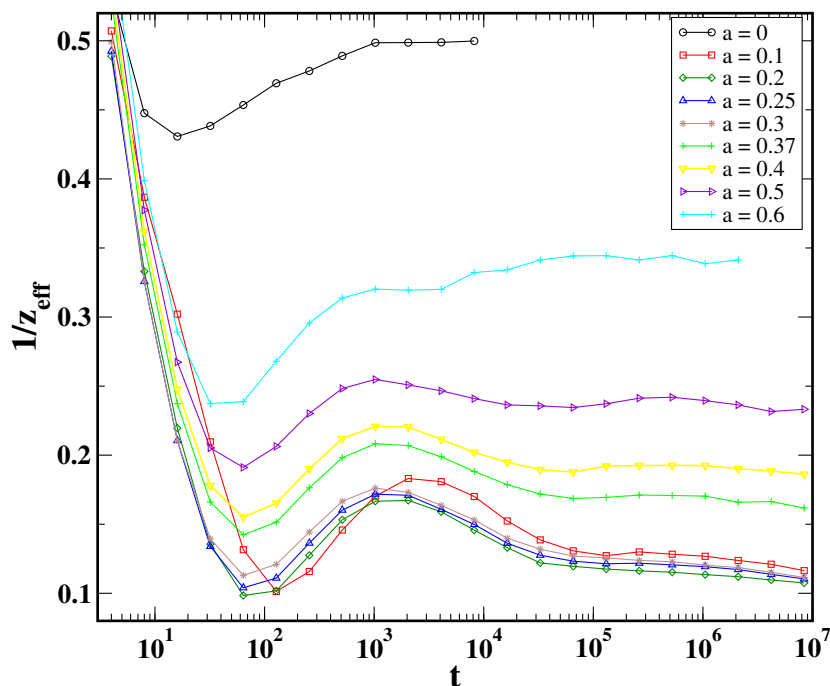


Figure 6.7: Log-linear plot of effective exponent  $1/z_{\text{eff}}(t)$  as a function of time for a quench at  $T = 0.75$ , for specified values of  $a$ .

Concerning the time dependence  $1/z_{\text{eff}}$ , our data clearly show that it keeps steadily decreasing in the late regime with  $t \gtrsim 10^4$  for all the values of  $a$  in the range  $0 < a \leq 0.3$ . The decrease is rather slow but reliable. This implies that the growth law of  $L(t)$  is slower than algebraic. Although the curves for  $L(t)$  span a vertical range that is too limited to allow a precise determination of such law (furthermore, a weak oscillation is present up to times of order  $10^4$ ), we can at least conclude that the decrease of  $1/z_{\text{eff}}$  agrees with the expectation of a logarithmic behavior. Data for  $a = 0.4 \simeq a_f$ , on the other hand, are quite well consistent with a constant behavior of  $1/z_{\text{eff}} \simeq 0.19$  at late times, and this also agrees with the conjecture discussed above. Finally, the effective exponent looks rather constant also for  $a = 0.37$ . This can be ascribed to the pre-asymptotic algebraic behavior induced by the proximity of the percolation point  $a = a_f$ . We expect, therefore, that a decrease of  $1/z_{\text{eff}}$  would also be observed for  $a = 0.37$  if sufficiently long times could be accessed in the simulations.

Notice that an algebraic law is also observed in the whole PM region. There-

## 6.4. Off-equilibrium Study of Growth Kinetics

---

fore, the different asymptotic behavior—i.e., algebraic versus logarithm—observed at  $a = a_f$  with respect to the rest of the FM region  $0 < a < a_f$  can also be interpreted upon thinking  $a_f$  as the lower limit of the PM region, where algebraic behaviors are observed. We will comment further on this point below.

### 6.4.2.2 Paramagnetic region $a_f < a < a_a$

In this region, we expect a kind of spin-glass order at  $T_f = 0$ . This can be appreciated at a qualitative level in Fig. 6.8 in which we plot the local overlap  $[q_i = s_i(t)s_i^{GS}]$ , as defined in Eq. (6.15) between the actual dynamical spin configurations and the GS, for different times after a quench to  $T_f = 0.4$ , and for three different choices of  $a$ . Interestingly, also in this PM phase, for any value of  $a$ , one clearly observes a coarsening phenomenon with domains of the two phases growing in a self-similar way in time, although quite slowly. This agrees with what was observed in Ref. [27]. Moreover, there is no signal of equilibration at any time, nor does the growth seems to be interrupted. As a further comment, we notice that configurations appear much more rugged for larger values of  $a$ .

In two-dimensional spin glasses (corresponding to  $J_0 = 0$  in our model) it was shown [27–29], that the existence of a spin-glass phase at  $T = 0$  rules the kinetic in a long lasting pre-asymptotic regime. It is found that as long as the pre-asymptotic stage is considered, a growing length can be identified which exhibits an algebraic behavior [27]. Clearly, from Fig. 6.5(b) for  $T_f = 0.75$ , one sees that data are consistent with an algebraic growth  $L(t) \propto t^{1/z}$ , with an  $a$ -dependent exponent, in agreement with the Ref. [27]. Data for  $a \geq 0.7$  clearly bend downwards at late times, indicating that equilibration is starting to be achieved.

The algebraic increase of  $L(t)$  can also be confirmed from inspection of the effective exponent  $z_{\text{eff}}$  in Fig. 6.7. This quantity stays basically constant, besides some noisy behavior, in the late time regime  $t \gtrsim 10^3$ - $10^4$ . Notice also that  $1/z_{\text{eff}}$  raises as  $a$  is increased. This can be ascribed, at least partly, to the fact that the largest barriers encountered are associated to the positive couplings (as  $J_+ \gg |J_-|$ ), and the number of the latter is reduced upon increasing  $a$ .

A power-law for  $L(t)$  in this PM region, as opposed to the logarithmic one in most disordered FM models, including the one at hand for  $0 < a < a_f$ , can

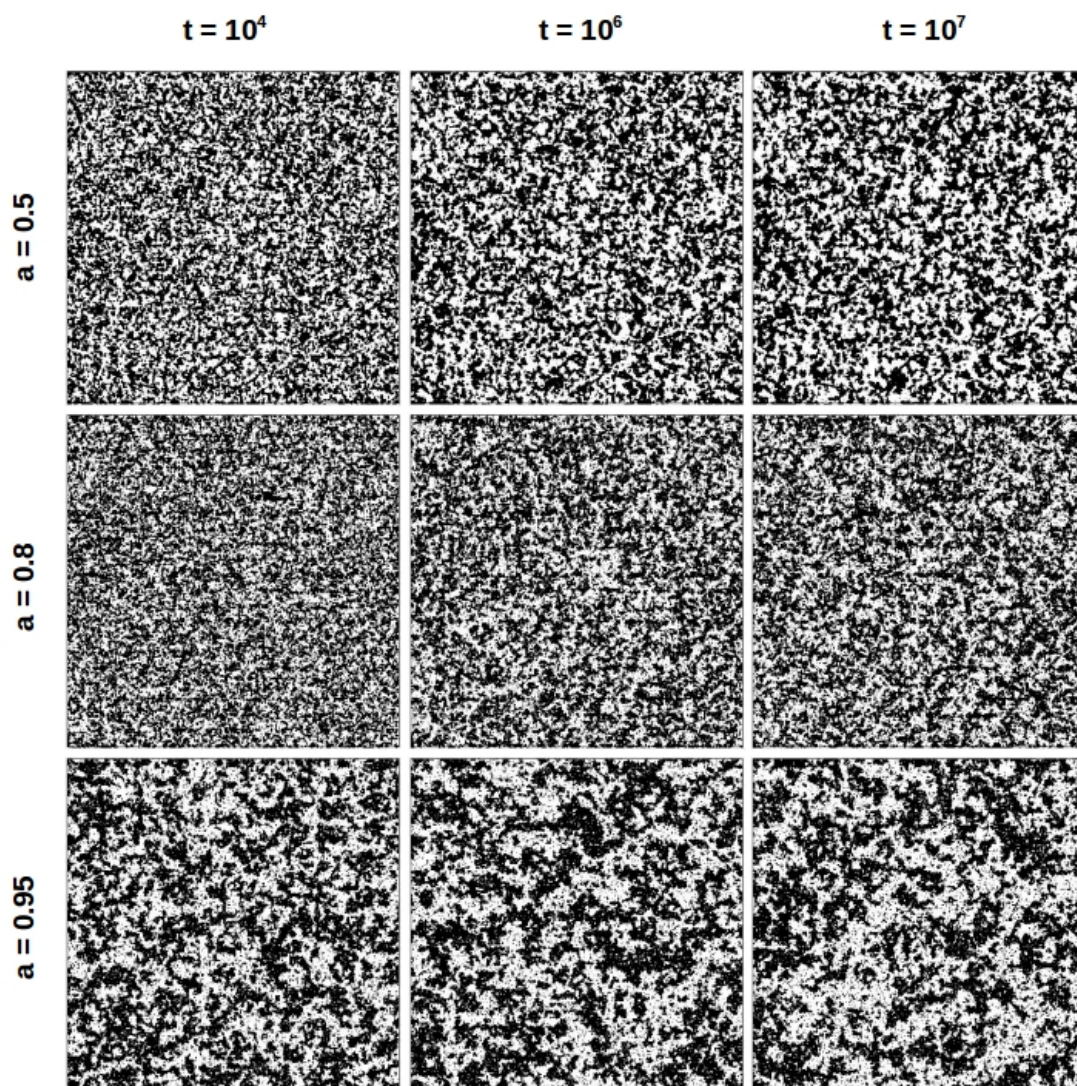


Figure 6.8: Evolution in the PM region in terms of overlap with the GS, i.e.,  $q_i = s_i(t)s_i^{GS}$  as defined in Eq. (6.15), for a quench to  $T_f = 0.4$ . Thus, these are the  $\{q_i\}$ -configurations on a  $512^2$  lattice and shown for  $a = 0.5$  (upper row),  $a = 0.8$  (central row), and  $a = 0.95$  (lower row) at time  $t = 10^4$  (left column),  $t = 10^6$  (central column), and  $t = 10^7$  (right column).  $\{q_i\} = 1$  are marked in black and  $\{q_i\} = -1$  are marked in white.

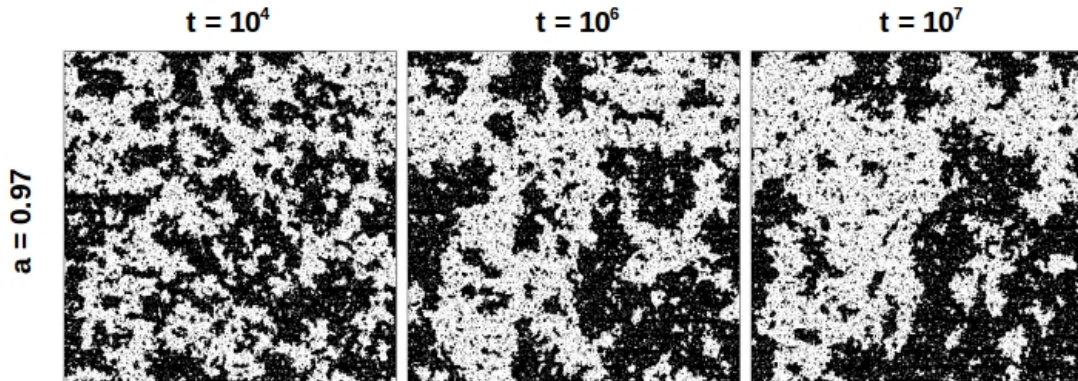


Figure 6.9: Evolution in the AFM region in terms of staggered spins, as defined in Eq. (6.11), for a quench to  $T_f = 0.4$ . Thus, these are the  $\{\sigma_i\}$ -configurations on a  $512^2$  lattice and shown for  $a = 0.97$  at time  $t = 10^4$  (left column),  $t = 10^6$  (central column), and  $t = 10^7$  (right column).  $\{\sigma_i\} = 1$  are marked in black and  $\{\sigma_i\} = -1$  are marked in white.

perhaps be read into the spin-glass structure, which has many quasi-equivalent low-energy states. Taking advantage of entropic effects, the system can move among these states lowering in this way the free-energy barriers. This could speed up the evolution from logarithmic to algebraic.

#### 6.4.2.3 Antiferromagnetic region $a \geq a_a$

In Fig. 6.9, we plot the configurations of the staggered spin  $\sigma_i$  [see Eq. (6.11)] at different times, which clearly show the coarsening phenomenon. In this region with AFM order we expect a situation mirroring the one discussed in the FM region, with the obvious correspondences  $a = 0 \leftrightarrow a = 1$ , and  $a = a_f \leftrightarrow a = a_a$ .

In this case  $T_c(a = 1) \simeq 0.567$ , as already discussed. Since  $T_f = 0.75 > T_c(a = 1)$ , there is no room left to observe coarsening for  $T_f = 0.75$  for any value of  $a < 1$  (indeed, in Fig. 6.5(b),  $L(t)$  flattens very soon, saturating to the equilibrium value). Let us then focus only the data for  $T_f = 0.4$  as shown in Fig. 6.5(a). Here, one observes the non-monotonic behavior of growth, like in the FM phase. Upon decreasing  $a$  from the pure antiferromagnet value  $a = 1$ , the growth kinetics quickly becomes much slower in going to  $a = 0.97$ , and then increases again until the upper limit of the PM phase is achieved at  $a = a_a \gtrsim 0.95$ .



## 6.5 Summary and Conclusion

Let us conclude this chapter with a summary and brief discussion of our results. We have studied numerically a frustrated case of two-dimensional RBIM where a fraction  $a$  of bonds are negative and the remaining ones are positive. Further, we made a choice that positive bonds  $J_+$  are stronger than the negative ones  $J_-$ . We have classified the low-temperature equilibrium states in different phases of the model as  $a$  is varied in the interval in the interval  $[0, 1]$ . This classification is presented on the basis of the values taken by the magnetization  $m$  and the staggered magnetization  $M$ . We have shown the existence of a FM and an AFM phase for  $a < a_f$  and  $a > a_a$ , respectively. In between, for  $a_f < a < a_a$ , there is a PM phase at any temperature  $T$ , presumably with a spin-glass order at  $T = 0$ .

Then, our main focus was on the off-equilibrium evolution of the model after a quench from an infinite temperature disordered state to low temperatures. We quenched the system at two different temperature  $T_f = 0.4$  and  $T_f = 0.75$ , and studied the coarsening phenomena on  $512^2$  lattices. The kinetics of growth is characterized by the typical domain's size  $L(t)$ . We have determined  $L(t)$  from the inverse of excess energy. The main results of this off-equilibrium study of evolution may be summarized as below.

- (a) The speed of growth varies in a non-monotonic way as the amount of disorder  $a$  is increased, similar to what was observed in other disordered ferromagnets [6–8]. Specifically, there exists a value  $a^* \sim 0.2$  where the kinetics is slower than for any other value of  $a$ .
- (b) We have been able to show that the growth law of  $L(t)$  is slower than algebraic, i.e., of a logarithmic type, in the whole FM region  $0 < a < a_f$  and AFM region  $a_a < a < 1$ . Interestingly enough, this is true both for  $0 \leq a < a^*$  and for  $a^* \leq a < a_f$ , though the FM structure of the equilibrium state at  $T = 0$  is different in these two sectors, as the system is a perfect ferromagnet (i.e.,  $m^2 = 1$  at  $T = 0$ ) in the former range while it contains a number of defects due to AFM inclusions in the latter (so that  $m^2 < 1$  at  $T = 0$ ).
- (c) In the PM region  $a_f < a < a_a$ , we find that  $L(t)$  grows algebraically in the

## 6.5. Summary and Conclusion

---

whole phase, irrespective of the fact that the geometrical properties of the bond network greatly changes as  $a$  is varied in  $[a_f, a_a]$ .

In conclusion, the non-monotonic dependence of the growth on disorder, which was already found in models of disordered magnets without frustration [6–8], extends its validity to the realm of frustrated systems. Therefore, it qualifies as a rather general property of FM systems, and a common interpretation of different models can be provided. The results of this chapter are pointing toward a general robustness.

## Appendix B

# Suppression of Ferromagnetic Order for $a \gtrsim a_f$

For  $a \gtrsim a_f$ , the amount of negative bonds is sufficient to spoil the FM order. This may happen, for instance, when the spanning sea of FM bonds have a thin part, like the horizontal path within the two dashed orange lines in the schematic Fig. B.1(a) on left side, along which spins cannot keep the same orientation without increasing the total energy. In the situation sketched, it is easy to check that the represented configuration, minimizes the energy.

This picture has been presented to easily grasp the properties of the GS, but it is not appropriate to describe the situation with  $a < a_p$ . Indeed, for such values of  $a$  there cannot be a spanning path of AFM bonds, while it is present in Fig. B.1(a) (along the dashed orange lines). However, one can easily check that the GS does not change if a certain fraction  $f \leq 1/q$  (in this case  $q = 4$ ) of the AFM bonds crossing the dashed orange lines are turned into FM ones. In this new situation there are no spanning clusters of AFM bonds, but the GS is still split into four pieces of different magnetization as schematically presented in Fig. B.1(a).

A computation of  $a_f$  looks very difficult, since this amount to evaluate the smallest probability  $a$  such that a spanning path formed by a fraction  $1 - f$  of AFM bonds exists. A rough estimation is the following. We know that at  $a = a_p$ , a spanning path of AFM bonds exists. If the probability is decreased to

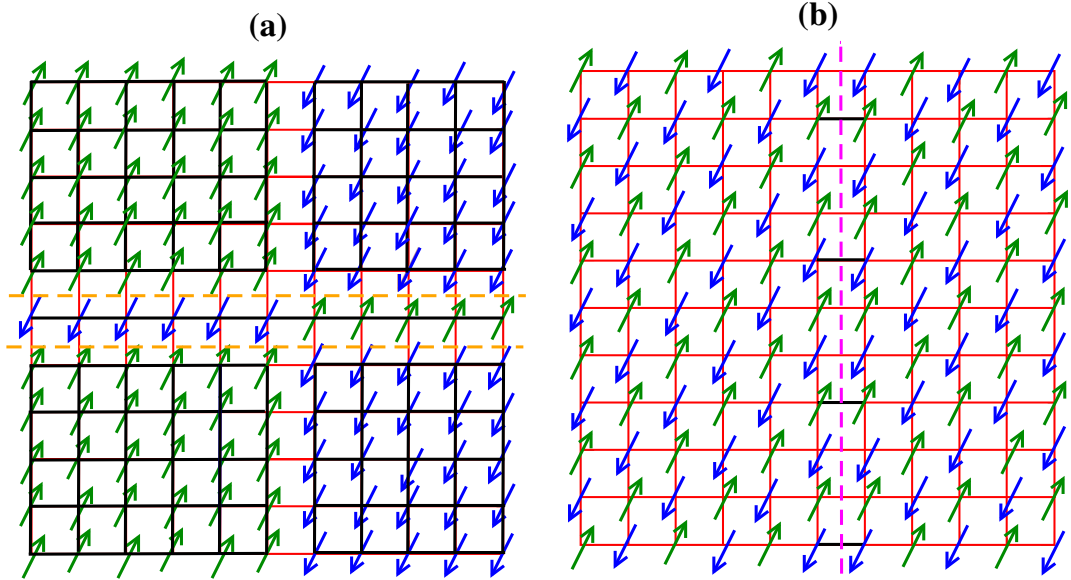


Figure B.1: Schematic representations of the ground states of the system in the regions (a)  $a_f < a < a_p$  (left) and (b)  $a_p < a < a_a$  (right). AFM and FM bonds are drawn in red and black, respectively. Spins up and down are colored in green and blue, respectively. In the left panel, the two dashed orange lines indicate paths of AFM bonds. In the right panel, the dashed magenta line is an interface in the AFM order.

$(1 - f)a_p$  when a fraction  $f$  of such AFM bonds convert into FM ones, then this gives  $a_f \simeq (1 - f)a_p$ . In our  $d = 2$  case, using  $f = 1/4$  and  $a_p = 0.5$ , it yields  $a_f \simeq 3/8 = 0.375$ , which can be compared with the observed value  $a_f \gtrsim 0.4$ .

# Appendix C

## Suppression of Antiferromagnetic Order for $a \lesssim a_a$

The reason why AFM order cannot establish up to fractions of negative bonds as large as  $a_a \simeq 0.95$  can be easily understood by looking at the schematic GS situation in Fig. B.1(b) on the right side. In this picture, it is seen that even a small amount of FM bonds can induce an interface (of the AFM type—marked by a dashed magenta line) in the system. Indeed, because the FM bonds are very strong, the removal of such an interface cost an higher energy. Clearly, the formation of the interface in Fig. B.1(b) becomes energetically unfavorable if the density of FM bonds (basically the distance between black bonds in Fig. B.1(b)) becomes too small. A rough estimation of the value of  $a$  where this occurs is the following.

The average distance between FM bonds is  $\lambda_f$ . It means that along an interface, such as the one plotted in Fig. B.1(b), there is a FM bond of strength  $J_+$  in every  $\lambda_f$  AFM ones (of strength  $J_-$ ). Hence, the interface cannot be sustained if  $\lambda_f|J_-| > J_+$ , namely for

$$(1 - a)^{-d} > \frac{J_+}{|J_-|}, \quad (\text{C.1})$$

where we have used Eq. (6.6). With our choice of  $J_+ = 2.25$  and  $J_- = -0.25$ , it predict the interface instability at  $a = a_a = 0.7$ . This is only a lower bound to the value of  $a_a$ , since it is clear that besides having condition (C.1) obeyed, other conditions must apply. For instance, an AFM bond must be guaranteed next to

---

the FM ones. Indeed, we see in Fig. 6.2 that the PM phase extends much beyond  $a = 0.7$ , at least up to  $a_a \sim 0.95$ .

# References

- [1] S. Puri, Phase Transitions **77**, 469 (2004).
- [2] F. Corberi, Comptes rendus - Physique **16**, 332 (2015).
- [3] F. Corberi, E. Lippiello, A. Mukherjee, S. Puri, and M. Zannetti, J. Stat. Mech. P03016 (2011).
- [4] H. Park and M. Pleimling, Phys. Rev. B **82**, 144406 (2010).
- [5] D. A. Huse and C. L. Henley, Phys. Rev. Lett. **54**, 2708 (1985).
- [6] F. Corberi, E. Lippiello, R. Burioni, A. Vezzani, and M. Zannetti Phys. Rev. E **91**, 062122 (2015).
- [7] F. Corberi, E. Lippiello, A. Mukherjee, S. Puri, and M. Zannetti, Phys. Rev. E **88**, 042129 (2013).
- [8] F. Corberi, E. Lippiello, and M. Zannetti, J. Stat. Mech. P10001 (2015).
- [9] F. Corberi, L. F. Cugliandolo, F. Insalata, and M. Picco Phys. Rev. E **95**, 022101 (2017).
- [10] E. Lippiello, A. Mukherjee, S. Puri and M. Zannetti, Europhys. Lett. **90**, 46006 (2010).
- [11] R. Paul, S. Puri and H. Rieger, Europhys. Lett. **68**, 881 (2004); Phys. Rev. E **71**, 061109 (2005).
- [12] J. H. Oh and D. Choi, Phys. Rev. B **33**, 3448 (1986).

- 
- [13] M. Henkel and M. Pleimling, Europhys. Lett. **76**, 561 (2006); Phys. Rev. B **78**, 224419 (2008);
- [14] A.G. Schins, A.F.M. Arts and H.W. de Wijn, Phys. Rev. Lett. **70**, 2340 (1993).
- [15] D. K. Shenoy, J. V. Selinger, K.A. Grüneberg, J. Naciri and R. Shashidhar, Phys. Rev. Lett. **82**, 1716 (1999).
- [16] H. Ikeda, Y. Endoh and S. Itoh, Phys. Rev. Lett. **64**, 1266 (1990).
- [17] V. Likodimos, M. Labardi, X. K. Orlik, L. Pardi, M. Allegrini, S. Emonin and O. Marti, Phys. Rev. B **63**, 064104 (2001); V. Likodimos, M. Labardi and M. Allegrini, Phys. Rev. B **61**, 14440 (2000).
- [18] F. Corberi, L. F. Cugliandolo, and H. Yoshino, in *Dynamical Heterogeneities in Glasses, Colloids, and Granular Media*, edited by L. Berthier, G. Biroli, J.-P. Bouchaud, L. Cipelletti, and W. Van Saarloos (Oxford University Press, Oxford, 2011).
- [19] C. Amoruso, E. Marinari, O. C. Martin, and A. Pagnani, Phys. Rev. Lett. **91**, 087201 (2003). T. Jorg, J. Lukic, E. Marinari, and O. C. Martin, Phys. Rev. Lett. **96**, 237205 (2006).
- [20] M. Mézard, G. Parisi, and M. A. Virasoro, *Spin glass theory and beyond*, World Scientific (Singapore 1987).
- [21] C. K. Thomas and A. A. Middleton, Physical Review B **76**, 220406, (2007).
- [22] H. Khoshbakht and M. Weigel, unpublished.
- [23] J. W. Landry and S. N. Coppersmith, Physical Review B **65**, 134404 (2002).
- [24] A.J. Bray, Adv. Phys. **43**, 357 (1994).
- [25] S. Puri, in *Kinetics of Phase Transitions*, edited by S. Puri and V. Wadhawan, CRC Press, Boca Raton (2009).



- [26] R. Burioni, D. Cassi, F. Corberi, and A. Vezzani Phys. Rev. E 75, 011113 (2007). Burioni, F. Corberi, and A. Vezzani, J. Stat. Mech. P02040 (2009); Phys. Rev. E **87**, 032160 (2013).
- [27] H. Rieger, G. Schehr, R. Paul, Prog. Theor. Phys. Suppl. **157**, 111 (2005).
- [28] H. Rieger, B. Steckemetz and M. Schreckenberg, Europhys. Lett. **27**, 485 (1994). J. Kisker, L. Santen, M. Schreckenberg and H. Rieger, Phys. Rev. B **53**, 6418 (1996). S. Franz, V. Lecomte, and R. Mulet, Phys. Rev. E **68**, 066128 (2003).
- [29] C. Chamon, F. Corberi, and L. F. Cugliandolo, J. Stat. Mech., P08015 (2011).

# Chapter 7

## Ordering Kinetics in the Random Bond XY Model

### 7.1 Introduction

In the previous chapters of the thesis, we have studied the systems in which spins are scalar variables. This chapter, instead, deals with vector spins. Particularly, we will study phase-ordering kinetics in disordered XY model. Considering the spins are the  $n$ -component vector quantities and  $d$  the dimensionality of the system, the topological defects are of dimension  $d - n$  [1]. Thus, their physical existence requires that  $n \leq d$ . For the case with scalar order-parameter, e.g., Ising spins, the topological defects are the domain walls, which are of dimension  $d - 1$ . For  $n = 2$ , e.g., XY model, these defects lie on the surface of dimension  $d - 2$ . For  $d = 2$ , these are point defects known as vortices and anti-vortices. In  $d = 3$ , these defects become vortex and anti-vortex lines. For  $n = 3$  and  $d = 3$ , the topological defects are monopoles [1].

The XY model has been widely studied in the literature. Experimentally, a large number of physical systems have been described by the XY model. For dimensionality  $d = 2$ , typical realizations of the XY model include magnetic films with planar anisotropy [2], thin-film superfluids or superconductors [3], Josephson-junction arrays [4, 5], hexatic liquid crystals [6], melting of two-dimensional solids [7], etc. In  $d = 3$ , physical systems such as superfluid  $^4\text{He}$  and planar spin

magnets have been described by the  $XY$  model. The critical behavior studies on 3D  $XY$  model [8–11] have shown that the  $\lambda$  transition in liquid  ${}^4\text{He}$  is in the same universality class with  $d = 3$   $XY$  model.

The  $XY$  model in  $d = 2$  exhibits the well-known *Berezinskii-Kosterlitz-Thouless* (BKT) transition at temperature  $T_{\text{KT}}$  [12–14]. At temperature  $T < T_{\text{KT}}$ , the model shows quasi-long-range order (QLRO), where the correlation-function decays as a power-law with temperature-dependent exponent  $\eta(T)$ . In this state, the morphology consists of bound states of vortex-antivortex pairs. At temperature  $T_{\text{KT}}$ , the vortex-antivortex pairs unbind and the correlation-function decays exponentially. The presence of quenched disorder has a strong effect on the BKT phase transition. For instance, various numerical studies [15–20] of the  $XY$  model with dilution (e.g., site-vacancies, bond-vacancies) have shown that  $T_{\text{KT}}$  decreases with increasing disorder. It becomes zero at a critical value of dilution, which is referred to as the percolation threshold. In  $d = 3$ , the  $XY$  model exhibits true long-range order (LRO) for  $T < T_c$  [21].

In this chapter, we are interested in the non equilibrium ordering kinetics of the disordered  $XY$  model subsequent to a quench from high  $T$ . When a pure  $XY$  system is quenched from high-temperature to low-temperature phase ( $T < T_{\text{KT}}$ ) or  $T < T_c$ , the coarsening process is characterized by the annihilation of vortex-antivortex pairs [22, 23]. The characteristic length scale  $R(t)$  typically grows as  $t^{1/2}$  for non-conserved vector fields in  $d \geq 3$  [24]. For  $d = 2$ , Yurke et al. [25] predicted a logarithmic correction to the diffusive growth as  $R(t) \sim (t/\ln t)^{1/2}$ , consistent with the previous works [26–28].

In recent years, there has been intense interest in the subject of domain growth in disordered systems. However, as we know, domain growth in disordered systems is not a trivial problem. In general, the domain boundaries become trapped at late times due to energy barriers introduced by the disorder, thereby slowing down the asymptotic domain growth-law [24]. Earlier studies on domain-growth in disordered Ising models (e.g., RFIM and RBIM) show a crossover from power-law growth to disorder-dominated logarithmic growth [29–36]. For RFIM, the crossover behavior has been clearly observed [29–35]. For RBIM, Corberi et al. [36] have performed a comprehensive numerical study in  $d = 2$  and observed a crossover from power-law growth in an intermediate-time regime to the log-

arithmetic growth in late time regime, but they were not able to determine the logarithmic growth-exponent.

However, the previous studies [37–39] does not even access the late-time logarithmic regime of domain growth. For instance, the RBIM study by Paul, Puri and Rieger [37] assumes that the energy barriers scale logarithmically with the domain size and they obtained an algebraic growth of domains with a disorder-dependent exponent, consistent with the other studies [38, 39]. Indeed, the power-law or algebraic growth has been found in an early study of a two-dimensional ferromagnetic system with random coupling [40]. Therefore, a clear understanding of domain-growth still requires more work regarding the existence of power law in the intermediate time regime.

In this chapter, we undertake the first study of a vector model with quenched disorder. Though, there have been many studies on phase-ordering kinetics in the pure  $XY$  model including its continuum version, i.e., the *time-dependent Ginzburg-Landau* (TDGL) model [1, 25, 26, 41–55], the ordering kinetics in disordered  $XY$  model still remains an open problem. Our aim is to study the *random-bond XY model* (RBXYM) where the quenched disorder is in the form of random coupling.

We perform an extensive, large-scale MC simulation of the RBXYM in  $d = 2, 3$ . Our study covers two important aspects. First, we study the effect of disorder on the transition temperature by using the Wolff cluster updating algorithm [56]. Second, we study ordering kinetics via the Metropolis algorithm [57] by quenching the system to a temperature below the transition temperature for all disorder values.

The main observations of our study are as follows:

- (a) The critical temperature is found to decrease with increasing disorder.
- (b) The correlation function shows dynamical scaling in  $d = 2$  and  $d = 3$ . Also, the scaling function is independent of disorder, and therefore shows a universal behavior. However, the superuniversality is found to be violated.
- (c) In  $d = 2$ , the growth law is power-law or algebraic with a disorder-dependent exponent.

- (d) In  $d = 3$ , the growth is slower than the power-law. But, our data is insufficient to further analyze the type of growth behavior.

This chapter is organized as follows. In Sec. 7.2, we introduce the model and present details of our numerical simulations. In Sec. 7.3, we present comprehensive numerical results from our simulations of the  $d = 2, 3$  RBXYM. Finally, in Sec. 7.4, we conclude this chapter with a summary and discussion of the results.

## 7.2 Modeling and Simulation Details

Recall the Hamiltonian for the RBXYM from Eq. (1.10), i.e.,

$$\mathcal{H} = - \sum_{\langle ij \rangle} J_{ij} \cos(\theta_i - \theta_j). \quad (7.1)$$

The quenched random-bond variables  $\{J_{ij}\}$  are drawn uniformly in the interval  $[1 - \epsilon/2, 1 + \epsilon/2]$ , where  $\epsilon$  quantifies the degree of disorder. The limit  $\epsilon = 0$  corresponds to the pure case ( $J_{ij} = 1$ ). Here, we focus on the ferromagnetic case where  $J_{ij} > 0$ . Therefore,  $\epsilon = 2$  corresponds to the maximum value of disorder.

### 7.2.1 Simulation Details for the Study of Critical Temperature

Before, we discuss nonequilibrium studies, it is important to understand the equilibrium properties of the RBXYM. In this context, let us discuss the simulation details for determining the critical temperature  $T_c$  (or  $T_{KT}$ ) in the presence of disorder ( $\epsilon$ ). For the pure  $XY$  model, the critical temperature is  $T_{KT} \simeq 0.89$  in  $d = 2$  [58–61] and  $T_c = 2.203$  in  $d = 3$  [8–10].

A standard tool to determine the transition temperature  $T_c(\epsilon)$  is the fourth-order Binder cumulant  $U_4(T, L)$  [20, 62–65], defined as<sup>1</sup>

$$U_4(T, L) = 1 - \frac{[\langle m^4 \rangle]}{3[\langle m^2 \rangle]^2}. \quad (7.2)$$

---

<sup>1</sup>In our earlier definition in Eq. (2.4), we have denoted the Binder-cumulant as  $U_4(\Delta, L)$  because there the critical point to be determined was the critical disorder  $\Delta_c$ . Presently, the critical point is  $T_c$ .

## 7.2. Modeling and Simulation Details

---

Here,  $m$  is the magnetization,  $\langle \dots \rangle$  and  $[\dots]$  denote the thermal and disorder averaging, respectively. The Binder cumulants  $U_4(T, L)$  are plotted against temperature  $T$  for different lattice sizes  $L$ . Then, in the scaling region near  $T_c$ , the Binder cumulant curves for different  $L$  have a unique intersection point [63], which is identified as  $T_c$ .

The magnetization  $m$  for the  $XY$  model is defined as

$$m = \frac{1}{N} \sqrt{\left(\sum_{i=1}^N \cos \theta_i\right)^2 + \left(\sum_{i=1}^N \sin \theta_i\right)^2}, \quad (7.3)$$

where  $N$  is the total number of sites, i.e.,  $N = L^d$ . The magnetization  $m$  is measured when the system has reached thermal equilibrium. To equilibrate the system at temperature  $T$ , we use the canonical sampling MC method with the Wolff cluster algorithm [56].

### *Wolff cluster algorithm*

A single MC update in the Wolff cluster algorithm can be described as follows:

- (i) Choose a random reflection  $\mathbf{r} = (\cos \phi, \sin \phi)$  and a random spin  $\mathbf{S}_i = (\cos \theta_i, \sin \theta_i)$  as the starting point for a cluster  $\mathcal{C}$  to be built.
- (ii) Flip  $\mathbf{S}_i \rightarrow R(\mathbf{r})\mathbf{S}_i = \mathbf{S}_i - 2(\mathbf{S}_i \cdot \mathbf{r})\mathbf{r}$ , i.e.,  $\theta_i \rightarrow \theta'_i = \pi - \theta_i + 2\phi$ .
- (iii) Visit all neighboring spins  $\mathbf{S}_j$  of  $\mathbf{S}_i$ , and add them to the cluster  $\mathcal{C}$  with the probability [56]

$$P(\mathbf{S}_i, \mathbf{S}_j) = 1 - \exp(\min[0, 2\beta J_{ij}(\mathbf{r} \cdot \mathbf{S}_i)(\mathbf{r} \cdot \mathbf{S}_j)]), \quad (7.4)$$

where  $\beta = (k_B T)^{-1}$ . In terms of the angle variables, the corresponding expression for the probability is

$$P(\theta_i, \theta_j) = 1 - \exp(\min[0, 2\beta J_{ij} \cos(\theta_i - \phi) \cos(\theta_j - \phi)]). \quad (7.5)$$

Then, flip  $\mathbf{S}_j$ , i.e.,  $\theta_j$ .

- (iv) Keep visiting all NNs of newly-added spins, add them to the cluster  $\mathcal{C}$  with probability  $P$  and flip them. Continue this process until no spin is left to add to  $\mathcal{C}$ .

### 7.2.2 Simulation Details for Study of Ordering Kinetics

Next, we study the ordering kinetics in the RBXYM by assigning a random initial orientation to each spin  $\theta_i \in (-\pi, \pi)$ , and rapidly quenching the system to  $T < T_c$  (or  $T_{KT}$ ) at time  $t = 0$ . The random initial condition mimics the high-temperature disordered state. We let the system evolve upto  $10^6$  MCS with the help of the Metropolis algorithm [57].

#### *Metropolis algorithm*

For the  $XY$  system, the Metropolis algorithm can be described as follows:

- (i) Select a random spin  $\theta_i$  and give it a small rotation  $\delta \in (-0.1, 0.1)$ , i.e.,  $\theta_i \rightarrow \theta'_i = \theta_i + \delta$ .
- (ii) The new spin  $\theta'_i$  is accepted with the probability

$$P = \min [1, \exp(-\beta\Delta\mathcal{H})]. \quad (7.6)$$

Here,  $\Delta\mathcal{H}$  is the change in energy resulting from the spin change  $\theta_i \rightarrow \theta'_i$  given by

$$\Delta\mathcal{H} = \sum_{j \in N_i} J_{ij} \{ \cos(\theta_i - \theta_j) - \cos(\theta'_i - \theta_j) \}. \quad (7.7)$$

Here,  $N_i$  refers to the NNs of site  $i$ .

### *Characterization of phase ordering*

As we know, a useful quantity to characterize phase ordering kinetics is the correlation function, defined as

$$C(\mathbf{r}, t) = \frac{1}{N} \sum_{i=1}^N \left[ \langle \mathbf{S}_i(t) \cdot \mathbf{S}_{i+\mathbf{r}}(t) \rangle - \langle \mathbf{S}_i(t) \rangle \cdot \langle \mathbf{S}_{i+\mathbf{r}}(t) \rangle \right], \quad (7.8)$$

$$= \frac{1}{N} \sum_{i=1}^N \langle \cos \{ \theta_i(t) - \theta_{i+\mathbf{r}}(t) \} \rangle, \quad (7.9)$$

where  $\langle \dots \rangle$  indicates the averaging over different realizations of bond randomness. Also we know from Sec. 1.5.1, the correlation function possess a dynamical scaling form:  $C(\mathbf{r}, t) = f(r/R)$ , when the system is isotropic and characterized by a single length scale  $R(t)$ . The corresponding dynamical scaling form for structure factor is  $S(k, t) = R(t)^d g(kR(t))$ . Bray and Puri [24], and Toyoki [66] have independently proposed that for a  $n$ -component vector field without disorder, the scaling function  $g(x)$  has the large- $x$  behavior:  $g(x) \sim x^{-(d+n)}$  for  $x \rightarrow \infty$ . This is usually referred to as the *generalized Porod tail*.

The characteristic length scale  $R(t)$ , we define, as the distance at which the correlation function decays to (say) 0.2 of its maximum value, i.e.,  $C(R, t) = 0.2$ . In the  $XY$  model, typical length-scale can also be determined from the density of topological defects [42, 43],  $\rho_{\text{def}}(t) = 1/L_v(t)^2$ , where  $L_v$  is the vortex-length or a measure of typical length-scale. However in the scaling regime, this definition will differ from the former one only by a prefactor and asymptotically both yield the same growth-law. We use the  $R(t)$  determined from the decay of correlation-function  $C(r, t)$  as this definition gives the much better scaling of  $C(r, t)$  [42, 43].

Before we present the numerical results of our simulations, let us review the physical arguments for the growth law in the pure  $XY$  model.

### 7.2.3 Growth Law for Pure XY Model

*In  $d = 2$*

Consider a single vortex-antivortex (defect) pair separated by a distance  $r$  with  $a$  as the dimension of the vortex-core. For a  $n$ -component vector model in  $d$



## 7.2. Modeling and Simulation Details

---

dimensions, the topological defects are lying on a surface of dimension  $d - n$  and therefore, the volume of the defect-core scales as  $r^{d-n}$  [1, 67]. For the XY model (as  $n = 2$ ), in  $d = 2$  the core-volume is a dimensionless constant. The defect pair energy  $E_p(r) \sim \ln(r/a)$  [1, 67, 68] and hence, the driving force per unit core-volume, which is responsible for the annihilation of the vortex-antivortex pair, is

$$F(r) = -\frac{dE_p}{dr} \sim -\frac{1}{r}. \quad (7.10)$$

The annihilation time of the defect pair is governed by the vortex mobility  $\mu$ , which depends logarithmically on the pair separation, i.e.,  $\mu \sim [\ln(r/a)]^{-1}$  [1, 67, 68]. As the mobility is related to the velocity via  $v = \mu F$ , we have

$$\frac{dr}{dt} \sim -\frac{1}{r \ln(r/a)}. \quad (7.11)$$

For a pair separated by a large distance  $r_0 \gg a$ , integrating this equation gives the annihilation time  $t \sim r_0^2 \ln(r_0/a)$ . This can be inverted to obtain

$$r_0 \sim \left[ \frac{t}{\ln(t/a^2)} \right]^{1/2}. \quad (7.12)$$

If one considers a characteristic length scale as  $R(t)$  in many vortex system, Eq. (7.12) yields the growth law  $R(t) \sim (t/\ln t)^{1/2}$  for pure XY model in  $d = 2$ .

### **In $d = 3$**

The topological defects are of dimension 1, i.e., strings. Thus, the defect pair energy  $E_p(r) \sim r \ln(r/a)$ , where we have included a factor of  $r$  for the defect-core volume. Then, the vortex force per unit defect-core volume typically scales as  $-\ln(r/a)/r$ . The relation  $v = \mu F$  gives

$$\frac{dr}{dt} \sim -\frac{1}{r}, \quad (7.13)$$

so that  $r(t) \sim t^{1/2}$ . Again, if one considers a characteristic length scale as  $R(t)$  in many vortex system, it yields the growth law  $R(t) \sim t^{1/2}$ .

## 7.3 Numerical Results

Now, we will present numerical results from our simulations of the  $d = 2, 3$  RBXYM. We consider the disorder values  $\epsilon = 0, 0.5, 1.0, 1.5$  and  $2.0$ — $\epsilon = 0$  is the pure case, and  $\epsilon = 2$  corresponds to the case with maximum disorder. First, we determine the transition temperature  $T_c(\epsilon)$  (or  $T_{\text{KT}}$ ). Then, we study ordering kinetics by quenching the system below  $T_c(\epsilon)$ .

### 7.3.1 Numerical Results for $d = 2$ RBXYM

#### 7.3.1.1 Estimation of transition temperatures

Let us first consider the  $d = 2$  RBXYM. We study this system on a square lattice ( $L^2$ ) of linear sizes  $L = 96, 128, \text{ and } 256$ . Starting from a random initial configuration, we let the system equilibrate using the Wolff cluster update algorithm. After equilibration, we measure  $m^2$  and  $m^4$  upto  $6 \times 10^5$  MCS, and do the disorder averaging over 200 independent runs of random-bond configurations. Then, one can determine the Binder cumulant  $U_4(T, L)$  from Eq. (7.2).

Figure 7.1 is a plot of  $U_4$  vs.  $T$  for  $\epsilon = 1.0$ . (We have zoomed in of the plot in the vicinity of  $T_{\text{KT}}$ .) The transition temperature ( $T_{\text{KT}}$ ) is estimated from the intersection of Binder cumulant curves for different  $L$ . The  $T_{\text{KT}}$ -values for various  $\epsilon$  are plotted in the inset of Fig. 7.1, and tabulated in Table 7.1. For the pure case ( $\epsilon = 0$ ), we found  $T_{\text{KT}} = 0.902 \pm 0.002$ , which is consistent with the expected value  $T_{\text{KT}} \simeq 0.893$  in the literature [13, 14, 58, 59]. With increasing  $\epsilon$ ,  $T_{\text{KT}}$  decreases from  $T_{\text{KT}} \simeq 0.902$  to  $T_{\text{KT}}(\epsilon = 2) = 0.729 \pm 0.007$ .

#### 7.3.1.2 Ordering kinetics

Next, we present numerical results for coarsening and domain growth-law in the  $d = 2$  RBXYM. The simulations are performed on a square lattice of size  $1024^2$  with periodic boundary conditions applied on both sides. After assigning a random initial orientation to each spin mimicking the high-temperature phase, the system is quenched at temperature  $T = 0.5$  and evolved upto  $t = 10^6$  MCS with the help of the Metropolis algorithm. Clearly, the quench temperature  $T = 0.5$  is

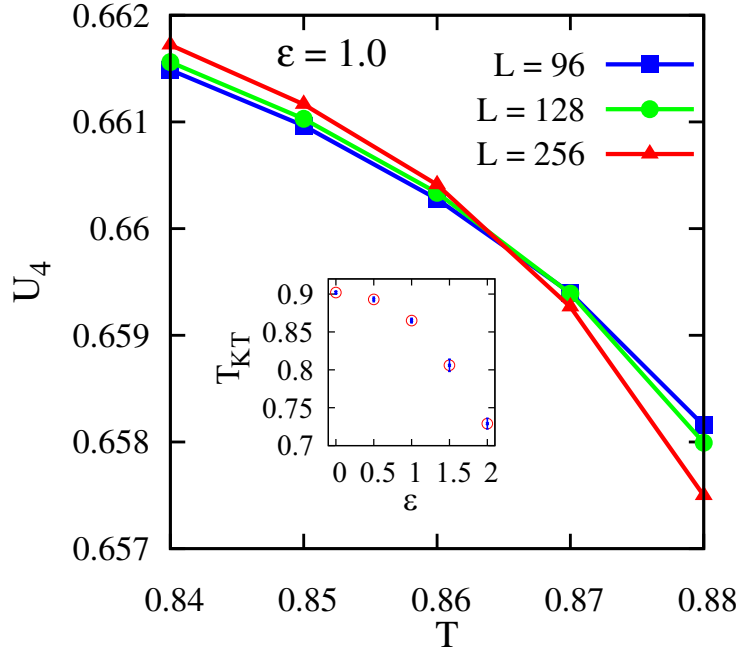


Figure 7.1: Plot of fourth-order Binder cumulant ( $U_4$ ) vs. temperature ( $T$ ) for  $d = 2$  RBXYM for  $\epsilon = 1.0$  and lattice-size  $L = 96, 128, 256$ . The critical temperature  $T_{KT}$  is determined from the intersection of different  $L$  curves. The inset shows the plot of  $T_{KT}$  with disorder  $\epsilon$ .

below the critical temperature  $T_{KT}$  for all  $\epsilon$ . All statistical results presented here are averaged over 20 independent runs (sometimes more) of  $\{J_{ij}\}$ -configurations.

In Fig. 7.2, we show the typical evolution snapshots for a temperature quench<sup>1</sup> at  $T = 0.2$ . The snapshots correspond to  $t = 10^6$  MCS and disorder amplitudes  $\epsilon = 0, 1, 2$ . We show the colormap plots of morphologies, where different shades in the colorbar correspond to the spins  $\theta_i$ 's. These colormap plots clearly show an increase in defect density with disorder, corresponding to slowing down of domain growth. In Fig. 7.3, we show vector plots in which we draw a unit vector

<sup>1</sup>Notice that, here, we show the evolution morphologies for a low temperature quench at  $T = 0.2$ , to realize better visualization of the morphological structures and the topological defects.

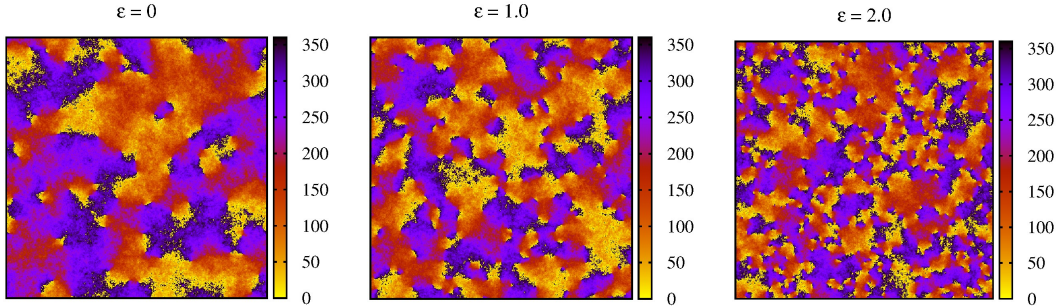


Figure 7.2: Evolution snapshots of RBXYM at time  $t = 10^6$  MCS after a quench from  $T = \infty$  to  $T = 0.2$  for  $\epsilon = 0, 1, 2$ . The lattice size is  $512^2$  lattice. These are the colormap plot of the spin configuration  $\{\theta_i\}$ , where the different shades in the colorbar correspond to the spins  $\theta_i \in (0, 360^\circ)$ .

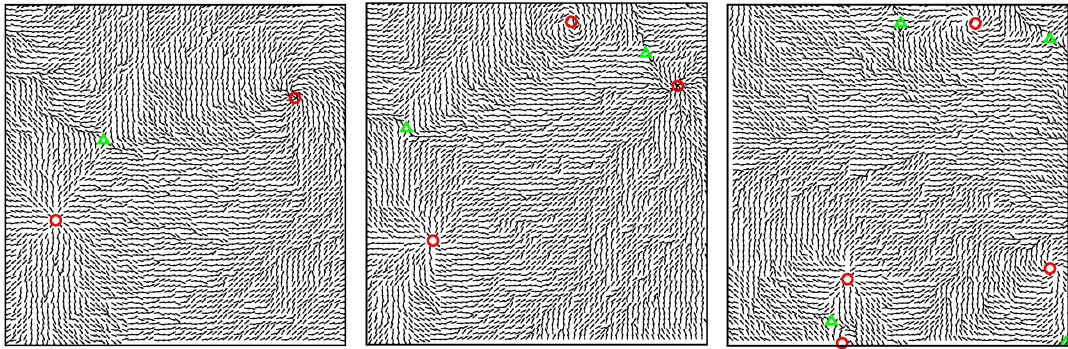


Figure 7.3: Vector plots for  $\{\theta_i\}$ -configurations in Fig. 7.2. At each lattice site, we draw a vector corresponding to  $S_i = (\cos \theta_i, \sin \theta_i)$ . For a better view, we show only a  $64^2$  corner of the  $1024^2$  lattice. Red-circles denote vortices and green-triangles denote antivortices, respectively.

for each spin  $\mathbf{S}_i = (\cos \theta_i, \sin \theta_i)$ . For a better visualization of vectors, we have shown only a  $64^2$  portion of  $512^2$  lattice in Fig. 7.2. Vortices and anti-vortices are marked by red circles and green triangles, respectively. These are characterized by calculating the net change in spin direction on a square plaquette. A vortex is identified if a spin rotates through  $2\pi$ , and an anti-vortex is identified if a spin rotates through  $-2\pi$ .

In Figs. 7.4(a) and (b), we plot the scaled forms of (a) the correlation function,  $C(r, t)$  vs.  $r/R$ ; and (b) the structure factor,  $S(k, t)R^{-3}$  vs.  $kR$ , respectively. We have confirmed (not shown here) that the data sets for a fixed value of  $\epsilon$  and different times show a good data collapse. Thus, dynamical scaling holds for each

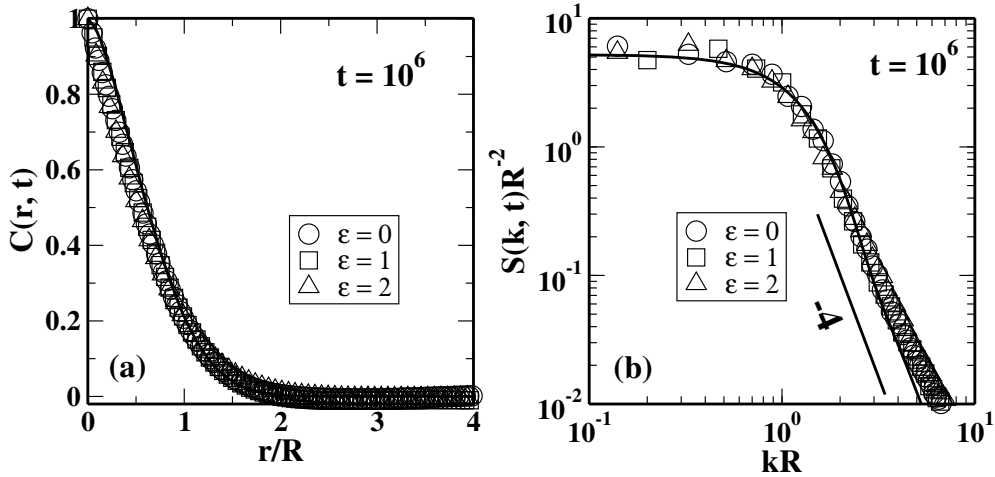


Figure 7.4: (a) Scaled correlation functions,  $C(r, t)$  vs  $r/R(t)$ , for the evolution of RBXYM after a quench at  $T = 0.5$ . We plot the data at a fix  $t = 10^6$  MCS for  $\epsilon = 0, 1, 2$ . (b) The corresponding scaled structure factors,  $S(k, t)R(t)^{-2}$  vs  $kR$ . The solid curves in (a) and (b) is the Bray-Puri-Toyoki (BPT) function in Eq. 7.14 for  $n = 2$  and its Fourier transform, respectively. A line of slope  $-4$  denotes the generalized Porod law:  $S(k, t) \sim k^{-(d+n)}$  for  $d = n = 2$ .

value of  $\epsilon$ . In Fig. 7.4, we check for the robustness of this scaling function by plotting scaled data at  $t = 10^6$  MCS for  $\epsilon = 0, 1, 2$ . The solid curve in Fig. 7.4(a) is a plot of the Bray-Puri-Toyoki (BPT) function [24, 66] for  $n = 2$ , which is an analytical result for ordering dynamics of the  $\mathcal{O}(n)$  model, i.e.,

$$f_{BPT}(r/R) = \frac{n\gamma}{2\pi} \left[ B\left(\frac{n+1}{2}, \frac{1}{2}\right) \right]^2 F\left(\frac{1}{2}, \frac{1}{2}; \frac{n+2}{2}; \gamma^2\right), \quad (7.14)$$

where  $\gamma = \exp(-r^2/R^2)$ . In Eq. (7.14),  $B(x, y) \equiv \Gamma(x)\Gamma(y)/\Gamma(x+y)$  is the beta function, and  $F(a, b; c; z)$  is the hypergeometric function. In Fig. 7.4(b), the solid curve is the Fourier transform of the BPT function, and the line of slope  $-4$  denotes the generalized Porod law:  $S(k, t) \sim k^{-(d+n)}$  for  $d = 2, n = 2$ . The data collapse confirms that the scaling function is independent of the disorder amplitudes. Therefore, this shows the universality of the scaling function, which is also found in earlier studies on the RBIM [37] and other system with quenched disorder such as binary alloys [69] or spinodal decomposition [70].

In order to check the validity of superuniversality (SU), we calculate two-time

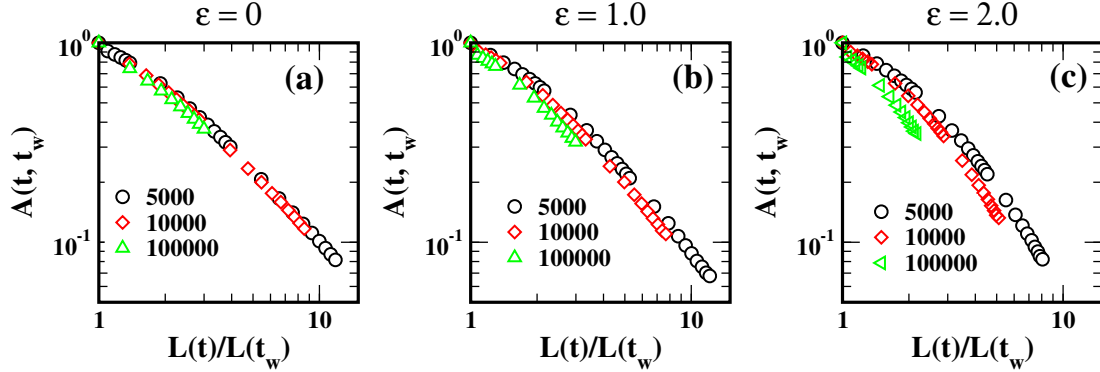


Figure 7.5: Plot of the auto-correlation function  $A(t, t_w)$  vs.  $R(t)/R(t_w)$  for (a)  $\epsilon = 0$ , (b)  $\epsilon = 1.0$ , and (c)  $\epsilon = 2$ . We plot data for the specified value of waiting time  $t_w = 5 \times 10^3, 10^4, 10^5$ . Clearly, the data for  $\epsilon = 2$  is not collapsing, showing a violation of superuniversality.

autocorrelation function  $C(t, t_w)$  defined as

$$\begin{aligned} A(t, t_w, \epsilon) &= \langle \mathbf{S}_i(t, \epsilon) \cdot \mathbf{S}_i(t_w, \epsilon) \rangle \\ &= \langle \cos(\theta_i(t, \epsilon) - \theta_i(t_w, \epsilon)) \rangle, \end{aligned} \quad (7.15)$$

where  $t_w \leq t$  is the waiting time and  $\langle \dots \rangle$  denotes ensemble averaging. According to the SU hypothesis [71],  $A(t, t_w, \epsilon)$  should obey

$$A(t, t_w, \epsilon) = G \left[ \frac{R(t, \epsilon)}{R(t_w, \epsilon)} \right], \quad (7.16)$$

where  $G$  is a scaling function. Fig. 7.5 shows the plot of autocorrelation function,  $A(t, t_w)$  vs  $R(t)/R(t_w)$ , for  $\epsilon = 0, 1, 2$ , for different values of waiting times  $t_w = 5 \times 10^3, 10^4, 10^5$  MCS. Clearly, the data for  $\epsilon = 2$  in Fig. 7.5(c) shows the effect of disorder, which depicts that two-time autocorrelation function has an explicit disorder dependence. Hence, the system doesn't obey SU in agreement with the SU violation behavior observed in the RBIM [36] and the RFIM [35].

The most important characteristic of a domain growth process is the growth law of the characteristic length scale  $R(t)$ . We define it as the distance at which the correlation function  $C(r, t)$  falls to 0.2 of its maximum value. Fig. 7.6(a) shows the plot of  $R(t)$  vs.  $t/\ln t$  on a log-log scale for different  $\epsilon$ -values. This

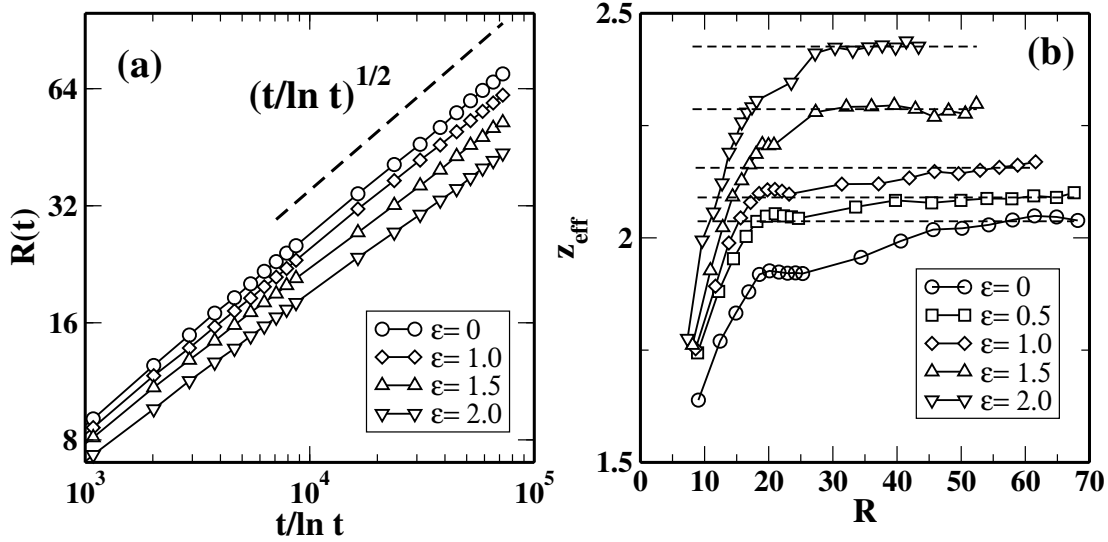


Figure 7.6: (a) Plot for domain growth  $R(t)$  vs.  $t/\ln t$  on a log-log scale for the specified values of  $\epsilon$ . The dashed line is of slope 0.5, which indicates the growth law for pure case  $R(t) \sim (t/\ln t)^{1/2}$ . (b) Plot of the effective exponents,  $z_{\text{eff}} = [d(\ln R)/d(\ln[t/\ln t])]^{-1}$  vs.  $R(t)$  for various  $\epsilon = 0, 0.5, 1.0, 1.5, 2.0$ . The dashed-lines to each curves indicates the disorder-dependent growth-exponent  $\bar{z}(\epsilon)$ .

plot is motivated by the logarithmic correction in the domain growth-law for the pure case. The dashed line denotes the power-law growth for the pure-case:  $R(t) \sim (t/\ln t)^{1/2}$  [26, 42, 67]. One can observe a slower growth at large time in the presence of disorder. The data sets in Fig. 7.6(a) suggest a power-law (over three decades of  $t$ ) with a disorder dependent exponent:

$$R(t) \sim \left(\frac{t}{\ln t}\right)^{\vartheta(\epsilon)} \simeq \left(\frac{t}{\ln t}\right)^{1/\bar{z}(\epsilon)}. \quad (7.17)$$

[Before proceeding, we should stress that the log-log plot of  $R(t)$  vs.  $t$  in the same time-window is also consistent with a power-law behavior. The only difference from Fig. 7.6(a) is that the effective exponent  $\bar{\vartheta}(\epsilon)$  is reduced by the logarithmic correction. We need at least five decades of data to differentiate the growth law between  $t^{\bar{\vartheta}}$  and  $(t/\ln t)^{\bar{\vartheta}}$ .]

For a qualitative study of the growth law, we determine the effective growth-

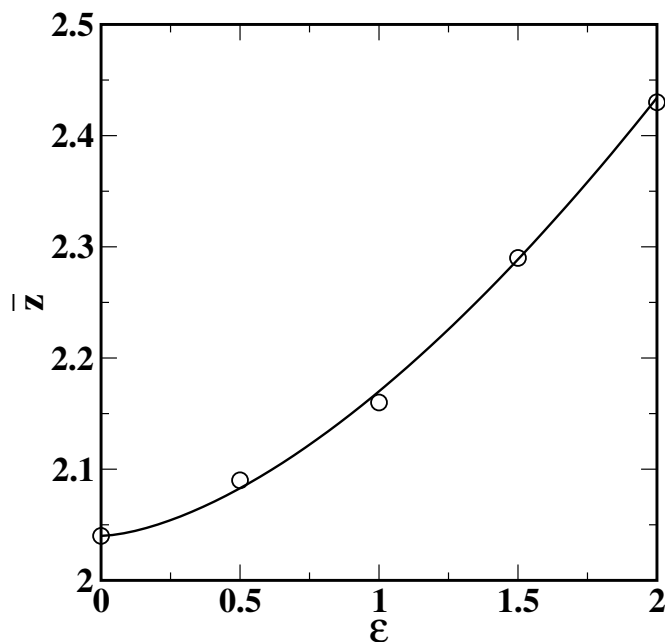


Figure 7.7: Plot of the disorder-dependent growth-exponent  $\bar{z}(\epsilon)$  vs  $\epsilon$ . The solid line is the best fit:  $\bar{z} = 2.03 + 0.13\epsilon^{1.16}$ .

exponent, defined as

$$\frac{1}{z_{\text{eff}}} = \frac{d[\ln R(t)]}{d\left[\ln\left(\frac{t}{\ln t}\right)\right]}. \quad (7.18)$$

In Fig. 7.6(b), we plot  $z_{\text{eff}}$  vs  $R(t)$  for the data in Fig. 7.6(a). This plot clearly shows an extended flat regime upto the time-scale ( $10^6$  MCS) of our simulation. This shows the algebraic-growth with disorder-dependent exponent, i.e.,  $R(t) \sim (t/\ln t)^{1/\bar{z}(\epsilon)}$ , which is in agreement with earlier studies on disordered Ising models [37–39]. The straight horizontal dashed-lines correspond to the disorder-dependent growth exponent  $\bar{z}(\epsilon)$ , which we tabulate in Table 7.1 and plot in Fig. 7.7. The solid line in Fig. 7.7 denotes the best fit:  $\bar{z} = 2.03 + 0.13\epsilon^{1.16}$ .

### 7.3.2 Numerical Results for $d = 3$ RBXYM

Now, we briefly present results for the  $d = 3$  RBXYM. As in the  $d = 2$  case, first we determine the transition temperature  $T_c(\epsilon)$ . Then, we study the phase ordering kinetics after quenching the system below  $T_c(\epsilon)$ .



$\epsilon$	$T_{\text{KT}}$	$\bar{z}$
0.0	$0.902 \pm 0.002$	$2.04 \pm 0.01$
0.5	$0.893 \pm 0.003$	$2.09 \pm 0.01$
1.0	$0.865 \pm 0.003$	$2.16 \pm 0.02$
1.5	$0.806 \pm 0.008$	$2.29 \pm 0.04$
2.0	$0.729 \pm 0.007$	$2.43 \pm 0.03$

Table 7.1: Critical temperature  $T_{\text{KT}}$  and growth-exponent  $\bar{z}$  for  $d = 2$  RBXYM.

$\epsilon$	$T_c$
0.0	$2.202 \pm 0.001$
0.5	$2.198 \pm 0.004$
1.0	$2.181 \pm 0.001$
1.5	$2.151 \pm 0.005$
2.0	$2.114 \pm 0.006$

Table 7.2: Transition temperature  $T_c$  for  $d = 3$  RBXYM.

### 7.3.2.1 Estimation of transition temperatures

To determine  $T_c(\epsilon)$ , we perform simulations on a simple cubic lattice of linear sizes  $L = 16, 24$  and  $32$ . After equilibration, data for  $m^2$  and  $m^4$  are thermally averaged over  $10^6$  MCS, and then averaged over 100 ensembles of  $\{J_{ij}\}$ -configurations. Fig. 7.8 shows the plot of  $U_4$  vs.  $T$  for  $\epsilon = 1.0$ . As before,  $T_c$  is determined from the intersection of Binder-cumulant curves for different  $L$ . The  $T_c$ -values for various  $\epsilon$  are given in Table 7.2, and plotted in the inset of Fig. 7.8. For the pure case ( $\epsilon = 0$ ), we obtain  $T_c \simeq 2.202$ , which agrees with the values reported in the literature [8, 9, 11]. With increasing  $\epsilon$ ,  $T_c$  decreases to  $T_c(\epsilon = 2) \simeq 2.114$ . For  $d = 3$ ,  $T_c$  does not change significantly with  $\epsilon$ , in contrast to the  $d = 2$  case.

### 7.3.2.2 Ordering kinetics

Next, let us briefly discuss numerical results for domain growth in the  $d = 3$  RBXYM. The simulations are performed on cubic lattices of size  $128^3$ . The system is quenched at temperature  $T = 1.0 < T_c(\epsilon)$  [in the unit of  $J/k_B$ ] and evolved upto  $t = 10^6$  MCS. The statistical data presented here is averaged over

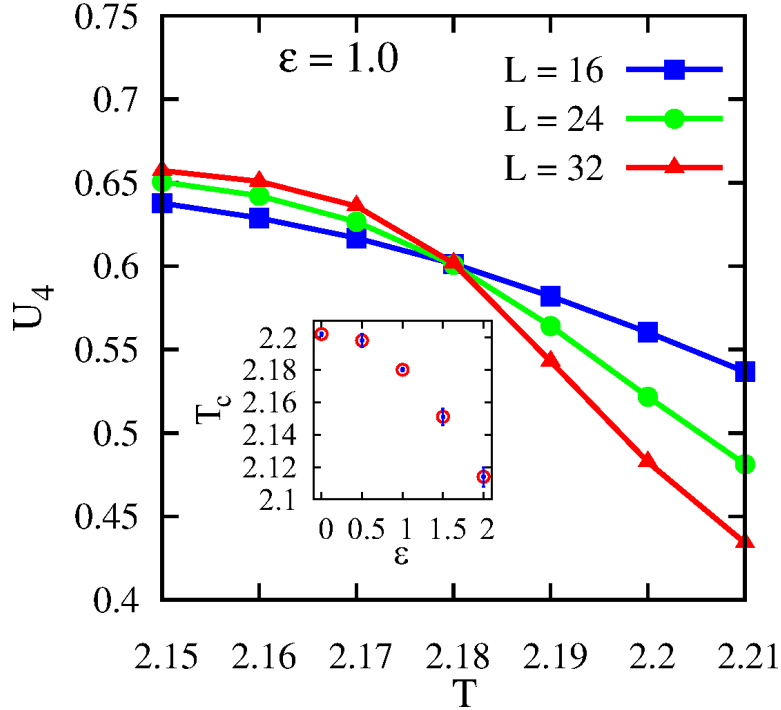


Figure 7.8: Plot of  $U_4$  vs  $T$  for  $d = 3$  RBXYM on a cubic lattices of  $L = 16, 24, 32$ . We show data for  $\epsilon = 1$ . In inset, we plot  $T_c$  vs  $\epsilon$ . For each  $\epsilon$ ,  $T_c$  is estimated from the intersection for different  $L$  curves.

10 independent realizations of disorder configurations.

Fig. 7.9(a) shows the typical evolution of the  $d = 3$  RBXYM system via topological defects for a temperature quench at  $T = 0.5$ . Here, the topological defects are of dimension 1, which are ‘strings’ or ‘vortex lines’ [24]. Fig. 7.9 shows the defect configuration of vortex-antivortex strings at  $t = 10^6$  for  $\epsilon = 0, 1, 2$ . The defect density reduces as the system evolves. In Fig. 7.9, we see that the defect density is higher for larger  $\epsilon$ , i.e., the growth is slower for larger values of  $\epsilon$ .

Fig. 7.10 shows the scaled correlation function,  $C(r, t)$  vs  $r/R(t)$ ; and the scaled structure factor,  $S(k, t)R(t)^{-3}$  vs.  $kR$ , for the evolution of the  $d = 3$  RBXYM after a quench at temperature  $T = 1.0$ . The data is shown for  $t = 10^5$  MCS and for  $\epsilon = 0, 1, 2$ . The solid lines in Fig. 7.10(a) and (b) denote the BPT function for  $n = 2$ , and the corresponding Fourier transform in  $d = 3$ , respectively. In Fig. 7.10(b), a dashed line of slope  $-5$  denotes the generalized Porod law:  $S(k, t) \sim k^{-(d+n)}$  for  $d = 3$  and  $n = 2$ . The data collapse is excellent, confirming

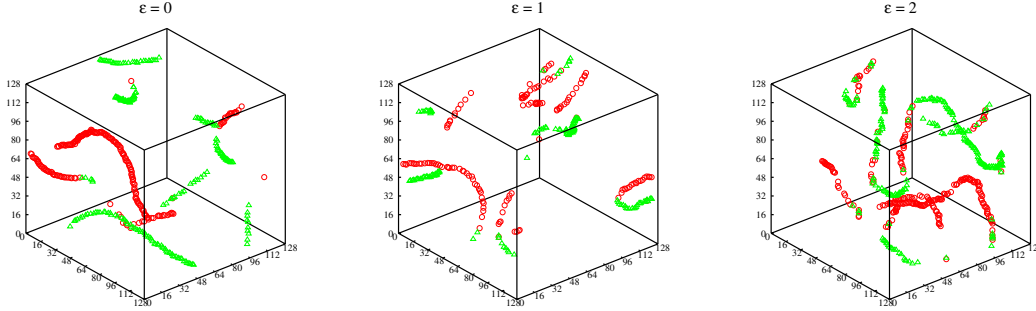


Figure 7.9: Typical defect-configurations of  $d = 3$  RBXYM for a temperature quench at  $T = 0.5$ . The lattice size is  $128^3$  and the configurations are shown at time  $t = 10^6$  and  $\epsilon = 0, 1, 2$ . These are the defect-configurations where we have shown only the topological defects of vortex and antivortex strings. Red-circles are marked for the vortices and green-triangles are the antivortices.

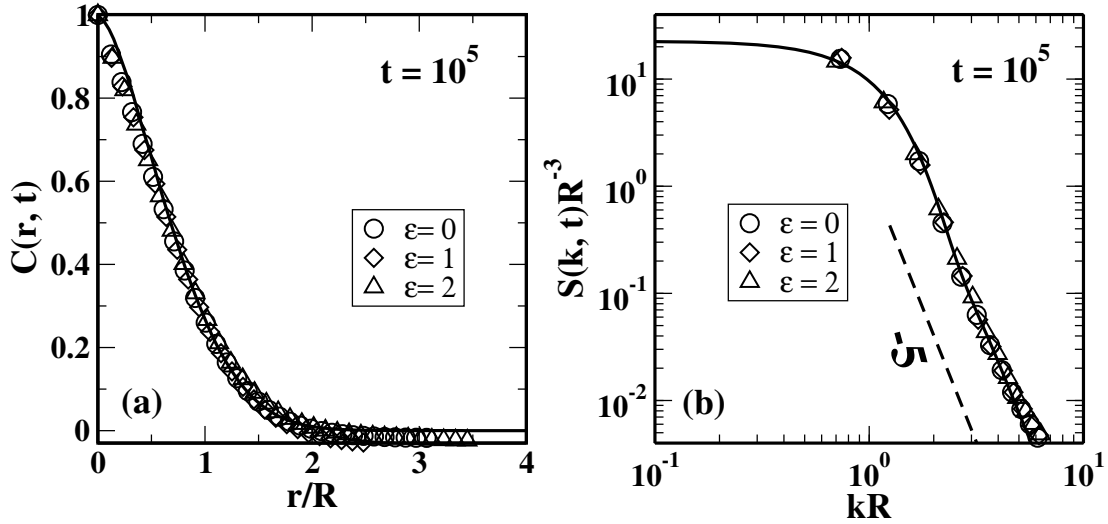


Figure 7.10: (a) Scaled correlation function,  $C(r, t)$  vs  $r/R(t)$ , for the evolution of 3D RBXYM after a quench at  $T = 1.0$ . We plot the data at a fix  $t = 10^5$  MCS for  $\epsilon = 0, 1, 2$ . (b) The corresponding scaled structure factor,  $S(k, t)R(t)^{-3}$  vs  $kR$ . The solid curves in (a) and (b) is the Bray-Puri-Toyoki (BPT) function [Eq. (7.14)] for  $n = 3$  and its Fourier transform, respectively. A dashed line of slope  $-5$  denotes the generalized Porod law:  $S(k, t) \sim k^{-(d+n)}$  for  $d = 3$  and  $n = 2$ .

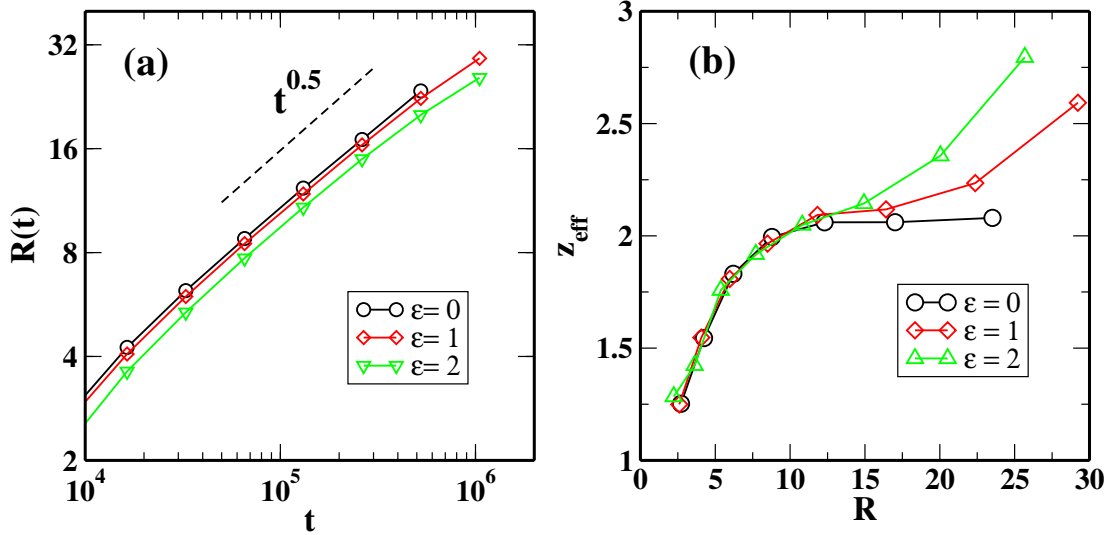


Figure 7.11: (a) Plot of  $R(t)$  vs  $t$  (on a log-log scale) for 3D random-bond  $XY$  model. The dashed line corresponds to the  $t^{1/2}$  growth for pure case. (b) Corresponding plot of  $z_{\text{eff}}$  vs  $R$  for the data in (a). Notice the slowing-down of growth at late times for higher  $\epsilon$ .

the universal behavior of the scaling function in  $d = 3$ , similar to the  $d = 2$  case.

Next in Fig. 7.11(a), we show the plot of typical length scale  $R(t)$  for  $\epsilon = 0, 1, 2$ . The solid line denotes the asymptotic growth law for the pure case:  $R(t) \sim t^{1/2}$ , which is found in many non-conserved systems [26]. To analyze the type of the growth behavior, here we define the effective exponent as

$$\frac{1}{z_{\text{eff}}} = \frac{d[\ln R(t)]}{d[\ln t]}. \quad (7.19)$$

The corresponding plot for effective exponents,  $z_{\text{eff}}$  vs  $R$ , is shown in Fig. 7.11(b). For the pure case, asymptotic growth-exponent  $z_{\text{eff}}$  is  $\simeq 2.05$ , which agrees with the expected value. Here, one can notice the deviation of  $z_{\text{eff}}$  from the pure case to the disordered case at late times, which predict the slowing-down of growth at late times. However, this deviation is very small which also observed at very late time  $t > 10^5$  MCS. Therefore, the data is not sufficient to further analyze the type of the growth behavior, and we leave this issue open.

## 7.4 Summary and Discussion

Let us now conclude this chapter with a summary and a brief discussion of our results. We have undertaken a comprehensive numerical study of the random-bond  $XY$  model in  $d = 2$  and  $d = 3$ . First, we have determined the transition temperatures using the Binder-cumulant method. The system is equilibrated and the measurements for Binder-cumulant are performed using the Wolff single cluster updating algorithm. We observe a systematic decrease in the transition temperatures as the disorder amplitude  $\epsilon$  increases, which however doesn't alter the nature of transition—the QLRO in  $d = 2$  and LRO in  $d = 3$ . Then, we have studied the phase-ordering kinetics by the quenching the system below  $T_{\text{KT}}$  or  $T_c$  and evolving it upto  $10^6$  MCS with the help of the Metropolis algorithm. A summary of our results is as follow:

- (a) The quantitative change in the  $T_{\text{KT}}$  (or  $T_c$ ) with  $\epsilon$  in  $d = 2$  is more striking than in  $d = 3$ . In  $d = 2$ ,  $T_{\text{KT}}$  decreases from  $T_{\text{KT}}(\epsilon = 0) \simeq 0.902$  to  $T_{\text{KT}}(\epsilon = 2) \simeq 0.729$ . Whereas in  $d = 3$ , the  $T_c$  decreases from  $T_c(\epsilon = 0) \simeq 2.202$  to  $T_c(\epsilon = 2) \simeq 2.114$ .
- (b) For ordering kinetics, the correlation function exhibits a dynamical scaling in  $d = 2, 3$ , and the scaling function shows the universal behavior ( $\epsilon$ -independent). However, the SU is found to be violated.
- (c) In  $d = 2$ , the domain growth-law shows the power-law behavior with the disorder-dependent growth-exponent,  $R(t) \sim (t/\ln t)^{1/\bar{z}(\epsilon)}$ , in agreement with the RBIM study [37, 38].
- (d) In  $d = 3$ , the growth for disordered case is slower than the power-law of pure case at late times. But, our data is inadequate to further analyze the type of the growth-behavior.

Though we did a large-scale numerical study, we do not observe any logarithmic-growth upto the time-scale ( $10^6$  MCS) in our simulations. However, we don't exclude this possibility (atleast for high- $\epsilon$ ), if we further extend our simulation to a very long-time and probe the growth of the system in the late-time regime, but this will require a huge numerical effort.

## 7.4. Summary and Discussion

---

In conclusion, our result is the detailed analysis of the coarsening behavior in the random-bond  $XY$  model (in  $d = 2, 3$ ) and provides a general framework for understanding the domain-growth in the random-bond systems.

# References

- [1] A.J. Bray, *Adv. Phys.* **43**, 357 (1994).
- [2] D. J. Bishop and J. D. Reppy, *Phys. Rev. Lett.* **40**, 1727 (1978).
- [3] K. Epstein, A. M. Goldman, and A. M. Kadin, *Phys. Rev. Lett.* **47**, 534 (1981).
- [4] A. F. Hebard and A. T. Fiory, *Phys. Rev. Lett.* **44**, 291 (1980).
- [5] M. R. Beasley, J. E. Mooij, and T. P. Orlando, *Phys. Rev. Lett.* **42**, 1165 (1979).
- [6] A. N. Pargellis, S. Green and B. Yurke, *Phys. Rev. E* **49**, 4250 (1994).
- [7] K. J. Strandburg, *Rev. Mod. Phys.* **60**, 161 (1988).
- [8] M. Hasenbusch and S. Meyer, *Phys. Rev. B* **241**, 238 (1990).
- [9] W. Janke, *Phys. Lett. A* **148**, 306 (1990).
- [10] A. P. Gottlob and M. Hasenbusch, *Physica A* **201**, 593 (1993).
- [11] M. Ferer, M. A. Moore, and M. Wortis, *Phys. Rev. B* **8**, 5205 (1973).
- [12] V. L. Berenziskii, *Sov. Phys. JETP* **32**, 493 (1970).
- [13] J. M. Kosterlitz and D. J. Thouless, *J. Phys. C: Solid State Phys.* **6**, 1181 (1973).
- [14] J. M. Kosterlitz, *J. Phys. C: Solid State Phys.* **7**, 1046 (1974).

- 
- [15] T. Surungan and Y. Okabe, *Phys. Rev. B* **71**, 184438 (2005).
- [16] S. A. Leonel, P. Z. Coura, A. R. Pereira, L. A. S. Ml, , and B. V. Costa, *Phys. Rev. B* **67**, 104426 (2003).
- [17] J. J. Alonso, *J. Magn. Magn. Mater* **322**, 1330 (2010).
- [18] A. K. Murtazaev, A. B. Babaev, *J. Magn. Magn. Mater* **321**, 2630 (2009).
- [19] A. B. Harris, *J. Phys. C: Solid State Phys* **7**, 1671 (1974).
- [20] G. M. Wysin, A. R. Pereira, I. A. Marques, S. A. Leonel, and P. Z. Coura, *Phys. Rev. B* **72**, 094418 (2005).
- [21] G. Kohring, R. E. Shrock, and P. Willst, *Phys. Rev. Lett.* **57**, 1358 (1996).
- [22] S. Puri and C. Roalnd, *Phys. Lett. A* **151**, 500 (1990).
- [23] S. Puri, *Phys. Lett. A* **164**, 211 (1992).
- [24] A. J. Bray and S. Puri, *Phys. Rev. Lett.* **67**, 2670 (1991).
- [25] B. Yurke, A. N. Pargellis, T. Kovacs, and D. A. Huse, *Phys. Rev. E* **47**, 1525 (1993).
- [26] A. J. Bray and A. D. Rutenberg, *Phys. Rev. E* **49**, R27 (1994).
- [27] A. J. Bray, A. J. Briant, and D. K. Jervis, *Phys. Rev. Lett.* **84**, 1503 (2000).
- [28] M. Cheon, K. Chung, M. Heo, and I. Chang, *Journal of Korean Physical Society* **53**, 527 (2008).
- [29] S. Puri and N. Parekh, *J. Phys. A: Math. Gen.* **26**, 2777 (1993).
- [30] E. Oguz, A. Chakrabarti, R. Toral, and J. Gunton, *Phys. Rev. B* **42**, 704 (1990).
- [31] E. Oguz, *J. Phys. A: Math. Gen.* **27**, 2985 (1994).
- [32] M. Rao and A. Chakrabarti, *Phys. Rev. Lett.* **71**, 3501 (1993).



- 
- [33] C. Aron, C. Chamon, L. F. Cugliandolo, and M. Picco, J. Stat. Mech. P05016 (2008).
- [34] M. Kumar, V. Banerjee and S. Puri, Europhys. Lett. **117**, 10012 (2017).
- [35] F. Corberi, E. Lippiello, A. Mukherjee, S. Puri, and M. Zannetti, Phys. Rev. E **85**, 021141 (2011).
- [36] F. Corberi, E. Lippiello, A. Mukherjee, S. Puri, and M. Zannetti, J. Stat. Mech., P03016 (2011).
- [37] R. Paul, S. Puri and H. Rieger, Europhys. Lett. **68**, 881 (2004); Phys Rev. E **71**, 061109 (2005).
- [38] M. Henkel and M. Pleimling, Phys. Rev. B **78** 224419 (2008); F. Baumann, M. Henkel and M. Pleimling, arXiv:0709.3228, (2007).
- [39] M. Henkel and M. Pleimling, Europhys. Lett. **76**, 561 (2006).
- [40] J. H. Oh and D.-I. Choi, Phys. Rev. B **33**, 3448 (1986).
- [41] R. Loft and T. A. DeGrand, Phys. Rev. B **35**, 8528 (1987).
- [42] F. Rojas and A. D. Rutenberg, Phys. Rev. E **60**, 212 (1999).
- [43] R. E. Blundell and A. J. Bray, Phys. Rev. E **49**, 4925 (1994).
- [44] J.-R. Lee, S. J. Lee, and B. Kim, Phys. Rev. E **52**, 1550 (1995).
- [45] H. P. Ying, B. Zheng, Y. Yu, and S. Trimper, Phys. Rev. E **63**, 035101 (2001).
- [46] M. Mondello and Nigel Goldenfeld, Phys. Rev. A **42**, 5865 (1990); Phys. Rev. E **47**, 2384 (1993).
- [47] A. J. Bray and K. Humayun, J. Phys. A: Math Gen. **23**, 5897 (1990); *ibid.* **25**, 2191 (1992).
- [48] R. E. Blundell, A. J. Bray, and S. Sattler, Phys. Rev. E **48**, 2476 (1993).

- 
- [49] A. J. Bray, Phys. Rev. E **47**, 228 (1993).
- [50] H. Toyoki, Mod. Phys. Lett. B **7**, 397 (1993).
- [51] T. J. Newman, A. J. Bray, and M. A. Moore, Phys. Rev. B **42**, 4514 (1990).
- [52] G. F. Mazenko and M. Zannetti, Phys. Rev. Lett. **53**, 2106 (1984); Phys. Rev. B **32**, 4565 (1985).
- [53] A. Coniglio and M. Zannetti, Europhys. Lett. **10**, 575 (1989).
- [54] H. Toyoki and K. Honda, Prog. Theor. Phys. **78**, 237 (1987).
- [55] H. Toyoki, Phys. Rev. A **42**, 911 (1990).
- [56] U. Wolff, Phys. Rev. Lett. **62**, 361 (1989).
- [57] N. Metropolis, A. W. Rosenbluth, M. N. Rosenbluth, A. H. Teller, and E. Teller, J. Chem. Phys. **21**, 1087 (1953).
- [58] J. F. Fernandez, M. F. Ferreira, and J. Stankiewicz, Phys. Rev. B **34**, 292 (1986).
- [59] J. Tobochnik and G. V. Chester, Phys. Rev. B **20**, 3761 (1979).
- [60] R. Gupta and C. F. Baillie, Phys. Rev. B **45**, 2883 (1992).
- [61] B. Zheng, M. Schulz, and S. Trimper, Phys. Rev. E **59**, R1351 (1999).
- [62] K. Binder and D. P. Landau, A Guide to Monte Carlo Simulations in Statistical Physics (Cambridge University Press, 2005).
- [63] K. Binder, Z. Phys. B **43**, 119 (1981).
- [64] D. Loison, J. Phys.: Condens. Matter **11**, L401 (1999).
- [65] M. Hasenbusch, J. Stat. Mech. **2008**, P08003 (2008).
- [66] H. Toyoki, Phys. Rev. B **45**, 1965 (1992).
- [67] A. D. Rutenberg and A. J. Bray, Phys. Rev. E **51**, 5499 (1995).

- [68] A. J. Bray, Phys. Rev. E **62**, 103 (2000).
- [69] S. Puri and N. Parekh, J. Phys. A: Math. Gen. **25**, 4127 (1992).
- [70] M. F. Gyure, S. T. Harrington, R. Strilka and H. E. Stanley, Phys. Rev. E **52**, 4632 (1992).
- [71] F. Corberi, C. R. Physique **16**, 332 (2015).